

eman ta zabal zazu



Universidad Euskal Herriko
del País Vasco Unibertsitatea

**UNIVERSIDAD DEL PAÍS VASCO /
EUSKAL HERRIKO UNIBERTSITATEA**
Facultad de Ciencia y Tecnología
Departamento de Química Inorgánica

Development of ceramic lithium ion electrolytes for high performance batteries

*A dissertation submitted to the University of the Basque Country
in partial fulfillments of the requirements for the degree of Ph.D.*

By

William Manalastas, Jr

Thesis Advisors:

Dr. Frederic Aguesse

Prof. John Anthony Kilner

Tutor:

Prof. Teófilo Rojo

December 2016

a mi familia

I believe that mathematical reality lies outside us, that our function is to discover or observe it, and that the theorems which we prove, and which we describe grandiloquently as our "creations," are simply the notes of our observations.

Godfrey Harold Hardy

Acknowledgments

My deepest gratitude goes, first of all, to my supervisors, John for having been a Master Yoda to me in the art of ceramics engineering, and Fred, my Obi-wan Kenobi since the first day I started this journey until its last. As their padawan, I have had my fair share both of “Eureka!” and disheartening moments, but they have been always there to guide me back to a rebalanced footing. This work is fruit of their patient dedication in nurturing their apprentices, in my case having empowered me to contribute in international conferences and attend workshops in 5 countries. I believe I will continue to dote upon them for many years to come, when I myself begin guiding another young padawan.

I thank my examiners for devoting the time and hope you may find delight and thought-provoking arguments as you pore through this work. I thank future readers as well and offer my best wishes that these accounts may help you.

I would also like to acknowledge funding from the CIC energigUNE fellowship and the ETORTEK program (Energigune13), which enabled me to pursue materials science for the past 4 years and interact with the wonderful people here in Spain, in Lithuania and in the United Kingdom.

With that, I am honored to have had Jokin Rikarte (inhouse), Juan Miguel Lopez del Amo (inhouse), Richard Chater (Imperial College London) and Tomas Salkus (Vilnius University) join ship in my curious ventures as my primary collaborators on experiment, and Randy Jalem (Nagoya University) as my primary collaborator on simulations. A great pleasure it has been with you, and cheers to the future!

My warm appreciation goes to my teammates and ex-teammates (Carlos, Anna, Lucy, Man, Ronan, Long, Audrey, Jakub and Brahim), fellow pilgrims in the quest for enlightenment in ceramic electrolytes for lithium-metal batteries. Throughout, I have also been indebted to Montse Casas, Marine Reynaud, Montse Galceran and Damien Saurel for helpful discussions which significantly advanced my grasps of diffraction-data refinement, electron microscopy and circuit analyses. In particular, I owe special thanks to Jon Ajuria for having granted me autonomy privileges in operating the SEM, the unbridled access to which was crucial for my experiments and made my PhD life so much easier.

On lighter notes, I will look back with smiles remembering Elena V., Nuria G., Julie, Eli, Javi C., Begoña A., Cristina B., Oihane, Roshan, Elena G., Nagore, Laida, Aitor V., Juan-Luis, Eider,

Gurpreet, Nebil, Ben and Lide who colored my daily office life. To my PhD buddies Antonio, Maider, Nerea, Aitor, Marya, Paula, Imanol, Edurnix and Elena, thank you for bringing me into the fold of your humor, celebrations and commiserations (which gave me invaluable companionship while in Spain); to Roman, for teaching me how to read Cyrillic; to Richard and Cristina U., for teaching me proper Castellano; to the Chinese community Yan, Chunmei, Javi, Jojo, Wei, Heng and Wangyang, for taking me in as adopted member and giving me a sense of belonging; to the Rockstar from TES, long may you live!

A wholehearted hug to Eva, blessed she be for having been my savior during all those nights I would have otherwise gotten marooned at work. Many thanks also to Abdo, Oleks, Cesar and most especially Cristina L., for the countless rides back home and your awesome company. I owe many thanks also to Teo, Asier, Iñaki, Cristina F., Silvia A., Desi, Sara, Begoña O., Lola, Jesus and Jose for always having been supportive in various ways and having taken care of innumerable administrative stuff to facilitate my smooth stay with the research center.

I have fond memories of Tomas, Vilma, Saulius, Edvardas, Algis, Dalius and Prof. Orliukas for a most enjoyable visit in Vilnius, and look forward to my turn hosting you. To friends from Imperial: Celeste and Mabel, thank you for introducing me to the world of Agricola and Munchkins; Sam, for staying to accompany until midnight on my final day at Imperial; Matt and Duke, for being awesome and cool seatmates; Florent (2x), Rowena, Chi, Cheng, Na, Ting, Andrea, Zonghao, George, Ainara, Stephen and the Spanish staff for warmly bringing me into the embrace of the Electroceramics group at Imperial.

To Morgane and Marijo, I will miss you... thank you for having treated me as family all these years...

To Seb, for having been my trusty buddy through thick and thin, in so many occasions full of emotion.

To Costana, Doc Nikko, Dr. J, Kuya Eben and Kasai-sensei, for having been sincere mentors who taught me so many things about this world. And to that list, I would also like to add Long-sempai, who informally gave me so much advice and readily extended help even when he had no obligation to.

Lastly, I owe the most to my wonderful wife and my awesome parents, for having believed in me for all this time, for their unconditional love, and for their commitment that no matter what happens, I would always have a warm home and hearts to go back to.

Table of Contents

Resumen	i
Abstract.....	viii
List of abbreviations ..	ix
1 Introduction	1
1.1 General background.....	1
1.1.1 Lithium-ion batteries: the perspective from the EV industry	1
1.1.2 The danger with organic liquid electrolytes	4
1.1.3 The design of solid electrolytes.....	6
1.1.4 Solid electrolyte candidates.....	7
1.2 Bibliographic review.....	16
1.2.1 $\text{Li}_5\text{La}_3\text{Ta}_2\text{O}_{12}$ syntheses in literature	16
1.2.2 $\text{Li}_7\text{La}_3\text{Zr}_2\text{O}_{12}$ syntheses in literature	22
1.3 Scope of the project.....	33
2 Experimental Framework	41
2.1 Polycrystalline ceramics production	41
2.1.1 Synthesis routes	41
2.1.2 Control of firing conditions	42
2.1.3 Green-body pressing.....	46
2.1.4 Pellet firing	46
2.1.5 Pellet polishing	46
2.1.6 Density measurement.....	46
2.2 Materials characterization	47
2.2.1 Structural and morphological characterization	47
2.2.2 Physico-chemical characterization.....	53
2.2.3 Electrochemical characterization.....	60
3 $\text{Li}_5\text{La}_3\text{Ta}_2\text{O}_{12}$: exploration of synthesis routes	71
3.1 Molecular dynamics simulations (mechanistic basis).....	71
3.2 Synthesis of stoichiometric $\text{Li}_5\text{La}_3\text{Ta}_2\text{O}_{12}$	72
3.3 Syntheses of $\text{Li}_{6.5}\text{La}_3\text{Ta}_{1.5}\text{Zn}_{0.5}\text{O}_{12}$ and $\text{Li}_{6.4}\text{La}_3\text{Ta}_{1.3}\text{Sc}_{0.7}\text{O}_{12}$	83
3.4 Chapter summary and perspectives	86

4	Li ₇ La ₃ Zr ₂ O ₁₂ (Ga-doping): synthesis for optimal Li-ion conductivity.....	93
4.1	Rationale	93
4.2	Molecular dynamics (MD) simulations	95
4.3	Experimental syntheses	96
4.3.1	Effects of choice of substitution site (Li vs Zr)	97
4.3.2	Effects of moisture on phase purity.....	101
4.3.3	Effects of Ga-substitution level	106
4.3.4	Effects of excess lithium in starting stoichiometry	110
4.4	Chapter summary.....	113
4.5	Perspectives	114
5	Li ₇ La ₃ Zr ₂ O ₁₂ (Ga-doping): On handling, storage and contamination	119
5.1	Effects of moisture on ionic diffusion	119
5.1.1	Moisture-corrosion effects on Li-ion conductivity: pellet level.....	121
5.1.1	Moisture-corrosion effects on Li-ion conductivity: powder level ..	123
5.1.2	Proton-diffusion in bulk ceramics: FIB-SIMS experiments	132
5.2	Effects of crucible choice/sintering protocol.....	136
5.3	Chapter summary and perspectives	152
6	Ceramic electrolyte integration in a full-cell device.....	155
6.1	Rationale	155
6.2	Experiments	158
6.3	Results and discussion	161
6.3.1	Charge/discharge cycling with LiFePO ₄ in a battery cell.....	161
6.3.2	Voltage bias experiments in multiple configurations	167
6.3.3	Thermal melting of Li metal on the ceramic electrolyte	182
6.4	Chapter summary and perspectives	190
7	General conclusions and perspectives	195
APPENDIX		
A.	On the model used for molecular dynamics simulations.....	197
B.	On the thermal reduction of Li ⁺ , Ga ³⁺ , La ³⁺ and Zr ⁴⁺ ions to their metallic states.....	198
C.	Modeling of lithium as a fluid reservoir	201
D.	Maximum compression work done at a point on the lithium metal/ceramic electrolyte interface with electrodeposition	203

Resumen

La presente tesis doctoral comenzó en Febrero del 2013, momento en el cual el doctorando fue contratado por el centro de investigación CIC Energigune, bajo la supervisión del Prof. John Kilner y Dr. Frederic Aguesse y, por el primer año, del Dr. Carlos Bernuy-López. La tesis ha sido adscrita en el Departamento de Química Inorgánica de la EHU/UPV y gran parte de la misma se realizó en las instalaciones que posee el centro de investigación CIC Energigune en el Parque Tecnológico de Álava (Miñano, Álava). La labor de este centro está enfocada al Almacenamiento de Energía, encuadrándose la presente tesis en el departamento de Almacenamiento de Energía Electroquímica, concretamente en el grupo de Electrolitos Sólidos, así como en los proyectos de investigación financiados por el Gobierno Vasco (Etortek10).

La tesis doctoral versa sobre del estudio de materiales cerámicos conductores de iones-litio, en concreto aquellos con estructura de granate (“garnet” en inglés) para aplicaciones como electrolito en baterías recargables de ión-litio. Para lo cual se estudiaron su estructura, sinterización, estabilidad, propiedades de transporte, y mecanismos de fallo como electrolito cerámico bajo polarización.

Las investigaciones expuestas se centran principalmente en dos familias de materiales sólidos: $\text{Li}_5\text{La}_3\text{Ta}_2\text{O}_{12}$ y $\text{Li}_7\text{La}_3\text{Zr}_2\text{O}_{12}$, para obtener un alta conductividad de iónica (10^{-3} S/cm) a temperatura ambiente. Tales materiales cerámicos permiten desarrollar baterías adecuadas para herramientas electrónicas de la sociedad moderna, las cuales requieren alta potencia y alta capacidad. Además pueden competir con electrolitos orgánicos líquidos (10^{-2} S/cm).

Hay tres motivaciones principales que dieron lugar a este trabajo:

- En primer lugar hacer realidad el uso de litio metálico como ánodo de baterías. Esto incrementaría al menos 10 veces la capacidad proporcionada por el grafito (actualmente empleado como ánodo de baterías de ordenadores portátiles y móviles). Por consiguiente, esta tesis se ha centrado en desarrollar un electrolito que podría conducir iones-litio y a la vez bloquear la penetración del litio metálico gracias a su

fortaleza mecánica, así que prevenir cortocircuitos que conducen inevitable muertes prematuras de baterías.

- En segundo lugar, a diferencia del resto de electrolitos (líquidos y polímeros), los electrolitos cerámicos previenen posibles explosiones y, en consecuencia, evitan el posible daño a las personas y a los equipos en los que estén integrados. Esto se debe a que los óxidos inorgánicos son totalmente incombustibles y no se descomponen a altas o bajas temperaturas, como demuestran las experiencias en módulos tecnológicos situados en medioambientes extremos (como es el espacio exterior). Esto representa una mejora significativa en la seguridad de la batería y es una propiedad muy valiosa. También, cabe destacar la amplia ventana de estabilidad electroquímica de esta familia de cerámicos, la cual limita la aplicabilidad los electrolitos orgánicos y sus compuestos.
- El tercer beneficio de los electrolitos cerámicos basados en óxidos es que únicamente conducirán los cationes; esto significa que los gradientes de concentraciones de aniones y su contribución a la resistencia interna a altas corrientes puede ser eliminada.

Por estas tres razones los electrolitos cerámicos representan, en principio, el “Santo Grial” del almacenamiento de energía electroquímica para aplicaciones que requieran condiciones extremas.

En esta tesis se presentan revelaciones sobre síntesis de óxidos de estructura de granate derivadas de trabajos experimentales, obtenidas mediante la combinación de diversas técnicas: difracción rayos-X (*XRD*, por sus siglas en inglés *X-Ray Diffraction*), espectroscopia de resonancia magnética nuclear (*NMR*, *Nuclear Magnetic Resonance spectroscopy*), microscopia electrónico de barrido (*SEM*, *Scanning Electron Microscopy*) y, finalmente, gracias a un colaboración con el Dr. Randy Jalem del *Nagoya University (Japon)*, simulaciones modelizadas (*MD*, *Molecular Dynamics*). Aquí se representa un resumen del trabajo en electrolitos cerámicos del centro de investigación desde su concepción. Así, una gran parte de la tesis se centra en establecer qué parámetros de la síntesis son importantes y cuáles no, para conseguir muestras cerámicas de alto rendimiento.

Por ejemplo, ya se ha visto que los conductores superiónicos de litio son muy reactivos a la humedad y dióxido de carbono, pero en las más de 200 publicaciones sobre estos materiales no presta atención a este factor durante la síntesis (ver Capítulo 1). Además, el rango de las conductividades reportadas, que es un indicador importante del rendimiento, es demasiado ancho (¡a veces variando 4 órdenes de magnitud para la misma composición!) y son destacables los problemas de reproducibilidad y falta de comprensión de las reacciones. Por esto, era necesario un estudio profundo y controlado para establecer un protocolo razonable para la producción a gran escala. En corolario, hay que tener en cuenta las trampas en síntesis para qué investigadores podrían expandir más este proyecto en estudios como cinéticos, síntesis en películas delgadas, defectos de dislocación y mucho más. Por lo tanto, esta tesis representa una etapa de gran importancia para asegurar que los estudios futuros sean reproducibles sistemáticamente y sin perjuicio de fiabilidad.

Para conseguir argumentos robustos y conclusiones definitivas, el doctorando ha realizado una estancia de 3 meses en Imperial College London (Reino Unido) realizada en el laboratorio del Dr. Ainara Agüero. La finalidad de dicha estancia, fue estudiar la difusión de isótopos en los cerámicos sintetizados, a través de los principios del “depth-profiling” y “focused ion-beam secondary ion mass spectrometry” (FIBSIMS). Además, el doctorando ha realizado medidas de espectroscopia de impedancia electroquímica (*EIS* o *Electrochemical Impedance Spectroscopy*) de banda ancha desde temperatura ambiente hasta altas temperaturas (800 K), colaborando con el Dr. Tomas Salkus en Vilnius University (Lituania).

El FIBSIMS se ha utilizado para estudiar la difusión de los protones en un cristal de granate y la evolución de la polarización del cerámico en contacto con litio metálico. Junto con la espectroscopia Raman y microscopia óptica, esta ha sido una técnica de gran utilidad para conocer la eventual modificación de la microestructura del material cerámico debida a la difusión dichos iones. Por otro lado, la EIS ha sido ampliamente utilizada para cuantificar valores de conductividad iónica de los materiales cerámicos estudiados y analizar los componentes (*bulk, grain boundary, interfacial resistances*) que la limitan. En cuanto a los métodos de síntesis llevados a cabo, han sido la síntesis en estado sólido y sol-gel.

El proyecto de tesis se estructura en un capítulo introductorio, la descripción de las técnicas experimentales empleadas, cuatro capítulos que contienen los resultados experimentales obtenidos y un capítulo final con las conclusiones generales. Finalmente, en un anexo se han descrito detalles sobre algunas computaciones termodinámicas.

Capítulo 1: Introducción

En el capítulo 1 se presentan brevemente las facetas económicas, reflejando que la demanda de baterías recargables de iones-litio mejores, más baratas y con alta densidad de energía está continuamente incrementando, especialmente en aplicaciones de vehículos eléctricos. Por otro lado, las baterías convencionales están casi en sus límites técnicos, y para seguir avanzando se necesitaría de una tecnología alternativa. Para superar la tecnología del estado del arte, es necesario introducir nuevos electrolitos, como los estudiados en este trabajo. Como punto de partida, se enumeran los electrolitos disponibles en la literatura como candidatos prometedores y se discute sobre las ventajas y desventajas de cada uno.

Además, se describe la estructura cristalina del granate junto con una revisión bibliográfica sobre $\text{Li}_5\text{La}_3\text{Ta}_2\text{O}_{12}$ y $\text{Li}_7\text{La}_3\text{Zr}_2\text{O}_{12}$. Para estos compuestos se muestran los diagramas de fases asociados y sus reacciones secundarias vinculadas con procesos de recocido. Toda esta información será útil en los siguientes capítulos.

Capítulo 2: Experimental

En el capítulo 2 se explican los principios fundamentales de los procedimientos experimentales utilizados. También se incluirá una descripción de los métodos de calibración, crucial para una buena interpretación de los datos experimentales, y equipos de adquisición de datos.

Este capítulo incluye asimismo la descripción del proceso de preparación de los materiales cerámicos, sus caracterizaciones estructurales, morfológicas, fisicoquímicas y electroquímicas.

Capítulo 3: $\text{Li}_5\text{La}_3\text{Ta}_2\text{O}_{12}$ - exploración de las rutas de síntesis

En el capítulo 3, se muestra un análisis comparativo de las muestras de $\text{Li}_5\text{La}_3\text{Ta}_2\text{O}_{12}$ sintetizadas mediante dos procedimientos diferentes: i) estado sólido y ii) sol-gel. Ambos métodos muestran ser muy efectivos para obtener la estructura cristalográfica deseada. No obstante, existen pequeñas diferencias entre ambos procedimientos de síntesis. El primero da lugar a sinterizaciones mucho más débiles, mientras que el segundo produce cerámicas más densas.

Además, se establece establecido que la conductividad iónica es independiente de los parámetros de red cristalográficos, pero si es función de la densidad. También se determina que los cerámicos con la composición estequiométrica $\text{Li}_5\text{La}_3\text{Ta}_2\text{O}_{12}$ no superan un valor de 10^{-4} S/cm incluso para una muestra completamente densificada. Por otro lado, el dopaje con escandio (y quizá otros elementos que aumenten el litio en la estequiometría) pueden superar este límite.

Capítulo 4: $\text{Li}_7\text{La}_3\text{Zr}_2\text{O}_{12}$ (Ga-doping) – síntesis para un conductividad óptima de ion-litio

A partir del capítulo 4, los resultados presentados corresponden a la síntesis sol-gel. Ya que los cerámicos con composición $\text{Li}_7\text{La}_3\text{Zr}_2\text{O}_{12}$ cristalizan en un polimorfo tetragonal (una estructura cristalográfica ordenada) que da lugar a bajas conductividades ($\sim 10^{-6}$ S/cm), una estrategia de sustitución parcial con galio es investigada para obtener un polimorfo cúbico (una estructura cristalográfica desordenada). Se investigan también los efectos de las posiciones de sustitución, nivel de sustituyente, exceso de litio y efecto de la humedad en la pureza de la fase sintetizada. Debido a estos experimentos, se determina que el Ga^{3+} muestra una mayor predisposición a sustituir posiciones de Li^+ en coordinación tetrahédrica (ver capítulo para visualización). Además, una composición que exhibe una conductividad de 1.3 mS/cm (la mayor para esta familia de materiales) se obtiene con la estequiometría $\text{Li}_{6.55}\text{Ga}_{0.15}\text{La}_3\text{Zr}_2\text{O}_{12}$ con un 10% de exceso de litio durante la preparación de los reactivos (es decir, 7.2 Li^+ en lugar de 6.55). Con un valor inferior las pastillas prensadas no sinterizan correctamente. Por otro lado, valores mayores provocan una contaminación elevada de Al^{3+} proveniente de los crisoles usados durante la cocción.

Se demuestra también que el parámetro cristalográfico de red no determina directamente la conductividad del litio en dichos cerámicos, sino que depende de la distribución de los iones de litio entre posiciones tetrahédricas y octahédricas en su subred.

Capítulo 5: $\text{Li}_7\text{La}_3\text{Zr}_2\text{O}_{12}$ (Ga-doping) – sobre la manipulación y contaminación

Siguiendo con el trabajo del capítulo 4, en el capítulo 5 se profundiza más en cuestiones del procedimiento y como evitar la contaminación de las muestras durante y posteriormente a sus síntesis. Se demuestra empíricamente que la humedad del ambiente y los crisoles, además de la velocidad de enfriamiento, en las que se lleva a cabo la sinterización afectan en gran medida a la estructura cristalográfica, microestructura y macroestructura de los productos cerámicos sintetizados. Se determina también mediante FIBSIMS que los protones no penetran de manera significativa en la estructura de granate aunque se utilice agua deuterada hirviendo (101.4°C). Asimismo, se muestra que los protones están concentrados solamente en las primeras 2 micras de la superficie de los cerámicos $\text{Li}_7\text{La}_3\text{Zr}_2\text{O}_{12}$ o $\text{Li}_{6.55}\text{Ga}_{0.15}\text{La}_3\text{Zr}_2\text{O}_{12}$, es decir que la profundidad de difusión de los protones no depende de la conductividad del litio.

En este capítulo también se determina un valor para la constante de difusión (D), $1.88 \times 10^{-12} \text{ cm}^2/\text{s}$ a 101.4°C , de protones en dichos cerámicos, el cual es muy bajo. Esto significa que el correcto sinterizado de dichos cerámicos permite el su transporte masivo independientemente de la atmósfera o condiciones atmosféricas, incluso bajo el agua. Lo que se necesita es simplemente pulir la superficie utilizando un láser de alta potencia. Finalmente, se muestra por primera vez visualmente la acción del aluminio para provocar un mecanismo de sinterización con un crecimiento anormal de grano o en inglés, *abnormal grain growth (AGG)*, de dichos cerámicos.

Capítulo 6: Integración del electrolito cerámico sobre una batería “full-cell”

Se ha montado una batería “full-cell” utilizando litio-metálico como ánodo, LiFePO_4 como material del cátodo, el $\text{Li}_{6.55}\text{Ga}_{0.15}\text{La}_3\text{Zr}_2\text{O}_{12}$ como electrolito cerámico y una pequeña cantidad de electrolito orgánico como “catholyte” (para aumentar el contacto entre el cátodo laminado y el cerámico, ya que ambos son sólidos rígidos). Durante los ciclos, se demuestra que el sistema podría utilizar la totalidad del material activo del cátodo, pero presenta problemas en sucesivas recargas. Se observa la rotura del material cerámico mediante la acción del litio metálico durante el proceso de polarización.

Este fenómeno está descrito y razonado utilizando ecuaciones termodinámicas y Newtonianas. Además, se demuestra también que el electrolito cerámico funciona como un fusible ya que detiene corto-circuitos debido a su baja conductividad térmica. Esta es una propiedad muy ventajosa que aporta más seguridad al sistema que lo integra.

En este capítulo también se muestra un esquema detallado de interacciones del litio metálico y el material cerámico.

Anexo

En el Anexo se describen los detalles más relevantes de sobre las simulaciones de dinámica molecular realizadas, predicciones termodinámicas utilizando diagramas de *Ellingham* y derivaciones de las ecuaciones de la presión causada por electrodeposición del litio-metálico sobre el superficie del cerámico durante la polarización.

Abstract

Balancing global energy demand and environmental sustainability calls for modular energy infrastructures. To be reliable, they need an energy vector that is flexible in time and space, a hallmark of Li-ion batteries. 21st century applications demand better batteries in terms of safety, power performance and storage efficiency, however, all of which cannot materialize without a superior solid electrolyte. A solid electrolyte that blocks electrons, blocks Li-dendrite formation, and conducts ions facily with a wide electrochemical stability window is the first-step towards Li-metal anodes and high-capacity cathode concepts. Ceramic oxide electrolyte technology seems promising for this and may make possible lower-cost, miniature or large-assembly devices.

'Li-stuffed' garnet ceramics with the general formula $\text{Li}_x\text{B}_3\text{C}_2\text{O}_{12}$ ($x>3$) are promising electrolytes for all-solid-state batteries for practical considerations: Li-ion conductivity rivaling liquids, wide voltage window ($>5\text{V}$ vs Li^+/Li), safety and lower interfacial resistance with common cathode/anode components compared to sulfur-based analogues. The objective of this project was to design Li-ion conducting garnet oxides through the understanding of the Li-mobility mechanisms and analysis of the relationship between crystal structure and lithium transport properties in different oxide materials.

An optimized synthesis protocol for fast-conducting cubic-phase $\text{Li}_{7-3x}\text{Ga}_x\text{La}_3\text{Zr}_2\text{O}_{12}$ materials was found. The crystallographic properties, atmospheric protonation effects and Li-ion-conductivities were monitored by XRD, MAS-NMR and EIS, respectively. Overall, the present study achieved four noteworthy points: 1) the finding that conductivity increases with less Ga-content and more Li-content; (2) fabricated ceramics with 93% relative densities by a readily-scalable simple process of uniaxial pressing and O_2 -gas sintering (cf. 70% for air-processed materials); (3) unprecedented room-temperature total conductivities 1.3 mS/cm in our air-isolated $\text{Li}_{7-3x}\text{Ga}_x\text{La}_3\text{Zr}_2\text{O}_{12}$ pellets by applying our moisture-exclusion protocol; (4) evidence of the instantaneous nature of proton-contamination. By avoiding proton-contamination from hampering Li-conduction, the study achieved stable and reproducible activation energies of 0.3 and 0.5 eV for air-protected and non-protected samples, respectively. Notably, air-processed ceramics present drops in ionic conductivity to the 0.001 mS/cm level.

An assembled full cell with LiFePO_4 cathode, organic catholyte, the garnet electrolyte and Li metal anode cycled well on discharge but not during the charging steps. A mechanism explaining why this occurs is presented.

LIST OF ABBREVIATIONS

acronym	meaning
AC	alternating current
ASTM	American Society for Testing Materials
ASR	associated surface resistance
BE	backscattered electrons
C	capacitance element
COD	Crystallography Open Database (by University of Cambridge)
CR	citrate-route
DC	direct current
DFT	Density Functional Theory
EDAX	energy-dispersive X-ray spectroscopy
EIS	electrochemical impedance spectroscopy
FIB-SIMS	focused-ion beam secondary ion mass spectrometry
Ga _{0.15} -LLZO	Li _{6.55} Ga _{0.15} La ₃ Zr ₂ O ₁₂
GB	grain boundary
ICP-OES	inductively-coupled plasma optical emission spectroscopy
ICSD	Inorganic Crystal Structure Database (by FIZ Karlsruhe and NIST)
IEDP	Isotopic Exchange Depth Profiling
LIB	lithium-ion battery
LIBS	laser-induced breakdown spectroscopy
LLZO	Li ₇ La ₃ Zr ₂ O ₁₂
MAS	magic-angle spinning
MD	molecular dynamics
<i>N</i>	dispersion factor (for constant-phase elements)
NMR	nuclear magnetic resonance
Oh	octahedral
PDF	Powder Diffraction File Database (by ICDD)
PSD	particle size distribution
PXRD	powder X-ray diffraction
<i>Q</i>	gas flowrate, constant-phase element or charge capacity (see usage)
<i>Q_{theo}</i>	theoretical charge capacity
<i>R</i>	resistance element
RT	room-temperature
RGA	residual gas analysis
SE	secondary electrons
SEM	scanning electron microscopy
SPN	simultaneous positive and negative
ssNMR	solid-state nuclear magnetic resonance
SSR	solid-state-route
Td	tetrahedral
<i>t_{Li+}</i>	lithium transference number (portion of total current carried by Li ⁺)

1 Introduction

Rechargeable Li-ion batteries (LIB) could replace gasoline as a universal energy vector. This is due to their favorable balance of energy/power densities, reversibility, lifetime, efficiency, zero gas emissions and practical integration to the preexisting electrical infrastructure. For these reasons, the global LIB market has grown to more than 10 billion US dollars today [1-2], and is expected to continue growing in the grid, automotive and consumer electronics sectors (Figure 1.1).

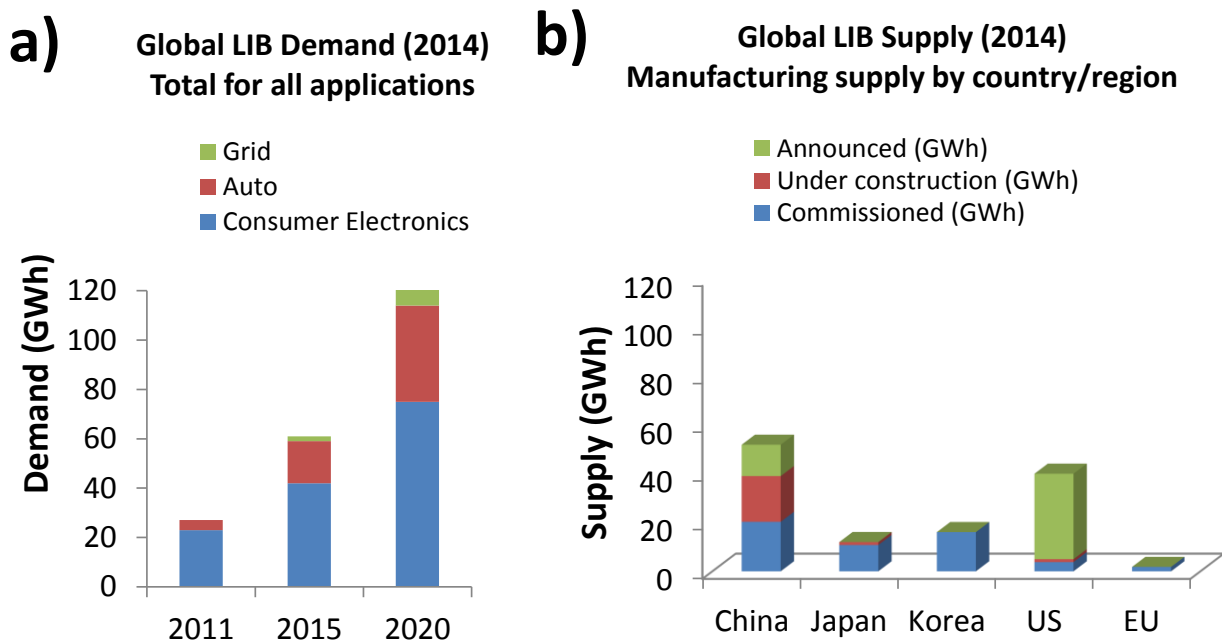


Figure 1.1: Projection of lithium-ion battery (a) demand per industry sector and (b) supply per country (modified from [3]).

1.1 General background

1.1.1 Lithium-ion batteries: the perspective from the EV industry

One hot topic concerning lithium-ion batteries (LIB) is the electrification of transport. Battery powertrains can propel vehicles from 0 km/h to 100 km/h and vice-versa within as little as 3 seconds, and with energy output unrestricted by Carnot thermodynamics (cf. 12.5% tank-to-wheel output using gasoline) [4, 5]. As part of its environmental benefits, modular batteries within automobiles can also double as auxiliary power supplies forming part of a smart-grid, i.e. while dormant in the garage they can shift the excess of generated electricity from off-peak hours to periods of peak demand [6].

Despite merits however, it is also the current state of lithium-ion battery technology which limits the mass-market adoption of electric vehicles (EV). Specifically, this is in terms of cost, drivable range and safety.

Battery costs (normalized per kWh) have been dropping steadily [7] due both to economies-of-scale and improved battery production (Figure 1.2). Manufacturing expenses are expected to be roughly 230 USD/kWh by the year 2018 with streamlining of anode/cathode production chains. Nonetheless, the United States Advanced Battery Consortium believes a more affordable level of 125 USD/kWh must be attained for EVs to be viable for the general population by the year 2020 [8]: an elusive goal considering cost trends [9]. One strategy to lower costs is reducing the amount of current collectors and packaging required (~30% of total LIB cost, [3]) by using more energy-dense materials, e.g. metallic lithium anodes and high-voltage cathodes.

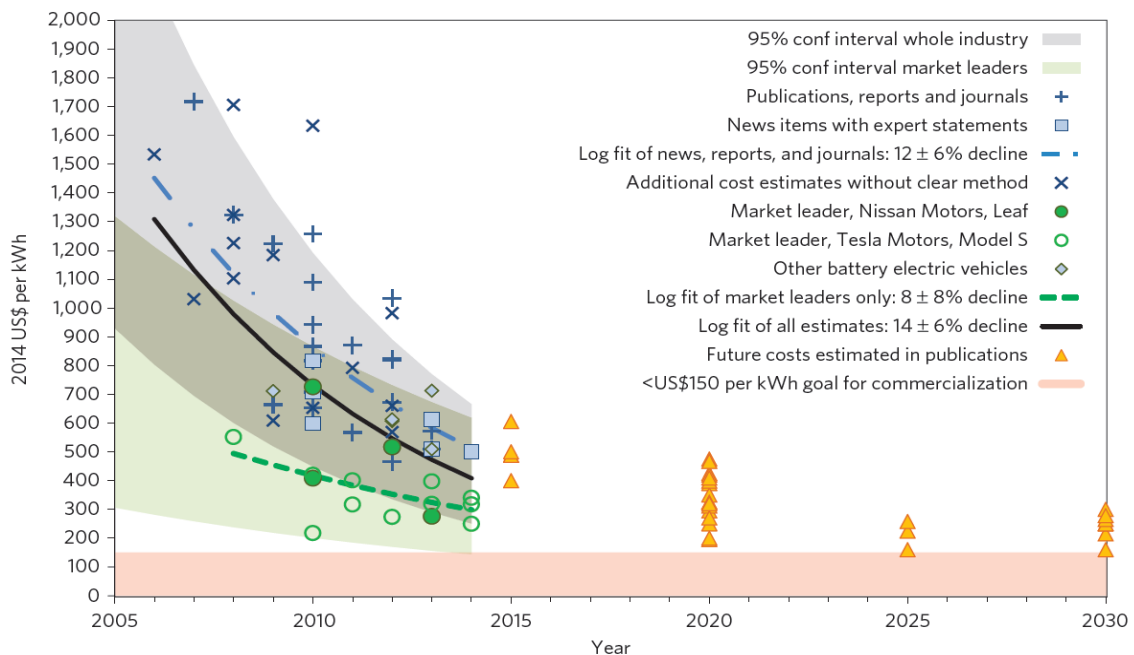


Figure 1.2: LIB cost projections on a kWh basis according to the electric vehicle industry (after [7]).

EVs will also require long mileage ranges and short recharging times to be a practical mode of transportation. Gasoline-based cars are capable of running ~800 km on a single full tank, with visits to the fuel station as short as 10 minutes for a refill. In contrast, top-of-the-line LIBs can only provide a maximum of 270 Wh/kg and 770 Wh/L on a single charge and must be plugged in overnight, translating to a maximum of 300 km mileage for a light automobile (Figure 1.3) on a per day basis. This is

already near the physicochemical limits of the commonly-used electrode materials [11], implying that the ability of EVs equipped with standard LIB technology to reach intercity destinations (e.g. the routine of the commuting workforce) and back is inherently restricted, unless new battery chemistries are developed.

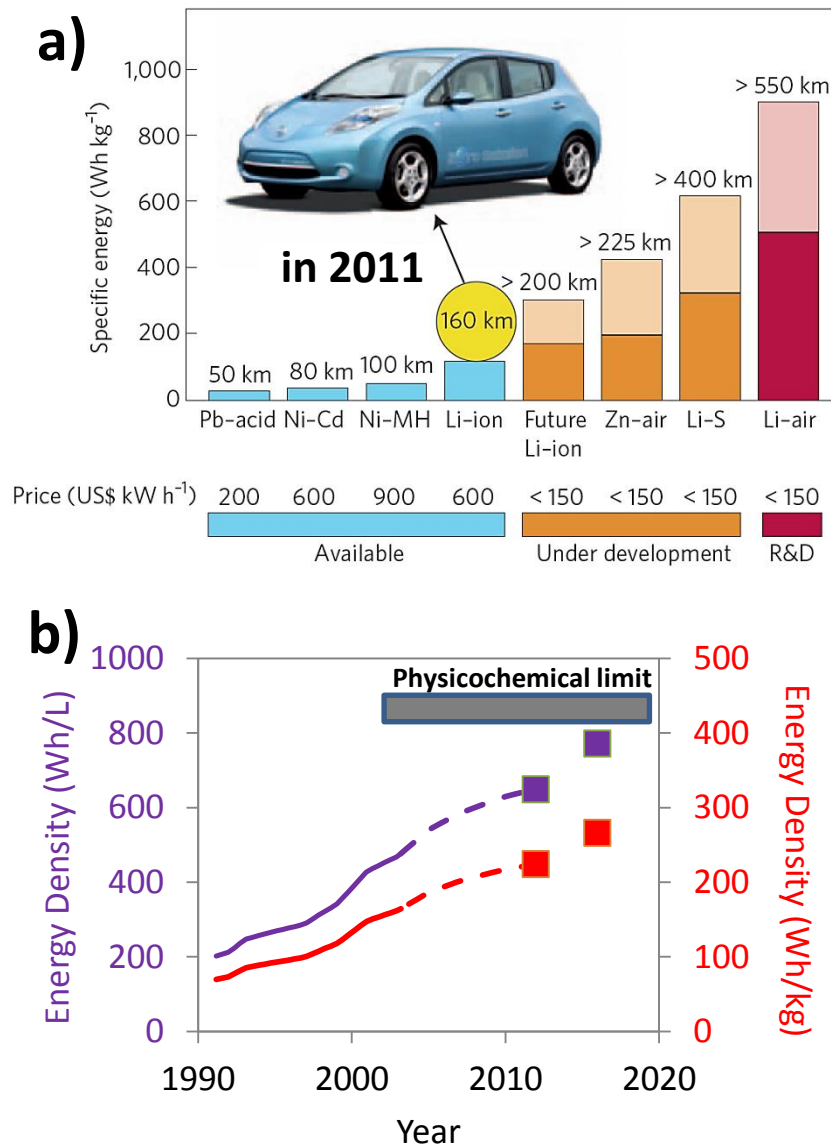


Figure 1.3: a) Outlook for vehicular mileage range as a function of battery chemistries (after [12]). b) Physicochemical limits of energy density in LIB systems (after [10, 11]).

The outlook for emerging battery chemistries such as lithium/sulfur and lithium/air systems is that they would pack higher energy densities. However, they also suffer from notorious parasitic reactions such as the polysulfide shuttle [13] or lithium oxide/peroxide irreversibility [10], which lock access to dischargeable capacities. The resultant poor cycling behaviors are an inherent consequence of using liquid organic electrolyte media. Besides this, electrolyte flammability is a critical safety hazard.

1.1.2 The danger with organic liquid electrolytes

Historically, Li-ion batteries proliferated as a combination of three key materials: graphite, lithium cobalt oxide (LCO) and separator sheets impregnated with lithium salts in cyclic carbonate solution (the Li^+ conducting electrolyte in Figure 1.4).

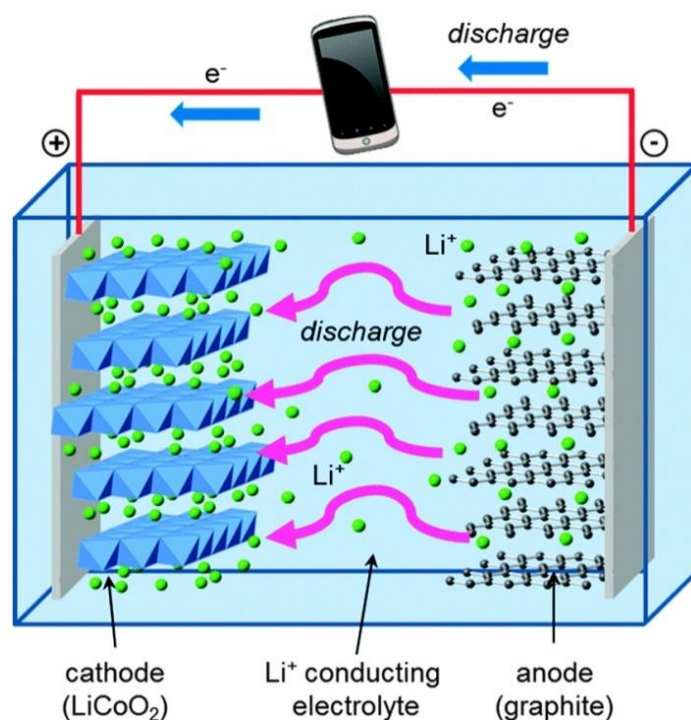


Figure 1.4: Schema depicting components of a traditional LIB and the Li-conducting electrolyte (after [14]).

The liquid electrolyte is responsible for maintaining wetting between all internal components, allowing for lithium shuttling as a coupled process to an external electronic discharge. Here, organic electrolytes have poor electrochemical stability, but battery operation as we know it is still possible thanks to the formation of a solid-electrolyte interphase (SEI) passivation layer which confers a virtual widening of the voltage stability window.* (see Peled for a deeper discussion on SEI [15]).

*The Pb-acid battery operates on this kinetic-limitation principle. A significant amount of hydrogen/oxygen gas evolution will occur at 1.3V with H_2SO_4 electrolyte using Pt electrodes, but a similar amount of decomposition current will occur with Pb electrodes only beyond 2V. Overpotential or voltage polarization losses derive from the product of current and internal resistance of the battery.

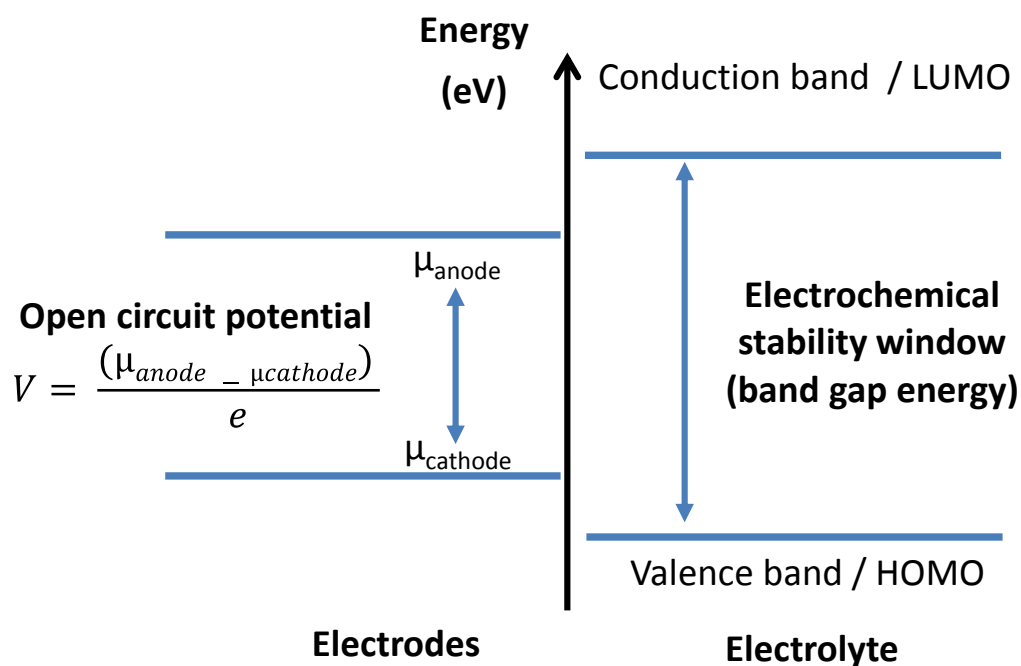


Figure 1.5: Schema of electrochemical potential window of an ideal electrolyte in relation to cathode/anode characteristic reaction potentials.

The chemical potential difference between the anode and the cathode store energy that can be delivered by the electrons (Figure 1.5). Releasing this energy in a controlled manner through the external circuit is prerequisite to a battery performing useful work. However, when electrons carrying high energies are provided an internal pathway of low resistance within the battery, a short-circuit occurs, sparking the organic electrolyte, culminating in a thermal runaway and ultimately a battery explosion.

The trigger for this is often a lithium metal dendrite which punctures the electronic insulation (e.g. a separator made of polypropylene or glass-fiber material) between the anode and the cathode. Dendrites occur with aging, poor manufacturing or current-density focusing under rapid charging in a conventional LIB.

The risk for dendrite-induced explosions can be managed by algorithms controlling current, voltage and internal temperature levels, but it will never be zero, unless the liquid organic electrolyte is replaced, for instance by an incombustible solid electrolyte.

1.1.3 The design of solid electrolytes

An ideal electrolyte has high ionic conductivity, low electronic conductivity and electrochemical stability against the various materials within the battery during charging/discharging cycles. These affect the battery in the following ways:

- a) A high ionic conductivity permits rapid charging and discharging for heavy-duty devices
- b) A low electronic conductivity ensures a low self-discharge of the battery during storage
- c) A wide electrochemical stability window enabling the use of metallic lithium anodes and high-voltage cathodes would open possibilities to drastic increases in energy density

A brief commentary on the common electrolyte systems is given:

Liquid organic electrolytes enable battery cycling up to 4V with high ionic conductivity ($\sim 10^{-2}$ S/cm at 25°C), but their risky flammable nature, leakage scenarios and inappropriate freezing temperatures are non-negotiable for large-scale applications. Alternatives such as ionic liquids do not combust and are stable up to 300-400°C [16] but are extremely difficult to produce and handle. Aqueous-based electrolytes would be very cheap, but would be limited to a meager ~ 1.3 V stability window (ergo low energy densities), short lifetime and electrode compatibility issues. Polymer-based electrolytes, on the other hand, are bottle-necked by low ionic conductivity ($\sigma \sim 10^{-5}$ S/cm at 25°C).

With that said, the lithium transference numbers (t_{Li^+} , which is the portion of current carried by lithium cations) in all these systems are low ($t = 0.3$ to 0.6), due to the propensity for counter-migration of anionic (e.g. LiX_2^- triplet) species [17] at high current demands. Whenever the negative charge is carried by internal ions instead of electrons traveling through an external circuit, energy is lost as heat.

As another disadvantage, these battery designs cannot prevent Li-dendrites from forming and short-circuiting the two electrodes, as current lines would always promote dendrite elongation once initiated within a Li^+ -rich liquid medium. This is unless auxiliary cation additives (e.g. Cs^+) are used, which in turn increase cell impedance [18, 19].

Inorganic Li-ion conductors could potentially solve all these problems and deliver, with mechanical blocking of dendrite formation on Li-metal anodes (as incorporated

within all-solid-state batteries) an added bonus. This was the context under which the present research was pursued.

1.1.4 Solid electrolyte candidates

Whether an all-solid-state battery will take minutes, hours or days to recharge will ultimately depend on how facile ion flux between the electrodes can occur. This implies great importance on the ionic conductivity of the solid electrolyte.

The Arrhenius plot illustrating the thermal dependence of ionic conductivities for various materials is presented in Figure 1.6. The best conductivity to date is that of the $\text{Li}_{10}\text{GeP}_2\text{S}_{12}$ solid electrolyte (12 mS/cm) reported by Kamaya *et al.*, which outperforms even liquid electrolytes at room temperature (considering the latter to be always applied in tandem with a non-ion conducting separator sheet, which reduces effective ion conductivity by 1-2 orders of magnitude) [20]. Despite apparently displaying electrochemical stability against Li metal on a macro level however, Wenzel has shown recently by in-situ XPS that $\text{Li}_{10}\text{GeP}_2\text{S}_{12}$ in fact decomposes at its interface with metallic lithium into Li_3P , Li_2S and a Li-Ge alloy [21].

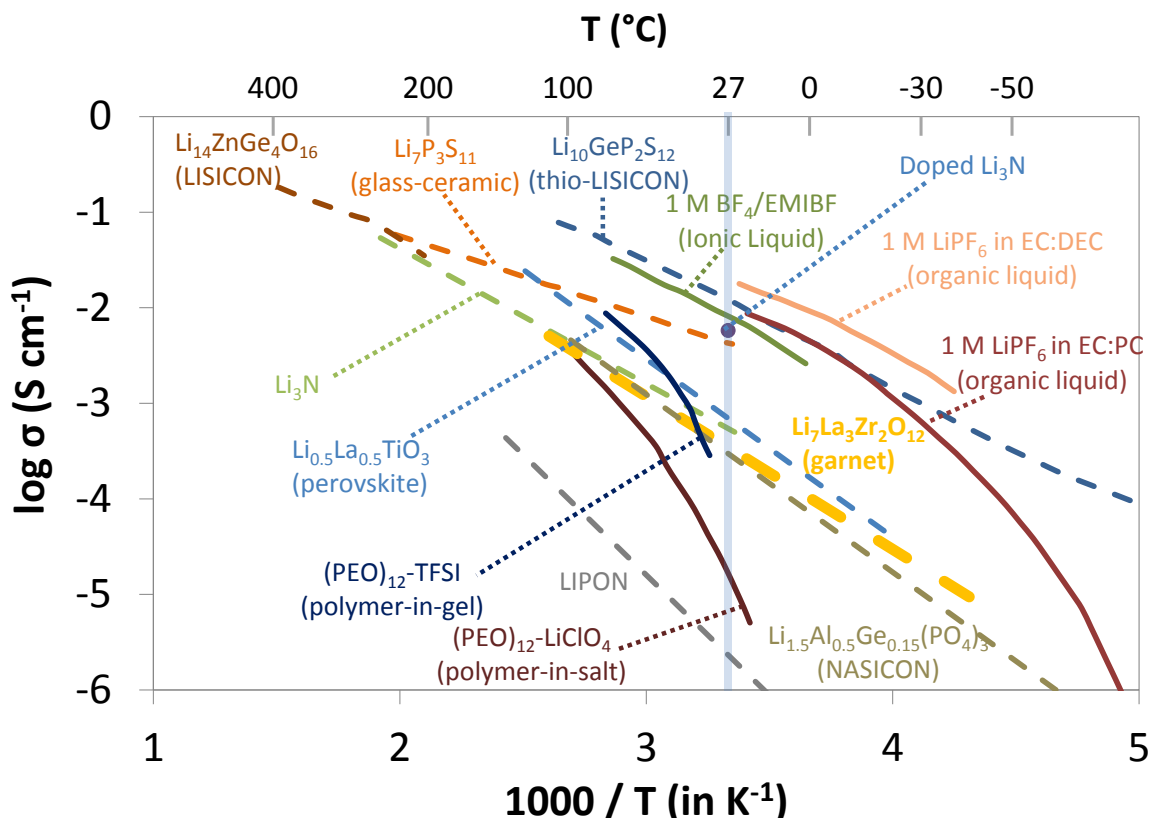


Figure 1.6: Temperature dependence of Li-ion conductivity behaviour of various electrolytes (modified after [11, 20]) Solid lines: organic electrolytes. Dashed lines: solid inorganic electrolytes.

Other candidate materials are examined below as potential Li-ion conducting electrolytes in all-solid-state batteries. Unless otherwise stated, the conductivity values mentioned correspond to those at room-temperature (25°C).

1.1.4.1 Polymers (dry-polymer-in-salt, and wet-polymer-in-gel)

Macromolecular branched polymers are generally valued for low density, ease of manufacturing and mechanical flexibility apt for absorbing volume changes caused by conversion reactions, for example in the case of high-capacity silicon anodes and metallic lithium anodes which undergo extreme expansion/contraction cycles.

However, they have practical ionic conductivities only when operating at temperatures higher than their respective glass transition temperatures (T_g), i.e. ion-motion is contingent on an amorphous solid-state. The reason is that Li-ion motion occurs via 3D voids produced at the atomic level by randomly-oriented polymer chains. The less stacking order there is, the higher the ion flux.

For instance, the joint action of plasticizers, ceramic additives and salts such as LiCF_3SO_3 , $\text{Li}(\text{CF}_3\text{SO}_2)_2\text{N}$, $\text{Li}(\text{C}_2\text{F}_5\text{SO}_2)_2$, LiClO_4 , $\text{LiB}(\text{C}_2\text{O}_4)_2$ dissolved in a polyethylene oxide (PEO) matrix reduces crystallinity and is a strategy already proven to improve polymer ion-conductivity, although still not enough for advanced applications at room-temperature. This is unfortunate for these “dry-polymer-in-salt” systems since PEO is electrochemically stable against Li-metal anodes and is known to resist dendrite-formation [22].

“Wet-polymers-in-gel” are soaked in liquid organic electrolyte (e.g. LiPF_6 in EC:DMC) during production, and behave as liquid-containing sponges, with consequently much higher ionic conductivities (see Figure 1.6). However, the drawbacks of liquid electrolytes are carried over as well (flammability, low lithium transference number, anionic concentration gradients). Adding room-temperature ionic liquids (RTIL) improves safety, but may further lower t_{Li^+} . Such materials may also require a mechanical support [23].

1.1.4.2 Amorphous inorganic materials

Amorphous inorganic materials typically require minimal heat treatments to produce compared to the high-temperature anneals required for crystalline counterparts. Ion mobility for such materials, once formed, is typically dependent on disordered interphases, free-volume or space-charge effects [24].

For glasses, Li-ion conduction is generally higher with sulfides (10^{-3} - 10^{-2} S/cm) compared to direct oxide analogues (10^{-5} - 10^{-6} S/cm), due to better atomic polarizability of the sulfur atoms, e.g. the $\text{GeS}_2+\text{Li}_2\text{S}+\text{LiI}$ and $\text{Li}_2\text{S}-\text{P}_2\text{S}_5-\text{Li}_4\text{SiO}_4$ glass-forming systems [25-27]. Unfortunately, sulfides also decompose readily upon exposure to both moisture and oxygen similar to Kamaya *et al.*'s $\text{Li}_{10}\text{GeP}_2\text{S}_{12}$, with a propensity for toxic H_2S gas release. Oxides pose less handling hazards, are stable against oxygen and may provide >5V electrochemical stability windows [28, 29]. Manufacturing simplicity by sputtering has also enabled the development of thin-film batteries using oxide glasses, such as in the case of lithium phosphorus oxinitrides ($\text{Li}_x\text{PO}_y\text{N}_z$) [30].

1.1.4.3 Crystalline inorganic materials

Sintered polycrystalline or ceramic electrolytes conduct ions through a balance of ion and vacancy motion. Their temperature-dependent kinetics can be described by Arrhenius-type relations. Examples of such materials are NASICON-, LISICON-, Thio-LISICON-, perovskite- and garnet-type Li-ion conductors.

1.1.4.3.1 NASICON-structured lithium ion conductors

The earliest works on NASICON-type materials exhibiting lithium-ion mobility can be traced back to Hong *et al.* [31] and Taylor *et al.* [32]. The general formula is $\text{LiM}_2(\text{PO}_4)_3$ where mainly $\text{M}^{\text{IV}}=\text{Ti}$, Ge, Hf or Zr.

Such materials have a $[\text{M}_2\text{P}_3\text{O}_{12}]^-$ subframework which can be described by neighboring spaces of corner-sharing MO_6 octahedrons and PO_4 tetrahedrons. These form size-modulated planar tunnels that enable fast Li-hopping between two different interstitial environments [24], reaching intragrain conductivities up to 3×10^{-3} S/cm. However, the grain boundaries usually suppress the total conductivity to two magnitudes lower, such as the case for $\text{Li}_{1.3}\text{Al}_{0.3}\text{Ti}_{1.7}(\text{PO}_4)_3$ (LATP). This means effective polycrystalline sintering plays a key factor in maximizing total conductivity, as demonstrated by Aono *et al.* while working with trivalent substitution chemistries for the octahedral Ti^{4+} by Cr, Ga, Fe, Sc, In, Lu, Y and La [33, 34].

Unfortunately, the runaway instability of NASICON-type materials against Li metal anodes due to Ti^{4+} to Ti^{3+} reduction (likely also but less pronounced for other Al- and Ge-dominant chemistries), diverts attention to other Li-ion conductor classes [35].

1.1.4.3.2 LISICONS and Thio-LISICONS

LISICON has a framework similar to the orthorhombic γ - Li_3PO_4 . Hong pioneered studies on the first LISICON (Lithium Superionic CONductor), and deduced its formula to be $\text{Li}_{14}\text{ZnGe}_4\text{O}_{16}$ [36]. Meanwhile, it was Bruce and West who described its conductivity behavior by a detailed interpretation of electrochemical impedance data [37].

LISICON was later discovered to be unstable in direct contact with Li metal. Kanno and coworkers worked around this problem by replacing O^{2-} with the larger and more polarizable S^{2-} species [38, 39]. These new chemistries, termed thio-LISICONS, have reportedly yielded room-temperature conductivities $2.2 \times 10^{-3} \text{ S/cm}$ for $\text{Li}_{4-x}\text{Ge}_{1-x}\text{P}_x\text{S}_4$ ($x=0.75$), negligible electronic conductivity, no reaction with Li metal, wide electrochemical stability window ($>5\text{V}$) and no phase transition up to 500°C . However, they also yield H_2S upon contact with moisture, possess high interfacial resistance problems with common oxide-based cathodes, and are reportedly unstable in bulk form [24, 40, 41, 42].

1.1.4.3.3 Perovskite solid solutions with A-site deficiencies

Perovskite (ABO_3) oxides with lithium ions incorporated in a $[\text{La}_{2/3}\square_{1/3}\text{TiO}_3]^{3x-}$ skeleton (\square =vacancy) can form fast-conducting lithium lanthanum titanates $\text{Li}_{3x}\text{La}_{(2/3-x)}\square_{(1/3-x)}\text{O}_3$ (LLTO, Figure 1.7). Tetragonal crystals with compositions $0 < x < 0.16$ maintain a large concentration of A-site vacancies, enabling substantial Li-hopping events through square planar O^{2-} bottlenecks between one A-site to the next [43].

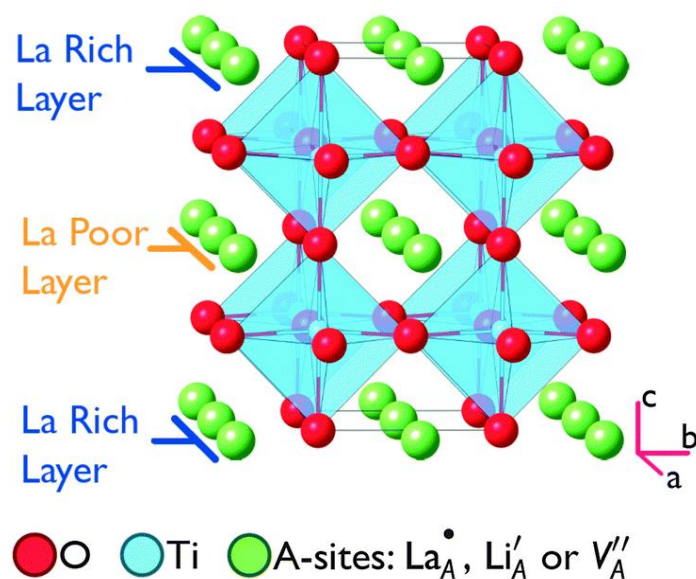


Figure 1.7: Crystal structure of $(\text{Li}_{3x}\text{La}_{2/3-x})\text{TiO}_3$, where the lanthanum-poor layers consist of La^{3+} , Li^+ or vacancies (after ref [44]).

Although intragrain (or bulk) conductivity can surpass 10^{-3} S/cm, there are three major problems with LLTOs. First, uncontrolled Li_2O losses due to high-temperature sintering (1300°C) distort target stoichiometries and resulting conductivities. Second, these ceramics are heavily limited by grain boundary resistances, arguably due to atmospheric corrosion which impedes sintering. Third, the framework is predisposed to $\text{Ti}^{4+}/\text{Ti}^{3+}$ reduction due to the corner-sharing BO_6 octahedral network. This chemical behavior is similar to that of NASICON-type chemistries aforementioned which will severely limit the voltage window for cathode/anode choices.

LLTOs have been reviewed in detail by Bohnke [45].

1.1.4.3.4 Garnet-type Li-ion conductors

Literature has reported Li-ion conductivities $>10^{-3}$ S/cm for at least one composition each among NASICONs, thio-LISICONs and perovskites. However, none has demonstrated simultaneous stability against Li-metal contact, zero risk of H_2S evolution, and a low interfacial resistance upon full-cell assembly with complementary high-voltage cathodes. “Li-stuffed” garnet-structured oxides can reportedly do all [41, 46, 47].

A typical garnet has a formula of $\text{A}_x\text{B}_3\text{C}_2\text{O}_{12}$. The lattice consists of mutually edge-shared BO_8 dodecahedra (Figure 1.8b) and supported by mutually-isolated CO_6 octahedra (Figure 1.8c). This framework generates space for interstitial occupancies: 3 tetrahedral and 6 octahedral cages p.f.u. (Figure 1.8d), formally termed **24d** and **48g**, respectively, using the Wyckoff notation. When **A** is lithium, the Li atoms enter these **24d** and **48g** interstitial sites.

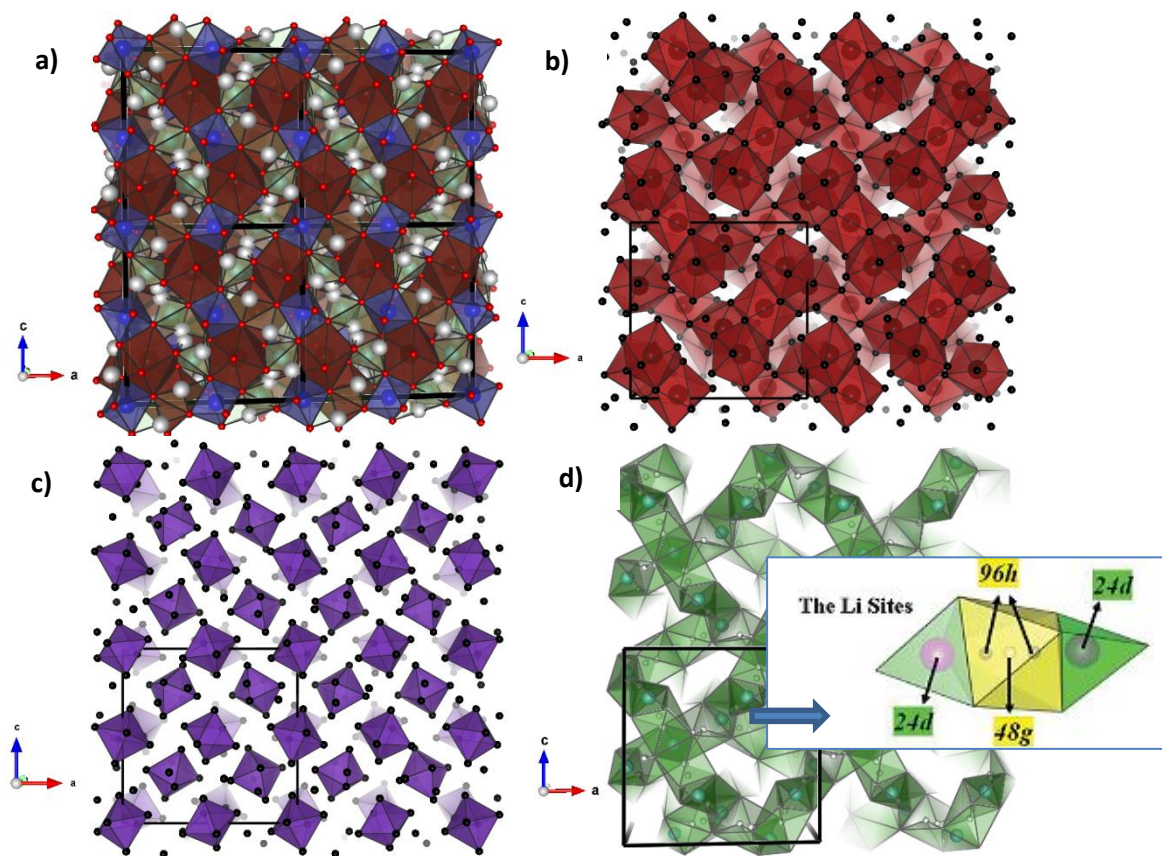


Figure 1.8: a) The $\text{Li}_7\text{La}_3\text{Zr}_2\text{O}_{12}$ cubic garnet structure. b) The LaO_8 dodecahedral sublattice. c) The ZrO_6 octahedral sublattice. d) The Li-conduction network formed by interstitial octahedral-site bridges linking tetrahedral $24d$ sites.

The $48g$ -sites are fully-vacant and the $24d$ -sites fully-occupied for $x=3$, as extensively shown by O'Callaghan and coworkers using neutron diffraction for a series of $\text{Li}_3\text{B}_3\text{Te}_2\text{O}_{12}$ compounds ($B = \text{Y}, \text{Pr}, \text{Nd}, \text{Sm}, \text{Lu}$) [48]. The $\text{Li}_3\text{B}_3\text{Te}_2\text{O}_{12}$ family has low Li-ion conductivities of $\sim 10^{-5}$ S/cm even at 600°C , and high activation energy (~ 1.2 V).

It was postulated that the $24d$ -sites act as defect traps, and that some degree of average $48g$ -occupancy was necessary for achieving appreciable ionic conductivity [24]. Indeed, Percival, *et al.* synthesized analogous $\text{Li}_5\text{B}_3\text{Sb}_2\text{O}_{12}$ (where $B = \text{La}, \text{Pr}, \text{Nd}, \text{Sm}, \text{Eu}, \text{etc.}$) compositions and obtained higher bulk conductivities ($\sim 10^{-4}$ S/cm at 25°C) as they introduced more Li p.f.u. in the stoichiometry [49]. Similar improvement was observed with $\text{Li}_5\text{La}_3\text{C}_2\text{O}_{12}$ ($C = \text{Ta}, \text{Nb}$) and related compositions (Figure 1.9) [50, 51]. To date, the highest conductivities have been recorded with synthesized garnets based on the parent formulae $\text{Li}_7\text{La}_3\text{Sn}_2\text{O}_{12}$ [52], $\text{Li}_7\text{La}_3\text{Hf}_2\text{O}_{12}$ [53, 54], $\text{Li}_5\text{La}_3\text{Nb}_2\text{O}_{12}$ [55] and $\text{Li}_5\text{La}_3\text{Ta}_2\text{O}_{12}$ [56] and $\text{Li}_7\text{La}_3\text{Zr}_2\text{O}_{12}$ [47, 57, 58].

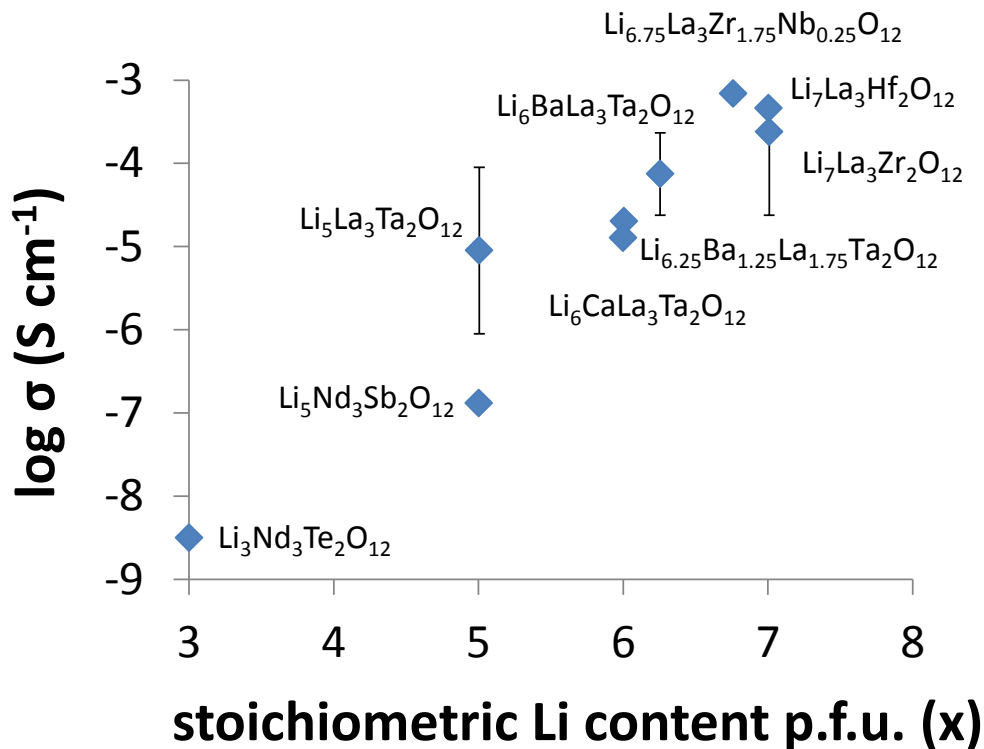


Figure 1.9: The room-temperature bulk conductivity of “Li-stuffed” garnets vs stoichiometric lithium content (x), modified from [51].

The 3D Li-tunneling network can be further described: each $24d$ tetrahedron has four neighboring $48g$ octahedra; each $48g$ octahedron has two neighboring $24d$ tetrahedra. When Li-content increases, occupied $24d$ -sites exert electrostatic repulsion on neighboring $48g$ -sites. The $48g$ -occupant is therefore pushed to what is termed as a **96h-split site**, a distorted $48g$ octahedron. This $96h$ -site occupant also exerts repulsion against its nearest $24d$ -site neighbor, leaving it empty. This means that any contiguous $24d$ - $96h$ - $24d$ unit must always have at least one vacant site. This further implies that a $24d$ -site partial depopulation must occur once the amount of lithium per formula unit exceeds 3 [58].

Due to this mechanism, O`Callaghan and Cussen detected Li-occupancies in all $24d$, $48g$ and $96h$ sites for a $\text{Li}_5\text{La}_3\text{Ta}_2\text{O}_{12}$ composition [61]. Xie and coworkers further predicted a theoretical upper limit of $\text{Li}_{7.5}\text{B}_3\text{C}_2\text{O}_{12}$ as the maximum Li-content that can be accommodated by the structure, with 1.5 Li in $24d$ sites and 6 Li in $96h$ sites based from this analysis [62].

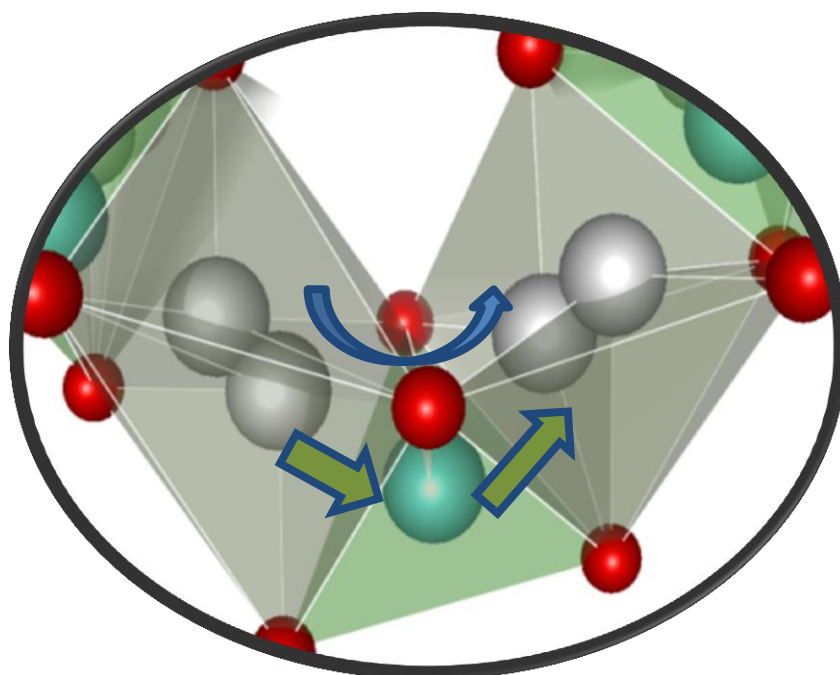


Figure 1.10: White spheres: lithium atoms. Green arrows: Cooperative motion for a Li trimer (48g/96h-24d-48g/96h). Blue arrow: edge-pass jump (48g/96h-48g/96h) as predicted by *ab initio*-MD [63].

Jalem and coworkers made investigations *in silico* using *ab initio* molecular dynamics (MD) simulations [63], finding that this 24d-96h repopulation is indeed thermodynamically-driven. They further elucidated, based from radial distribution function (RDF) analyses, that a concerted migration mechanism occurs via two types of ion-jump events (Figure 1.10): cooperative motion for a Li trimer (48g/96h-24d-48g/96h) or alternatively, a direct edge-pass jump (48g/96h-48g/96h). Xu *et al.* reached a similar conclusion [51]. Notably, these simulations were run at $>600^{\circ}\text{C}$, and agreed well with neutron diffraction data by Han *et al.* (Figure 1.11) [64].

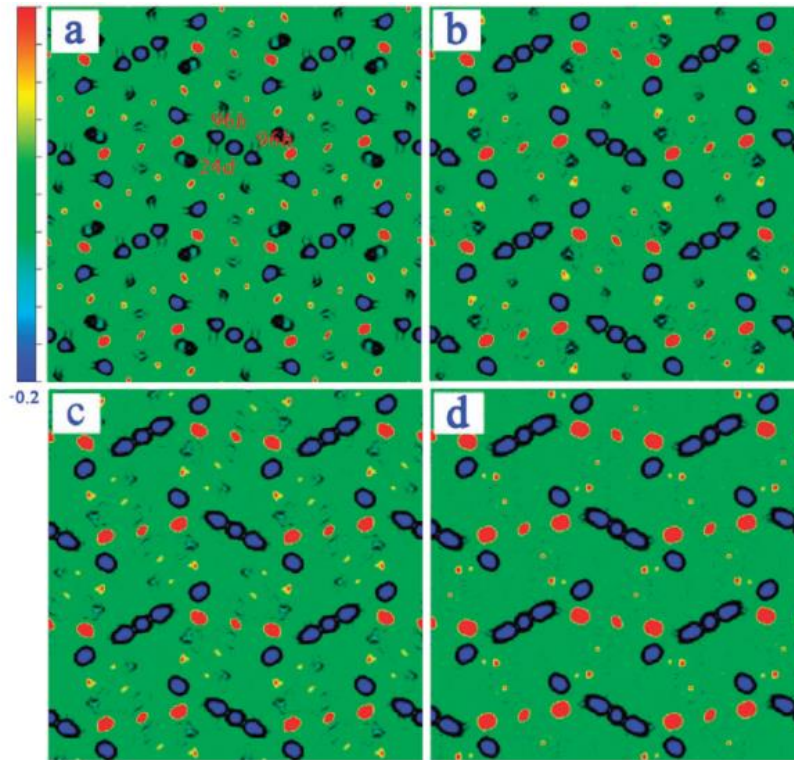


Figure 1.11: Two-dimensional contour maps from neutron-diffraction data sliced on the (001) planes at (a) room temperature (b) 200°C (c) 400°C and (d) 600°C; Li delocalizes along the 3D chain, Li(24d)-Li(96h)-Li(24d)-Li(96h)-Li(24d), with no structural collapse for the La, Zr and O positions (after [64]).

One more significant peculiarity about the garnet crystal structure is that the mutual isolation of the CO_6 octahedra (Figure 1.8c) help impede electron-hopping mechanisms. This has been explained by DFT simulations, i.e. certain elements with multiple cationic states such as Ta and Nb, can be incorporated in the **C**-sites without electroactive degradation by Li-metal contact (Figure 1.12) because they have low effective nuclear charges [59].

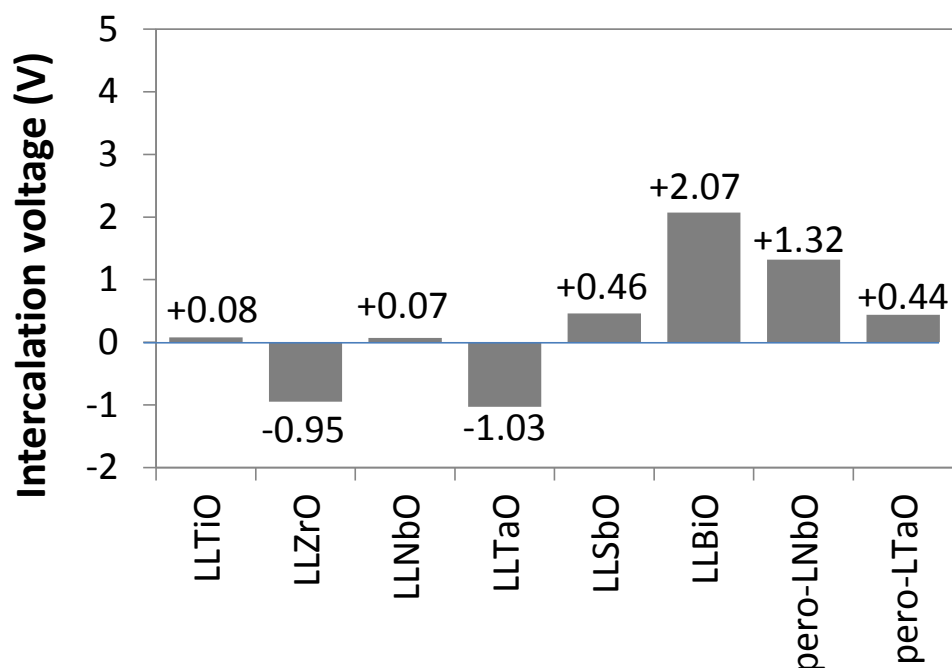


Figure 1.12: Li-intercalation voltages as predicted by density functional theory (DFT). A negative intercalation voltage predicts that only a Li-based anode more electropositive than Li will reduce the electrolyte. [LLMO] denotes $\text{Li}_x\text{La}_3\text{M}_2\text{O}_{12}$ -garnets, pero-[LMO] denotes perovskite-type $\text{La}_{1/3}\text{MO}_3$ [59], where M is a metallic (e.g. Ti, Zr, Nb, Ta or Sb) or metalloid element (Bi).

1.2 Bibliographic review

1.2.1 $\text{Li}_5\text{La}_3\text{Ta}_2\text{O}_{12}$ syntheses in literature

Scientific accounts on lithium lanthanum tantalates are limited. The reader will be briefed on what is available regarding: phase-diagrams, conductivities and materials processing.

1.2.1.1 Phase-diagrams

Thangadurai *et al.* [65] and Murugan *et al.* [66] are often credited for the discovery of lithium ion conductivity and electrochemical stability of lithium-“stuffed” garnets. However, the earliest successful synthesis with the cubic $Ia\bar{3}d$ symmetry was actually reported by Hayashi *et al.* [67] after an 850°C-anneal for a $\text{Li}_7\text{La}_3\text{Ta}_2\text{O}_{13}$ (sic) stoichiometry from a Li_2O - La_2O_3 - Ta_2O_5 ternary mix (Figure 1.13).

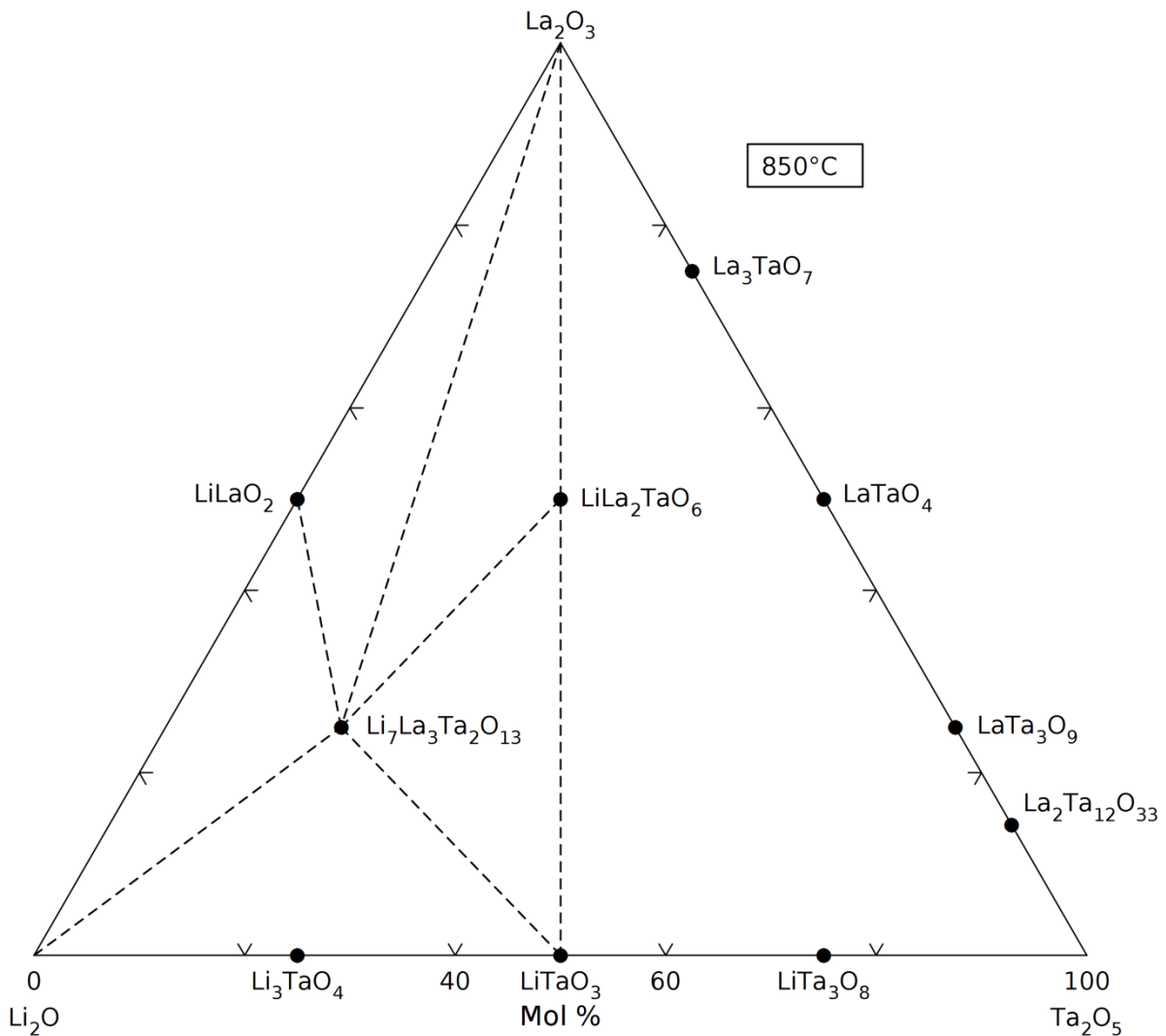


Figure 1.13: Ternary phase diagram of the Li_2O - La_2O_3 - Ta_2O_5 system at 850°C [67].

The associated phase diagrams leading to this phase suggest the existence of oxide intermediaries with high thermal stabilities. Lithium tantalates (e.g. Li_3TaO_4 within the Li_2O - Ta_2O_5 binary system) may persist in a solid phase without melting until 1400°C (Figure 1.14) [68] while lanthanum tantalates (e.g. LaTaO_4 within the Li_2O - Ta_2O_5 binary system) are refractory until 1790°C (Figure 1.15) [69]. On the other hand, lithium lanthalates (e.g. LiLaO_2) despite little information on the thermal response of the Li_2O - La_2O_3 binary system, are crystalline until at least 1000°C [70, 71] This set of information suggests phase-formation and sintering might be challenging for $\text{Li}_5\text{La}_3\text{Ta}_2\text{O}_{12}$ as would be expounded on in Chapter 3. From similar work, Ray reported $\text{LiLa}_2\text{TaO}_6$ to be a persistent crystalline impurity during annealing of stoichiometric $\text{Li}_5\text{La}_3\text{Ta}_2\text{O}_{12}$ [72].

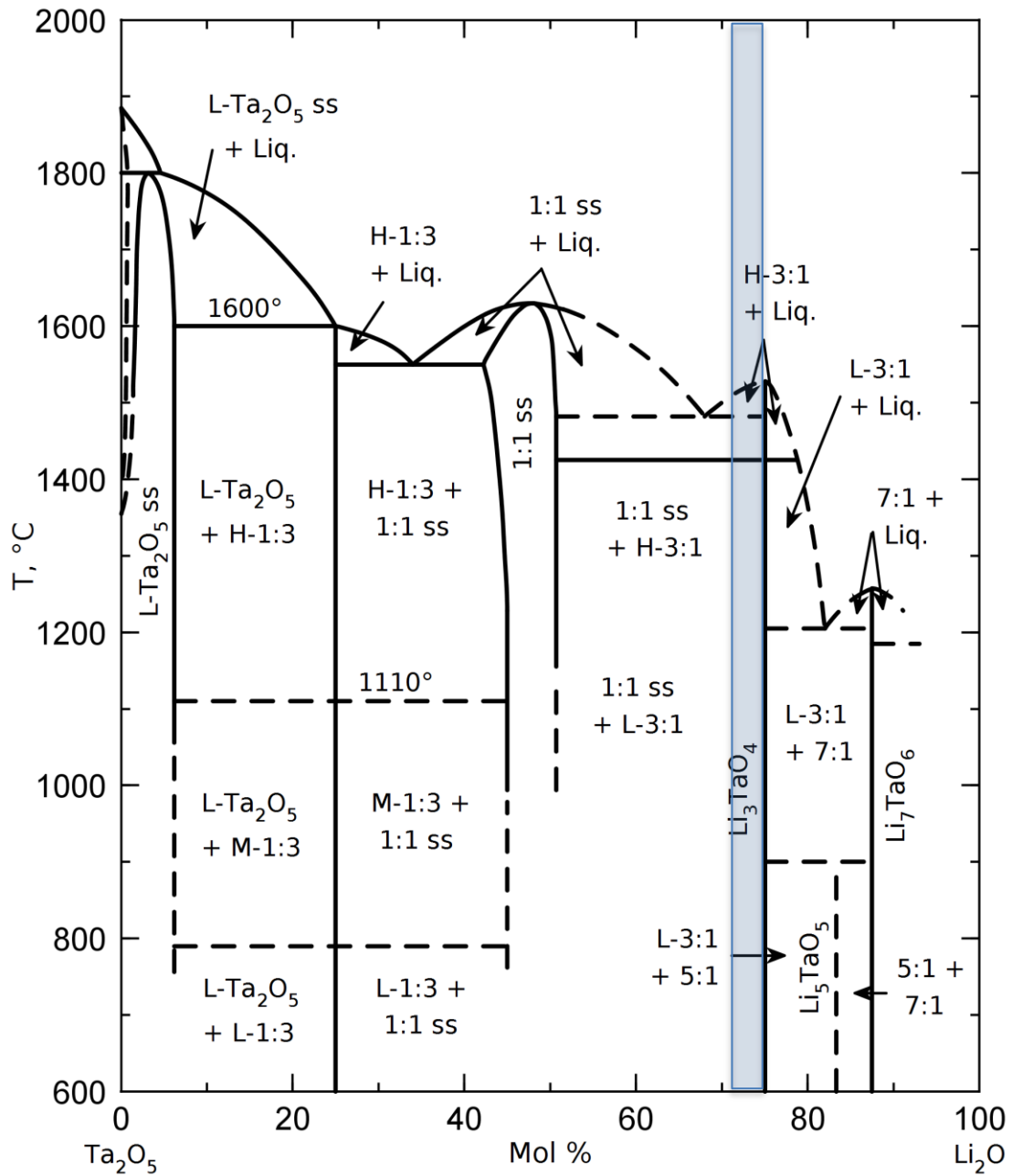


Figure 1.14: Binary phase diagram of the $\text{Li}_2\text{O}-\text{Ta}_2\text{O}_5$ system, where the blue shade denotes the proportion of Li vs Ta in the preparative stoichiometry of $\text{Li}_5\text{La}_3\text{Ta}_2\text{O}_{12}$ [68].

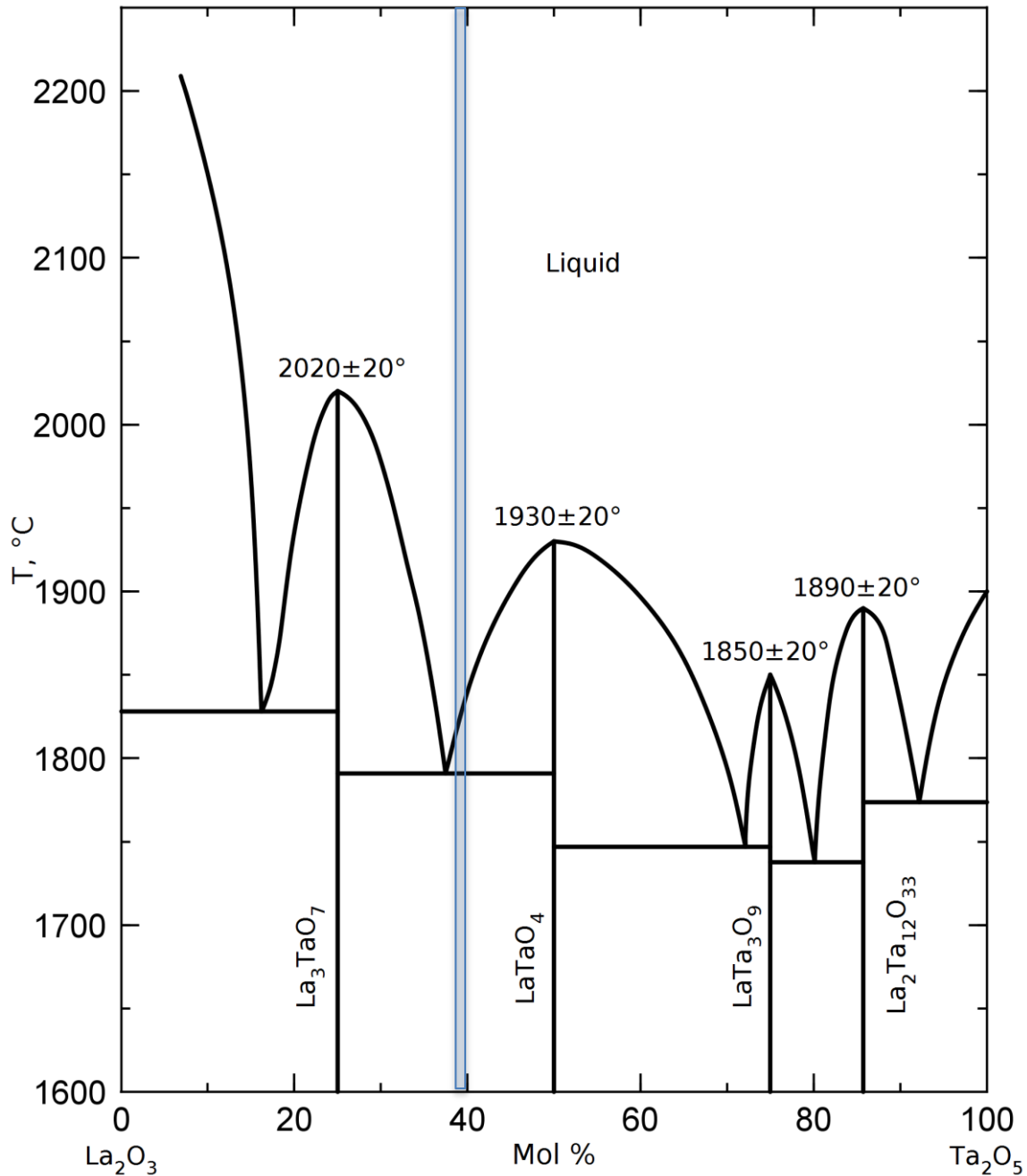


Figure 1.15: Binary phase diagram of the La₂O₃-Ta₂O₅ system, where the blue shade denotes the proportion of La vs Ta in the preparative stoichiometry of Li₅La₃Ta₂O₁₂ [69].

1.2.1.2 Ionic and electronic conductivities

Molecular dynamics simulations have predicted the limits of ionic conductivity for single-crystal Li₅La₃Ta₂O₁₂ to range between 10^{-4} - 10^{-3} S/cm depending on the extent of interstitial clustering effects [73, 74]. The values obtained by experiment (Table 1.1) are a far miss however, mostly falling short by about two orders of magnitude, with the exception of Kotobuki *et al.* [56] who reported a value of $\sim 10^{-4}$ S/cm.

Attempts via defect chemistry to alter the ion:vacancy ratio in the lithium network have been made in $\text{Li}_5\text{La}_3\text{Ta}_2\text{O}_{12}$. These have been through alkaline earth metal ($\text{Mg}^{2+}, \text{Ca}^{2+}, \text{Sr}^{2+}, \text{Ba}^{2+}$) substitutions unto the La^{3+} site or through other transition metals ($\text{Nb}^{5+}, \text{Sn}^{4+}, \text{Y}^{3+}$) unto the Ta^{5+} site. The best among these, $\text{Li}_6\text{La}_3\text{Ta}_{1.5}\text{Y}_{0.5}\text{O}_{12}$, had a reported total ionic conductivity of about $\sim 10^{-4}$ S/cm.[†]

An exhaustive tabulation is provided in Table 1.2.

Table 1.1: Reported ionic conductivity values of undoped lithium lanthanum tantalates in literature.

material	reported by	synthesis route	total ionic conductivity ($\mu\text{S}/\text{cm}$ at RT)	activation energy (eV)
$\text{Li}_5\text{La}_3\text{Ta}_2\text{O}_{12}$	[72]	solid-state (conventional)	20	0.22
$\text{Li}_5\text{La}_3\text{Ta}_2\text{O}_{12}$	[75]	modified Pechini sol gel	4	0.33
$\text{Li}_5\text{La}_3\text{Ta}_2\text{O}_{12}$	[76]	solid-state (spark plasma sintering)	1	0.64
$\text{Li}_5\text{La}_3\text{Ta}_2\text{O}_{12}$	[77]	solid-state (conventional)	5	0.6
$\text{Li}_5\text{La}_3\text{Ta}_2\text{O}_{12}$	[78]	modified Pechini sol gel	1.5	0.57
$\text{Li}_5\text{La}_3\text{Ta}_2\text{O}_{12}$	[56]	solid-state (conventional)	130	n/a
$\text{Li}_5\text{La}_3\text{Ta}_2\text{O}_{12}$	[65]	solid-state (conventional)	1.2	0.56
$\text{Li}_7\text{La}_3\text{Ta}_2\text{O}_{13}$	[79]	solid-state (conventional)	3	0.45
$\text{Li}_7\text{La}_3\text{Ta}_2\text{O}_{13}$	[80]	solid-state (conventional)	3 (40°C)	0.62

Table 1.2 Reported ionic conductivity values of partially-substituted lithium lanthanum tantalates in literature.

material	reported by	synthesis route	total ionic conductivity ($\mu\text{S}/\text{cm}$ at RT)	activation energy (eV)
$\text{Li}_6\text{BaLa}_2\text{Ta}_2\text{O}_{12}$	[81]	Pulsed laser deposition (thin film)	2	0.42
$\text{Li}_6\text{BaLa}_2\text{Ta}_2\text{O}_{12}$	[82]	solid-state (conventional)	8.8	0.41
$\text{Li}_6\text{BaLa}_2\text{Ta}_2\text{O}_{12}$	[83]	solid-state (conventional)	13	0.44
$\text{Li}_6\text{BaLa}_2\text{Ta}_2\text{O}_{12}$	[84]	solid-state (conventional)	15	0.47
$\text{Li}_6\text{BaLa}_2\text{Ta}_2\text{O}_{12}$	[75]	modified Pechini sol-gel	22	0.4
$\text{Li}_6\text{BaLa}_2\text{Ta}_2\text{O}_{12}$	[85]	solid-state (conventional)	40	0.4
$\text{Li}_6\text{BaLa}_2\text{Ta}_2\text{O}_{12}$	[77]	solid-state (conventional)	47	0.43

[†] The special case of Zr^{4+} - Ta^{5+} mixed occupancy for the disjoint octahedral sites (16a) is relegated to the next section, on lithium lanthanum zirconates (Section 1.2.2).

$\text{Li}_6\text{BaLa}_2\text{Ta}_2\text{O}_{12}$	[86]	solid-state (conventional)	~50	0.39
$\text{Li}_{5+x}\text{BaLa}_2\text{Ta}_2\text{O}_{11.5+0.5x}$ ($1.00 \leq x \leq 1.75$)	[87]	solid-state (conventional)	~100-200	0.42
$\text{Li}_6\text{MgLa}_2\text{Ta}_2\text{O}_{12}$	[87]	solid-state (conventional)	2.7 (50°C)	0.51
$\text{Li}_6\text{CaLa}_2\text{Ta}_2\text{O}_{12}$	[83]	solid-state (conventional)	2.2	0.50
$\text{Li}_6\text{CaLa}_2\text{Ta}_2\text{O}_{12}$	[84]	solid-state (conventional)	2.2	0.47
$\text{Li}_6\text{CaLa}_2\text{Ta}_2\text{O}_{12}$	[87]	solid-state (conventional)	3.6 (50°C)	0.53
$\text{Li}_6\text{SrLa}_2\text{Ta}_2\text{O}_{12}$	[84]	solid-state (conventional)	5.4	0.45
$\text{Li}_6\text{SrLa}_2\text{Ta}_2\text{O}_{12}$	[87]	solid-state (conventional)	8.8	0.50
$\text{Li}_6\text{Sr}_{0.5}\text{Ba}_{0.5}\text{La}_2\text{Ta}_2\text{O}_{12}$	[84]	solid-state (conventional)	7.1	0.45
$\text{Li}_6\text{Sr}_{0.5}\text{Ba}_{0.5}\text{La}_2\text{Ta}_2\text{O}_{12}$	[87]	solid-state (conventional)	50 (50°C)	0.44
$\text{Li}_6\text{Sr}_{0.5}\text{Ca}_{0.5}\text{La}_2\text{Ta}_2\text{O}_{12}$	[84]	solid-state (conventional)	3.2	0.50
$\text{Li}_6\text{BaLa}_2\text{Nb}_{0.5}\text{Ta}_{1.5}\text{O}_{12}$	[82]	solid-state (conventional)	4.2	0.47
$\text{Li}_6\text{BaLa}_2\text{NbTaO}_{12}$	[82]	solid-state (conventional)	3.1	0.47
$\text{Li}_6\text{BaLa}_2\text{Nb}_{1.5}\text{Ta}_{0.5}\text{O}_{12}$	[82]	solid-state (conventional)	1.1	0.50
$\text{Li}_{6.5}\text{La}_3\text{Ta}_{0.5}\text{Sn}_{1.5}\text{O}_{12}$	[88]	solid-state (conventional)	24	0.39
$\text{Li}_6\text{La}_3\text{Ta}_{1.5}\text{Y}_{0.5}\text{O}_{12}$	[89]	solid-state (conventional)	183	0.33

With regards to electronic conductivity, Mariappan *et al.* measured a value of about 10^{-2} $\mu\text{S}/\text{cm}$ for bulk $\text{Li}_5\text{La}_3\text{Ta}_2\text{O}_{12}$ [80]. Thangadurai and Weppner reported ≤ 1 $\mu\text{S}/\text{cm}$ for bulk $\text{Li}_6\text{BaLa}_2\text{Ta}_2\text{O}_{12}$, whereas Reinacher *et al.* reported $\leq 10^{-3}$ $\mu\text{S}/\text{cm}$ for thin-film $\text{Li}_6\text{BaLa}_2\text{Ta}_2\text{O}_{12}$ [81, 85]. The respective transference numbers for lithium (t_{Li^+}) are therefore greater than 98% (quoted >99.999% in the case of the $\text{Li}_6\text{BaLa}_2\text{Ta}_2\text{O}_{12}$ thin film) meaning most of the measured current during operation is due to ionic transport. It can be inferred that analogue garnet oxides with low level substitutions among the Li-La-Ta-O elements will also be electronically-insulating.

1.2.1.3 Microstructural and macrostructural control: processing methods

The processability of ceramic electrolytes for lithium-based batteries is also important. Sintered ceramics are generally brittle with poor mechanical compliance, making forms other than discrete bars, cylinders or plates especially challenging.

Kokal [75] produced $\text{Li}_5\text{La}_3\text{Ta}_2\text{O}_{12}$ material possessing a tailored 3D macroporosity by anchoring precursors on polystyrene beads prior to phase-formation annealing at 700°C. Adapting similar chemistry for 3D-printing garnet-based ceramic electrolytes unto dimensions as may be required by microbattery assemblies or large-cell designs has been suggested possible by the Wachsman group [90, 91].

On the other hand, Xiao X *et al.* found that $\text{LiLa}_2\text{TaO}_6$ is a key intermediate prior to the phase-formation of $\text{Li}_5\text{La}_3\text{Ta}_2\text{O}_{12}$, and that from this material and by using lithium hydroxide as a flux, $\text{Li}_5\text{La}_3\text{Ta}_2\text{O}_{12}$ single crystals can be grown at as low as 500°C [92].

1.2.2 $\text{Li}_7\text{La}_3\text{Zr}_2\text{O}_{12}$ syntheses in literature

The nominal stoichiometry of “fast-ion conducting $\text{Li}_7\text{La}_3\text{Zr}_2\text{O}_{12}$ (LLZO)” is a misnomer. Pure LLZO exhibits a tetragonal polymorph at room-temperature ($I4_1/acd$ space group). With rising temperature, its lattice expands until about $610\text{--}650^\circ\text{C}$ wherein it undergoes a volume-conserving transition to a cubic phase ($Ia\bar{3}d$ space group), the structure of which is the one described in section 1.1.4.3.4 [60, 93, 94].

1.2.2.1 Crystallographic considerations

The tetragonal phase is a remarkably poor ion conductor ($10^{-3}\text{--}10^{-1}$ mS/cm at RT) due to its ordered lattice (i.e. no vacancies) in contrast to the cubic polymorph (0.1-1 mS/cm at RT). Rendering the latter stabilized at room-temperature is therefore highly desired. Much research has focused on maximizing the ionic conductivity of LLZO (over 270 publications).

The tetragonal-to-cubic phase stabilization can be achieved in three ways:

- 1) use of aliovalent cation “dopants”
- 2) use of $\text{H}_2\text{O}/\text{CO}_2$

1.2.2.1.1 Cubic-phase stabilization using aliovalent dopants

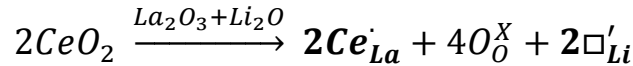
When supervalent cations replace lattice occupants in the LLZO structure (subject to ion size constraints) [95, 96], charge neutrality is achieved at lower lithium count and generate implicit vacancies. This destroys the degeneracy of fully-occupied interstitials in the tetragonal-phase and lowers its thermodynamic stability closer to its cubic-phase counterpart.

One must keep in mind that the LLZO lattice is comprised of a network of LiO_4 ($24d$), LiO_6 ($48g/96h$), LaO_8 ($24c$) and ZrO_6 ($16a$) cages (wherein the Wyckoff-symbols represent the cation positions). Assuming all oxygen sites are fully-occupied, the formalism developed by Kroger and Vink [97] can describe the defect chemistry applied in three scenarios:

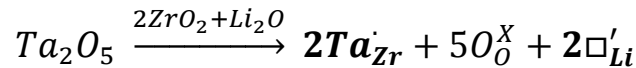
For a 24d or 48g/96h-site substitution (Li-site):



For a 24c-substitution (La-site):



For a 16a-substitution (Zr-site):



Here, the term " $Al_{Li}^{\cdot\cdot}$ " denotes an Al atom replacing a Li atom in its lattice-site, effecting a +2 change in site-specific local charge (as represented by the two dots). The term " \Box " (in lieu of Kroger and Vink's usage of " V ") represents a vacancy. The superscript " X " means the original site-charge is preserved, whereas each apostrophe ($'$) means one negative charge unit is added.

Using this approach, an assortment of substituted compositions has been reported (Table 1.3).

Table 1.3: Reported LLZO doped chemistries (as intended) and their respective ionic conductivities.

Dopant and substituted cation site	total conductivity (mS/cm)	activation energy (eV)	references
Al^{3+} (unspecified site)	0.1-1.0	0.34-0.37	[47, 66, 98-102]
Ga^{3+} (unspecified site)	0.5	0.32-0.37	[103]
Ge^{4+} (unspecified site)	0.8	--	[104]
Al^{3+} on Li^+	0.3-0.6	0.29-0.55	[105-111]
Ga^{3+} on Li^+	0.4	---	[112, 113]
Fe^{3+} on Li^+	1.4	0.29	[114]
Ca^{2+} on Zr^{4+}	0.5	0.27	[115]
Cr^{3+} on Zr^{4+}	0.5	0.39	[116]
Mo^{6+} on Zr^{4+}	---	0.29	[117]
Nb^{5+} on Zr^{4+}	0.8	0.31	[58, 118-121]
Sb^{5+} on Zr^{4+}	0.8	0.34	[122]
Sr^{2+} on La^{3+}	0.5	0.31	[123]
Ta^{5+} on Zr^{4+}	0.6-1.0	0.34-1.18	[119, 121, 124-131]

Te^{5+} on Zr^{4+}	1.0	0.4	[57]
Ti^{4+} on Zr^{4+}	0.005	0.44	[124]
W^{6+} on Zr^{4+}	0.5-0.8	0.35-0.42	[132, 133]
Y^{3+} on Zr^{4+}	0.8	0.26	[134, 135]
Ce^{4+} on La^{3+}	0.01	---	[136]
Y^{3+} on La^{3+}	0.3	0.31	[137]

The earliest of these, i.e. when Murugan *et al.* published their landmark paper on $\text{Li}_7\text{La}_3\text{Zr}_2\text{O}_{12}$ superionic conductivity, had unwittingly introduced Al^{3+} unto the sample from its alumina crucible by action of the $\text{Li}_2\text{O}-\text{Al}_2\text{O}_3$ eutectic above 1055°C (Figure 1.16) [66]. The role of Al^{3+} has since been recognized as a prime “dopant” when reporting garnet syntheses and electrochemical behavior.

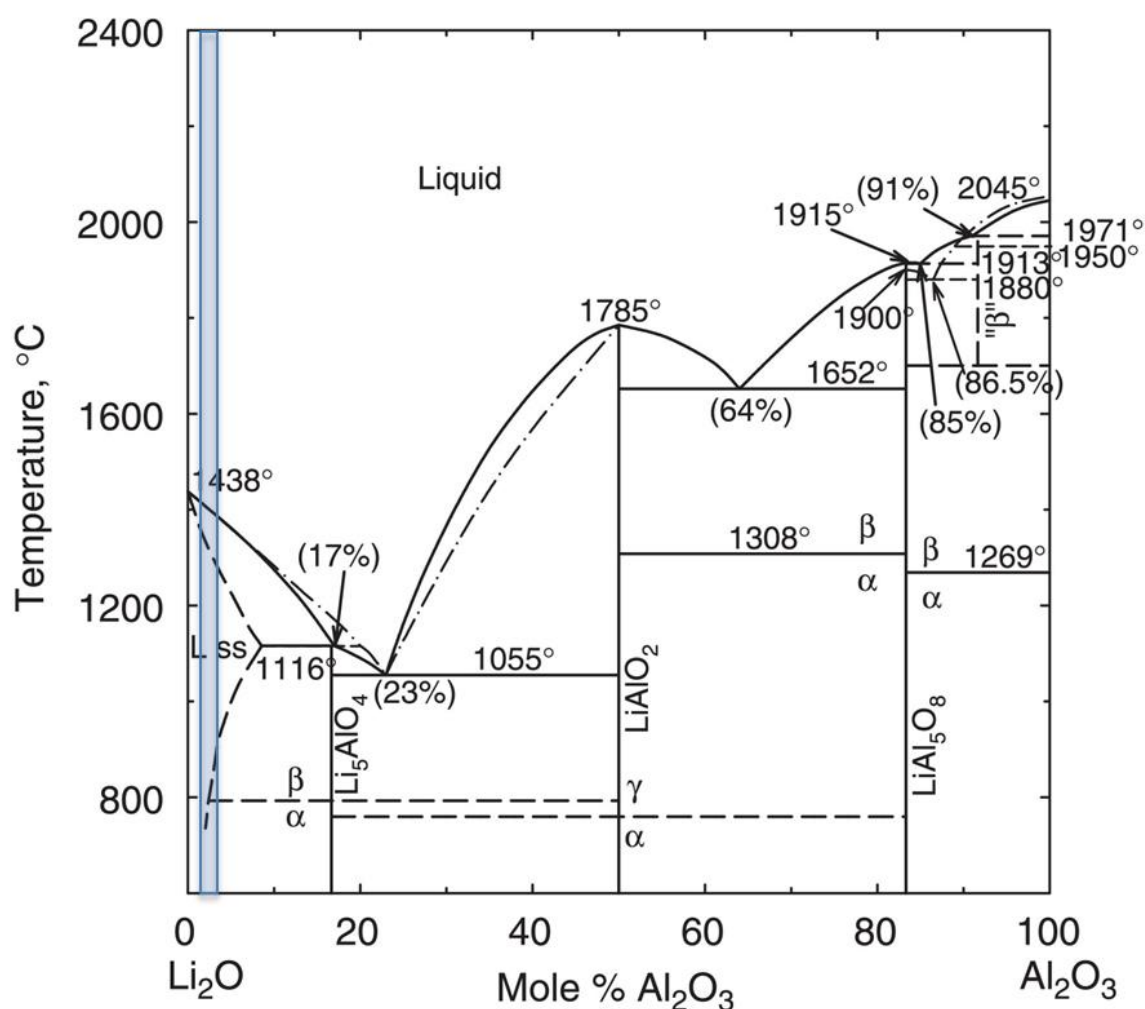


Figure 1.16: Binary phase diagram of the $\text{Li}_2\text{O}-\text{Al}_2\text{O}_3$ [138], where the blue shade denotes the proportion of Li vs Al in the stoichiometry of $\text{Li}_{6.4}\text{Al}_{0.2}\text{La}_3\text{Zr}_2\text{O}_{12}$ to $\text{Li}_{6.28}\text{Al}_{0.24}\text{La}_3\text{Zr}_2\text{O}_{12}$.

This formation of a $\text{Li}_2\text{O-Al}_2\text{O}_3$ melt during high-temperature sintering leads to reduced precision of Al^{3+} doping control. While the melt seeps from the crucible upwards the LLZO-based green body, it has been believed to bring with it liquid-facilitated mass transport and abnormally accelerated grain growth [139]. This may likely create a distribution of Al-graded compositions within one ceramic sample [140], and has, probably through this way, made structural elucidation of Al-doped LLZO quite challenging.

For instances, using solid-state nuclear magnetic resonance (ssNMR) techniques, Buschmann, *et al.* deduced Al^{3+} to occupy the Li tetrahedral (*24d*) sites [105], whereas Geiger, *et al.* interpreted ^{27}Al resonances to correspond to Al^{3+} in both Li tetrahedral (*24d*) and octahedral sites (*48g/96h*) [141]. Van Wullen and coworkers tried to merge the two interpretations, asserting that the final distribution of Al^{3+} among tetrahedral vs octahedral sites actually depends on the final annealing process [142]. However, two drastically different perspectives were also offered by Rettenwander, *et al.* [143] and Duvel, *et al.* [144]. The former reasoned from DFT simulations that Al^{3+} actually prefers the Li *96h*-sites (the distorted *48g* octahedral) but gives a false tetrahedral NMR resonance that most people had readily ascribed to a *24d*-site, whereas the latter proposed that Al^{3+} can actually also enter La^{3+} and Zr^{4+} with excessive doping. There is clear confusion, but despite author-to-author disagreements, a prevailing opinion is that 0.20-0.24 mol Al^{3+} p.f.u., intentionally added or not, is sufficient to stabilize the cubic-phase of LLZO [145].

On the other hand, Rietveld refinement of neutron diffraction data by Gu *et al.* and Wang *et al.* showed a favorable fit by modeling Al^{3+} in the *24d* site [119, 133]. This was echoed by Chen *et al.* [146], who found that forcing a *96h* allocation yielded unphysical Al^{3+} occupancies of negative values upon refinement of their diffractograms. Diffraction scientists thus supported Buschmann's original thesis [105].

The use of subvalent dopants to increase lithium stoichiometry as an alternative route to a disordered lithium configuration (i.e. a cubic-phase garnet) has also been explored (Table 1.3). Xie *et al.* pegged 7.5 Li p.f.u. as the maximum interstitial occupancy prior to unphysical Li-Li distances and lattice-destabilizing electrostatic repulsion [62].

Ionic conductivity trends

Thangadurai has provided an extensive tabulation of various doping chemistries for LLZO to crystallize in the cubic-phase, drawing attention to a direct trend between the stoichiometric Li p.f.u. and the bulk ionic conductivity [96].

Cussen was the first to suggest that the Li tetrahedral (24d) sites might behave as “ion traps” which suppress effective jump rates within the lithium conduction pathway [147]. In relation to this, Kihira *et al.*, Nozaki *et al.*, and Thompson *et al.* suggested that an optimum lithium content of ~6.5 Li p.f.u. exists, and that only a small fraction of lithium ions (10-15%) actually participate in lithium conduction [148-150]. That is, they correlated high ion conductivity to optimal Li-Li distances and a migration of average occupancies more towards the octahedral 48g/96h sites than the tetrahedral 24d sites, an opinion echoed by Adams' [58]. To put speculations to rest, Wang, *et al.* who showed empirically from a combination of ^6Li - ^6Li 2D exchange NMR and ^7Li PFG-NMR (pulsed field gradient) experiments that the lithium residence at the tetrahedral 24d-site was indeed the rate-limiting step in the ion conduction chain [133]. Thus is the general picture where the lithium sublattice is only occupied by Li atoms (e.g. with or without partial Zr-site substitution by Ta^{5+} or Nb^{5+}).

A fundamental distinction exists once foreign cations (Al^{3+} , Ga^{3+} , Zn^{2+}) begin to be placed directly along the lithium conduction pathway, the repercussions of which on a network-level had not been treated in detail prior to Jalem, *et al.* [74]. Furthermore, such doping chemistries have roused rich observations on the materials processing aspects: Gu *et al.* reported lattice parameter hysteresis under rapid cooling when using Al^{3+} and Ga^{3+} dopants and inferred this effect to be a reflection of unequilibrated cation distributions within the lithium sublattice [119]. Extrinsic of the LLZO lattice, Geiger *et al.* [141] and Buschmann *et al.* [105] detected via NMR a LaAlO_3 minority-phase in their respective Al-doped LLZO powders whereas El Shinawi showed by SEM-EDAX analyses that gallium acted as a sintering aid for LLZO [103].

The exact crystallographic position of Ga^{3+} within the LLZO lattice had thus also proven difficult to ascertain, paralleling the confusion with Al-doped LLZO. Howard *et al.* assigned a broad NMR peak with a chemical shift ~221 ppm as 24d-site Ga^{3+} , whereas both Rettenwander *et al.* [151] and Allen *et al.* [152] deduced a 96h-site Ga^{3+} occupancy. Only recently, diffraction data refinements have shown that Ga-doped LLZO can crystallize in a reduced symmetry space group ($\bar{I}43d$ rather than $Ia\bar{3}d$), albeit still with cubic lattice parameters (single crystal neutron data [153] powder neutron data [154] powder x-ray data [155]). These works attest to the need

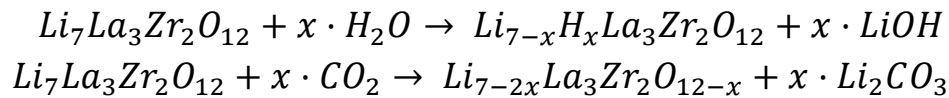
for stringent processing controls in both Al^{3+} and Ga^{3+} doping within LLZO to obtain the desired conduction network sublattice.

Other relevant literature on dopants will be found in-text within Chapter 4 and Chapter 5 as called upon by the flow of the discussion.

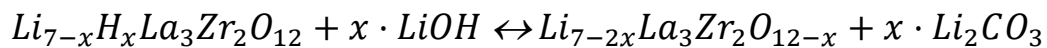
1.2.2.1.2 Cubic-phase stabilization using $\text{H}_2\text{O}/\text{CO}_2$

When stoichiometric LLZO is thermally-activated in the presence of atmospheric $\text{H}_2\text{O}/\text{CO}_2$, the temperature for the tetragonal-to-cubic phase transition occurs at a drastically lowered 100°C - 200°C (in lieu of $>600^\circ\text{C}$). This cubic-phase is retained even upon cooling back to room-temperature.

The chemistries behind, according to thermogravimetric studies [133], are as follows:



Either mechanism can occur independently, i.e. in the presence of only H_2O or only CO_2 . What is interesting is that the equilibrium $2\text{LiOH} + \text{CO}_2 \leftrightarrow \text{Li}_2\text{CO}_3 + \text{H}_2\text{O}$ is reversible. People have also reported that the first reaction can progress to the second reaction and vice-versa [94]. This could be interpreted using a Le Chatelier-type chemical equilibrium as:



Environmental conditions (i.e. humidity and CO_2 levels) thus affect the product identity. In both cases, the lithium content is reduced facilitating a disordered Li sublattice. However, interaction with water inserts protons unto the LLZO lattice [94], whereas interaction with CO_2 creates oxygen vacancies and deposits Li_2CO_3 along grain boundaries [93]. Rich subequilibria between lithium, protons and oxygen must therefore exist. This has been barely investigated. Experimentally, it has been found that H_2O -interactions are kinetically more facile compared to CO_2 interactions, and thus the former has been one focus of the present research (Section 5.1) [93].

The atmosphere-stabilized materials revert to tetragonal-phases at high-temperature however, accompanied by expulsion of H_2O or CO_2 . Water expulsion occurs between 200 - 350°C [94, 133]; CO_2 expulsion begins above 450°C [94, 156, 157].

Lattice structure of protonated LLZO

The existence of hydrogarnets, obtained from proton-exchange of anhydrous garnets (e.g. $\text{Ca}_3\text{Al}_2(\text{O}_4\text{H}_4)_3$ from $\text{Ca}_3\text{Al}_2\text{Si}_3\text{O}_{12}$) [158] or indeed even natively in their natural mineral states [159], is not a recent discovery.

A useful review for the case of lithium-“stuffed” garnets has been provided by Galven *et al.* [160]. Mainly, they found that Li^+/H^+ exchange occurs readily only for garnet stoichiometries with greater than 3 Li p.f.u. The propensity for the exchange reaction to occur was suggested independent of Li-ion conductivity or lattice parameters, but did lead to lattice enlargements whenever it occurred as a result of strong Li-O bonds being replaced by relatively weaker O-H \cdots O bonds. This is one-way of interpreting why the recently-reported “low-temperature syntheses” of cubic-phase LLZO samples (Table 1.4), have yielded relatively larger cubic-symmetry unit cells (highlighted in grey).

Table 1.4: Recent works on high-temperature synthesis and low-temperature synthesis of cubic-phase LLZO.

XRD Sample	Reference	synthesis route	lattice dimension (Å)	Al content (% wt)	Heating treatment
powder	[66]	solid-state	12.9682(6)	Unknown	1230°C 36h
single-crystal	[161]	solid-state	12.9827	Unknown	1250°C (duration not stated)
single-crystal	[141]	solid-state	12.9751 (1)	0.23%	900°C-1100°C overnight
powder	[105]	solid-state	12.9727 (2)	0.90%	1230°C 30h
powder	[47]	sol-gel	12.9720	0.61%	1200°C 36h
powder	[62]	sol-gel	12.9947	Unknown	780°C 4h
powder	[156]	sol-gel	13.0319	Unknown	800°C 20h
powder	[94]	sol-gel	12.9859(2)	not stated	300°C 30h (from a pre-synthesized tetragonal-phase garnet)

The crystallographic changes accompanying stoichiometric LLZO with moisture interaction have been further scrutinized by the Sanjuán group. They have shown via NMR analyses that deep hydration of LLZO powder shifts lithium occupancy from the distorted octahedral (48g/96h) sites unto the tetrahedral (24d) sites [162]. Different aging/heating protocols also led to structurally-distinct hydrogarnets: $I\bar{4}3d$ (at temperatures below 150°C) and $Ia\bar{3}d$ (at temperatures above 350°C) [163], both

cubic-phases but varying with respect to the spatial orientations of the hydrogen atoms. These proton-exchanged materials were suggested to form O_4H_4 units creating numerous hydrogen bonds, conferring thermal stability to the proton-exchanged garnet structure until at least 300°C.

Stability in liquid H_2O

The crystallographic stability of a solid-electrolyte (SE) in contact with aqueous media is interesting for lithium-battery systems directly incorporating water as a component. The application could be in this configuration: Li-metal/SE/water/cathode. Here water can act as a catholyte for active material laminates, medium for dissolved oxygen, or even possibly a direct reactant for a lithium-based fuel cell.

However, the actual aqueous stability of LLZO is debated.

Jin found crystallized $La(OH)_3$ precipitates after one year of atmospheric exposure of sintered LLZO, resulting in a friable mass [164]. Orera, *et al.* [163] and Ma, *et al.* [165] found excellent stability of the cubic-phase LLZO garnets under protonation (up to 63.6% H^+/Li^+ exchange), although they differed in opinion regarding space groups produced at low-temperature protonation ($I\bar{4}3d$ and $Ia\bar{3}d$, respectively). In the same paper however, Ma, *et al.* showed an excellent reversibility of the proton-lithium exchange by immersion in concentrated LiOH (2M). In contrast, Shimonishi detected ion-conductivity degradation after immersion in a lower concentration of LiOH (1M), but excellent stability under saturated LiCl for over a week at elevated temperature (50°C) [166]. The Li-ion conductivity was thus suggested to depend heavily on the chemical activity of lithium-ions when in contact with aqueous solutions. Radhakrishnan investigated this thermodynamically [167] using DFT and posited that between pH 4-10 the LLZO garnet will not dissolve in solution due to the formation of stable passivation layers (e.g. Li_2ZrO_3).

With regards to chemistries analogous to LLZO, some examples are as follows: Wang *et al.* [168] demonstrated $LiOH \cdot H_2O$ crystallization on $Li_5La_3Ta_2O_{12}$ with atmospheric exposure, while Truong *et al.* [169] argued by pH measurements after water immersion that $Li_5La_3Ta_2O_{12}$ undergoes less proton-exchange than $Li_5La_3Nb_2O_{12}$. On the other hand, Li [170] found that protons caused a reduction in Li occupancy on the octahedral sites (48g/96h), similar to Larraz's conclusions [162] and that water dissolves amorphous $LiAlO_2$ species in the grain boundaries between $Li_{6.5}La_3Zr_{1.5}Ta_{0.5}O_{12}$ grains.

1.2.2.2 Processing and handling considerations

1.2.2.2.1 Production

Ceramics are produced by energetically-activating a mix of reagents to form polycrystalline materials of desired phases. These are then ground to achieve fine powders, the high-surface areas of which drive sintering to proceed within an industrially-feasible number of hours. The conventional solid-state route is most often employed due to practical reasons as will be explained in Chapter 3.

Mechanical compaction during sintering aids to expedite the process. Techniques such as hotpressing and spark-plasma fields shorten the sintering timescale from a question of hours to minutes, and due to piston stability requirements, avoid atmospheric contaminants as they are done in relative vacuum or inert atmosphere conditions. However, they are very expensive systems even for basic equipment models (~€100,000-~€200,000).

Conventional sintering

The use of controlled atmospheres for engineering sintered ceramics is a cornerstone of modern solid-state chemistry. The use of dry oxygen in particular, in addition to minimizing unintended oxygen vacancies or cation reduction at high temperatures, has been demonstrated to significantly aid oxide ceramic densification, both in the $\text{Li}_{0.34}\text{La}_{0.55}\text{TiO}_3$ perovskite [171] and the $\text{Li}_{6.75}\text{La}_3\text{Zr}_{1.75}\text{Ta}_{0.25}\text{O}_{12}$ garnet [172].

Attention must be turned also to the identity of reagent materials. Lithium in particular is highlighted for being a rather adventitious component miscible in an abundance of phase diagrams. For example, the use of lithium hydroxide rather than lithium carbonate, as lithium source has shown better sintering action in particular for $\text{Li}_{6.75}\text{La}_3\text{Zr}_{1.75}\text{Ta}_{0.25}\text{O}_{12}$ [173]. Chen *et al.* [146] explained this via in-situ neutron diffraction while ramping to LLZO sintering temperature as due to the premature evaporation of lithium if in the form of Li_2CO_3 . A side-conclusion they had was that the formation of both tetragonal and cubic garnet phases are always in dynamic equilibrium, and that the tetragonal/cubic phase-ratio is dictated by diffusion-controlled local segregation of cations. “Active dopants” for that matter, such as Al^{3+} , which form stable intermediates with lithium, aid to conserve Li_2CO_3 from evaporation. This has been partially echoed by Rao *et al.* [174], who found that the cubic $\text{Li}_7\text{La}_3\text{Zr}_2\text{O}_{12}$ phase formed not through solid-state diffusion, but via mediation from a lithium-rich melt (Figure 1.17).

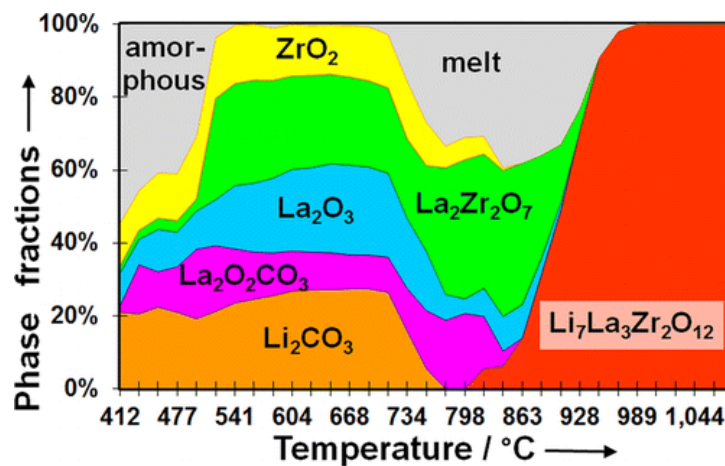


Figure 1.17: Reactant evolution as a function of temperature for LLZO as probed via neutron diffraction [174].

Hotpressing and Spark-plasma sintering (SPS)

How to control how this lithium-rich melt diffuses across the ceramic green-body during sintering, or the extent of stoichiometric lithium loss during the same period, may be construed as a universal challenge for the production of superior lithium-ion conducting ceramics. Hot-pressing can lower effective sintering temperature whereas spark-plasma sintering is a flash heating/cooling technique, and both can be considered to minimize lithium loss risks.

To achieve densities above 90%, conventional sintering of LLZO requires about 1100°C-1250°C. Hot-pressing can achieve 97% density of cubic-phase LLZO (Al-doped) using 1hr at 1000°C [175], and 98% density of tetragonal-phase LLZO (stoichiometric) using 1hr at 1050°C [176]. The total ionic conductivities obtained with hotpressing are in the 10^{-4} S/cm scale, with reportedly fairly negligible grain boundary resistances [177]. Suzuki Y *et al.* obtained transparent LLZO by hot-pressing under isotatic pressure, yielding 9.9×10^{-4} S/cm conductivities at room-temperature [101], and inferred full densification, given that opacity derives from light scattering within pores. South Korean groups have also reported $>10^{-4}$ S/cm with SPS-produced Nb-doped LLZO [178].

1.2.2.2.2 Full-cell stability

The electrochemical stability window for LLZO garnets had long been believed to range between 0V to as much as 8V (vs Li^+/Li). However, recent reports of dendrite formation against lithium have prompted a thermodynamic reexamination [99].

Zhu *et al.* [179] employed an analysis of DFT energies and found that LLZO is intrinsically stable only between 0.05V and 2.91V (vs Li^+/Li); the “extended electrochemical stability” only being due to an interfacial passivation mechanism. On the other hand, Miara *et al.* [180] showed that a thermodynamic driving force for LLZO-decomposition exists when contacted against LiFePO_4 , LiMnO_2 and LiCoO_2 , the last being theoretically the least degrading. Experimentally though, pulsed laser deposition at 700°C of LiCoO_2 unto $\text{Li}_7\text{La}_3\text{Zr}_2\text{O}_{12}$ has been shown to produce a 50nm La_2CoO_4 interfacial layer [181].

This brings attention to interfacial properties that are observed when LLZO is coupled to electrodes. That is, because ceramics are heavy, a weight penalty against energy density can only be offset by using thin ceramic membranes ($\sim 100\mu\text{m}$ or less), even with a shift to lithium metal anodes [182]. At such dimensions the associated interfacial resistances may dictate more the cell-level battery performance, rather than bulk conductivity. Solving the interfacial problems may then be of paramount importance at least as a first stage to making possible any all-solid-state battery prototypes at all.

The Doeff group has systematically investigated the lithium metal/LLZO garnet interfacial phenomena. Using attrition-milling techniques, sieving and heterogenous particle size distributions, they synthesized large-grained (100-200 μm) and small-grained (20-40 μm) LLZO ceramics in sintered form. What they found were the following:

- 1) Garnet-surface Li_2CO_3 created immense interfacial resistances (associated surface resistance or ASR) to the order of 5000 Ω compared to pristine surfaces (109 Ω), which led to immediate short-circuits through the ceramic when polarized in contact with lithium metal [183]
- 2) An Al-rich LLZO (large-grained) surface was more highly susceptible to Li_2CO_3 precipitation compared to an Al-depleted LLZO (small-grained) surface [184]
- 3) The annealing history of the mother powder used to cover green-body pellets poised for sintering directly affected the total ionic conductivity and interfacial resistance of sintered pellets [184]
- 4) There was not much difference between the grain orientation and grain boundary misorientation (as analyzed from Laue X-ray microdiffraction experiments) between large-grain and small-grain ceramics, and that dendrites formed in large-grained samples seemingly due to current focusing along the few low-conductivity grain boundaries [184].

Long *et al.* shared similar opinions, and made a further assertion that Al-doped garnets will have lithium aluminates unstable against contact with lithium-metal [125]. However, they did further work and showed that even in hot-pressed Al-free garnets of 99% ceramic density, dendrites were forming along grain-boundaries as a consequence of current-focusing due to difficulties in creating an optimal Li-metal/ceramic contact. At elevated temperatures (50°C) and using a gold buffer layer (sputtered), current densities as high as 0.5 mA/cm² were stable. Why this was possible was attributed to a higher activation energy for grain boundary conductivity, which meant significantly-raised conductivities with slight increases in temperature.

In the prevailing backdrop of grain boundary penetration as lithium dendrite propagation mechanism, a different but complementary perspective will be presented in this thesis.

1.3 Scope of the project

This PhD project consisted of two aims:

- (1) Design a synthesis protocol for garnet-structured electroceramics exhibiting high Li-ion conductivity based on two parent compositions: Li₅La₃Ta₂O₁₂ and Li₇La₃Zr₂O₁₂, with explorations of how meticulous the control of defect chemistry, contaminants and sintering behavior should be
- (2) Apply the best material as a mechanically-rigid solid electrolyte in a lithium-metal battery prototype, investigate its cycling performance, and lay out a foundation study for improving all-solid-state-batteries to be investigated in the future

REFERENCES:

- [1] Goodenough, J. B. and Park, K.-S. *Journal of the American Chemical Society* **135**(4), 1167–1176 (2013).
- [2] Ji, L., Lin, Z., Alcoutlabi, M. and Zhang, X. *Energy & Environmental Science* **4**(8), 2682–2699 (2011).
- [3] Das, S., Mann, M., Woodhouse, M., Chung, D., Elgqvist, E., Mone, C. and Gossett, S. *Clean Energy Manufacturing Analysis Center (CEMAC) 2015 Research Highlights*. National Renewable Energy Laboratory: Technical Report (2015); Chung D., Elgqvist E., and Santhanagopalan S. *Automotive Lithium-ion Cell Manufacturing: Regional Cost Structures and Supply Chain Considerations*. National Renewable Energy Laboratory: Technical Report NREL/TP-6A20-66086 (2016)
- [4] Hardman, S., Shiu, E. and Steinberger-Wilckens, R. *Transportation Research Part A-Policy and Practice* **88**, 40–57 (2016).
- [5] Sun, Y. *Nano Energy* **2**(5), 801 – 816 (2013).

- [6] Kundu, D., Talaie, E., Duffort, V. and Nazar, L. F. *Angewandte Chemie-International Edition* **54**(11, SI), 3431–3448 (2015).
- [7] Nykvist, B. and Nilsson, M. *Nature Climate Change* **5**(4), 329–332 (2015).
- [8] *USABC Goals for Advanced Batteries for EVs - CY 2020 Commercialization*. Web Article: http://www.uscar.org/commands/files_download.php?files_id=364. United States Advanced Battery Consortium (2014).
- [9] Hensley R., Newman J. and Rogers M. *Battery technology charges ahead*. Web article: <http://www.mckinsey.com/business-functions/sustainability-and-resource-productivity/our-insights/battery-technology-charges-ahead>. Mckinsey Quaterly (2012).
- [10] Bruce, P. G., Freunberger, S. A., Hardwick, L. J. and Tarascon, J.M. *Nature Materials* **11**(1), 19–29 (2012).
- [11] Janek, J. and Zeier, W. G. *Nature Materials* **16**141, 141 (2016).
- [12] Bruce, P. G., Freunberger, S. A., Hardwick, L. J. and Tarascon, J.M. *Nature Materials* **11**(1), 19–29 (2012).
- [13] Manthiram, A., Fu, Y., Chung, S.H., Zu, C. and Su, Y.S. *Chemical Reviews* **114**(23), 11751–11787 (2014).
- [14] Islam, M.S. and Fisher, C.A.J. Lithium and sodium battery cathode materials: computational insights into voltage, diffusion and nanostructural properties. *Chemical Society Reviews*. **43**, 185-204 (2014)
- [15] Peled, E. *Journal of The Electrochemical Society* **126**(12), 2047–2051 (1979); Peled, E., Golodnitsky, D. and Penciner, J. *The Anode/Electrolyte Interface*, 479–523. Wiley-VCH Verlag GmbH & Co. KGaA (2011).
- [16] Scrosati, B., Hassoun, J. and Sun, Y. K. *Energy & Environmental Science* **4**(9), 3287–3295 (2011).
- [17] Bruce, P. G., Evans, J. and Vincent, C. A. *Solid State Ionics* **28-30, Part 2**(0), 918–922 (1988).
- [18] Ding, F., Xu, W., Chen, X., Zhang, J., Shao, Y., Engelhard, M. H., Zhang, Y., Blake, T. A., Graff, G. L., Liu, X., and Zhang, J.G. *Journal of Physical Chemistry C* **118**(8), 4043–4049 (2014).
- [19] Hartmut, W. and Greyhard, K. *Electrochemical engineering : science and technology in chemical and other industries*. Springer, Berlin; New York, (1999).
- [20] Kamaya, N., Homma, K., Yamakawa, Y., Hirayama, M., Kanno, R., Yonemura, M., Kamiyama, T., Kato, Y., Hama, S., Kawamoto, K. and Mitsui, A. *Nature Materials* **10**(9), 682–686 (2011).
- [21] Wenzel, S., Randau, S., Leichtweiß, T., Weber, D. A., Sann, J., Zeier, W. G., and Janek, *Chemistry of Materials* **28**(7), 2400–2407 (2016).
- [22] Cheng, H., Zhu, C., Lu, M. and Yang, Y. *Journal of Power Sources* **173**(1), 531–537 (2007).
- [23] Lu, Y., Moganty, S. S., Schaefer, J. L. and Archer, L. A. *J. Mater. Chem.* **22**, 4066–4072 (2012).
- [24] Knauth, P. *Solid State Ionics* **180**(14-16), 911–916 (2009).
- [25] Vinatier, P., Menetrier, M. and Levasseur, A. *Solid State Ionics* **116**(1-2), 35–45 (1999).
- [26] Saienga, J. and Martin, S. W. *Journal of Non-Crystalline Solids* **354**(14), 1475–1486 (2008).
- [27] Tatsumisago, M., Mizuno, F. and Hayashi, A. *Journal of Power Sources* **159**(1), 193 – 199 (2006).
- [28] Obayashi, H., Nagai, R., Gotoh, A., Mochizuki, S. and Kudo, T. *Materials Research Bulletin* **16**(5), 587–590 (1981).
- [29] Hayashi, A., Muramatsu, H., Ohtomo, T., Hama, S. and Tatsumisago, M. *Journal of Materials Chemistry A* **1**, 6320–6326 (2013).
- [30] Long, J. W., Dunn, B., Rolison, D. R. and White, H. S. *Chemical Reviews* **104**(10), 4463–4492 (2004).
- [31] Hong, H. P. *Materials Research Bulletin* **11**(2), 173–182 (1976).
- [32] Taylor, B., English, A. and Berzins, T. *Materials Research Bulletin* **12**(2), 171–181 (1977).
- [33] Aono, H. and Sugimoto, E. *Journal of the Electrochemical Society* **136**, 590 (1989).

- [34] Aono, H., Sugimoto, E., Sadaoka, Y., Imanaka, N. and Adachi, G. *Journal of The Electrochemical Society* **137**(4), 1023–1027 (1990).
- [35] Hartmann, P., Leichtweiss, T., Busche, M. R., Schneider, M., Reich, M., Sann, J., Adelhelm, P. and Janek, J. *The Journal of Physical Chemistry C* **117**(41), 21064–21074 (2013).
- [36] Hong, H. P. *Materials Research Bulletin* **13**(2), 117–124 February (1978).
- [37] Bruce, P. G. and West, A. R. *Journal of the Electrochemical Society* **130**(3), 662–669 (1983).
- [38] Kanno, R. and Maruyama, M. *Journal of the Electrochemical Society* **148**(7), A742–A746 (2001).
- [39] Kanno, R., Murayama, M., Inada, T., Kobayashi, T., Sakamoto, K., Sonoyama, N., Yamada, A. and Kondo, S. *Electrochemical and Solid-State Letters* **7**(12), A455–A458 (2004).
- [40] Nagao, M., Imade, Y., Narisawa, H., Kobayashi, T., Watanabe, R., Yokoi, T., Tatsumi, T. and Kanno, R. *Journal of Power Sources* **222**(0), 237–242 (2013).
- [41] Ohta, H., Mizoguchi, T., Aoki, N., Yamamoto, T., Sabarudin, A. and Umemura, T. *Applied Physics Letters* **100**(17), 173107 (2012).
- [42] Aboulaich, A., Bouchet, R., Delaizir, G., Seznec, V., Tortet, L., Morcrette, M., Rozier, P., Tarascon, J.M., Viallet, V. and Dolle, M. *Advanced Energy Materials* **1**(2), 179–183 (2011).
- [43] Stramare, S., Thangadurai, V. and Weppner, W. *Chemistry of Materials* **15**(21), 3974–3990 (2003).
- [44] Jay, E. E., Rushton, M. J. D., Chroneos, A., Grimes, R. W. and Kilner, J. A. *Physical Chemistry Chemical Physics* **17**(1), 178–183 (2015).
- [45] Bohnke, O. *Solid State Ionics* **179**(1-6), 9–15 (2008).
- [46] Goodenough, J. B. *Journal of Solid State Electrochemistry* **16**(6), 2019–2029 (2012).
- [47] Li, Y., Han, J.T., Wang, C.-A., Vogel, S. C., Xie, H., Xu, M. and Goodenough, J. B. *Journal of Power Sources* **209**, 278–281 (2012).
- [48] O’Callaghan, M. P., Lynham, D. R., Cussen, E. J. and Chen, G. Z. *Chemistry of Materials* **18**(19), 4681–4689 (2006).
- [49] Percival, J., Kendrick, E. and Slater, P. *Solid State Ionics* **179**(27-32), 1666–1669 (2008).
- [50] Howard, M. A., Clemens, O., Knight, K. S., Anderson, P. A., Hafiz, S., Panchmatia, P. M. and Slater, P. R. *Journal of Materials Chemistry A* **1**, 14013–14022 (2013).
- [51] Xu, M., Park, M. S., Lee, J. M., Kim, T. Y., Park, Y. S. and Ma, E. *Physical Review B* **85**(5), 052301 (2012).
- [52] Saranya, K., Deviannapoorani, C., Dhivya, L., Ramakumar, S., Janani, N. and Murugan, R. *Materials Letters* **77**(0), 57–59 (2012).
- [53] Zaiß, T., Ortner, M., Murugan, R. and Weppner, W. *Ionics* **16**(9), 855–858 (2010).
- [54] Gupta, A., Murugan, R., Paranthaman, M. P., Bi, Z., Bridges, C. A., Nakanishi, M., Sokolov, A. P., Han, K. S., Hagaman, E. W., Xie, H., Mullins, C. B. and Goodenough, J. B. *Journal of Power Sources* **209**, 184–188 (2012).
- [55] Thangadurai, V. and Weppner, W. *Journal of Solid State Chemistry* **179**(4), 974–984 (2006).
- [56] Kotobuki, M. and Kanamura, K. *Ceramics International* **39**(6), 6481–6487 (2013).
- [57] Deviannapoorani, C., Dhivya, L., Ramakumar, S. and Murugan, R. *Journal of Power Sources* **240**(0), 18–25 (2013).
- [58] Adams, S. and Rao, R. P. *Journal of Materials Chemistry* **22**(4), 1426–1434 (2012).
- [59] Nakayama, M., Kotobuki, M., Munakata, H., Nogami, M. and Kanamura, K. *Physical Chemistry Chemical Physics* **14**, 10008–10014 (2012).
- [60] Bernstein, N., Johannes, M. D. and Hoang, K. *Physical Review Letters* **109**, 205702 (2012).
- [61] Abrahams, I., Bruce, P. G., David, W. I. F. and West, A. R. *Acta Crystallographica Section B* **45**(5), 457–462 (1989).
- [62] Xie, Q., Gu, M., Qian, B., Wu, X., Jiang, Z., Zou, J. and Gao, J. *Journal of Crystal Growth* **318**(1) 580–585 (2011).

- [63] Jalem, R., Yamamoto, Y., Shiiba, H., Nakayama, M., Munakata, H., Kasuga, T. and Kanamura, K. *Chemistry of Materials* **25**(3), 425–430 (2013).
- [64] Han, J., Zhu, J., Li, Y., Yu, X., Wang, S., Wu, G., Xie, H., Vogel, S. C., Izumi, F., Momma, K., Kawamura, Y., Huang, Y., Goodenough, J. B. and Zhao, Y. *Chemical Communications* **48**(79), 9840–9842 (2012).
- [65] Thangadurai, V., Kaack, H. and Weppner, W. J. F. *Journal of the American Ceramic Society* **86**(3), 437–440 (2003).
- [66] Murugan, R., Thangadurai, V. and Weppner, W. *Angewandte Chemie-international Edition* **46**(41), 7778–7781 (2007).
- [67] Hayashi, K., Noguchi, H. and Fujiwara, S. *Materials Research Bulletin* **21**, 289–293 (1985).
- [68] Castrejon, M. E. V. *Caracterizacion de soluciones solidas de niobato y tantalato de litio contaminadas con iones de Eu^{3+} y Mn^{2+}* . PhD thesis, Universidad Autonoma Metropolitana -Mexico, (1991).
- [69] Afonskii, N. and Neiman, M. *Inorganic Materials* **3**, 1132–1134 (1967).
- [70] Pantyukhina, M. I., Martem'yanova, Z. S. and Batalov, N. N. *Inorganic Materials* **44**(10), 1110–1114 (2008).
- [71] Galitskii, I.N., Demidov, A. I. and Morachevskii, A. *Zhurnal Prikladnoi Khimii (S. Peterburg)* **65**, 38 (1992).
- [72] Ray, B. *A study of the lithium ionic conductor $\text{Li}_5\text{La}_3\text{Ta}_2\text{O}_{12}$: From synthesis through materials and transport characterization*. PhD thesis, (2014).
- [73] Wang, Y., Klenk, M., Page, K. and Lai, W. *Chemistry of Materials* **26**(19), 5613–5624 (2014).
- [74] Jalem, R., Rushton, M. J. D., Manalastas, W., Nakayama, M., Kasuga, T., Kilner, J. A. and Grimes, R. W. *Chemistry of Materials* **27**(8), 2821–2831 (2015).
- [75] Kokal, I., Ramanujachary, K., Notten, P. and Hintzen, H. *Materials Research Bulletin* **47**(8), 1932–1935 (2012).
- [76] Ahmad, M. M. *Nanoscale Research Letters* **10**, 58 (2015).
- [77] Ahmad, M. M. and Al-Jaafari, A. *Journal of Materials Science: Materials in Electronics* **26**(10), 8136–8142 (2015).
- [78] Gao, Y., Wang, X., Wang, W. and Fang, Q. *Solid State Ionics* **181**(1-2), 33 – 36 (2010).
- [79] Wang, W. G., Wang, X. P., Gao, Y. X. and Fang, Q. F. *Solid State Ionics* **180**(23-25), 1252–1256 (2009).
- [80] Mariappan, C., Gnanasekar, K., Jayaraman, V. and Gnanasekaran, T. *Journal of Electroceramics* **30**(4), 258–265 (2013).
- [81] Reinacher, J., Berendts, S. and Janek, J. *Solid State Ionics* **258**, 1–7 (2014).
- [82] Zhong, Y., Zhou, Q., Guo, Y., Li, Z. and Qiang, Y. *Ionics* **19**(4), 697–700 (2013).
- [83] Awaka, J., Kijima, N., Takahashi, Y., Hayakawa, H. and Akimoto, J. *Solid State Ionics* **180**(6-8), 602 – 606 (2009)
- [84] Zeier, W. G. *Dalton Transactions* **43**(43), 16133–16138 (2014).
- [85] Thangadurai, V. and Weppner, W. *Advanced Functional Materials* **15**(1), 107–112 (2005).
- [86] Truong, L., Colter, J. and Thangadurai, V. *Solid State Ionics* **247**, 1–7 (2013).
- [87] Murugan, R., Thangadurai, V. and Weppner, W. *Applied Physics A-Materials Science and Processing* **91**(4), 615–620 (2008).
- [88] Deviannapoorani, C. and Ramakumar, S. Ud Din, M. M. and Murugan, R. *RSC Advances*. **6**(97), 94706–94716 (2016).
- [89] Narayanan, S., Ramezanipour, F. and Thangadurai, V. *Inorganic Chemistry* **54**(14), 6968–6977 (2015).

- [90] Wachsmann, E. D. *Ion conducting batteries with solid state electrolyte materials*. United States Patent: US20140287305 A1 (2016).
- [91] McOwen, D., Hitz, G., Wen, Y., Hamann, T., Hu, L. And Wachsmann, E.D. *Advanced Manufacturing of Solid State Ionic Devices 1. ECS Meeting Abstracts 2996* (2016).
- [92] Xiao, X., Wagata, H., Hayashi, F., Onodera, H., Yubuta, K., Zettsu, N., Oishi, S. and Teshima, K. *Crystal Growth and Design* **15**(10), 4863–4868 (2015).
- [93] Lai, W. and Haile, S. *Journal of the American Ceramic Society* **88**(11), 2979–2997 (2005).
- [94] Larraz, G., Orera, A. and Sanjuan, M. L. *Journal of Materials Chemistry A* **1**, 11419–11428 (2013).
- [95] Shannon, R. D. *Acta Crystallographica Section A* **32** (SEP1), 751–767 (1976).
- [96] Thangadurai, V., Narayanan, S. and Pinzaru, D. *Chemical Society Reviews*. **43**, 4714–4727 (2014).
- [97] Kroger, F. and Vink, H. *Solid State Physics* **3**, 307-435 (1956).
- [98] Kotobuki, M., Munakata, H., Kanamura, K., Sato, Y. and Yoshida, T. *Journal of the Electrochemical Society* **157**(10), A1076–A1079 (2010).
- [99] Sudo, R., Nakata, Y., Ishiguro, K., Matsui, M., Hirano, A., Takeda, Y., Yamamoto, O. and Imanishi, N. *Solid State Ionics* **262**, 151-154 (2014).
- [100] Jin, Y. and McGinn, P. *Journal of Power Sources* **196**(20), 8683–8687 (2011).
- [101] Suzuki, Y., Kami, K., Watanabe, K., Watanabe, A., Saito, N., Ohnishi, T., Takada, K., Sudo, R. and Imanishi, N. *Solid State Ionics* **278**, 172–176 (2015).
- [102] Takano, R., Tadanaga, K., Hayashi, A. and Tatsumisago, M. *Solid State Ionics* **255**, 104-107 (2014).
- [103] El Shinawi, H. and Janek, J. *Journal of Power Sources* **225**, 13–19 (2013).
- [104] Huang, M., Dumon, A. and Nan, C.W. *Electrochemistry Communications* **21**, 62–64 (2012).
- [105] Buschmann, H., Doelle, J., Berendts, S., Kuhn, A., Bottke, P., Wilkening, M., Heitjans, P., Senyshyn, A., Ehrenberg, H., Lotnyk, A., Duppel, V., Kienle, L. and Janek, J. *Physical Chemistry Chemical Physics* **13**(43), 19378–19392 (2011).
- [106] Kuhn, A., Choi, J.Y., Robben, L., Tietz, F., Wilkening, M. and Heitjans, P. *Zeitschrift Fur Physikalische Chemie-international Journal of Research in Physical Chemistry & Chemical Physics* **226**(5-6), 525–537 (2012).
- [107] Matsuda, Y., Sakamoto, K., Matsui, M., Yamamoto, O., Takeda, Y. and Imanishi, N. *Solid State Ionics* **277**, 23 – 29 (2015).
- [108] Amores, M., Ashton, T. E., Baker, P. J., Cussen, E. J. and Corr, S. A. *Journal of Materials Chemistry A* **4**, 1729–1736 (2016).
- [109] Cheng, L., Park, J. S., Hou, H., Zorba, V., Chen, G., Richardson, T., Cabana, J., Russo, R. and Doeff, M. *Journal of Material Chemistry A* **2**(1), 172–181 (2014).
- [110] Zhang, Y., Chen, F., Tu, R., Shen, Q., Zhang, X. and Zhang, L. *Solid State Ionics* **284**, 53 – 60 (2016).
- [111] Xia, W., Xu, B., Duan, H., Guo, Y., Kang, H., Li, H. and Liu, H. *ACS Applied Materials & Interfaces* **8**(8), 5335–5342 (2016).
- [112] Howard, M. A., Clemens, O., Kendrick, E., Knight, K. S., Apperley, D. C., Anderson, P. A. and Slater, P. R. *Dalton Trans.* **41**, 12048–12053 (2012).
- [113] Wolfenstine, J., Ratchford, J., Rangasamy, E., Sakamoto, J. and Allen, J. L. *Materials Chemistry and Physics* **134**(2-3), 571-575 (2012).
- [114] Wagner, R., Redhammer, G. J., Rettenwander, D., Tippelt, G., Welzl, A., Taibl, S., Fleig, J., Franz, A., Lottermoser, W. and Amthauer, G. *Chemistry of Materials* **28**(16), 5943–5951 (2016).
- [115] Song, S., Sheptyakov, D., Korsunsky, A. M., Duong, H. M. and Lu, L. *Materials & Design* **93**, 232-237 (2016).
- [116] Song, S., Yan, B., Zheng, F., Duong, H. M. and Lu, L. *Solid State Ionics* **268** (Part A) 135 – 139 (2014).

- [117] Bottke, P., Rettenwander, D., Schmidt, W., Amthauer, G. and Wilkening, M. *Chemistry of Materials*. **27**(19), 6571–6582 (2015).
- [118] Ohta, S., Kobayashi, T. and Asaoka, T. *Journal of Power Sources* **196**(6), 3342 – 3345 (2011).
- [119] Gu, W., Ezbiri, M., Rao, R. P., Avdeev, M. and Adams, S. *Solid State Ionics* **274**, 100–105 (2015).
- [120] Imagawa, H., Ohta, S., Kihira, Y. and Asaoka, T. *Solid State Ionics* **262**, 609-612 (2014).
- [121] Nemori, H., Matsuda, Y., Mitsuoka, S., Matsui, M., Yamamoto, O., Takeda, Y. and Imanishi, N. *Solid State Ionics* **282**, 7-12 (2015).
- [122] Ramakumar, S., Satyanarayana, L., Manorama, S. V. and Murugan, R. *Physical Chemistry Chemical Physics*. **15**, 11327–11338 (2013).
- [123] Dumon, A., Huang, M., Shen, Y. and Nan, C.-W. *Solid State Ionics* **243**, 36-41 (2013).
- [124] Abreu-Sepulveda, M., Williams, D. E., Huq, A., Dhital, C., Li, Y., Paranthaman, M. P., Zaghbi, K. and Manivannan, A. *Ionics* **22**(3), 317–325 (2016).
- [125] Tsai, C.L., Roddatis, V., Chandran, C. V., Ma, Q., Uhlenbruck, S., Bram, M., Heitjans, P. and Guillon, O. *ACS Applied Materials & Interfaces* **8**(16), 10617–10626 (2016).
- [126] Inada, R., Kusakabe, K., Tanaka, T., Kudo, S. and Sakurai, Y. *Solid State Ionics* **262**, 568 – 572 (2014).
- [127] Hamao, N., Kataoka, K., Kijima, N. and Akimoto, J. *Journal of the Ceramic Society of Japan* **124**(6), 678–683 (2016).
- [128] Liu, T., Ren, Y., Shen, Y., Zhao, S.X., Lin, Y. and Nan, C.W. *Journal of Power Sources* **324**, 349-357 (2016).
- [129] Yow, Z. F., Oh, Y. L., Gu, W., Rao, R. P. and Adams, S. *Solid State Ionics* **292**, 122-129 (2016).
- [130] Janani, N., Ramakumar, S., Kannan, S. and Murugan, R. *J. Am. Ceram. Soc.* **98**(7), 2039–2046 (2015).
- [131] Li, Y., Han, J.T., Wang, C.-A., Xie, H. and Goodenough, J. B. *Journal of Materials Chemistry* **22**(30), 15357-15361 (2012).
- [132] Li, Y., Wang, Z., Cao, Y., Du, F., Chen, C., Cui, Z. and Guo, X. *Electrochimica Acta* **180**, 37-42 (2015).
- [133] Wang, D., Zhong, G., Wei, K. P., Guo, Z., Li, Y., McDonald, M. J., Fu, R. Q., Mi, J. and Yang, Y. *Chemistry of Materials*. **27** (19), 6650-6659 (2015).
- [134] Murugan, R., Ramakumar, S. and Janani, N. *Electrochemistry Communications* **13**(12), 1373-1375 (2011).
- [135] Hitz, G. T., Wachsman, E. D. and Thangadurai, V. *Journal of the Electrochemical Society* **160**(8), A1248–A1255 (2013).
- [136] Rangasamy, E., Wolfenstine, J., Allen, J. and Sakamoto, J. *Journal of Power Sources* **230**(0), 261–266 (2013).
- [137] Deviannapoorani, C., Shankar, L. S., Ramakumar, S. and Murugan, R. *Ionics* **22**(8), 1281–1289 (2016).
- [138] Cook L. P. and Plante E. R. *Ceramic Transactions* **27**, 193-222 (1992)
- [139] German, R. M., Suri, P. and Park, S. J. *Journal of Materials Science* **44**(1), 1–39 (2009).
- [140] Ahn, J. H., Park, S.Y., Lee, J.M., Park, Y. and Lee, J.H. *Journal of Power Sources* **254**, 287–292 (2014).
- [141] Geiger, C. A., Alekseev, E., Lazic, B., Fisch, M., Armbruster, T., Langner, R., Fechtelkord, M., Kim, N., Pettke, T. and Weppner, W. *Inorganic Chemistry* **50** (3), 1089–1097 (2011).
- [142] van Wuellen, L., Echelmeyer, T., Meyer, H.W. and Wilmer, D. *Physical Chemistry Chemical Physics* **9**(25), 3298–3303 (2007).
- [143] Rettenwander, D., Blaha, P., Laskowski, R., Schwarz, K., Bottke, P., Wilkening, M., Geiger, C. A. and Amthauer, G. *Chemistry of Materials* **26**(8), 2617–2623 (2014).

- [144] Duvel, A., Kuhn, A., Robben, L., Wilkening, M. and Heitjans, P. *Journal of Physical Chemistry C* **116**(29), 15192–15202 (2012).
- [145] Rangasamy, E., Wolfenstine, J. and Sakamoto, J. *Solid State Ionics* **206**, 28–32 (2012).
- [146] Chen, Y., Rangasamy, E., Lang, C. and An, K. *Chemistry of Materials* **27**(16), 5491–5494 (2015).
- [147] Cussen, E. J. *Journal of Materials Chemistry* **20**(25), 5167–5173 (2010).
- [148] Kihira, Y., Ohta, S., Imagawa, H. and Asaoka, T. *ECS Electrochemistry Letters* **2**(7), A56-A59 (2013).
- [149] Nozaki, H., Harada, M., Ohta, S., Watanabe, I., Miyake, Y., Ikedo, Y., Jalarvo, N. H., Mamontov, E. and Sugiyama, J. *Solid State Ionics* **262**, 585–588 (2014).
- [150] Thompson, T., Sharafi, A., Johannes, M. D., Huq, A., Allen, J. L., Wolfenstine, J. and Sakamoto, J. *Advanced Energy Materials* **5**(11), 1-9 (2015).
- [151] Rettenwander, D., Geiger, C. A., Tribus, M., Tropper, P. and Amthauer, G. *Inorganic Chemistry* **53**(12), 6264–6269 (2014).
- [152] Allen, J., Wolfenstine, J., Rangasamy, E. and Sakamoto, J. *Journal of Power Sources* **206**, 315–319 (2012).
- [153] Wagner, R., Redhammer, G. J., Rettenwander, D., Senyshyn, A., Schmidt, W., Wilkening, M. and Amthauer, G. *Chemistry of Materials* **28**(6), 1861-1871 (2016).
- [154] Rettenwander, D., Redhammer, G., Preishuber-Pfluegl, F., Cheng, L., Miara, L., Wagner, R., Welzl, A., Suard, E., Doeff, M. M., Wilkening, M., Fleig, J. and Amthauer, G. *Chemistry of Materials* **28**(7), 2384-2392 (2016).
- [155] Robben, L., Merzlyakova, E., Heitjans, P. and Gesing, T. M. *Acta Crystallographica Section E-Crystallographic Communications* **72**(3), 287-289 (2016).
- [156] Toda, S., Ishiguro, K., Shimonishi, Y., Hirano, A., Takeda, Y., Yamamoto, O. and Imanishi, N. *Solid State Ionics* **233**, 102-106 (2013).
- [157] Matsui, M., Sakamoto, K., Takahashi, K., Hirano, A., Takeda, Y., Yamamoto, O. and Imanishi, N. *Solid State Ionics* **262**, 155-159 (2013).
- [158] Lager, G., Armbruster, T. and Faber, J. *American Mineralogist* **72**(7-8), 756–765 (1987).
- [159] Bell, D., Ihinger, P. and Rossman, G. *American Mineralogist* **80**(5-6), 465–474 (1995).
- [160] Galven, C., Fourquet, J.-L., Crosnier-Lopez, M.P. and Le Berre, F. *Chemistry of Materials* **23**(7), 1892–1900 (2011).
- [161] Awaka, J., Takashima, A., Kataoka, K., Kijima, N., Idemoto, Y. and Akimoto, J. *Chemistry Letters* **40**(1), 60–62 (2011).
- [162] Larraz, G., Orera, A., Sanz, J., Sobrados, I., Diez-Gomez, V. and Sanjuan, M. L. *Journal of Materials Chemistry A* **3**(10), 5683–5691(2015).
- [163] Orera, A., Larraz, G., Rodriguez-Velamazán, J., Campo, J. and Sanjuan, M. L. *Inorganic Chemistry* **55**(3), 1324–1332 (2016).
- [164] Jin, Y. *Processing and characterization of secondary solid-state Li-ion batteries*. PhD thesis, University of Notre Dame (2013).
- [165] Ma, C., Rangasamy, E., Liang, C., Sakamoto, J., More, K. L. and Chi, M. *Angewandte Chemie-International Edition* **54**(1), 129–133 (2015).
- [166] Shimonishi, Y., Toda, A., Zhang, T., Hirano, A., Imanishi, N., Yamamoto, O. and Takeda, Y. *Solid State Ionics* **183**(1), 48–53 (2011).
- [167] Radhakrishnan, B. and Ong, S. P. *Frontiers in Energy Research* **4**, 1–5 (2016).
- [168] Wang, Y., Li, H., He, P., Hosono, E. and Zhou, H. *Nanoscale* **2**(8), 1294–1305 (2010).
- [169] Truong, L., Howard, M., Clemens, O., Knight, K. S., Slater, P. R. and Thangadurai, V. *Journal of Materials Chemistry A* **1**, 13469–13475 (2013).
- [170] Li, Y., Han, J.T., Vogel, S. C. and Wang, C. A. *Solid State Ionics* **269**, 57–61 (2015).

- [171] Aguesse, F., Lopez del Amo, J. M., Roddatis, V., Aguadero, A. and Kilner, J. A. *Advanced Materials Interfaces* **1**(7), 1300143 (2014).
- [172] Li, Y., Wang, Z., Li, C., Cao, Y. and Guo, X. *Journal of Power Sources* **248**, 642–646 (2014).
- [173] Ren, Y., Shen, Y., Lin, Y. and Nan, C.W. *Electrochemistry Communications* **57**, 27-30 (2015).
- [174] Rao, R. P., Gu, W., Sharma, N., Peterson, V. K., Avdeev, M. and Adams, S. *Chemistry of Materials* **27**(8), 2903–2910 (2015).
- [175] David, I. N., Thompson, T., Wolfenstine, J., Allen, J. L. and Sakamoto, J. *Journal of the American Ceramic Society* **98**(4), 1209–1214 (2015).
- [176] Wolfenstine, J., Rangasamy, E., Allen, J. L. and Sakamoto, J. *Journal of Power Sources* **208**(0), 193–196 (2012).
- [177] Tenhaeff, W. E., Rangasamy, E., Wang, Y., Sokolov, A. P., Wolfenstine, J., Sakamoto, J. and Dudney, N. J. *ChemElectroChem* **1**(2), 375–378 (2014).
- [178] Baek, S.W., Lee, J.M., Kim, T. Y., Song, M.S. and Park, Y. *Journal of Power Sources* **249**, 197–206 (2014).
- [179] Zhu, Y., He, X. and Mo, Y. *ACS Applied Materials and Interfaces* **7**(42), 23685–23693 (2015).
- [180] Miara, L. J., Richards, W. D., Wang, Y. E. and Ceder, G. *Chemistry of Materials* **27**(11), 4040–4047 (2015).
- [181] Kim, H. R., Kim, J. C., Lee, K. R., Ji, H. I., Lee, H. W., Lee, J. H. and Son, J. W. *Physical Chemistry Chemical Physics* **13**(13), 6133–6137 (2011).
- [182] Luntz, A. C., Voss, J. and Reuter, K. *Journal of Physical Chemistry Letters* **6**(22), 4599–4604 (2015).
- [183] Cheng, L., Crumlin, E. J., Chen, W., Qiao, R., Hou, H., Lux, S. F., Zorba, V., Russo, R., Kostecki, R., Liu, Z., Persson, K., Yang, W., Cabana, J., Richardson, T., Chen, G. and Doeff, M. *Physical Chemistry Chemical Physics* **16**(34), 18294–18300 (2014).
- [184] Cheng, L., Chen, W., Kunz, M., Persson, K., Tamura, N., Chen, G. and Doeff, M. *ACS Applied Materials and Interfaces* **7**(3), 2073–2081 (2015).

2 Experimental Framework

This chapter introduces the experimental techniques applied in this work. It covers two themes: polycrystalline ceramics production and associated characterization methods.

2.1 Polycrystalline ceramics production

2.1.1 Synthesis routes

Scalable production of ceramics generally follows either solid-state or sol-gel syntheses routes. In this thesis, both routes were explored.

A conventional solid-state route begins with mixing together precursor powders. Considering reaction thermochemistry, the choice of reagents can be made from a list of procurable metal oxides, nitrites, nitrates, carbonates, phosphates, carbides, hydroxides, among others. The mix, after being fed unto a high-energy mechanical milling step, may directly form amorphous or glassy phases. However, crystalline ceramics typically require thermal activation to form. This phase-formation step is rate-limited by slow atomic diffusion between chemically-distinct reactant grains, implying that large diffusion distances (i.e. tens of microns or larger) often will necessitate multiple cycles of mechanical grinding, high-temperature and long-duration anneals prior to achieving reaction completion.



Figure 2.1: A sol-gel route preparation (citrate-nitrate type): a) reagent nitrates are dissolved in a citric acid solution, b) the water component is minimized via heat-driven evaporation until a gel forms, and c) furnace combustion at a relatively low temperature (e.g. 600°C) to burn off a large portion of organics, In preparation for crystalline phase-formation in a subsequent calcination step.

On the other hand, examples of sol-gel routes are Pechini-type protocols. As illustrated in Figure 2.1, a liquid solution is concocted containing two main ingredients: the desired elemental stoichiometry and chelating agents to impede precipitation. The solvent is gently boiled off until the mixture jellifies. The gel is fired within a muffle furnace to promote combustion of organics, which leaves behind an inorganic residue retaining a homogenous elemental dispersion. The key advantage here is that minimal diffusion barriers for crystalline phase-formation are established. This makes viable shorter and lower-temperature anneals, keeping Ostwald ripening processes in check, while still producing crystalline powders and with finer particle sizes [1]. In this thesis, the particular sol-gel route variant used was the ***citrate route***, for which citric acid acts as the chelating agent for cations of dissolved reagent nitrates.

2.1.2 Control of firing conditions

The operation of furnace equipment without knowledge of actual firing conditions carries risks which may affect the quality of produced ceramics.

When two or more chemical components are present in a system, there exist phase equilibria balancing decomposition, reformation and phase-segregation behaviors [2]. These equilibria shift as a function of temperature, but can also be disrupted by extraneous agents such as atmospheric moisture. This is a common problem with lithium- and lanthanum-based solids which tend to be hygroscopic or deliquescent, e.g. LiOH, La₂O₃, La(OH)₃. Such water-interacting components are particularly susceptible to a vaporization-condensation reflux which promotes zone-segregation from a solid-state mixture during firing, thus inhibiting single-phase formation. This will be exemplified in the syntheses studies in Chapters 3-5 [3]. It is for such reasons that the actual temperature and moisture conditions within a firing tube must therefore be well-controlled.

The furnace setup used in this thesis is illustrated in Figure 2.2.

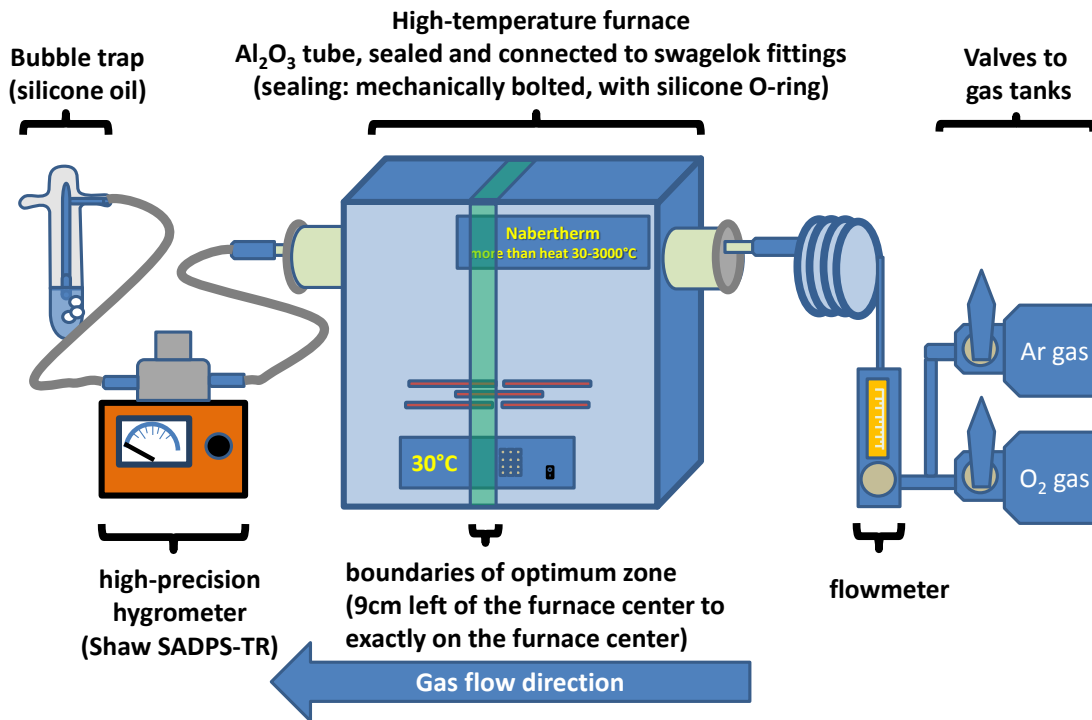


Figure 2.2: The furnace setup used for firing inorganic materials (thermal etching, calcination and sintering).

The inbuilt temperature reader of the furnace (Nabertherm RHTC 80-230/15) was calibrated using a Type N thermocouple (TC-SA, Barcelona) under two conditions: static air and dynamic gas flow (pressurized Ar for fire safety reasons, 99.9% purity).

Disengaging the hygrometer and bubble trap (Figure 2.2), the thermocouple rod was inserted through a heat-insulating porous alumina muffle at the gas-exit port. This rod was moved back and forth to map the actual dwell temperatures within the heated furnace tube. It was determined with data illustrated in Figure 2.3 that the optimum zone begins from the furnace center and extends 9cm towards the gas-exit port. This zone carries a maximum deviation of -25°C from programmed temperatures, with or without gas flow (at the flowrate of 180 mL/min used for standard firing).

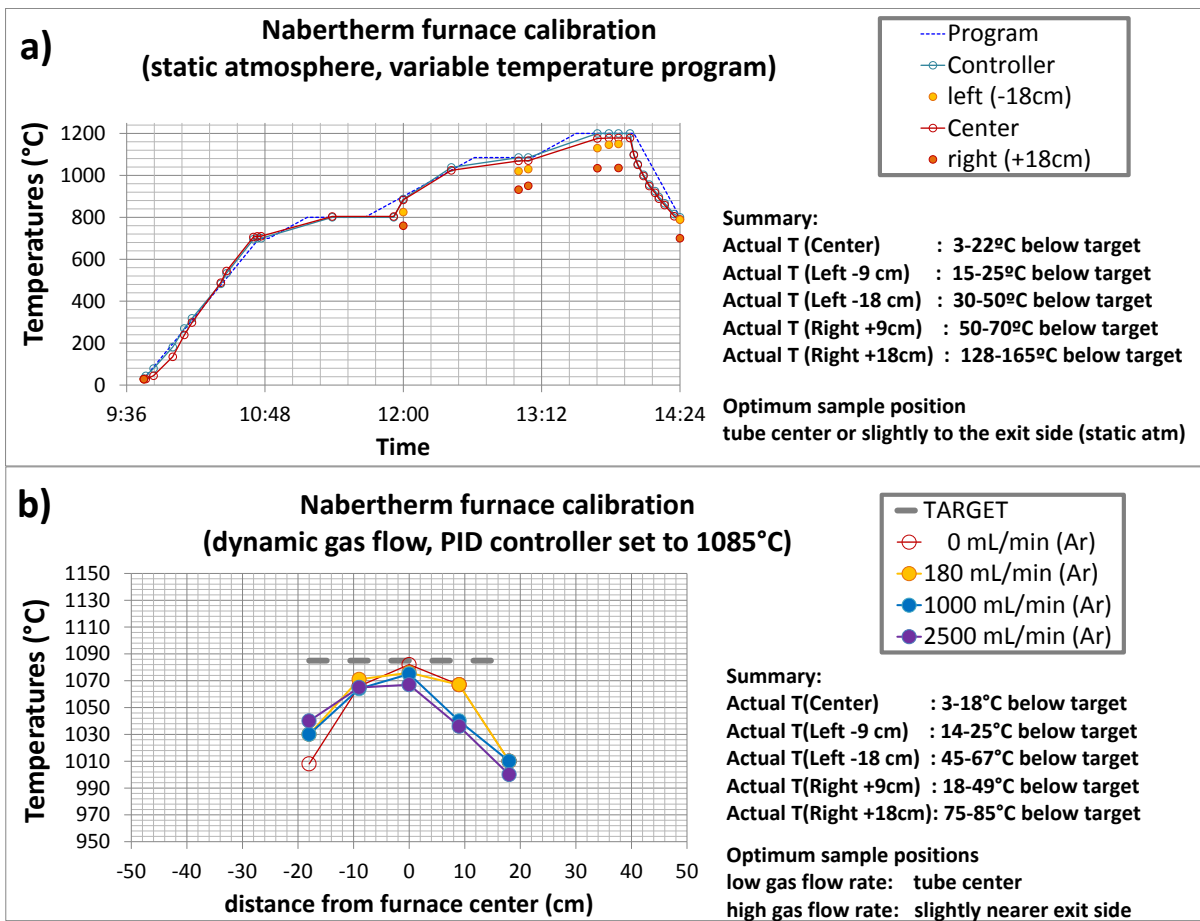


Figure 2.3: Temperature calibration of furnace zones, taken with: a) static atmosphere and b) dynamic gas flow.

To examine moisture evolutions, the furnace tube was aerated for 3 days prior to testing. The expulsion of enclosed moisture within the sealed furnace tube was monitored using a high-precision hygrometer (Shaw SADPS-TR). The purging duration necessary was compared between a simulated continuous gas-dilution (Figure 2.4a) and what was experimentally recorded (Figure 2.4b).

The simulation was based on the Basic Room Purge Equation (Equation 2.1), where C_{ending} and $C_{initial}$ are given as the final and initial vapor concentrations, respectively. Q corresponds to the flowrate of the purging gas, V is the total tube volume and t is the total purging duration.

$$\ln \left[\frac{C_{ending}}{C_{initial}} \right] = - \frac{Qt}{V}$$

Equation 2.1: The Basic Room Purge Equation for modeling continuous venting under a dry gas flow

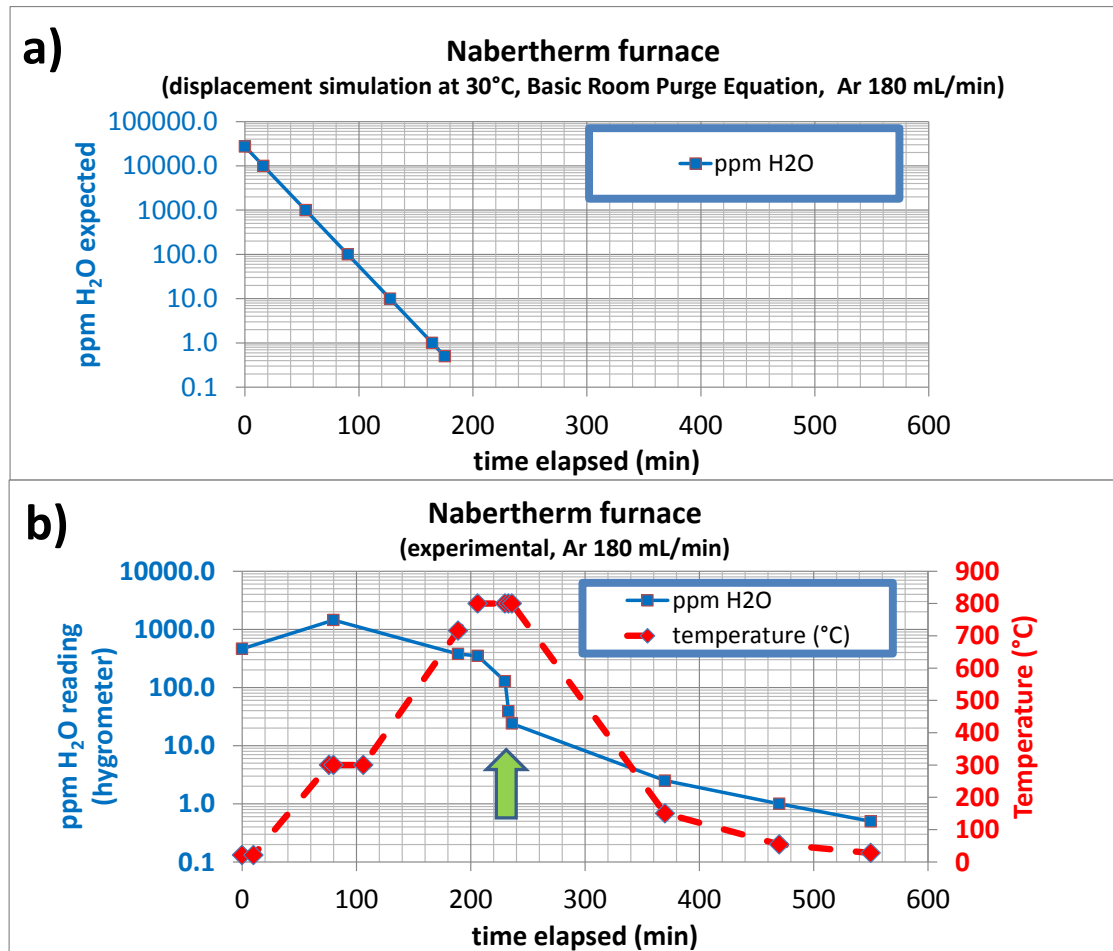


Figure 2.4: Moisture concentrations within the furnace tube as a function of purging time using 180mL Ar/min: a) simulated and b) experimental. The green arrow indicates a period of rapid drop in humidity.

This equation necessitates that the initial and target moisture concentrations be known. The city statistics office reported 68-82% relative humidity in the technological park housing the furnace equipment, with the temperature varying between 1°C to 29°C during a year [4]. To model the expected maximum purging duration necessary, ambient conditions of 30°C and 100% RH were assumed, corresponding to ~28000 ppm H₂O at the geographic elevation. Taking into account that the alumina tube had an enclosed volume of 2900 cm³ and using the arbitrary gas flow rate fixed for syntheses experiments (180 mL/min), the model yielded the plot shown in Figure 2.4a, suggesting that only 3.5 hours were necessary to attain a residual vapor concentration of 0.1 ppm H₂O.

The experimental results (Figure 2.4b) using pressurized Ar (99.9% purity) as purging gas disagreed. Moisture expulsions proceeded sluggishly relying on gas displacement. A baking dwell at 800°C aided significantly as reflected by the steep humidity drop (100ppm to 20ppm in under 20 mins; green arrow). Throughout the test, it was noted that the end fittings were cool by touch and began warming only once the central hot zone reached 800°C. It was thus deduced that the large surface capacity for adsorbed water of the porous heat-insulating alumina mufflers, was a crucial factor preventing a rapid drying of the furnace tube.

2.1.3 Green-body pressing

When powder compaction was required, green-body pellets were formed by cold uniaxial hydraulic pressing in cylindrical dies. The optimum pressing loads were determined to be 1.5 tons for a diameter of 6.35 mm (520 MPa) and 3 tons for a diameter of 10 mm (375 MPa). Much care was taken to minimize atmospheric exposure. This was due to an observation that non-sintered pellets left in the bench for a week spontaneously disintegrated.

2.1.4 Pellet firing

Protective mother powder was loosely applied on the tops and bottoms of test-pellets prior to firing. Such powder support provided ~4 mm clearance between the pellets and the crucible surface. Al₂O₃ boats were normally used as substrates. ZrO₂ boats were used in special cases (Chapter 5). Pellets were fired in ambient air, Ar (99.9% purity) or O₂ (99.99% purity) gas flows.

2.1.5 Pellet polishing

The mother powder created partly-fused agglomerates on the pellet surface upon sintering. These were progressively abraded using 800, 1200, 2400 and 4000-grit SiC polishing papers (Lamplan®) to a lustrous pellet finish, within an Ar-filled glovebox (0.1 ppm O₂, <0.1 ppm H₂O).

2.1.6 Density measurement

Only geometrical densities are reported. Computations assumed perfectly cylindrical pellets. Unaccounted imperfections give artificially higher volumes. Reported densities are hence lower limits of the true material densities. This carries over in the computation for relative density (Equation 2.2):

$$\text{Relative density (\%)} = \frac{\text{geometrical density}}{\text{unit cell density (as deduced from XRD)}}$$

Equation 2.2: The formula for relative density: the experimental mass/volume of a fabricated material compared to the predicted density for a single crystal.

Archimedes' procedure could not be applied due to possible contamination issues with liquid media that would invalidate further characterizations, as required by the design of the studies. Liquids (e.g. alcohols, ketones, oils) may contain moisture which may react with the lithium component or prove difficult to extricate from pores once infiltrated, without losing the protection from atmospheric exposure provided by the Ar-glovebox.

2.2 Materials characterization

This section is divided into three parts: structural/morphological (PXRD, SEM), physico-chemical (NMR, Raman, ICP-OES, FIB-SIMS) and electrochemical characterization (EIS). The acronyms are spelled out below in the subsection headings.

2.2.1 Structural and morphological characterization

2.2.1.1 Powder X-ray diffraction (PXRD): data acquisition

Ceramics are made of inorganic crystallites. The fundamental structure of each crystal is a regular atomic distribution in periodically repeating cages called *unit cells*. It has long-range order, meaning an atomic model can be used for predicting properties of perfect materials in bulk form: density, chemistry and electronic behavior.

The primary tool for elucidating a crystal structure is x-ray diffraction (XRD). The idea is that electron clouds (ergo atomic positions) can elastically scatter monochromatic radiation. However, by using the appropriate wavelength (e.g. X-rays) and certain orientations, it is possible to guide electromagnetic waves into constructive interference using atoms as scattering points.

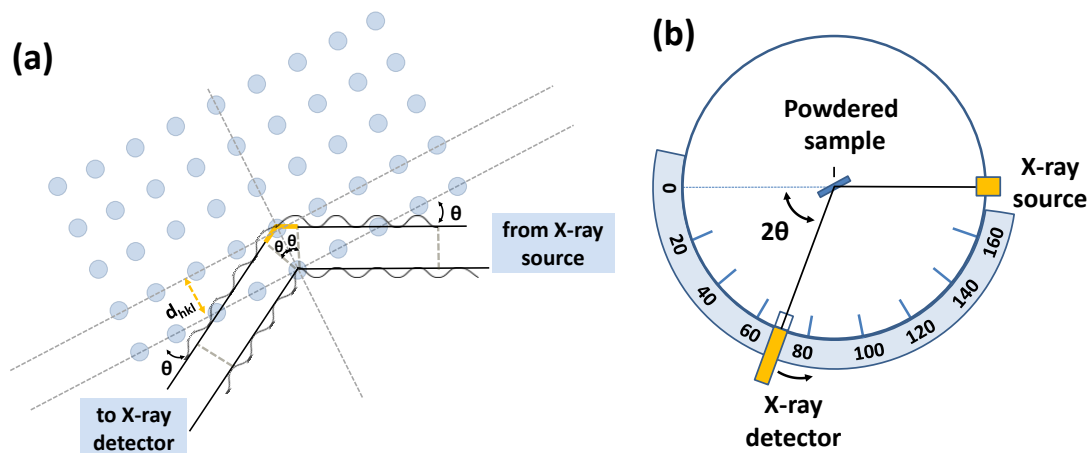


Figure 2.5: Illustrations of (a) Bragg's law condition of the first order ($n=1$) and (b) the XRD setup (Bragg Brentano geometry) for powder samples.

When this happens, the extra distance (green lines, Figure 2.5a) traveled by the photon in penetrating from one atomic layer to the next ($2d_{hkl} \sin\theta$) is exactly a multiple of its wavelength ($n\lambda$). This leads to a net increase in wave amplitude, and allows for coherent specular reflection with atomic layers (or lattice planes) acting as mirrors. This is a Bragg's reflection condition, as expressed in Equation 2.3. The shortest path between the two atomic layers is d_{hkl} , corresponding to a Miller index notation (h,k,l) of a particular lattice plane.

$$n\lambda = 2d_{hkl} \sin\theta$$

Equation 2.3: Bragg's Law

In practice, the positional configuration between the X-ray source, crystalline sample and the X-ray detector are varied (Figure 2.5b). The positions fulfilling the Bragg condition produce significantly higher X-ray intensity (holding exposure periods normalized). Because each crystal structure populates atoms in 3D space differently, they produce unique diffractograms.

Single-crystal XRD uses one single-phase grain to map all lattice reflections in 3D space (θ, ϕ angles in Cartesian coordinates), rotating the detector in a sphere of precise goniometer radius. Powder XRD shortens scan times by relying on statistics of random grain orientations in a fixed volume. As such, it uses an enormous amount of small crystalline grains, and only needs to rotate the detector in one 2D circle (θ). Powder XRD is more aptly called polycrystalline XRD, and assumes that the incident X-ray beam

impinges on the sample in equal representation of crystal orientations as it would have had in performing the θ - ϕ angular scans with single-crystal XRD.

Powder XRD is thus a powerful and efficient technique, but comes with three caveats: First, an inevitable loss of information occurs in passing from a 3D domain to a 2D domain, i.e. peak overlaps complicate analytical discernment of the true structure due to an increased number of possible candidates. Second, this technique is highly dependent on the sample preparation step to avoid preferential orientation and inhomogeneous packing artifacts. Third, powders inherently expose large surface areas, drastically increasing atmospheric interaction. In this research, special sample holders (Figure 2.6) made of amorphous polymeric material, i.e. polymethylmethacrylate (PMMA), and polyimide films (Kapton®) isolated powders from external contamination after preparation within the Ar-glovebox. A tiny piece of Plasticine® was sometimes used to hold powder samples of scant quantity in place. XRD patterns were collected at ambient temperature and pressure conditions, except in explicitly-stated cases.

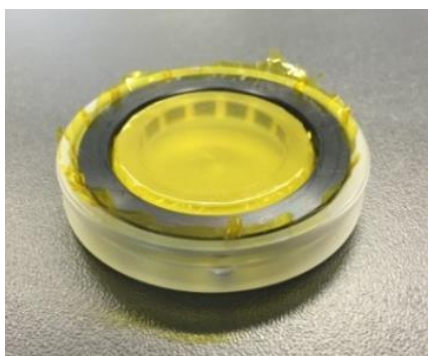


Figure 2.6: Inhouse sample holder for air-sensitive samples (designed to fit on the sample stage of the Bruker D8 diffractometers).

XRD patterns were recorded using two Bruker instruments: the older model D8 Advance® ($\lambda_{\text{CuK}\alpha 1}=1.54056 \text{ \AA}$, $\lambda_{\text{CuK}\alpha 2}=1.5443 \text{ \AA}$), and the recently-acquired D8 Discover® ($\lambda_{\text{CuK}\alpha 1}=1.54056 \text{ \AA}$). X-rays were generated by impinging electrons on copper anodes at 50kV acceleration and 30mA, with Ge monochromators suppressing undesired output energies (e.g. $\text{CuK}\beta$). Knife edge collimators in combination with slits (1mm slit size for the X-ray source and 5mm for the X-ray detectors) were installed to minimize axial divergence effects of the beam trajectories.

Unless otherwise indicated, the data in this thesis were obtained using the dichromatic D8 Advance. Diffractograms were recorded in the 2θ -angle range from 15° to 80° using a step size of 0.02° spread over a total counting time of 60-minutes.

2.2.1.2 Powder X-ray diffraction (PXRD): data analysis

XRD was routinely used to monitor phase-formation, identify impurities and study degradation, by matching peak positions against materials documented in the ICSD (FIZ Karlsruhe) and PDF2-2010 (ICDD) databases. XRD patterns were fitted using the Fullprof software [5].

Phase-pure samples were refined by the LeBail method to obtain their unit cell parameters [6]. This method matches peak positions according to a set of reflection rules provided by the expected symmetry, with no specific model for atomic content.

The inclusion of **atomic scattering factors** (f , Figure 2.7) accounts for the observed intensities, and provides insights as to how atoms populate the lattice, i.e. their exact spatial positions. The Rietveld method approaches this structural puzzle by finding the best fit between the experimental XRD pattern and a theoretical XRD pattern derived from a model structure [7].

However, atomic scattering factors are small for light elements and also exhibit additional Bragg-angle-dependent decays ($\sin\theta/\lambda$, where θ is given in radians). Hence, X-ray techniques may prove imprecise for exact structural determination involving low-concentration dopants and lithium-rich structures (e.g. 7 Li per 24 atoms in $\text{Li}_7\text{La}_3\text{Zr}_2\text{O}_{12}$). The sensitive intensity fluctuations due to these light atoms are masked further due to non-ideal statistics of grain-sizes from hand-milled sintered ceramics. In light of these challenges, this study had been reluctant to engage in full structural refinement using the current XRD data.

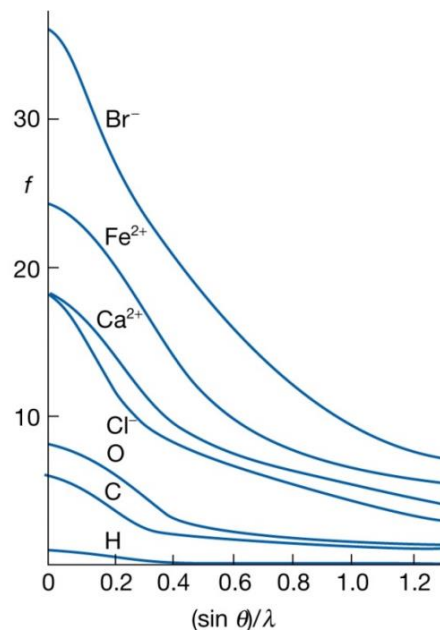


Figure 2.7: X-ray scattering factors for sample atoms (adapted from [8]).

Nonetheless, garnet-structured oxides are known to crystallize in either $Ia\bar{3}d$ and $I41/acd$ space groups. Structural models of the parent $\text{Li}_7\text{La}_3\text{Zr}_2\text{O}_{12}$ have also been properly derived using single crystals and neutron diffraction data in literature, as discussed in Section 1.1.4.3.4.

By combining precise Le Bail-fit models of crystal parameters and fixed atomic parameters within crystal lattices as described in literature, multiphase samples could be confidently analyzed using a pseudo-Rietveld approach to obtain the weight percentage of each phase.

2.2.1.3 Scanning Electron Microscopy (SEM)

A scanning electron microscope is a system composed of an electron gun mounted with electromagnetic objectives for focusing an electron beam towards a material surface, scanning pointwise across a 2D grid, and relaying each signal to an imaging system. It is a technology founded on the wave-particle duality of free electrons interacting with atoms in a solid.

As a wave, an electron beam obeys the rules of optics, just like visible light. Its trajectory can be bent using waveguide condensers to achieve arbitrary spot sizes. Its wavelength can be modulated by conferring energy to the electron beam, i.e. by

ramping an acceleration voltage from the electron gun to the substrate material according to Equation 2.4. The more the energy conferred, the shorter the wavelength and the higher the resolution [9].

$$\lambda = \frac{hc}{[eV(2m_0c^2 + eV)]^{\frac{1}{2}}}$$

Equation 2.4: The electron beam wavelength as a function of acceleration voltage within the electron microscope (relativistic correction for rest energy and kinetic energy included).

Here, h is the Planck constant, m_0 is the rest mass of an electron, e is the elementary charge, V is the accelerating voltage and c is the speed of light. This equation means that in commercial electron microscopes, a voltage range of 5kV to 1000kV will generate wavelengths between 0.173-0.0087Å, giving access to spatial resolutions at higher magnifications unattainable using only visible light (400-700nm).

As particles, free electrons can dislodge substrate electrons at impact, creating three types of emissions: low-energy secondary electrons ($\leq 50\text{eV}$), high-energy backscattered electrons ($\geq 50\text{ eV}$) and X-ray photons. Each has a characteristic interaction volume from whence the emissions originate from for a fixed beam voltage, and can be comparatively illustrated as in Figure 2.8. Secondary electrons (SE) are ejected from the immediate surface as products of inelastic collision and hold valuable topological information. Backscattered electrons (BE) are ejected from a cascade of elastic collisions across larger interaction volumes and exhibit intensities proportional to the atomic number of the elements composing the substrate. X-rays are emitted when an electron near the core-shell of an atom is knocked off and a valence electron descends to occupy the electron vacancy, and hence display characteristic energies depending on the identity of the element (the detector for which is called EDAX or Energy Dispersive X-ray Spectrometer).

In this work, SEM has been highly valued for its versatility in confocal localized sampling, microstructural visualization and elemental analysis. The equipment used was a FEI Quanta-200FEG model equipped with EDAX analysis capabilities. The acceleration voltages used were varied between 8kV to 30kV. All samples were mounted on conductive carbon tapes held by aluminum stubs.

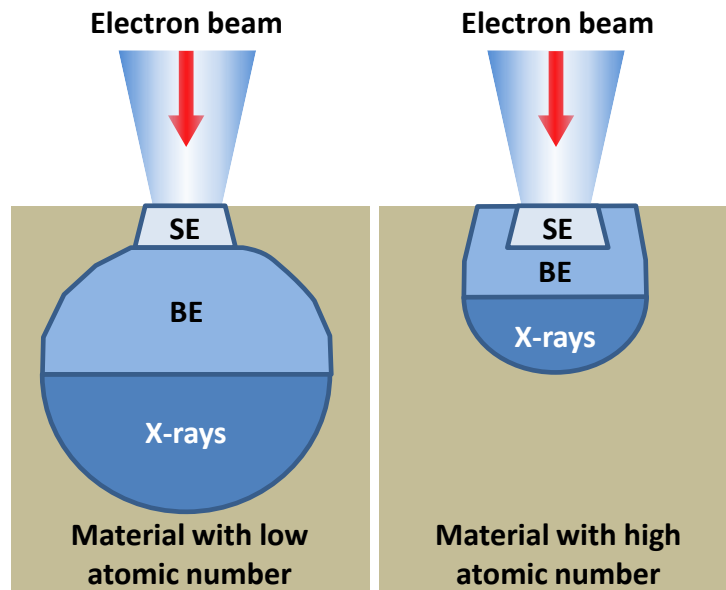


Figure 2.8: The interaction area between an electron beam and the material under study, detailing the origin of the secondary electrons (SE), backscattered electrons (BE) and X-ray photons. SEs originate from electron-impinging interactions on the nanometer-scale from the surface, whereas BEs and X-ray typically result from penetration in the order of microns.

2.2.2 Physico-chemical characterization

2.2.2.1 Inductively coupled plasma-optical emission spectroscopy (ICP-OES)

The elemental stoichiometry of ceramic pieces was determined using two methods: SEM-EDAX and ICP-OES. Whereas the former is a focused-beam analysis technique, the latter requires bringing the chemical elements comprising a ceramic into solution. As such, ICP-OES is a sample destructive procedure.

Basically, plasma incineration of an aspirated analyte produces its excited atoms and ions. Upon relaxation, they emit photons of characteristic wavelengths. The calibrated intensities correspond to analyte/ion concentrations, and can therefore determine elemental ratios. The exceptional value of ICP-OES is in trace analyses, as is the case with low-concentration dopant elements, due to its high temperatures (>6000 K) ensuring elemental excitation.

This research work used a Horiba Ultima 2 optical emission spectrometer. The feed is nebulized within the equipment, therefore ceramic chunks were predissolved in

ultrapure HNO₃ acid (67-69%, trace-metal grade, Fischer Scientific) using a microwave-irradiated Teflon digester. To protect the equipment tubing, all solutions fed to the spectrometer were diluted in deionized water (Millipore, registering 13.1 MΩcm at 25°C) to have <2% HNO₃ concentration.

For elemental calibrations, ultrapure standard solutions (Fluka, TraceCERT® grade) of Li⁺ (in 2% HNO₃), La⁺ (in 2% HNO₃) and Zr⁺ (in 2% HNO₃ and 2% HF) were used prior to each measurement. An inhouse Ga³⁺ standard solution was formulated from solid Ga₂O₃ (Aldrich, ≥99.99%) using the shelf-stock of ultrapure HNO₃ mentioned above.

2.2.2.2 Focused-ion beam Secondary Ion Mass Spectrometry (FIB-SIMS)

A FIB-SIMS system is analogous to an SEM system, except that it uses an ion beam instead of an electron beam to interact with a material surface. Its key component is the ion gun, basically a tungsten needle tip to which a liquid metal ion source (e.g. gallium) flows to undergo ionization, field emission and from there be subject to an acceleration voltage between 1kV and 50kV. When the ions impinge upon the target, the momentum transferred is much greater compared to electrons due to mass considerations. Each collision can create free positive ions, negative ions, neutral molecules and/or electrons in a statistical distribution, essentially an atomic sputtering effect. This implies a sensitive layer-by-layer analysis of a material block is theoretically possible by using two ion detectors (positive and negative ion collectors) and applying principles of mass spectrometry [10].

The practical implementation of this in ion-conducting electroceramics is through Isotopic Exchange Depth Profiling (IEDP). IEDP is done by a controlled-time exposure of a ceramic to an enriched isotope (e.g. deuterium) to allow a concentration gradient to build, then quenching the atomic ensemble to stasis immediately, thus creating a “snapshot” of the diffusion process. This information is retrieved via elemental depth profiling within the FIBSIMS instrument and applying Crank’s solution to Fick’s equations with the assumption that the conversion from sputter-rate to sputter-depth is linear for an ion beam making its way through the uniform elemental distribution of each single crystal [11, 12, 13].

For the FIBSIMS experiments, the operational expertise of Dr. Richard Chater is acknowledged. The ceramics were mounted using clips onto the sample stage and sputtered with a 30keV gallium ion beam incident at 30° normal to the ceramic surface to produce craters. The instrument was equipped with detectors for secondary

electrons, positive ions and negative ions to allow an asynchronous semi-simultaneous signal acquisition [14]. Positive ions were detected by an FEI SIMS detector whereas negative ions were detected by a Hiden EQS SIMS detector system.

2.2.2.3 Raman Spectrometry

Raman spectroscopy is based on laser light interactions with matter. Specifically, the use of monochromatic radiation in the visible, near-infrared or near-ultraviolet spectra induces vibrations in chemical bonds. This creates an excited state which can revert to its original low-energy state or relax to an intermediate vibrational mode, in both cases emitting a photon.

The former emits a photon of resonant frequency, whereas the latter emits a photon of shifted frequency. Raman spectra are plotted with respect to the laser frequency, arbitrarily offset to 0 cm^{-1} . This scale facilitates a mapping of the intermediate vibrational energy states by using the frequencies (ν) where signal peaks appear and Planck's constant (h), i.e. $E=h\nu$.

Because vibrational modes are uniquely dependent on chemical composition and bond configurations, recorded energy bands are spectral fingerprints of different materials. When light is not absorbed and reemitted with a different energy, e.g. shiny metals, no Raman peaks are recorded.

In this thesis, confocal Raman spectra were collected at room-temperature with an inVia Renishaw confocal microscope, operated by Jokin Rikarte (inhouse). The excitation wavelength of 532nm from an Ar⁺ ion laser was used. The laser spot size was <2.0 micrometers at 1.5mW with a time step of 50s. Signals were accumulated within the wavenumber range 100-800 cm^{-1} .

2.2.2.4 Nuclear Magnetic Resonance (NMR)

Nuclear magnetic resonance exploits the magnetic properties of special atomic nuclei to gain knowledge about their mobility and environment. Herein, the examinable nuclei are only those with an odd number of either protons or neutrons, i.e. a non-zero nuclear quantum spin.

In this work, how structural lithium, gallium and proton nuclei behaved before and after atmospheric moisture exposure were monitored by $^7\text{Li}/^{71}\text{Ga}/^1\text{H}$ MAS-NMR with a 11.7T Bruker AV-III-500. The DMFIT software was used to conduct spectral fittings [15].

The basic principle is as follows: when immersed in a static magnetic field of strength B_0 , nuclear spins attempt to align parallel or anti-parallel to the magnetic field direction. The anti-parallel configuration occurs in an elevated energy state (Figure 2.9).

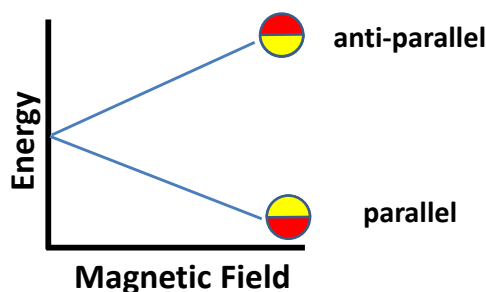


Figure 2.9: The energy difference (ΔE) between two spin states increases with the applied magnetic field (B_0).

The spin directions are populated based on a Boltzmann distribution (Equation 2.5). Herein, N^- is the number of high energy nuclei, N^+ is that of the low energy nuclei, ΔE is the energy difference between two spin states, k_B is the Boltzmann constant and T is the temperature in kelvins.

$$\frac{N^-}{N^+} = e^{\left(-\frac{\Delta E}{k_B T}\right)}$$

Equation 2.5: The equilibrium distribution of nuclei spins among low and high energy states within an external magnetic field

Stimulating the system using radiofrequency (RF) waves of appropriate energies will promote a temporary increase in the high energy population (N^-) and shifts the net magnetization vector. As the system relaxes back to steady-state equilibrium, the nuclei oscillate along transverse axes and generate an electromagnetic field that can be transduced into an electric signal. This registers as a **free induction decay**, which can be Fourier-transformed to generate NMR signals in the frequency domain as indicated in **Figure 2.10**.

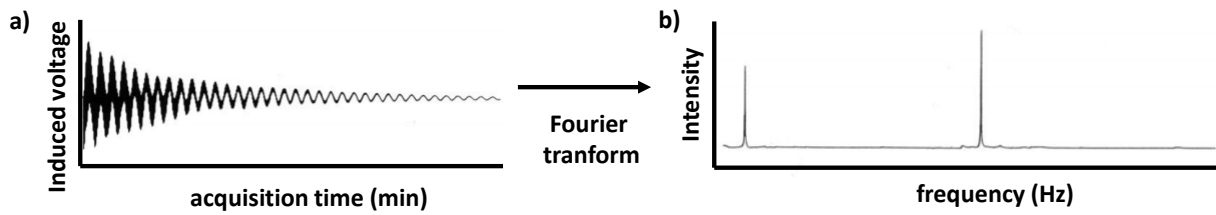


Figure 2.10: a) The free induction decay: the voltage signal induced in the receiver coil versus time. b) The Fourier transform of plot a generates the NMR spectrum.

An advanced application of this excitation principle is the saturation recovery experiment. The N^-/N^+ population can be saturated by repeated RF bursts to provide torque rotating the net magnetization vector 90° relative to the axis of the external static magnetic field B_0 . This way the two spin populations (N^-/N^+) equal each other and the B_0 -parallel magnetization component becomes 0. When the readout signal is taken, the intensity would follow an exponential decay function, which may be composed of one or more subcomponents depending on the number of distinct nuclei reservoir (Figure 2.11). This is known as a T_1 relaxation process, and the time constant describing the probable lifetime of an excited state is called the **spin-lattice relaxation time (T_1)** in Equation 2.6.

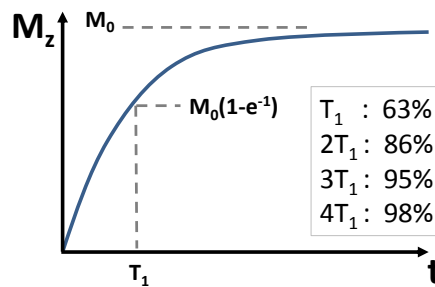


Figure 2.11: The graph of the evolution of net magnetization (M_z) with time t during T_1 relaxation of a single nuclei reservoir along the external magnetic field with respect to the initially induced net magnetization (M_0).

$$M_z = M_0 \left(1 - \exp\left(-\frac{t}{T_1}\right) \right)$$

Equation 2.6: The equation of the evolution of net magnetization (M_z) with time t during T_1 relaxation of a single nuclei reservoir along the external magnetic field with respect to the initially induced net magnetization (M_0)

T_1 relaxations occur by a wobbling motion of excited nuclei as the ensemble relaxes back to equilibrium. This is called a precession, and each turn about the B_0 axis follows a characteristic frequency (ν) related to the magnetic field (B) and nuclei-specific gyromagnetic ratios (γ_g) according to the **Larmor** equation (Equation 2.7). However, unequal magnetic fields maybe experienced by nuclei due to varied nearby electron cloud environments. This would be reflected in the Larmor frequency and therefore the T_1 relaxation. This in turn means that non-identical spin reservoirs and different mobilities can be identified.

$$\nu = \gamma_g B$$

Equation 2.7: The expression for the Larmor precession frequency as determined by the gyroscopic ratio (γ_g) and magnetic field strength felt by a nucleus (B)

NMR data can also be interpreted using spectral lineshape analyses on the basis of chemical shifts. Anisotropic dipolar coupling may cause poor spectral resolution however. That is, in solution NMR, spectra consist of very sharp transitions due to motional averaging of nuclear dipole-dipole coupling, chemical shift anisotropy and quadrupolar coupling by rapid random tumbling. Static NMR spectra of solids are typically broad as the interactions just mentioned do not average out in the NMR timescale (Figure 2.12).

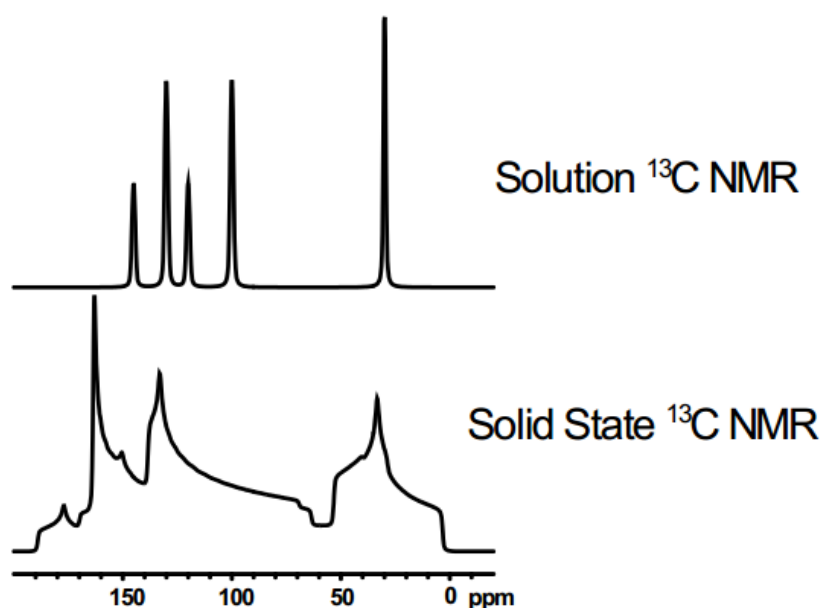


Figure 2.12: Solution vs solid-state NMR. Matrix anisotropy effects are evident in solid-state NMR due to lack of motional averaging.

Obtaining finer NMR information on solid samples is possible with magic angle spinning. By spinning the sample at sufficient speeds at the magic angle (54.74°) relative to the magnetic field vector, the dipole-dipole coupling and anisotropy average out allowing normally broad lines to be narrower and sometimes improving resolution to the solution level (Figure 2.12). Quadrupolar interaction remnants can be treated by special pulse techniques [16].

$$b_{12} = -\frac{\mu_0 \gamma_1 \gamma_2 \hbar}{4\pi r_{12}^3}$$

Equation 2.8: Dipolar coupling relation fundamentally relating heteronuclear gyroscopic constants and the distances between the two nuclei.

However, if the spinning speed is insufficient, *satellite* or *spinning sidebands* which progressively separate as a function of spinning speed (in Hz) become visible. The spinning sidebands are remnants of dipolar coupling interactions resulting from two spins mutually generating magnetic fields oriented parallel to the nuclear spin vector, thus causing a different effective magnetic field B_{eff} on each. The strength of the dipole-dipole coupling b_{12} depends strongly on the spin-spin distance r_{12}^3 as well as the gyromagnetic ratios γ_1 and γ_2 of the coupled spins, and the magnetic dipole moment (μ_0) as expressed in Equation 2.8. The reduced Planck constant is represented by \hbar .

2.2.3 Electrochemical characterization

2.2.3.1 Electrochemical impedance spectroscopy (EIS): data acquisition

Electrochemical impedance spectroscopy (EIS) is a powerful technique for studying corrosion, interfacial kinetics and ion-selective electrolytes [17]. Applied in this work, its main interest is in measuring the ionic conductivity of electroceramic pellets.

EIS explores materials by considering them as part of an electrical circuit. The typical setup is a two-probe configuration: A pellet sample with electronically-conductive contacts on its opposite basal planes is plugged to an alternating voltage generator. The machine transmits a sinusoidal voltage waveform $v(t) = V_m \sin(\omega t)$ and measures the alternating current (AC) response waveform $i(t) = I_m \sin(\omega t + \vartheta)$.

Each excitation frequency ω generates one datapoint. By performing a frequency sweep under Fourier transform, impedance $\mathbf{Z}(j\omega)$ values can be rapidly generated using the excitation voltage (V_m) and feedback current (I_m) amplitudes in accordance with Ohm's law (Equation 2.9).

$$Z(j\omega) = \frac{V_m(j\omega)}{I_m(j\omega)} = \sqrt{R^2 + \chi^2}$$

Equation 2.9: Impedance expression modelled as an ohmic circuit response.

The impedance $\mathbf{Z}(j\omega)$ can be viewed as the joint response of multiple resistor, capacitor and inductor components in an electronic circuit. Its nature as a complex quantity (herein $j = \sqrt{-1}$) means its components can be represented in a complex plane: a **Nyquist diagram**. The frequency-independent components (resistance R) contribute to the real axis (\mathbf{Z}'), whereas the frequency-dependent components (reactance χ) contribute to the imaginary axis (\mathbf{Z}'').

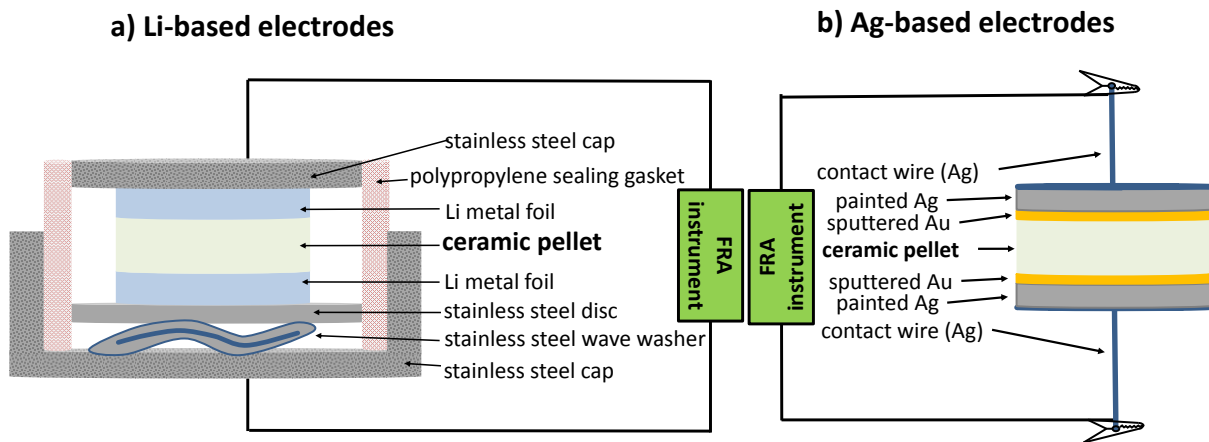
Experimental setup: samples

Figure 2.13: EIS testing configurations using a) metallic lithium electrodes (non-lithium-ion-blocking) and b) silver-paint (lithium-ion-blocking).

It is possible to measure ionic conductivity of candidate electrolyte materials using this technique. For this thesis, the Li-ion conductivities of sintered ceramics were analyzed using the 1260 impedance/gain-phase analyzer from Solartron Analytical®. After polishing pellets according to section 2.1.5, equal diameters of lithium-blocking electrodes or non-lithium-ion blocking electrodes were applied on each pellet face. One purpose for these is to form good homogeneous contacts between the ceramic sample and the leads to the EIS equipment.

For non-lithium-ion blocking electrodes (Figure 2.13a), each pellet was sandwiched between two Li-metal discs, placed inside a 2032 coin cell and hermetically closed while within an Ar-filled glovebox (<0.1 ppm H₂O). These coin cells were measured in the 0-86°C temperature range as regulated using an ice bath or a Buchi glass oven. The activation energies acquired were later revalidated using the inhouse PPMS (Physical Properties Measurement System by Quantum Design Inc.) platform, which provided high precision temperature control of ±0.02°C.

The coin cell was then dismantled and the pellet polished to remove the metallic lithium on the surface. The recovered pellet was then stored inside the Ar-filled glovebox for a complementary set of measurements using lithium-blocking electrodes.

For lithium-blocking electrodes (Figure 2.13b), masked pellets were pre-sputtered with 20nm Au as monitored by a quartz microbalance prior to application of Ag-paint (SPI Flash-Dry™ Silver Paint) and Ag-wire contacts. The paint was allowed to dry and set within the Ar-filled glovebox (<0.1 ppm H₂O) overnight, prior to impedance measurements using grounded coaxial (BNC) cables. The reader is reminded however that the Li-blocking nature of Au/Ag contacts is limited. The existence of Li-Au and Li-Ag alloys has been reported [18, 19] and may form at the electrode interface. However, such alloying fronts proceed sluggishly even with thin films [20].

Experimental setup: instrument

Two examples demonstrate why cross-checking spectral datasets using multiple acquisition settings for each sample was rigorously implemented in this research:

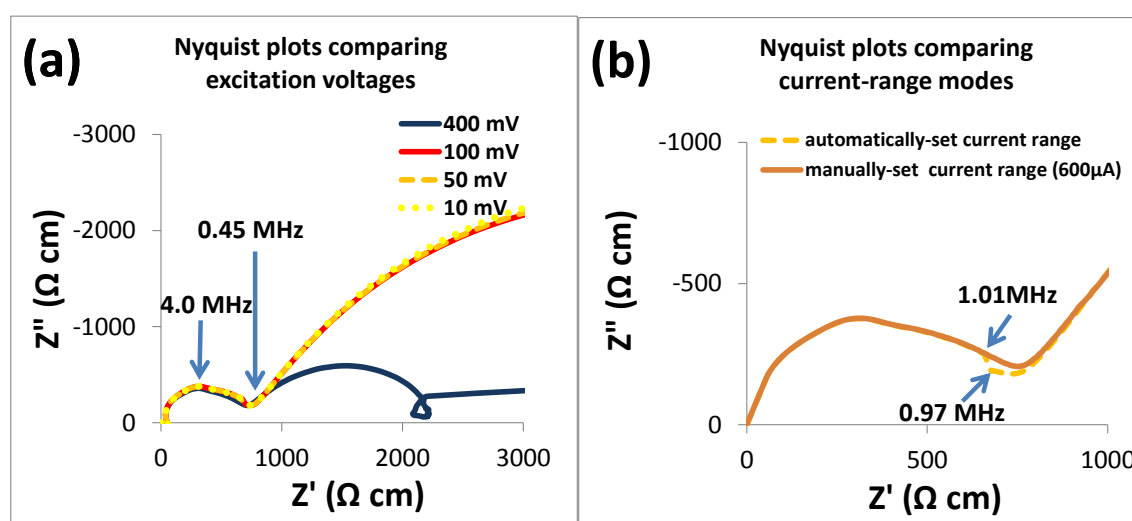


Figure 2.14: EIS spectra (Nyquist) of a $\text{Li}_{6.55}\text{Ga}_{0.15}\text{La}_3\text{Zr}_2\text{O}_{12}$ pellet acquired with varying (a) excitation voltages and (b) current-detection range. The test pellet was taken from Section 4.3.3.

1. A high excitation voltage increases the signal-to-noise ratio, but there is a limited range of linearity between V_m and I_m prior to the loss of steady-state acquisition conditions. Beyond a certain excitation amplitude, the spectrum is markedly distorted, as demonstrated by the Nyquist diagram corresponding to a 400mV-excitation (Figure 2.14a).

2. Under conditions of negligible wiring induction, reactance χ components are eliminated at infinite AC frequency. Samples permit large current flows at high frequencies and minimum current flow at low frequencies. Thus, current ranges often span several orders of magnitude and require different levels of detector sensitivity. The frequency response analyzer (FRA) built within the Solartron 1260 instrument solves this by simultaneously measuring using three dynamic ranges. However, when the waveform generator (output signal) and the instrument-selected gauge sensitivity (input signal) are mismatched due to poor calibration, a discontinuity artifact occurs in the acquired spectrum. Here it is observed when transitioning through 1MHz (Figure 2.14b). This can be fixed by a manual override to assign the correct dynamic range and current sensitivity required for each frequency range.

Table 2.1: Summary of EIS experimental settings.

Setting	Value
DC bias	0 V
Amplitude	50mV
Frequency range	3.2MHz – 1 Hz
Frequency steps	50 points /decade
Integration cycles	10

The Z-plot software (version 3.3c) provided by Scribner Associates, provided the control interface for the AC-voltage generator. The optimized parameter settings are indicated in Table 2.1, and only the optimized spectra are shown in this work.

2.2.3.2 Electrochemical impedance spectroscopy (EIS): data analysis

EIS analysis relies on the dielectric relaxation theory. Extensive mathematical treatments are provided by Jonscher [21], Barsoukov/McDonald [22], and Tribollet/Orazem [23], but the physical concepts can be summarized as follows:

An AC circuit excites charged particles to follow its alternating electric field. This creates resonance or relaxation mechanisms depending on the applied frequency (Figure 2.15). Above 10^{11} Hz, phase-resonance is observed for elementary charge oscillations. Below 10^{11} Hz, phase-delays with respect to the excitation waveform can set in, dispersing transported energy via relaxation.

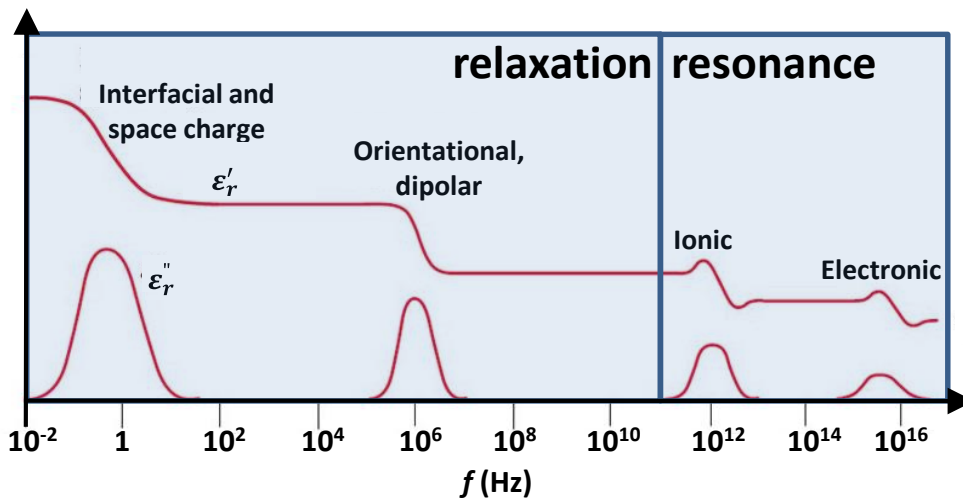


Figure 2.15: Trends of dielectric responses ($\epsilon_r = \epsilon_r' - i\epsilon_r''$) to applied AC-frequencies (after [24]).

Relaxations exhibit characteristic times (frequencies) for equilibration which depend on the identity and environment of charge carriers. This implies that in materials with unique charge carriers, the influence of local environments can be analytically examined. This is the case with single-ion conductors of negligible electronic conductivity,

When the material is a polycrystalline electrolyte, most of the frequency range between 10^{-2} and 10^{10} Hz can be used to probe ion transport across its microstructural domains. This is demonstrable using Figure 2.16.

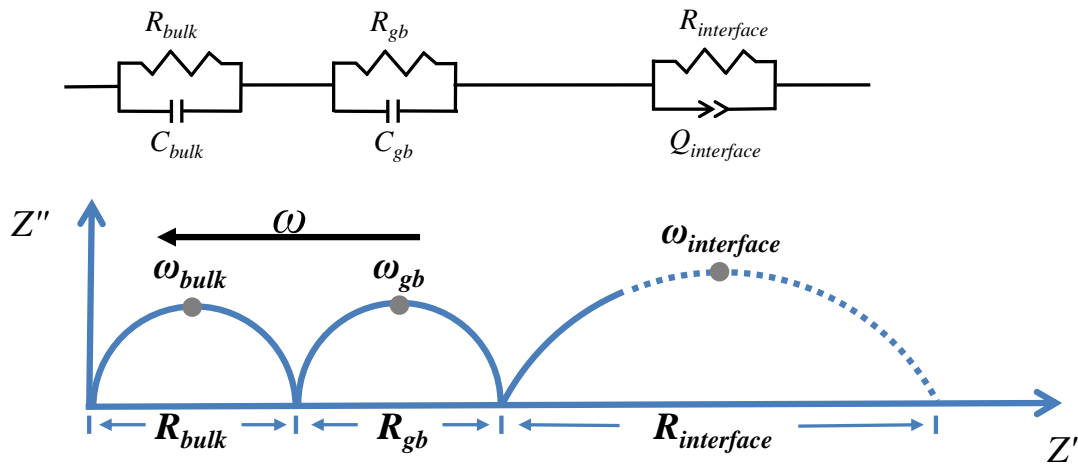
Nyquist diagram interpretation

Figure 2.16: Typical Nyquist diagram for a polycrystalline ceramic that conducts only lithium ions, modelled as an aggregate of parallel RC-elements linked together in series. A constant-phase element (Q) is an aggregated distribution of capacitance elements with proximal values.

EIS spectra can yield rich information, normally concealed in a DC response. A DC-bias can be viewed as an AC-bias with frequency approaching the limit of zero. In such a situation, the ionic current is limited by a Riemann sum of resistance domains: each attributable to either the grain bulk (r_{bulk}), the grain boundaries (r_{gb}) or the ceramic contact with another material ($r_{\text{interface}}$). These resistances can be lumped together as aggregated components: R_{bulk} , R_{gb} and $R_{\text{interface}}$.

Each microstructural domain has a distinct frequency-dependent relaxation. By scanning an AC-frequency range, the stepwise “cancellation” of resistance components (R_{bulk} , R_{gb} , $R_{\text{interface}}$) can thus be facilitated. The higher the AC frequency, the higher the current passed.

A circuit can model this behavior using multiple units of a capacitor (C) and a resistor (R) coupled in parallel, termed **Randles** cells or simply **parallel RC units**. Randles cells exhibit semicircles in the Nyquist plane and one peculiarity about each unit is that the imaginary component Z'' is a maximum only at one AC frequency (ω_{max}). At this point, a circuit law (Equation 2.10) applies equating the product of the resistance (R) and capacitance (C) to a characteristic relaxation time (τ).

$$\omega_{max} = \frac{1}{RC} = \frac{1}{\tau}$$

Equation 2.10: The expression for the RC time constant for a Randles cell overlaid in a Nyquist diagram

Each semicircle in the Nyquist diagram corresponds to an associated relaxation process (e.g. $R_{bulk}-C_{bulk}$, $R_{gb}-C_{gb}$, $R_{interface}-C_{interface}$). However, explicitly identifying which is which, based on a τ criterion, is not empirically sound as ion mobility can be higher either within the grain bulk or the grain boundaries, depending on the ceramic type. Irvine *et al.* solve this by making assignments using capacitances considering relative scalar dimensions [25].

The bulk component can be modeled using parallel-plate capacitor physics (Equation 2.11) taking the permittivity of free space (ϵ_0), the relative permittivity (ϵ_r), the basal area and thickness of the test sample (A and l , respectively). Herein, ϵ_r is typically on the order of tens, whereas A/l is about 1 cm, which gives a capacitance value about 1×10^{-12} F for C_{bulk} . Furthermore in sintered ceramics, grain boundaries are typically thinner by a factor 10-10000x compared to single grains, hence dimensional analysis (Equation 2.12) can be used to estimate the C_{gb} range. Irvine *et al.* detail typical capacitance values for a range of other phenomena in Table 2.2 [25].

$$C = \epsilon_0 \epsilon_r \frac{A}{l}$$

Equation 2.11: The capacitance formula for two parallel plates of area A and interplanar separation l with a dielectric material in between.

$$\frac{C_{bulk}}{C_{gb}} = \frac{l_{gb}}{l_{bulk}}$$

Equation 2.12: The inverse relationship between dielectric layer thickness and capacitance, as applied to the grain bulk vis-a-vis the grain boundary.

Table 2.2: Typical capacitance (C) values and respective possible interpretations [after [25]].

Capacitance / F	Phenomenon Responsible
10^{-12}	Bulk
10^{-11}	Minor, second phase
$10^{-11} - 10^{-8}$	Grain boundary
$10^{-10} - 10^{-9}$	Bulk ferroelectric
$10^{-9} - 10^{-7}$	Surface layer
$10^{-7} - 10^{-5}$	Sample-electrode interface
10^{-4}	Electrochemical reactions

Polycrystalline ceramics exhibit a range of grain sizes. When the size distribution becomes wide enough, the relative thickness between grains and grain boundaries (l_{gb}/l_{bulk} in Equation 2.12) results in a non-singular C_{gb} and distorts the semicircle, i.e. it then consists of $R_{gb1}-C_{gb1}, R_{gb2}-C_{gb2}, R_{gb3}-C_{gb3}$, so on and so forth. A method to simplify data is to use a constant-phase element (**Q**) to represent this capacitance distribution. A parallel R-Q unit forms a semicircle depressed against the real axis Z' in the Nyquist diagram, and can be used to derive an average capacitance value to compare with Table 2.2 using Equation 2.13.

Other distortions exist as well, such as inductance effects due to leads linking the sample to the equipment, extra serial capacitances due to long cables to the instrument, and non-homogeneity effects in the interfacial contribution ($Q_{interface}$) due to surface roughness.

$$C = (R^{1-n}Q)^{1/n}$$

Equation 2.13: Correction equation for deriving capacitance from the measured resistance R and constant phase element CPE values.

In this research, Nyquist plots obtained were analysed with the Z-view application. Conductivities (σ) were normalized from the resistance (**R**), surface area (**A**) and pellet thickness (**L**) for each sample according to the Equation 2.14:

$$\sigma = \frac{L}{RA}$$

Equation 2.14: The formula for geometric normalization of EIS conductivity values measured using sintered pellets.

Finally, it is evident by formula substitution that the characteristic frequencies (Equation 2.10) for solid-state dielectric relaxation are independent of sample dimensions, i.e. they are a material property. After all, the product of R (Equation 2.14) and C (Equation 2.11) is $\epsilon_0 \epsilon_r / \sigma$, all independent of sample size.

REFERENCES:

- [1] Pechini, M. *Method of preparing lead and alkaline earth titanates and niobates and coating method using the same to form a capacitor*. United States Patent: 3,330,697 (1967).
- [2] Gibbs, J. *On the equilibria of heterogeneous substances*. Yale University Press, New Haven, CT, (1948).
- [3] Niania, M., Podor, R., Skinner, S. and Kilner, J. *ECS Transaction* **68**, 665–670 (2015).
- [4] Retrieved from the world wide web:
<http://www.vitoria.gasteiz.org/wb021/http/contenidosEstaticos/adjuntos/es/71/96/47196.pdf>
- [5] Carvajal, J. *Abstracts of the Satellite Meeting on Powder Diffraction of the XV Congress of the IUCr* (1990).
- [6] Le Bail, A. *Powder Diffraction* **20**(4), 316–326 (2005).
- [7] Rietveld, H. *Journal of Applied Crystallography* **2**(2), 65–71 (1969).
- [8] Hurd, A. J. and McGreevy, R. L. *Neutron applications in earth, energy and environmental sciences*. Neutron Scattering Applications and Techniques. Springer, Dordrecht, (2008).
- [9] de Broglie, L. *The reinterpretation of wave mechanics*. Foundation of Physics, (1970).
- [10] Skoog, D.A., W. D. and Holler, J. *Fundamentals of Analytical Chemistry 9th edition*. New York: Sanders College Publishing, (2004).
- [11] Chater, R., Carter, S., Kilner, J. and Steele, B. *Solid State Ionics* **53**(2), 859–867 (1992).
- [12] Kilner, J., Steele, B. and Ilkov, L. *Solid State Ionics* **12** (MAR), 89–97 (1984).
- [13] Crank, J. *The Mathematics of Diffusion*. Oxford Science Publications, (1975).
- [14] Chater, R. J., Shollock, B. A., McPhail, D. S., Smith, A. J. and Cooke, G. *Surface and Interface Analysis* **46**(1, SI), 372–374 (2014). 19th International Conference on Secondary Ion Mass Spectrometry (SIMS), Jeju, SOUTH KOREA, SEP 29-OCT 04, 2013.
- [15] Massiot, D., Fayon, F., Capron, M., King, I., Le Calve, S., Alonso, B., Durand, J., Bujoli, B., Gan, Z. and Hoatson, G. *Magnetic Resonance in Chemistry* **40**(1), 70–76 (2002).
- [16] Man, P. *Quadrupole couplings in nuclear magnetic resonance, general*. Encyclopedia of analytical chemistry, (2000).
- [17] Lai, W. and Haile, S. *Journal of the American Ceramic Society* **88**(11), 2979–2997 (2005).
- [18] Yuan, L., Liu, H. K., Maaroo, A., Konstantinov, K., Liu, J. and Cortie, M. *Journal of New Materials for Electrochemical Systems* **10**(2), 95–99 (2007).
- [19] Taillades, G. and Sarradin, J. *Journal of Power Sources* **125**(2), 199–205 (2004).
- [20] Bach, P., Stratmann, M., Valencia-Jaime, I., Romero, A. and Renner, F. *Electrochimica Acta* **164**, 81 – 89 (2015).
- [21] Jonscher, A. *Journal of Physics D-Applied Physics* **32**(14), R57–R70 (1999).

- [22] Barsoukov, E. and McDonald, J. *Impedance Spectroscopy: Theory, Experiment, and Applications*. Wiley: New Jersey, (2005).
- [23] Tribollet, B. and Orazem, M. *Electrochemical Impedance Spectroscopy*. Wiley: New Jersey, (2008).
- [24] Lasaga, A. and Cygan, R. *American Mineralogist* **67**(3-4), 328–334 (1982).
- [25] Irvine, J. T. S., Sinclair, D. C. and West, A. R. *Advanced Materials* **2**(3), 132–138 (1990).

3 $\text{Li}_5\text{La}_3\text{Ta}_2\text{O}_{12}$: exploration of synthesis routes

This chapter recounts initial experiments to produce lithium-rich garnet ceramics and it suggests how to optimize conventional synthesis protocols.

3.1 Molecular dynamics simulations (mechanistic basis)

The impetus to investigate $\text{Li}_5\text{La}_3\text{Ta}_2\text{O}_{12}$ by experiment, as a lithium-ion electrolyte, came from collaborative simulation work with Dr. Randy Jalem (Nagoya University).

The incentives were two-fold:

1. At room-temperature, $\text{Li}_5\text{La}_3\text{Ta}_2\text{O}_{12}$ crystals maintain a cubic phase with a disordered lithium distribution. This is indicative of activated ionic conduction.
2. *Ab-initio* MD simulations predicted a lower energy penalty for a Td-Oh jump event in the case of $\text{Li}_5\text{La}_3\text{Ta}_2\text{O}_{12}$ compared to that of $\text{Li}_7\text{La}_3\text{Zr}_2\text{O}_{12}$, as illustrated in Figure 3.1a. This suggested a higher degree of isotropy. Extrapolation of the predicted ionic conductivity to room temperature gave a value of ~ 1 mS/cm [1]. The actual extent of clustering effects among ions and vacancies in $\text{Li}_5\text{La}_3\text{Ta}_2\text{O}_{12}$ due to its peculiar occupancy distribution (Figure 3.1b) remains experimentally not understood however.

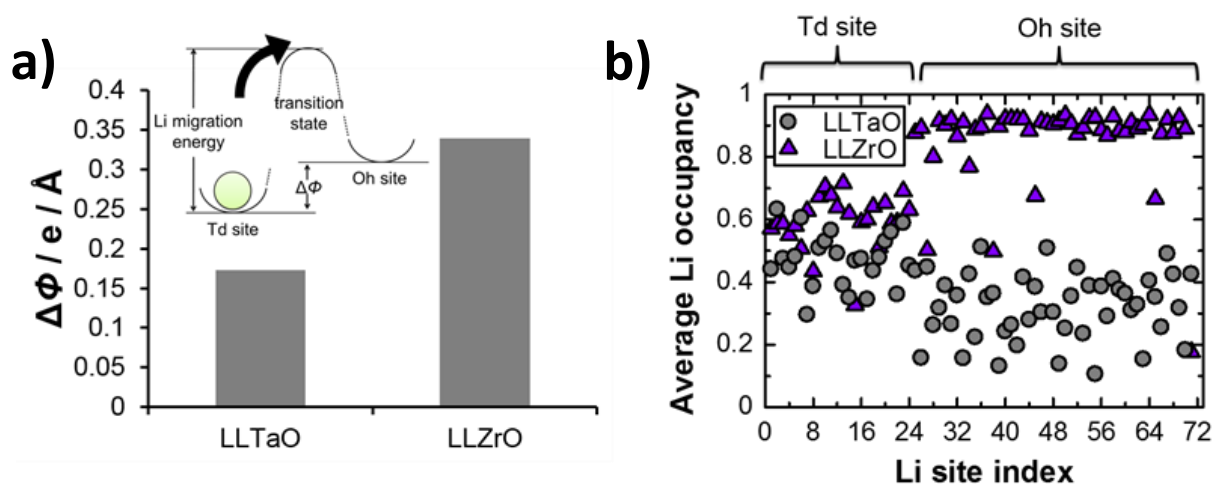


Figure 3.1: a) Electrostatic site potential difference $\Delta\phi$ for Li-migration steps between Td-Oh sites in $\text{Li}_5\text{La}_3\text{Ta}_2\text{O}_{12}$ and $\text{Li}_7\text{La}_3\text{Zr}_2\text{O}_{12}$. b) Statistical Li occupancy distributions between Td and Oh sites in $\text{Li}_5\text{La}_3\text{Ta}_2\text{O}_{12}$ and $\text{Li}_7\text{La}_3\text{Zr}_2\text{O}_{12}$ derived from 1273-K MD runs. The site-index is based on a $1 \times 1 \times 1$ unit cell composed of $\text{Li}_{40}\text{La}_{24}\text{Ta}_{16}\text{O}_{96}$ and $\text{Li}_{56}\text{La}_{24}\text{Zr}_{16}\text{O}_{96}$ where lithium atoms are spread over a total of 72 possible sites (after [1]).

As mentioned in Section 1.2.1, little experimental data exists in the literature for $\text{Li}_5\text{La}_3\text{Ta}_2\text{O}_{12}$. Those that do, report a wide range of bulk ionic conductivities (10^{-3} to 10^{-1} mS/cm) for the cubic phase material, suggesting the existence of a neglected variable in reported syntheses [2-4]. The previous studies shared one thing in common: syntheses under ambient air conditions. However, lattice Ta can exist in a number of oxidation (+3,+4,+5) and coordination states (VI,VII,VIII) [5]. This may lead to unintended defect formation as a charge compensation mechanism, produce materials with poor adherence to compound design or induce electronic conductivity via electron-hopping mechanisms. Therefore in this study, strict atmospheric controls were introduced at the outset, i.e. syntheses under pure oxygen (99.99%) to promote a standardized oxygen stoichiometry and oxidation states of the cations.

3.2 Synthesis of stoichiometric $\text{Li}_5\text{La}_3\text{Ta}_2\text{O}_{12}$

$\text{Li}_5\text{La}_3\text{Ta}_2\text{O}_{12}$ preparation begins from limited choices of Ta-based precursors. Ta_2O_5 (Ta^{5+}) powders are commercially available at 4-12€/g (Sigma-Aldrich: CAS# 1314-61-0 for 99% to 99.99% trace metals basis), which was found to be an oxide not entering aqueous solution by pH adjustment, hydrothermal nor microwave-aided means, except under HF-etching conditions [6, 7]. On the other hand, liquid organic ethoxides

(11-17€/g, Sigma-Aldrich: CAS# 6074-84-6) exist but pose explosion risks and decompose in contact with H_2O to yield solid Ta_2O_5 aggregates. Since Ta would have been in solid Ta_2O_5 form either way, the solid state synthesis route was chosen for these materials.

Conventional solid-state synthesis routes rely on long-range elemental diffusion during calcination, bordering partial sintering. This implies progressively larger grains and wider particle size distributions, compared to the starting reagent powders. Mechanical milling usually promotes better tap densities and denser grain packing. However as the elements Fe and Zr are known garnet-site substituents, using stainless steel or ZrO_2 milling balls inevitably introduces impurities which may complicate the interpretation of results. All materials in Chapter 3 were thus hand-milled using only an agate mortar and pestle.

The reagents used were: Li_2CO_3 (Alfa-Aesar, 99.9%), La_2O_3 (Alfa-Aesar, 99.9%) and Ta_2O_5 (Alfa-Aesar, 99.99%). Powders were calcined for 12h at 865°C , then ground inside an Ar-filled glovebox, and pelletized into 6.35mm (1/4") green bodies. Duplicate specimens were sintered for 6h at 1200°C , 1300°C , 1350°C , 1375°C and 1415°C , respectively, all anneals being carried out under dry O_2 flow. Sintered pellets were polished and characterized in accordance with Chapter 2. The theoretical density was taken as 6.36 g/cm^3 as computed from Cussen's early work (ICSD #171168) on the subject [8].

An analogous synthesis was initiated with the "**citrate-route**" described in Section 2.1.1 using the same reagents as above. This is in fact, a semi-"citrate-route" due to the insolubility of Ta_2O_5 . Due to the mixture becoming a suspension rather than a solution, the Ta_2O_5 particles were kept well-dispersed by extra mechanical agitation. This was through alternate tilting of the evaporating dish while a magnetic stirrer homogenized the mix until gel-setting. Gels were combusted at 600°C for 12h within a muffle furnace under a fumehood extractor. Calcination (865°C for 12h) and sintering (1250°C for 6h) anneals took place under a dry O_2 atmosphere.

Phase purity was monitored at each step by powder x-ray diffraction. Representative PXRD patterns along with refined Bragg reflections are shown in Figure 3.2 and Figure 3.3 (goodness-of-fit in Table 3.1). Interestingly, the cubic-phase $\text{Li}_5\text{La}_3\text{Ta}_2\text{O}_{12}$ readily formed in a single calcination step, whether via the solid-state route or the citrate-route. Some La_2O_3 was observed for the latter, possibly indicating atmospheric $\text{H}_2\text{O}/\text{CO}_2$ -induced reactions due to the larger surface area of the finer citrate route powders (cf. samples investigated in Chapter 4-5).

PXRD patterns of annealed $\text{Li}_5\text{La}_3\text{Ta}_2\text{O}_{12}$

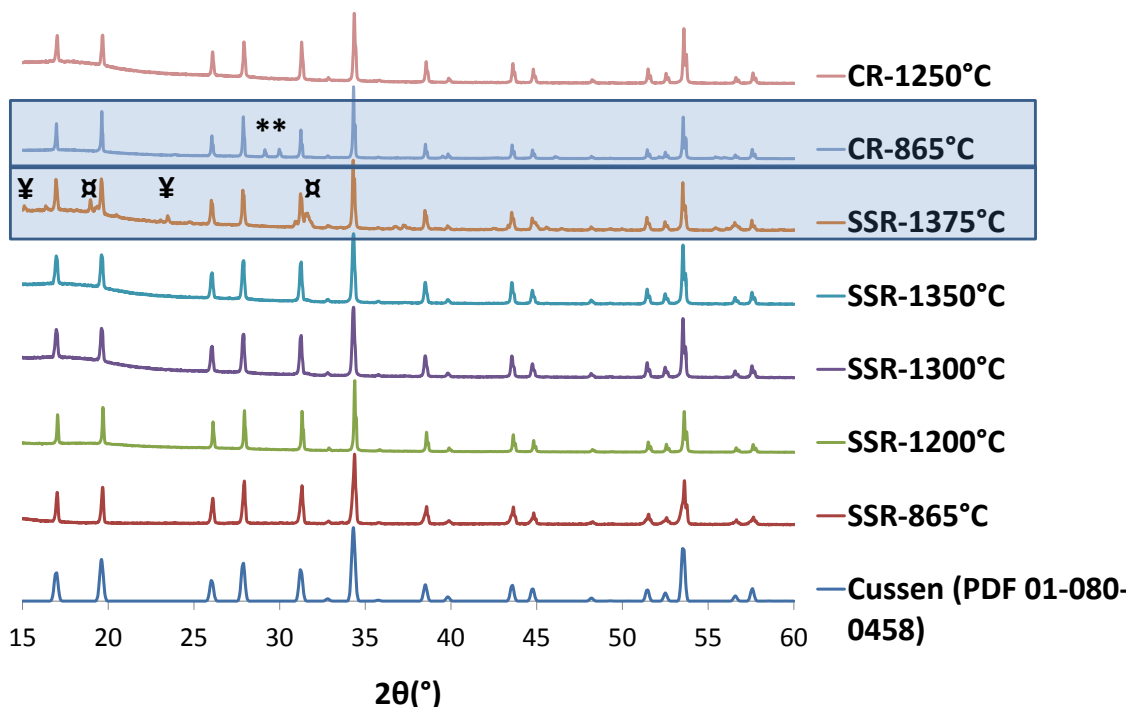


Figure 3.2: The crystallographic phase purity of powdered $\text{Li}_5\text{La}_3\text{Ta}_2\text{O}_{12}$ samples were ascertained using Le Bail-fits and comparison to the PDF2010 database (Bruker EVA software). SSR corresponds to materials produced using the solid-state-route; CR to those via the citrate route. Highlighted in blue are cubic-phase samples with detectable impurities: La_2O_3 (*), $\text{La}_2\text{LiTaO}_6$ (α), $\alpha\text{-Li}_3\text{TaO}_4$ (¥).

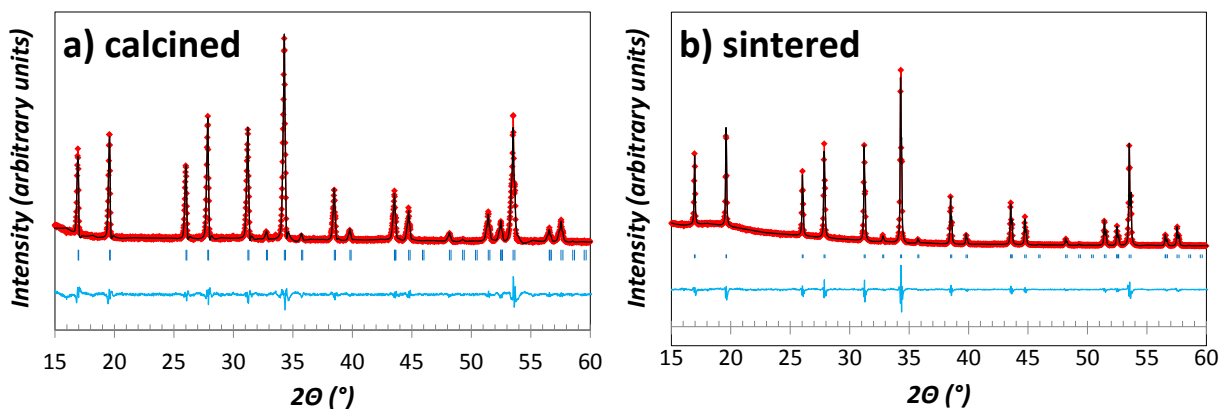


Figure 3.3: Example Le Bail-fits for XRD patterns taken from calcined (865°C) and sintered (1200°C) $\text{Li}_5\text{La}_3\text{Ta}_2\text{O}_{12}$ powders (solid-state route, annealed in dry O_2 flow). The diffraction peak angles (blue sticks) and difference map (blue line) conform well to the extinction rules for $Ia\bar{3}d$ cubic symmetry. The material is single-phase (expected <1% crystalline impurities).

Table 3.1 The figures of merit for the pattern refinements (Lebail fits) in Figure 3.3

	χ^2	R_p	R_{wp}	R_{exp}
Calcined (865°C)	3.77	5.99	8.24	4.24
Sintered (1200°C)	4.94	3.74	5.94	2.67

Solid-state-route materials

Calcined powders produced single-phase materials after firing to appropriate sintering temperatures. Beyond 1350°C however, major second phase impurities identifiable as $\text{La}_2\text{LiTaO}_6$ (PDF 00-039-0897) and $\alpha\text{-Li}_3\text{TaO}_4$ (PDF 01-075-1144) began to appear, with trace reflections from LiAlO_2 (PDF 01-074-2232) and Al_2O_3 (PDF 01-075-0278).

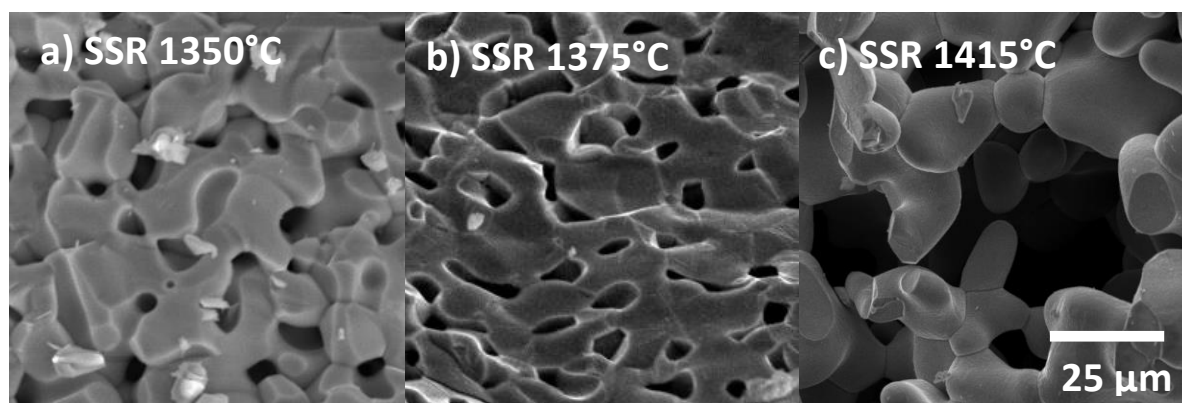


Figure 3.4: Secondary electron (SE) images of fracture cross-sections of ceramic-route pellets of $\text{Li}_5\text{La}_3\text{Ta}_2\text{O}_{12}$. Each image corresponds to a pellet subjected to a different firing temperature. Green bodies were formed from the same unique powder stock from a single calcination run, to facilitate comparison. Densities: 80%, 84% and 81%, respectively.

For solid-state-route materials, the densification behavior can be better visualized from the SEM micrographs (Figure 3.4,a-c). The pellet densities generally increased with higher sintering temperature, up to 1375°C (resulting in 84(±1)% theoretical) before decreasing. Scattered porosity was evident in all samples but most significant in the 1415°C-fired sample.

At this point it is useful to note that the 1350°C-fired sample is a phase-pure material; 1375°C a mixed phase; 1415°C, a completely decomposed material. The trend suggested a competition between sintering and thermal decomposition. By consideration of mass conservation, the decomposition can be further inferred to proceed via a scheme accounting for the irreversible volatilization and loss of Li_2O :



This reaction, examined based from the sum of normalized crystal volumes of products (ICSD #171168, 173180, 192270, 9112) against that of $\text{Li}_5\text{La}_3\text{Ta}_2\text{O}_{12}$ (ICSD# 01-074-9856), implies a volume expansion of 70%. This is because the crystallographic unit cell of $\text{Li}_5\text{La}_3\text{Ta}_2\text{O}_{12}$ is a very efficient packing of the atoms involved. In fact, when the constituent oxides undergo the first phase-forming calcination, a macroscopic contraction of the fired mass is readily observable. That the reverse process (decomposition) is accompanied by entropic release is therefore logical, so are scattered porosity growths due to Li_2O evaporation.

Given thermal decomposition and milling constraints, ceramics obtained via the solid-state-route series were thus limited to poor densities, and further trials were discontinued.

Citrate-route samples

Next, how optimal powder packing influences densification was examined with the citrate-route powder. Finer powder should have higher tap density and produce more compact green bodies. A firing temperature of 1250°C was arbitrarily chosen as a compromise between diffusion-induced sintering and thermal Li_2O vaporization of the finer powder. A rule of thumb is that the onset of densification usually begins at a temperature offset of 100°C lower in citrate-route powders compared to counterparts from the solid-state route. This is due to better mixing of constituent atoms and higher sintering rates due to increased surface areas.

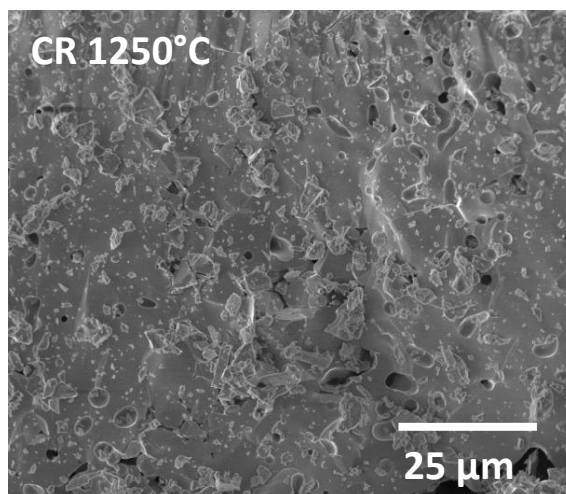


Figure 3.5: SE image of fracture cross-section of a citrate-route pellet of $\text{Li}_5\text{La}_3\text{Ta}_2\text{O}_{12}$, sintered at 1250°C for 6h under dry O_2 . This pellet had a relative density 89%.

Whereas the solid-state-route pellets showed high porosity (e.g. Figure 3.4a), the citrate-route pellet achieved a much higher density of $89(\pm 1)\%$ with no observable discrete grains (Figure 3.5). This suggested that either the individual grains were much tinier, i.e. submicron, or that the densification had already progressed from a necking to a coalescence stage via liquid phase sintering [9]. For information, there are three types of sintering mechanisms: solid-state sintering (atomic-scale diffusion), liquid-phase sintering (forms a small amount of molten flux to aid mass-transport and creates abnormal grain growth) and reactive sintering (wherein sintering progresses simultaneously with crystalline phase formation).

The denser samples obtained via the citrate route prompted ionic conductivity measurements using the two terminal AC impedance technique. Analysis revealed a special phenomenon. The bulk and grain-boundary contributions could not be deconvoluted (Figure 3.6a). The high-frequency semicircle yielded a capacitance ($C_{\text{bulk+GB}}$) that was in the middle of the characteristic ranges for bulk and grain-boundary relaxations (Table 3.2, see section 2.2.3.2 for typical capacitance values), whereas the low-frequency semicircle had an excessive capacitance ($C_{\text{interface}}$) which made it unlikely to be a grain boundary-related process.

By lumping the two phenomena of bulk and grain boundary relaxations together, a provisional circuit assignment was established (Figure 3.6b). By analyzing sintered pellets of varied densities systematically, it was further suspected that this convoluted Randles cell mainly consisted of a bulk transport contribution.

This was because according to conventional solid-state sintering theory, poorly-sintered ceramics tend to contain more constriction regions or narrowly-contacting necks and thus result in markedly low capacitances [10]. The converse means that well-sintered samples should have high equivalent capacitances. This relationship was not observed (see Table 3.3) suggesting that the high density did not come from conventional solid-state sintering.

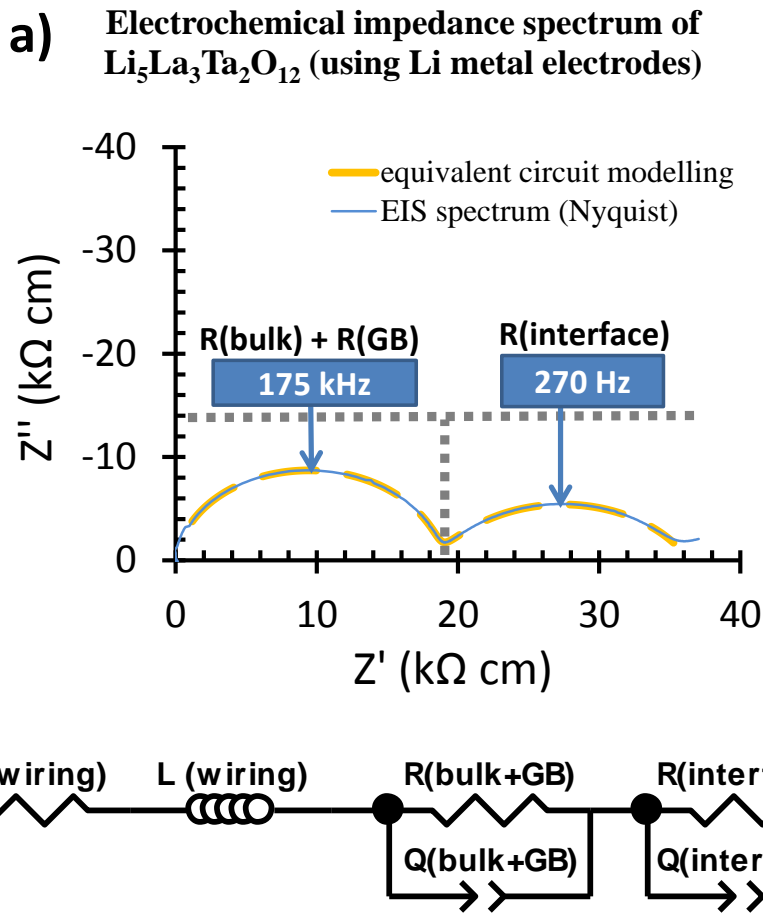


Figure 3.6: EIS spectrum (a) of a $\text{Li}_5\text{La}_3\text{Ta}_2\text{O}_{12}$ pellet derived from citrate-route powder and sintered at 1250°C (6h) and equivalent circuit fittings (b), along with characteristic frequencies for each regime.

Table 3.2: Circuit component values obtained by least-squares optimization of Figure 3.6 ($\chi^2=2.5 \times 10^{-5}$). The capacitance value for the second Randles element is not modeled due to n being out of the 0.8 to 1.0 range, for which a conversion from a constant-phase-element value to an equivalent capacitance value is invalid.

Circuit components	Values
R (wiring)	1Ω
L (wiring)	10^{-6} H
R (bulk+GB)	$18.3 \text{ k}\Omega \text{ cm}$
Q (bulk+GB)	$5.8 \times 10^{-11} \text{ F cm}^{-2} \text{ s}^{(n-1)}$
n (bulk+GB)	0.98
extracted C (bulk+GB)	$4.1 \times 10^{-11} \text{ F}$
R (interface)	$18.2 \text{ k}\Omega \text{ cm}$
Q(interface)	$5.0 \times 10^{-7} \text{ F cm}^{-2} \text{ s}^{(n-1)}$
n (interface)	0.68

Another feature was that whereas the low-density samples (72% and 80%) exhibited non-Debye dispersion for the first constant-phase-element (Q), the high-density sample (89%) showed near-Debye behavior. This is consistent with a single-grain material, which would have exhibited Debye-relaxation characteristics (i.e. $n=1$).

Taking these two analyses in consideration, there was thus high likelihood that liquid-phase sintering had indeed occurred, creating some abnormal grain growths.

Table 3.3: Relationship of densification vs fitted capacitance values for sintered $\text{Li}_5\text{La}_3\text{Ta}_2\text{O}_{12}$ samples.

relative density	extracted capacitance value of the 1 st semicircle ($Q_{\text{bulk+GB}}$)	Capacitance dispersion of 1 st semicircle ($n_{\text{bulk+GB}}$)
72%	$5.3 (\pm 0.3) \times 10^{-11}$	0.90
80%	$5.6 (\pm 0.4) \times 10^{-11}$	0.88
89%	$4.1 (\pm 0.1) \times 10^{-11}$	0.96

More definitive experiments to support this assignment will be presented in the Section 4.3.3. Meanwhile the normalized ionic conductivity, excluding the electrode-pellet interfacial contribution, was determined to be 0.051 mS/cm (25°C) for the sample illustrated in Figure 3.6a. The Zview fitting algorithm using this equivalent circuit model (Figure 3.6b) was later applied to other pellets.

Parameters analyses

With the refined lattice parameters, density and ionic conductivity values on hand, an attempt to identify key factors for fabrication of desired ceramics could be initiated. Figure 3.7 provides information to illustrate this effort. Within the figures, the propagated errors were computed to be less than 5% (duplicate samples for each datapoint). The deviations were so small that the markers were effectively masking the error bars.

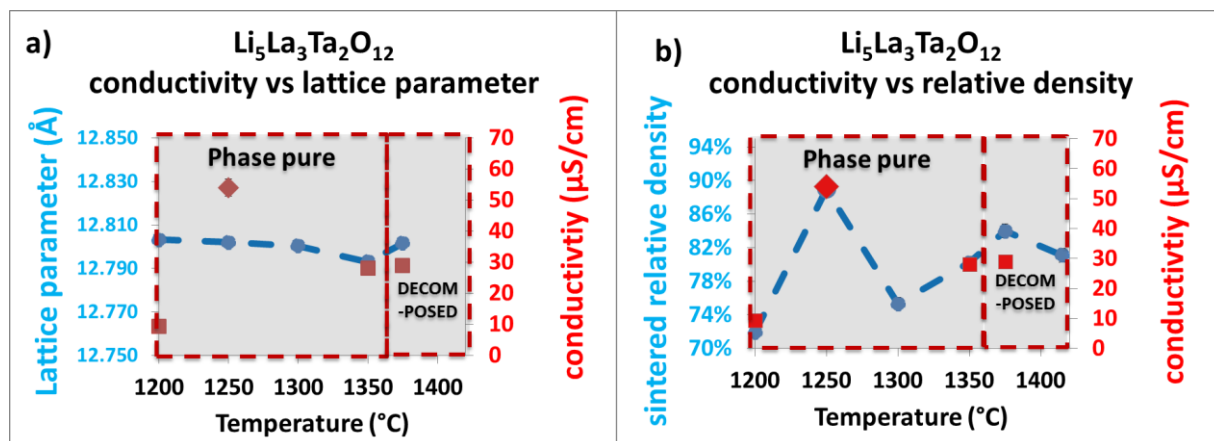


Figure 3.7: a) Correlation of ionic conductivity with lattice parameter. b) Correlation of ionic conductivity with sintered pellet density. All conductivity values are reported at room-temperature. Axes and markers are denoted by the same color schemes. The red diamond for each figure corresponds to the sample synthesized using citrate-route powder at 1250°C. The remainder (red squares) were produced by the solid-state route.

The lattice constant for the $\text{Li}_5\text{La}_3\text{Ta}_2\text{O}_{12}$ unit cell was reproducible over a wide range of temperatures indicating little hysteresis. However, a slight contraction was observed at the onset of phase decomposition. This may be construed as a solid-solution zone wherein atoms were partially leaching out on a supercell level, for example from $\text{Li}_{40}\text{La}_{24}\text{Ta}_{16}\text{O}_{96}$ to $\text{Li}_{38}\text{La}_{24}\text{Ta}_{16}\text{O}_{95} + \text{Li}_2\text{O}$. Outside this solid solution range, the crystal system began to compensate by forming secondary phases. No apparent correlation was holding between the conductivity and the associated lattice constants for samples sintered at different temperatures. But a direct correlation between ceramic density and ionic conductivity seemed to hold, similar to what has previously been observed in oxygen-ion conductors [11].

Contaminants

At this stage, experiments investigating contamination were carried out. First, lithium-rich compounds are known to be reactive to atmospheric H_2O and CO_2 , although the kinetics of such reactions vary from material to material. Second, analogous garnets have been reported to absorb adventitious Al from alumina crucibles during sintering (see section 1.2.2.1.1).

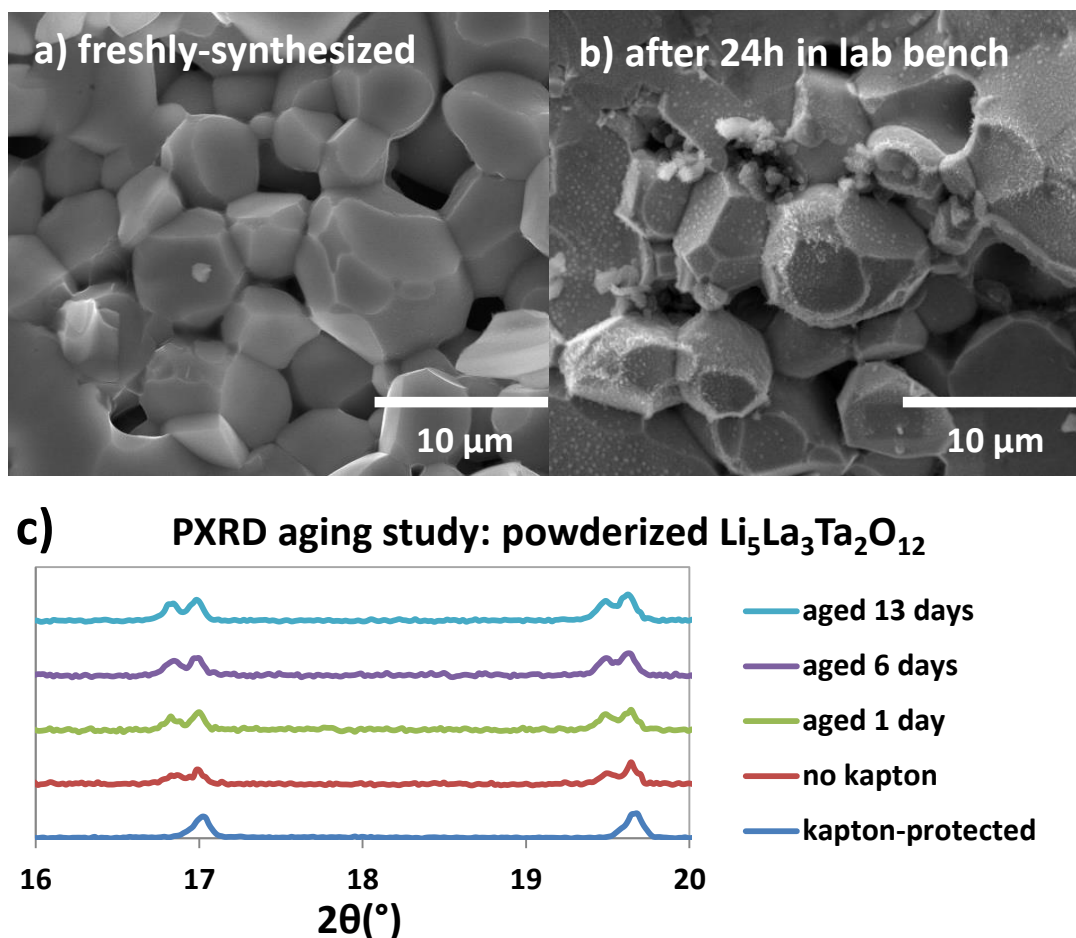


Figure 3.8: a) SE micrograph of a freshly-prepared cross-section from a sintered $\text{Li}_5\text{La}_3\text{Ta}_2\text{O}_{12}$ pellet (sintered from solid-state-route powder, fired at 1200°C for 6h); b) SE micrograph of the sample in (a) after aging under ambient air conditions for one day; c) PXRD patterns collected while monitoring the aging behavior of $\text{Li}_5\text{La}_3\text{Ta}_2\text{O}_{12}$ hand-milled powder.

To address the first ($\text{H}_2\text{O}/\text{CO}_2$ -interaction), an atmospheric aging study was performed using SEM and XRD. The main noticeable feature in the microstructures was the emergence of corrosion layers in a pristine ceramic surface after 24h in the lab bench (Figure 3.8a-b). Whereas $\text{Li}_5\text{La}_3\text{Ta}_2\text{O}_{12}$ powder which had been isolated from ambient air throughout synthesis, storage and XRD scanning showed single sharp Bragg peaks, crystallites showed peak splitting in as little as 30 minutes of air exposure (Figure 3.8c). The peak-splitting persisted for at least 2 weeks of continuous air exposure.

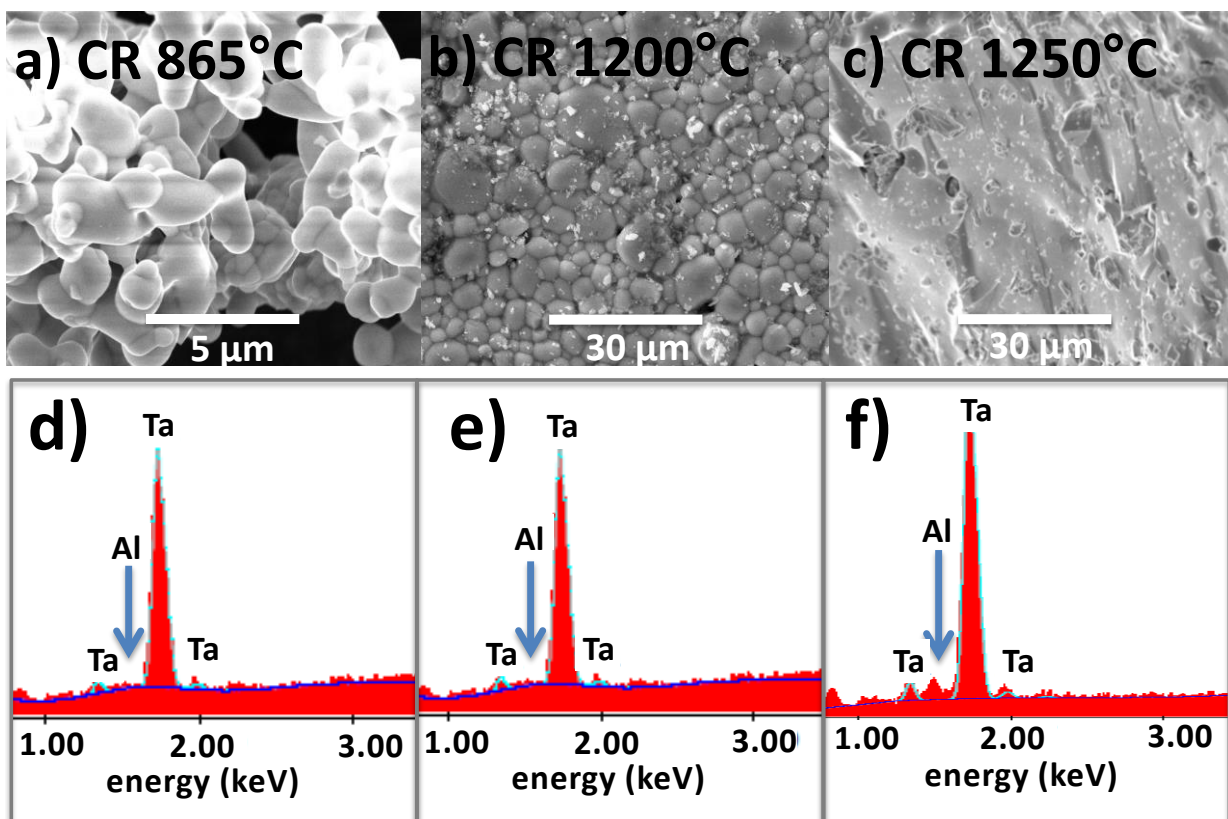


Figure 3.9: SE micrographs of citrate-route $\text{Li}_5\text{La}_3\text{Ta}_2\text{O}_{12}$ samples: a) 865°C-calcined, b) 1200°C-sintered, c) 1250°C-sintered. d-f) associated EDAX spectra collected at 30kV for a-b-c, respectively. Blue arrows indicate the energy region of the Al K X-ray line.

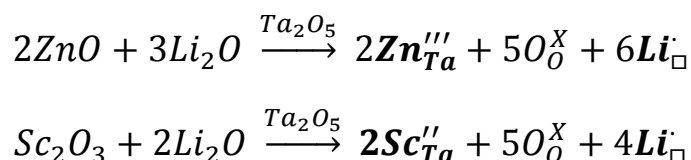
To address the second (Al-interaction), EDAX spectra of cross-sections of sintered pellets were collected. Citrate-route samples revealed varying levels of Al-contamination (Figure 3.9). For lower temperatures (865°C to 1200°C), Al was below the detection limit. After 1250°C-sintering however, the sample produced registered an equivalent of 0.35 Al p.f.u. As a sidenote, the 865°C-calcined powder exhibited 1-4 μm particle size, whereas its 1200°C-sintered counterpart only grew to $\sim 3\text{-}10\ \mu\text{m}$. Grains coalesced significantly leaving no traces of necking at 1250°C. This provided additional evidence that Al-facilitated liquid-phase sintering was being observed.

In contrast, solid-state-route pellets had <0.04 Al p.f.u. even at a sintering temperature of 1375°C (EDAX not shown). One may speculate that either grain morphology, i.e. the observation that CR grains are rounded (e.g. Figure 3.9b) whereas SSR grains have sharp facets (Figure 3.8a), or the chronology of intermediate phase formation (section 1.2.1.1) are crucial parameters dictating whether liquid phase sintering sets in or not for $\text{Li}_5\text{La}_3\text{Ta}_2\text{O}_{12}$ within a 6h-sintering timeframe.

3.3 Syntheses of $\text{Li}_{6.5}\text{La}_3\text{Ta}_{1.5}\text{Zn}_{0.5}\text{O}_{12}$ and $\text{Li}_{6.4}\text{La}_3\text{Ta}_{1.3}\text{Sc}_{0.7}\text{O}_{12}$

The highest bulk conductivity and density had been achieved using a citrate-route at a sintering temperature of 1250°C for 6h for pure $\text{Li}_5\text{La}_3\text{Ta}_2\text{O}_{12}$. But the ionic conductivity of 0.051 mS/cm is insufficient for practical electrolyte applications. Attempts at inducing higher Li carrier vs vacancy ratio by strategic Ta-site substitution were carried out using Zn^{2+} or Sc^{3+} dopants to achieve the following compositions: $\text{Li}_{6.5}\text{La}_3\text{Ta}_{1.5}\text{Zn}_{0.5}\text{O}_{12}$ and $\text{Li}_{6.4}\text{La}_3\text{Ta}_{1.3}\text{Sc}_{0.7}\text{O}_{12}$.

ZnO (99.9%, Alfa Aesar) and Sc_2O_3 (99.9%, Aldrich) powders served as the additives, resulting in these substitution chemistries (return to Section 1.2.2.1.1 for a brief refresher on the Kroger-Vink notation).



As mentioned in Section 1.1.4.3.4, it was theoretically predicted via bond-valence models that garnet oxides can accommodate a maximum lithium content of 7.5 per formula unit before unrealistic Li-Li distances set in. Experimental reports further estimated optimal conductivity to occur at about 6.5 Li p.f.u. This was thus the value aimed for in this part of the study. The citrate-route was used to fabricate these materials.

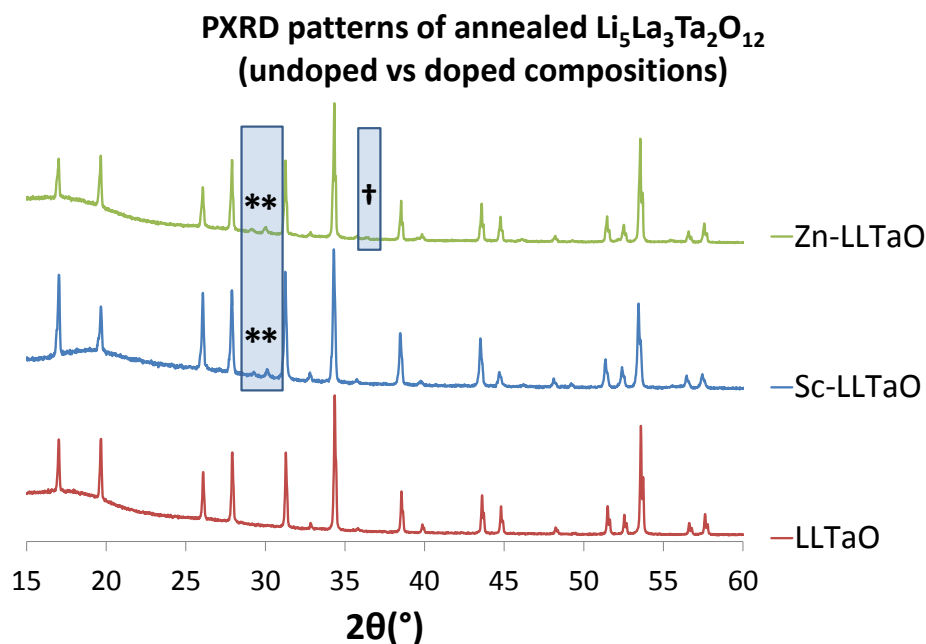


Figure 3.10: PXRD patterns of $\text{Li}_5\text{La}_3\text{Ta}_2\text{O}_{12}$ (LLTaO), $\text{Li}_{6.4}\text{La}_3\text{Ta}_{1.3}\text{Sc}_{0.7}\text{Zr}_2\text{O}_{12}$ (Sc-LLTaO) and $\text{Li}_{6.5}\text{La}_3\text{Ta}_{1.5}\text{Zn}_{0.5}\text{Zr}_2\text{O}_{12}$ (Zn-LLTaO) after pulverizing sintered pellets. (*) and (†) indicate Bragg peaks due to La_2O_3 (ICSD# 192270) and $\text{Li}_{0.086}\text{Zn}_{0.914}\text{O}_{0.957}$ (COD # 1527031), respectively.

Both syntheses yielded minor impurities at the sintered stage as demonstrated in Figure 3.10, notably La_2O_3 . Examination of typical ionic radii (Table 3.4) yields clues. First, Li^+ and Zn^{2+} ions might replace one another based on size considerations (CN=4). Competition for Li sites may have expelled Zn (as Li is present in 10% stoichiometric excess) to form Li-doped ZnO marked by (†).

Another argument may be that the octahedral cages (CN=6) housing Ta^{5+} cannot accommodate the larger ionic radius of the substituting elements. This reasoning is quite unlikely though given that Zr^{4+} (CN=6) has an ionic radius of 0.72 and is known to be successfully accommodated by the garnet framework to form phase-pure $\text{Li}_7\text{La}_3\text{Zr}_2\text{O}_{12}$. This ionic radius is not very different from those of the present dopants (~0.74). As the doping concentrations are quite high, the excess La_2O_3 generated by the off-stoichiometry would also have been significant, which was not observed in the XRD peaks (*).

Finally a third argument along parallel reasoning may have been that the designed substitution did occur, but that the maximum substitution limit was surpassed, prompting substitution unto the La^{3+} sites (CN=8).

Table 3.4: Ionic radii of selected substituent and substituted atoms [5].
 Highlighted in yellow are the coordination numbers of the lattice positions of substitutable atoms in $\text{Li}_5\text{La}_3\text{Ta}_2\text{O}_{12}$.

	Ionic radii (CN=4) tetrahedral	Ionic radii (CN=6) octahedral	Ionic radii (CN=8) dodecahedral
Li (+)	0.59	0.76	0.92
La (3+)	n/a	1.03	1.16
Ta (5+)	n/a	0.64	0.74
Sc (3+)	n/a	0.745	0.87
Zn (2+)	0.6	0.74	0.9

EDAX mapping provides a clearer picture of the distribution and composition of the secondary phases (Figure 3.11).

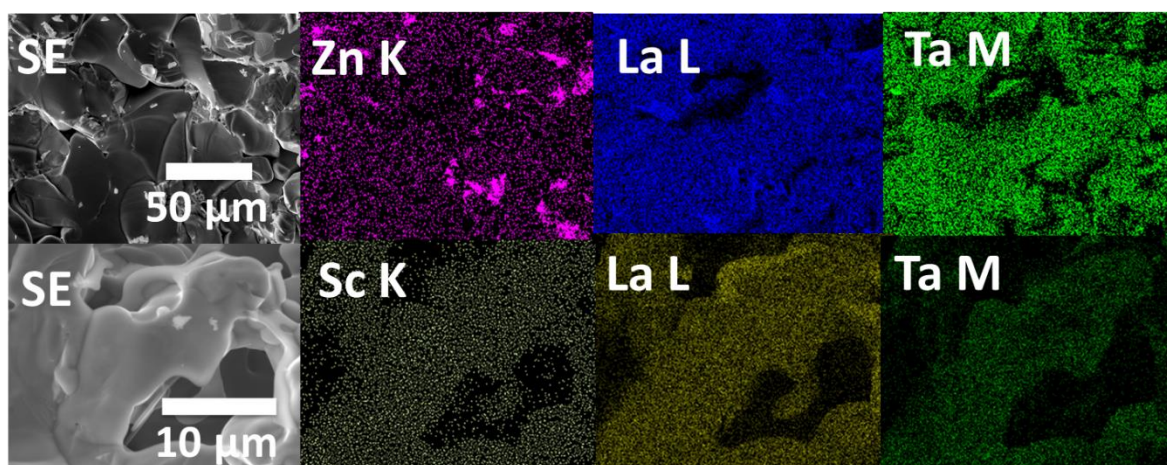


Figure 3.11: EDAX mapping (12kV acceleration voltage) of Zn-LLTaO (top row) and Sc-LLTaO (bottom row).

Phase segregation was clearly evident in the Zn-doped case, compared to the uniform distribution in the Sc-doped material. This was despite a lower amount of Zn per formula unit (0.5 vs 0.7 for Sc-LLTaO). Zn therefore did not substitute, but segregated and may have also acted as a sintering aid facilitating a 96% relative density of the sintered Zn-LLTaO pellet.

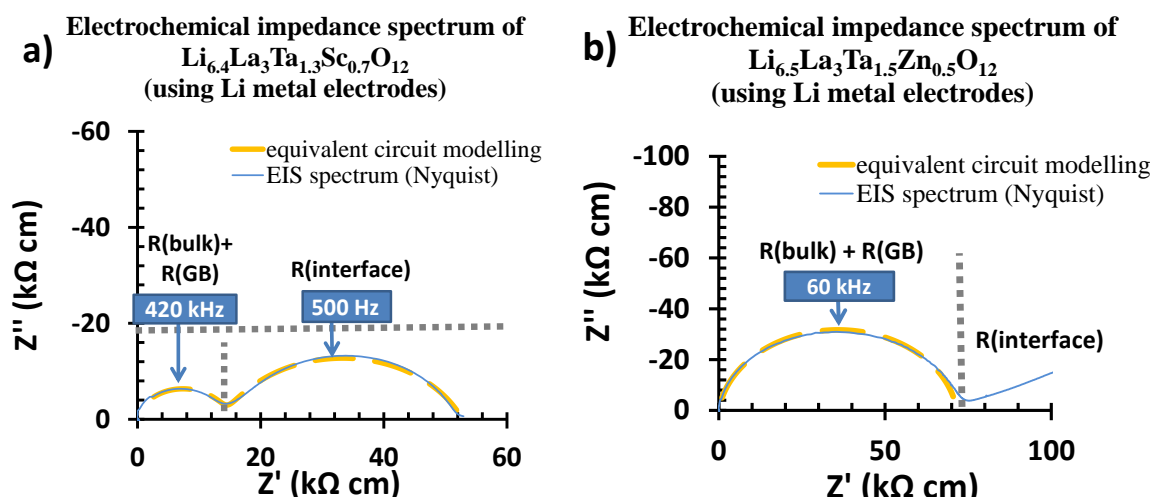


Figure 3.12: Nyquist (Cole-Cole) plots for a) $\text{Li}_{6.4}\text{La}_3\text{Ta}_{1.3}\text{Sc}_{0.7}\text{Zr}_2\text{O}_{12}$ (Sc-LLTaO) and b) $\text{Li}_{6.5}\text{La}_3\text{Ta}_{1.5}\text{Zn}_{0.5}\text{Zr}_2\text{O}_{12}$ (Zn-LLTaO), and corresponding equivalent circuit fittings: $\chi^2 < 0.0008$ for both cases.

The effects of the dopant chemistries on ionic conductivity (25°C) are clearly seen in Figure 3.12. Whereas Sc-doping yielded an improvement to 0.071 mS/cm (bulk, 69% dense), the Zn-doped material declined to 0.014 mS/cm (bulk, 96% dense). With a promising conductivity at low-doping concentrations, Sc-doping may warrant further investigation whereas Zn-doping may be dropped.

3.4 Chapter summary and perspectives

Exploratory trials with $\text{Li}_5\text{La}_3\text{Ta}_2\text{O}_{12}$ had yielded a working protocol for ceramic processing. It was determined that citrate-route powders produced denser $\text{Li}_5\text{La}_3\text{Ta}_2\text{O}_{12}$ ceramics. As each synthesis run is time-consuming, an efficient study calls for eliminating as many uncertain parameters as possible. For one, minimizing grain size uncertainties prior to green-body pressing is logical. Hence, all succeeding experiments used materials produced only from citrate-route powders.

It was empirically shown that pellet density and bulk ionic conductivity are highly correlated. This is not a new idea. Mukai *et al.* applied a line integral function to model pore surface areas as extra diverted distances that Li-ions need to traverse, thus lowering bulk conductivity [12]. The model assumed though that all pores occurring in ceramics were spherical in shape. Notwithstanding, their conclusion was that the **measured apparent conductivity is approximately linearly correlated to relative density** according to this equation:

$$\sigma_{\text{Li}}^{\text{int}} = \left(\frac{3\pi}{\zeta} - \frac{3\pi}{8} + 1 \right) \sigma_{\text{Li}}^{\text{app}}$$

where $\sigma_{\text{Li}}^{\text{int}}$ = theoretical bulk ionic conductivity for a fully-dense material

$\sigma_{\text{Li}}^{\text{app}}$ = measured bulk ionic conductivity

ζ = the pellet's relative density compared to a single crystal

A less restricted model of aggregate pore contribution to the total pellet impedance can be geometrically devised.

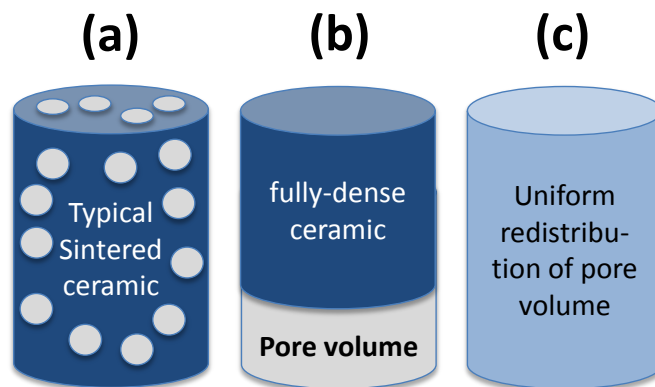


Figure 3.13: A pore redistribution thought experiment for sintered ceramics: (a) an experimentally-synthesized sintered ceramic (b) the same sample but with all pore volume virtually concentrated and (c) the same sample but with all pore volume virtually spread in a uniform manner throughout the apparent volume of the pellet.

Consider a cylindrical sintered pellet with scattered porosity (Figure 3.13a). If all the pore volume were to be concentrated on one side of a test pellet, while keeping the diameter of the pellet fixed, the unit would give rise to a ratio between the cylindrical length of a fully-dense ceramic and that of the pore volume (Figure 3.13b). Since impedance measurements are made over fixed contact areas, applying a correction factor by virtually adjusting the apparent pellet thickness should in principle be capable of yielding the true pellet volume. This forms one pore redistribution limit. The other limit is to spread the pore volume uniformly within the material volume on an atomic scale, such that all ions thus need to travel identical extra distances, effectively averaging out ion traffic (Figure 3.13c). It can be shown that a correction factor derived this way agrees well with Mukai's model, as plotted in Figure 3.14.

Extrapolation of bulk ionic conductivity from relative density (theoretical)

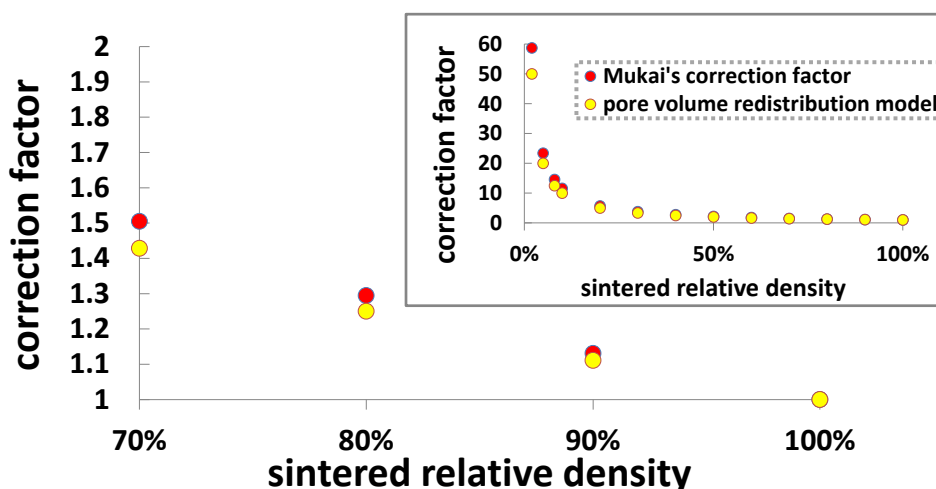


Figure 3.14: Theoretical effects of geometric pores on bulk ionic conductivity at a given temperature, and the correction factor to extrapolate the bulk conductivity of a porous sample to that of the dense sample.

Unfortunately however, both models fail the test against the experimental data (Figure 3.15). Whereas $\text{Li}_5\text{La}_3\text{Ta}_2\text{O}_{12}$ is predicted by a linear trend to exhibit $\sim 80 \mu\text{S}/\text{cm}$ for a fully-dense material, reverse extrapolation to 70% ceramic density predicted $\sim 53 \mu\text{S}/\text{cm}$ but exhibited only $\sim 11 \mu\text{S}/\text{cm}$ experimentally. This may have been a consequence either of increased Al-concentration in the 89% density sample (1250°C -sintered from citrate-route powder) which altered the lithium stoichiometry or an effect of poor grain-to-grain interconnectivity in ceramics with very high porosities. Unfortunately, ICP-OES analysis was unsuccessful as $\text{Li}_5\text{La}_3\text{Ta}_2\text{O}_{12}$ proved insoluble even under microwave-assisted digestion.

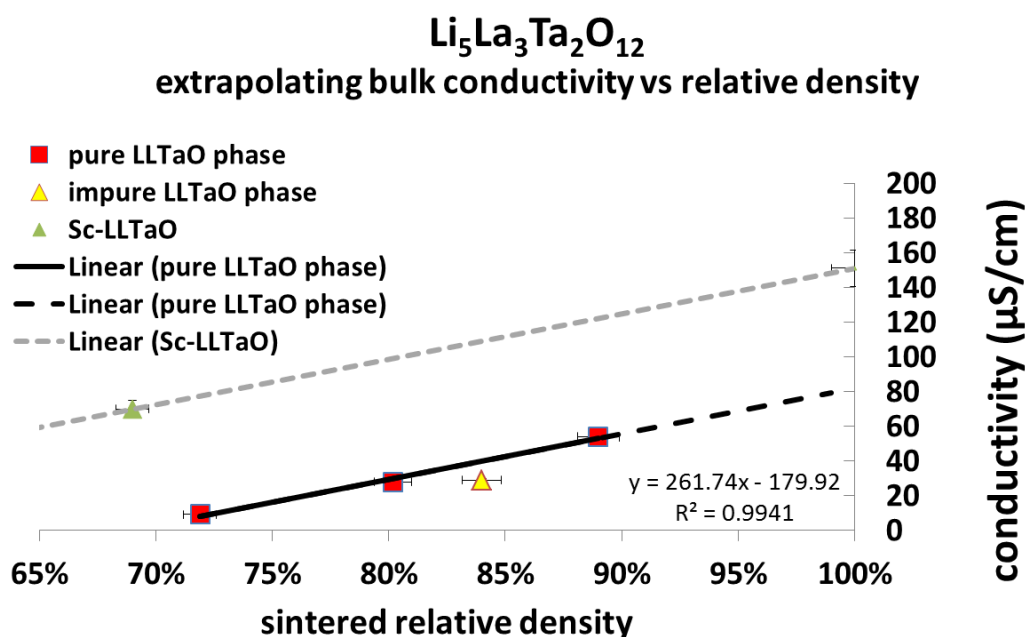


Figure 3.15: Expected bulk ionic conductivity values at 25°C for dense $\text{Li}_5\text{La}_3\text{Ta}_2\text{O}_{12}$ -based materials.

At this point, the reader is reminded that plots in Figure 3.15 consisted of pure phase samples assuming predominantly bulk and negligible grain boundary contributions. A fully-dense $\text{Li}_5\text{La}_3\text{Ta}_2\text{O}_{12}$ pellet would yield $60\mu\text{S}/\text{cm}$ at 25°C using the present model of pore redistribution. Extrapolating a linear trend would yield $80\mu\text{S}/\text{cm}$. A fully-dense $\text{Li}_{6.4}\text{La}_3\text{Ta}_{1.3}\text{Sc}_{0.7}\text{Zr}_2\text{O}_{12}$ would yield at minimum $100\mu\text{S}/\text{cm}$, but likely to be greater than $160\mu\text{S}/\text{cm}$ if the same linear extrapolation applies. This implies that Sc-doped $\text{Li}_5\text{La}_3\text{Ta}_2\text{O}_{12}$ is a promising material for further investigation, with focus on the purity and density problems (currently 69%).

On the question of sintering, **an intermediate calcination step is indispensable to achieve dense phase-pure garnets, under conventional processing conditions (i.e. cold pressed pellets fired in an ambient-pressure tube furnace).**

Protocols that skip a calcination step are known as reactive sintering routes. Densification under this regime is a convolution of volume changes during phase formation and driving forces towards reduction in surface area. Perovskites and largely “empty” crystals can be synthesized successfully with this method, but not Li-stuffed garnets.

First, the atomic packing efficiency of $\text{Li}_5\text{La}_3\text{Ta}_2\text{O}_{12}$ leads to volume reduction of 21% compared to its constituent oxides (Li_2O , La_2O_3 , Ta_2O_5). Second, sintering onset is accompanied by as much as a 12% contraction in one dimension (Figure 3.16). Because the two processes occur simultaneously in time but not in space, fragmented local sintering and uneven cation consumption due to mass transport differences (e.g. interference of Li-Al eutectic) during phase-formation imply mechanically-poor and possibly phase-impure end products.

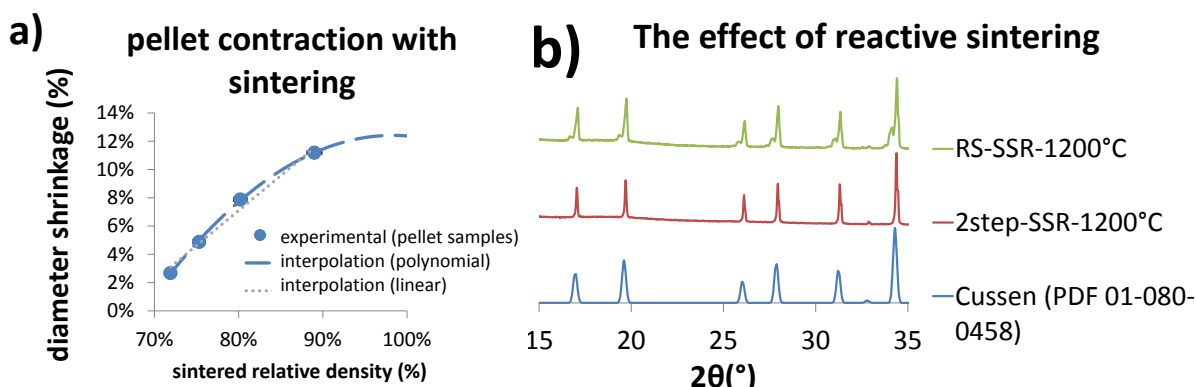


Figure 3.16: a) Empirical trends in volume changes through a sintering step for a green body pellet measuring 6.35 mm in diameter and ~1.5 mm thick. Data collected from this study. b) XRD patterns showing two pellets: one following reactive sintering (RS-SSR-1200°C, 6h firing, O_2 atm) and a pellet following the 2-step procedure (2step-SSR-1200°C, see above for protocol). The reactively-sintered pellet yielded 32% relative density vs 72% for the latter.

A hot-press may solve this problem, by coupling the two processes to occur at the same time in the same space, and/or the use of crucibles unreactive with lithium.

REFERENCES:

- [1] Jalem, R., Nakayama, M., Manalastas, W., Kilner, J. A., Grimes, R. W., Kasuga, T. and Kanamura, K. *Journal of Physical Chemistry C* **119**(36), 20783–20791 (2015).
- [2] Kotobuki, M. and Kanamura, K. *Ceramics International* **39**(6), 6481 – 6487 (2013).
- [3] Gao, Y., Wang, X., Wang, W. and Fang, Q. *Solid State Ionics* **181**(1-2), 33 – 36 (2010).
- [4] Ray, B. *A study of the lithium ionic conductor $\text{Li}_5\text{La}_3\text{Ta}_2\text{O}_{12}$: From synthesis through materials and transport characterization*. PhD thesis (2014).
- [5] Shannon, R. D. *Acta Crystallographica Section A* **32** (SEP1), 751–767 (1976).
- [6] Pourbaix, M. *Atlas of Electrochemical Equilibria in Aqueous Solutions*. Pergamon Press, New York (1966).
- [7] Sapra, S., Li, H., Wang, Z. and Suni, I. *Journal of the Electrochemical Society* **152**(6), B193–B197 (2005).
- [8] Cussen, E. J. *Chemical Communications* **41**, 412–413 (2006).
- [9] German, R. M., Suri, P. and Park, S. J. *Journal of Materials Science* **44**(1), 1–39 (2009).
- [10] Irvine, J. T. S., Sinclair, D. C. and West, A. R. *Advanced Materials* **2**(3), 132–138 (1990).
- [11] Perez-Coll, D., Sanchez-Lopez, E. and Mather, G. C. *Solid State Ionics* **181**(21-22), 1033 – 1042 (2010).
- [12] Mukai, K., Nunotani, N. and Moriyasu, R. *ACS Applied Materials and Interfaces* **7**(36), 20314–20321 (2015).

4 Li₇La₃Zr₂O₁₂ (Ga-doping): synthesis for optimal Li-ion conductivity

A shift to explore zirconates (Li₇La₃Zr₂O₁₂) was spurred by 3 disadvantages of tantalates (Li₅La₃Ta₂O₁₂):

- 1) the low ionic conductivity of bulk Li₅La₃Ta₂O₁₂: ~0.1 mS/cm limit at 25°C
- 2) the high cost of Ta-based reagents : ~670€/mol Ta vs ~18€/mol Zr (oxides basis)
- 3) the powder processing limitations associated with Ta-chemistry (section 3.2)

However, stoichiometric Li₇La₃Zr₂O₁₂ crystallizes in a tetragonal phase. Ga-doping strategies were thus pursued to stabilize the cubic polymorph known to exhibit higher ionic conductivity.

4.1 Rationale

The crystal structure of cubic-phase LLZO has already been illustrated in section 1.1.4.3.4. It consists of a network of LiO₄, LiO₆, LaO₈ and ZrO₆ cages. By consideration of ionic radii (Table 4.1), substituting Ga atoms may selectively replace occupants from one of three candidate sites: Li tetrahedral (24d), Li octahedral (48g/96h) or Zr octahedral (16a) sites. Assuming a charge-balanced structure with no anion defects, Ga-substitution on Li-sites would decrease Li content (Li_{7-3x}Ga_xLa₃Zr₂O₁₂) whereas its entry onto Zr-sites would increase it (Li_{7+x}La₃Zr_{2-x}Ga_xO₁₂). In Kroger-Vink notation (section 1.2.2.1.1), the vacancy counts of lithium interstitials would vary so:

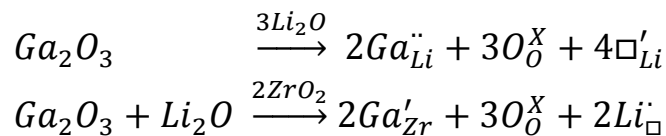


Table 4.1: Ionic radii of Ga and substitutable atoms in the LLZO structure [1].
Highlighted in yellow are the relevant site-occupancy coordination numbers for each element.

	Tetrahedral (Td)	Octahedral (Oh)	Dodecahedral (Ih)
Li (+)	0.59	0.76	0.92
La (3+)	n/a	1.03	1.16
Zr (4+)	0.59	0.72	0.84
Ga (3+)	0.47	0.62	n/a

The reader is reminded that there are a total of 9 possible lithium sites (3 Td + 6 Oh) per LLZO formula unit in a cubic $Ia\bar{3}d$ symmetry. Cubic LLZO is a tightly-packed structure, and its constraints induce electrostatic repulsion between Li atoms, illustrated in Figure 4.1.

Consider a Li ion on a 24d-site (Td). Each 24d-Li pushes a neighboring 48g-Li off-center (Oh), to a metastable split 96-site (Oh). In turn, any 96h-site occupant creates a vacancy in an adjacent 24d-site (Td). When this effect is extended, it is clear that in no instance can any Td-Oh-Td or Oh-Td-Oh chains have full Li occupancy. This effect sums up what is commonly termed “disorder” in these stuffed garnets. As a consequence, vacancies are thus inherent in the cubic lattice. What site-substituting aliovalent dopants do is to alter what proportion of the 9 lithium sites are occupied and which are vacant.

A garnet structure with a low lithium content (e.g. Li=3) is thermodynamically stable in the cubic phase. When the lithium content is progressively increased, stress is introduced unto the system due to Li-Li electrostatic repulsion. There is a vague critical point (ca. Li=6.5) when the Li sublattice is overpopulated and the repulsive forces can no longer be contained. The crystal relieves this stress through a symmetry reduction to a tetragonal $I41/acd$ symmetry that shatters the lithium disorder. The vacancy positions are eliminated, and the lithium sublattice evolves to completely-filled octahedral sites (16f/32g), as described in experimentally-synthesized Li₇La₃Zr₂O₁₂ single crystals (i.e. Li=7) [2].

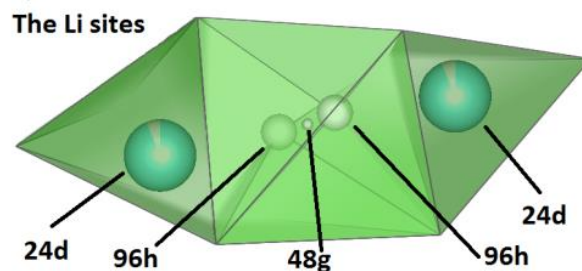


Figure 4.1: The possible lithium sites in a cubic $Ia\bar{3}d$ LLZO garnet: 24d tetrahedral site and 48g/96h octahedral sites.

What this means is at the point of cubic-to-tetragonal phase transformation, a high energy penalty already exists barring a tetragonal-to-cubic distortion by forcing in Li>7 p.f.u. Further, this would also constitute a violation of lattice volume constraints

predicted by Bernstein [3]. Hence, the expected result with $\text{Li}_{7+x}\text{La}_3\text{Zr}_{2-x}\text{Ga}_x\text{O}_{12}$ was a tetragonal-phase garnet with various phase impurities. What is desired is a controlled decrease in the Li content until the cubic-phase starts to form, as with $\text{Li}_{7-3x}\text{Ga}_x\text{La}_3\text{Zr}_2\text{O}_{12}$.

A tailored stoichiometry (i.e. preparing $\text{Li}_{7-3x}\text{Ga}_x\text{La}_3\text{Zr}_2\text{O}_{12}$ ratio of elemental mixes rather than $\text{Li}_{7+x}\text{La}_3\text{Zr}_{2-x}\text{Ga}_x\text{O}_{12}$ in the citrate solution) should best achieve the goal of pushing equilibria towards the desired phase, if existent at all. This is an inference from Le Chatelier's principle.

4.2 Molecular dynamics (MD) simulations

MD simulations provided guidelines of expected results from experimental Ga-doping. These were performed by R Jalem (Nagoya University) as part of collaborative work. Under the pretext that $\text{Li}_{7-3x}\text{Ga}_x\text{La}_3\text{Zr}_2\text{O}_{12}$ would more likely form cubic-phases, three Ga-distribution scenarios were considered: Td-only (24d), Oh-only (48g/96h) and mixed Td-Oh. For supplementary discussion on the methodology see Appendix A or reference [4].

A simple force-field approach was used to follow the trends in site preference for the Ga dopant. Figure 4.2a shows the result of these calculations and shows a small preference for the Ga to occupy the Td-site with increasing Ga concentration.

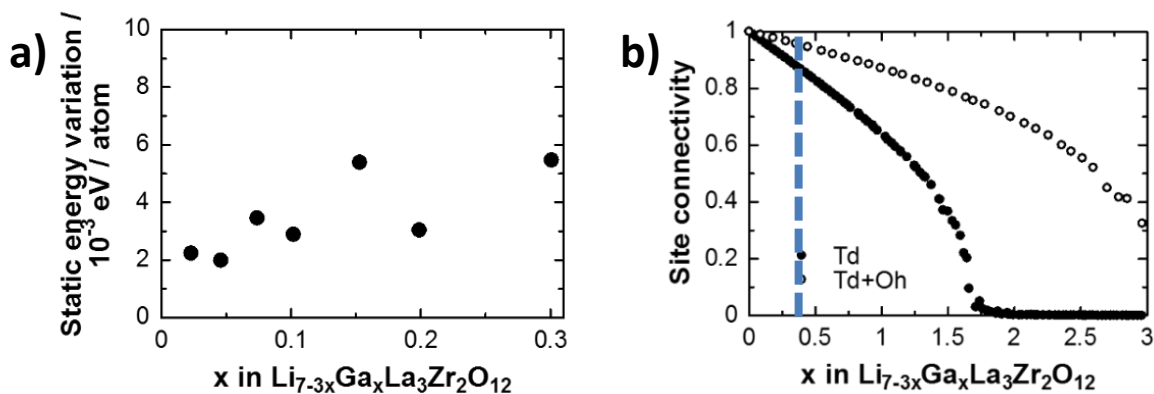


Figure 4.2: a) Statistical energy preference for gallium displacing lithium atoms in all-Td vs in all-Oh models. b) Proportion of the lithium sublattice that is not isolated from the rest, taken using $10 \times 10 \times 10$ supercells with varied levels of Ga content, either in all-Td or mixed Td-Oh configuration. The dotted line indicates the composition with 0.3 Ga p.f.u. [4].

Each immobile Ga^{3+} sitting in a Li-site blocks one part of the interconnected Td-Oh-Td lithium pathways and hence diverts long-range ion migration. By adding more Ga^{3+} , a critical threshold would inevitably exist wherein bottlenecks evolve to block global Li

migration. Percolation theory analysis reveals that 90% of the lithium pathway (Td-Oh-Td-Oh-...) is maintained even at 0.3 Ga atoms per formula unit (Figure 4.2b). This implies a strategy based on aliovalent substitution on Li sites will not seriously disadvantage the ion-conduction network up until this doping level.

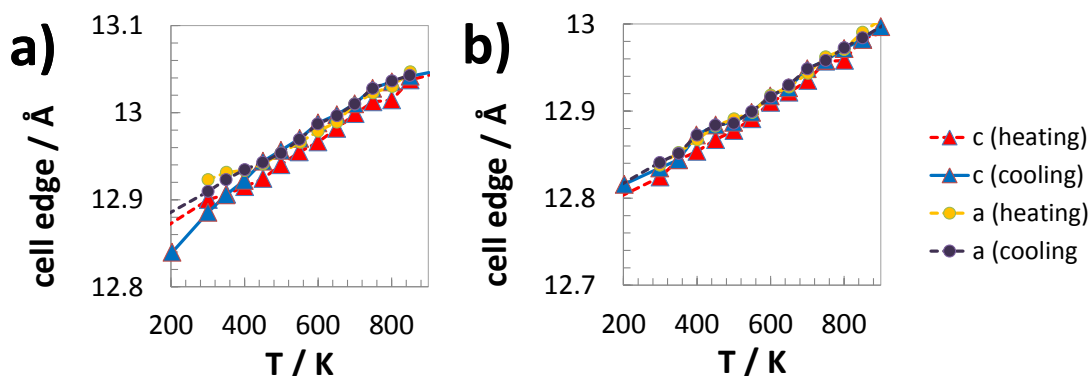


Figure 4.3: Simulated annealing via 1x1x1 simulations of LLZO with (a) 1 Ga atom and (b) 2 Ga atoms. The data correspond to Td-site substitutions [4].

Finally, MD-based annealing cycles (Figure 4.3) between 300K and 1000K were simulated on a unit cell containing either 1 Ga atom or 2 Ga atoms (Li₅₃GaLa₂₄Zr₁₆O₉₆ and Li₅₀Ga₂La₂₄Zr₁₆O₉₆, respectively). A deviation from linear thermal expansion of lattice parameters was detected for the former but not for the latter. This suggested that the lower limit for Ga-doping to stabilize cubic-phase LLZO at room-temperature must be between these two compositions, i.e. in terms of empirical formula units: Li_{6.625}Ga_{0.125}La₃Zr₂O₁₂ and Li_{6.250}Ga_{0.25}La₃Zr₂O₁₂.

4.3 Experimental syntheses

Materials were produced via the citrate-route following experience described in Chapter 3. The reagents used were: Ga₂O₃ (≥99.99%, Sigma-Aldrich), La(NO₃)₃·6H₂O (≥99.99%, Sigma-Aldrich), Zr(C₅H₇O₂)₄ (>98%, Alfa Aesar), and LiNO₃ (>99.0%, Sigma-Aldrich). This included a few drops of concentrated HNO₃ to aid dissolution. Unless otherwise specified, a 10% Li excess was added to the stoichiometric mix to offset Li losses during high-temperature sintering. The gels produced were combusted at 600°C for 12h in air to burn off the organic components, at a ramp rate of 2°C/min. After this treatment, the powder was ground and fired at 800 °C for 12 h, either in ambient air or 99.99% O₂ flow, at a ramp rate of 5°C/min. Al₂O₃ crucibles were used unless otherwise specified.

The previous chapter exposed issues related to powder packing. This chapter will probe deeper into the effects of aliovalent substitution, firing atmosphere, excess lithium, aging, crucible material and other sintering parameters.

4.3.1 Effects of choice of substitution site (Li vs Zr)

The initial goal was identifying the range of Ga-substitution levels which would experimentally stabilize at room-temperature, a cubic-phase garnet.

If the MD predictions were accurate, the onset of the cubic phase should begin at $x=0.125$ to $x=0.250$ for a Li-site replacement in the stoichiometry $\text{Li}_{7-3x}\text{Ga}_x\text{La}_3\text{Zr}_2\text{O}_{12}$. Whereas throughout the range of Zr-site replacements in the stoichiometry $\text{Li}_{7+x}\text{La}_3\text{Zr}_{2-x}\text{Ga}_x\text{O}_{12}$, it was expected that only a tetragonal phase should form.

Syntheses and processing were initially carried out in ambient atmosphere using box furnaces. This was decided after a quick check on standard reduction potential and ionic radii revealed no indication of other cationic states for Li^+ , Ga^{3+} , La^{3+} and Zr^{4+} [1]. This is important because variable valency may interfere with the stoichiometric ratios in the material or induce electronic conductivity via electron-hopping mechanisms.

The XRD patterns of calcined powders (800°C, 12h, air) are juxtaposed in Figure 4.4.

The Ga-Zr substitution strategy, i.e. $\text{Li}_{7+x}\text{La}_3\text{Zr}_{2-x}\text{Ga}_x\text{O}_{12}$, (Figure 4.4a) produced tetragonal phases for compositions from $x=0$ to 0.600 p.f.u. A cubic phase fraction was detected for $x=0.100$, but due to the trend for the rest, $x=0.200$ to $x=0.600$, could be construed as more likely a small amount of $\text{Li}_{7-3x}\text{Ga}_x\text{La}_3\text{Zr}_2\text{O}_{12}$ instead. Indeed, an overstoichiometry of La was detected, with or without the Ga component ($^{\dagger}\text{La}_4\text{Ga}_2\text{O}_9$ and $^{\ddagger}\text{La}_2\text{O}_3$), suggesting Ga^{3+} entry onto Zr^{4+} sites was not favored. This agreed with expectations.

The Ga-Li substitution strategy (Figure 4.4b) produced only garnet phases between $x=0$ to $x=0.450$ p.f.u. The composition with $x=0.450$ corresponds to $\text{Li}_{5.650}\text{Ga}_{0.450}\text{La}_3\text{Zr}_2\text{O}_{12}$. Beyond this doping level, $\text{La}_2\text{Zr}_2\text{O}_7$ impurity (*) was obtained no matter the number of recalcination cycles. Stoichiometric $\text{Li}_7\text{La}_3\text{Zr}_2\text{O}_{12}$ ($x=0$) conformed perfectly to the tetragonal symmetry ($I41/acd$ space group) as expected. A mixed cubic-tetragonal phase was evident from inspection by eye for $x=0.125$, whereas it was not so obvious for $x=0.200$. Quantitative phase determination using Rietveld refinement (atomic parameters unrefined) yielded Figure 4.5. The calcined materials yielded trends

suggesting pure cubic-phases to occur between these two compositions: Li_{6.235}Ga_{0.255}La₃Zr₂O₁₂ and Li_{5.692}Ga_{0.436}La₃Zr₂O₁₂, the lower bound coinciding well with the MD predictions.

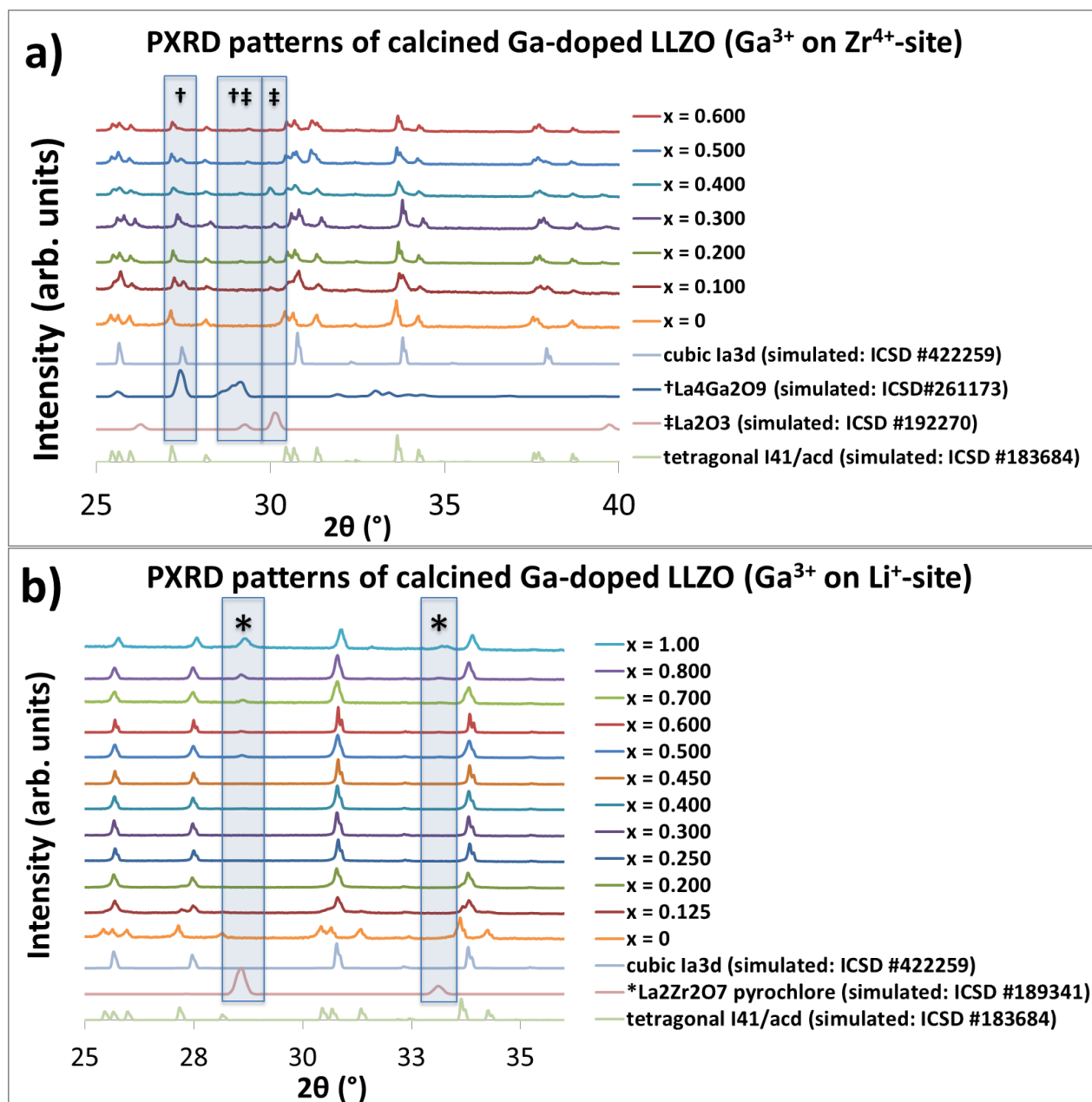


Figure 4.4: XRD patterns of varied compositions calcined at 800°C for 12h in ambient atmosphere of a) Li_{7+x}La₃Zr_{2-x}Ga_xO₁₂ and b) Li_{7-3x}Ga_xLa₃Zr₂O₁₂. Symbols (*, †, ‡) indicate the expected 2θ positions of possible impurity phases.

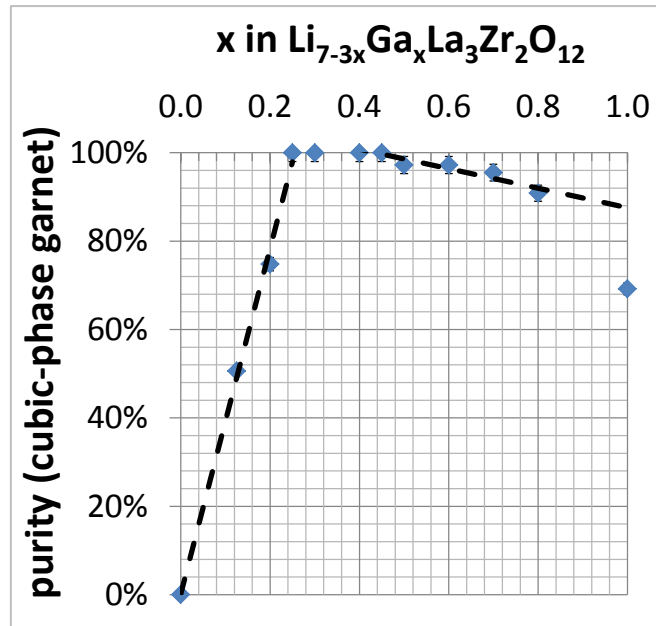


Figure 4.5: Percentage of the cubic garnet phase ($Ia\bar{3}d$ SG) as a function of Ga³⁺ concentration p.f.u. Rietveld refinement data from citrate-route powder calcined in air, corresponding to XRD patterns in Figure 4.4b. The intrapolated line ca. lower bound denotes competition between tetragonal ($I41/acd$ SG) and cubic ($Ia\bar{3}d$ SG) garnet phases. The extrapolated line ca. upper bound denotes competition between La₂Zr₂O₇ (pyrochlore) impurity and cubic ($Ia\bar{3}d$ SG) garnet phase. The trendlines intersected at $x=0.255$ and $x=0.436$, respectively.

The behavior of the lower bound, i.e. compositions with a partial tetragonal phase fraction ($x < 0.250$), can be interpreted in two ways: a) insufficient number of Li-site vacancies, or b) inhomogeneous dispersion of Ga³⁺ dopants, e.g. difficulty of Ga₂O₃ to enter aqueous solution.

Both scenarios may explain the discrepancy with Rettenwander *et al.*'s results [5]. Rettenwander *et al.* found a pure cubic phase at as low as $x=0.08$ in Li_{7-3x}Ga_xLa₃Zr₂O₁₂, but did not test for adventitious Al³⁺ incorporation from the crucible while taking samples to sintering temperature (1050°C) for long periods (17h). This was important because they used Li₂CO₃ which has a melting point ~780°C in a solid-state route synthesis.

Al³⁺ is also known to stabilize Li₇La₃Zr₂O₁₂ into a cubic-phase garnet. On the other hand, the current experimental trend agrees well with El Shinawi and Janek, who highlighted that a significant portion of Ga³⁺ may be retained across particle surfaces or grain boundaries after syntheses [6]. Both references just cited also had syntheses

performed in ambient air conditions. This has an important impact as will be shown in the next chapter.

The behavior of the upper bound at $x > 0.450$, i.e. compositions with partial La₂Zr₂O₇ impurity fractions, can be interpreted using Figure 4.6.

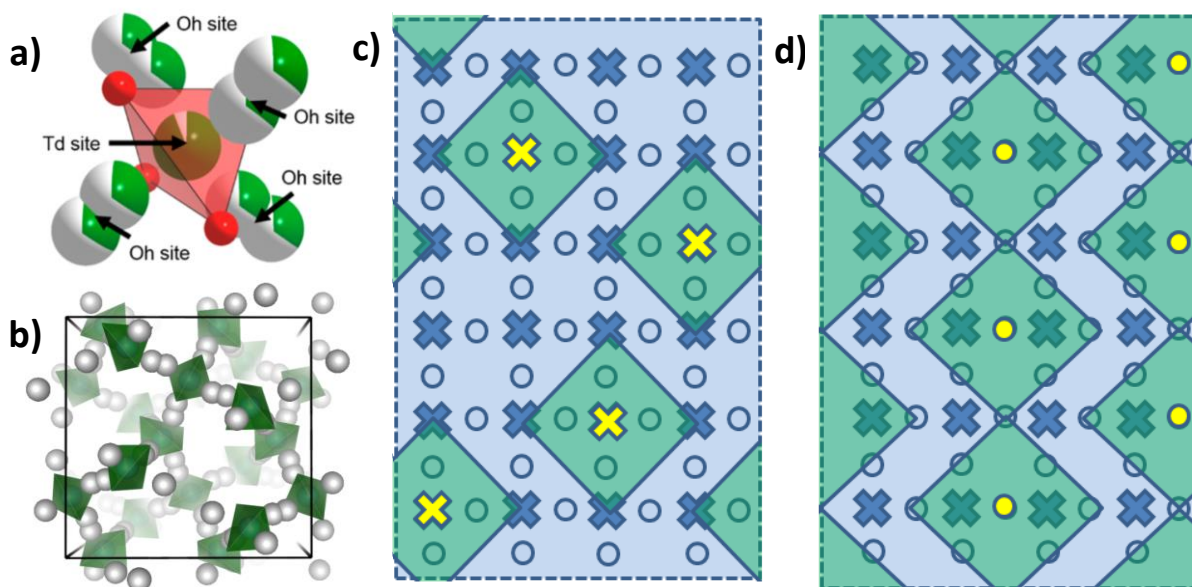


Figure 4.6: a) The available lithium sites: tetrahedral (Td, 24d) and octahedral (Oh, 48g/96h). b) The lithium-conduction network within one unit cell of a cubic-phase garnet. Due to Li-Li repulsion, a 48g Oh-site may evolve into 96h-split sites, but only one atom may occupy the 48g/96h cage at any one time. c-d) Equivalent stereographic 2D view of b, wherein crosses (X) represent Td-sites (24d) and circles (o) represent Oh-sites (48g/96h), The green areas represent the electrostatically-influenced areas of each Ga atom in Td-sites for (c) and Oh-sites for (d). Ga atoms are marked in yellow.

A unit cell for Li₇La₃Zr₂O₁₂ contains 24 Li tetrahedral sites (Td) and 48 Li octahedral sites (Oh). The lithium network is formed by interconnected Td-Oh chain links as shown in Figure 4.6a-b. Each Td site links four Oh sites, and each Oh site bridges two Td sites. Thanks to these peculiar site coordinations, 2D stereographic projections can make analyses easier, as shown in Figure 4.6c-d. The 2D bounds are arbitrary and represent repeating units. What is important is that the total number of Td and Oh sites, correspond to that of the LLZO unit cell.

Replacing a Li⁺ atom sitting in a 24d tetrahedral site by Ga³⁺ increases the electrostatic repulsion by a factor 3. Given how a 24d Li⁺ repulses its 48g Li⁺ neighbors to 96h sites, it can be expected that each 24d Ga³⁺ would force adjacent 48g/96h sites to be

invariably unoccupied. The same analogy can be applied to adjacent 24d sites: two 24d Ga³⁺ would mutually exert an increase in electrostatic repulsion. Hence, only one of them should be occupied by Ga³⁺. Each Ga³⁺ dopant atom thus gives rise to a zone where occupancy by a second Ga is unlikely, as illustrated the by green areas in Figure 4.6c. No corner-sharing or edge-sharing is allowed in this projection, as these constitute 3D proximity when referring back to Figure 4.6b. Because Ga³⁺ exists as ions, and not as metal clusters or polyatomic molecules, Ga³⁺-Ga³⁺ repulsion favors isolated Ga occupancy of the 24d-sites and ensures entropy in Ga distribution.

The overall result is that per garnet unit cell, only a maximum of 4 Ga can be accommodated assuming only Td-site occupancy, as schematized in Figure 4.6c (each green zone takes 5 Td sites). This value corresponds to x=0.500 p.f.u. Once this limit has been passed secondary phases have lower energy and thus form. The impurities most probably precipitate as a mix of an unknown Ga-containing phase and the observed pyrochlore (La₂Zr₂O₇) formation.

The same analysis can be applied to an exclusive Ga occupancy of the Li octahedral (Oh) sites as shown in Figure 4.6d. In this case Oh-sites have a higher degree of branching and dihedral degrees of freedom. This permits a certain degree of corner-sharing of the green zones. The maximum Ga-occupancy permitted in a stable garnet structure in this case, before pyrochlore onset, would be x=0.750 p.f.u, which is 50% higher than experimentally observed. This discrepancy strengthens the argument that Ga prefers to enter the Td-sites. The conclusion agrees well with ⁷¹Ga MAS-NMR experiments to be shown in section 5.1.1.1.

4.3.2 Effects of moisture on phase purity

The Ga-substitution strategy formed a cubic garnet phase and thus high ionic conductivity was expected. An expected consequence was high chemical reactivity and ergo, degradation. One basic question was the long-term behavior under ambient atmosphere of this material.

For this purpose, powders were kept in vials for 3 months and the XRD spectra taken anew. Results confirmed some atmospheric decomposition to the pyrochlore impurity (Figure 4.7).

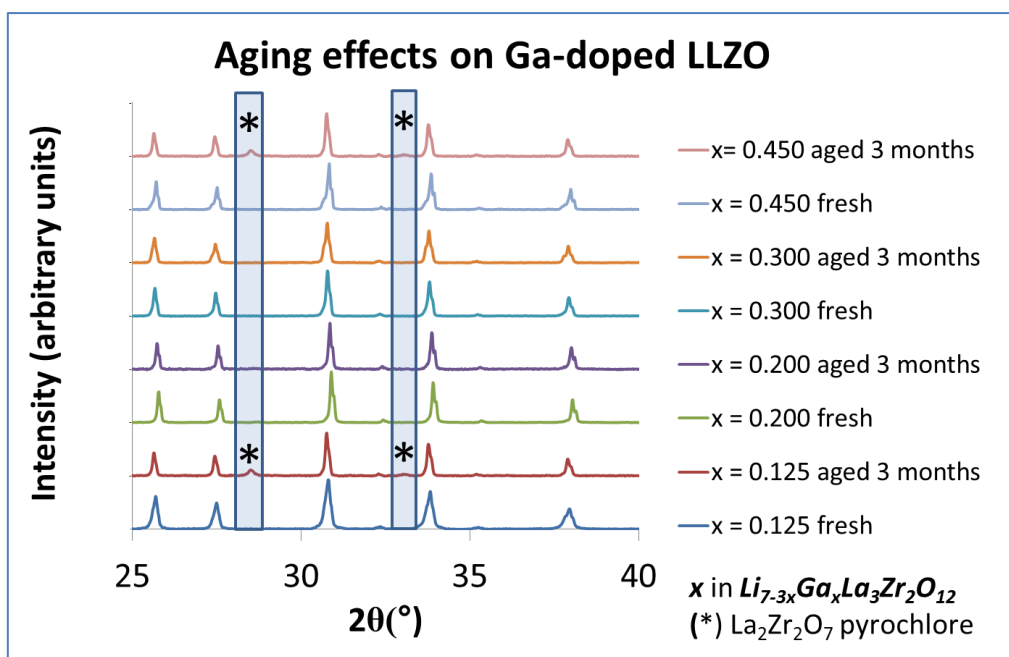


Figure 4.7: XRD spectra of $\text{Li}_{7-3x}\text{Ga}_x\text{La}_3\text{Zr}_2\text{O}_{12}$ compositions taken after fresh preparation, and again after 3 months.

This finding raised questions about **phase-formation kinetics** and **accelerated aging** via **high-temperature XRD**. The setup consisted of a Bruker D8 Advance[®] diffractometer equipped with a modular radiation-type heating chamber (MTC-Furnace[®]). Precalcined powders ($x=0.150$, processed at 800°C for 12h under 99.99% O_2 atm) were placed on a thin corundum plate which functioned as the sample holder. The temperature was ramped at $5^{\circ}\text{C}/\text{min}$ until reaching the particular set temperatures. The dwell periods consisted of a 30min temperature stabilization prior to XRD pattern acquisition. Similar heating schedules were followed for two sets of experiments: one under ambient air, one under dynamic vacuum down to a residual pressure of 4×10^{-4} mbar. These high-temperature XRD patterns are juxtaposed in Figure 4.8.

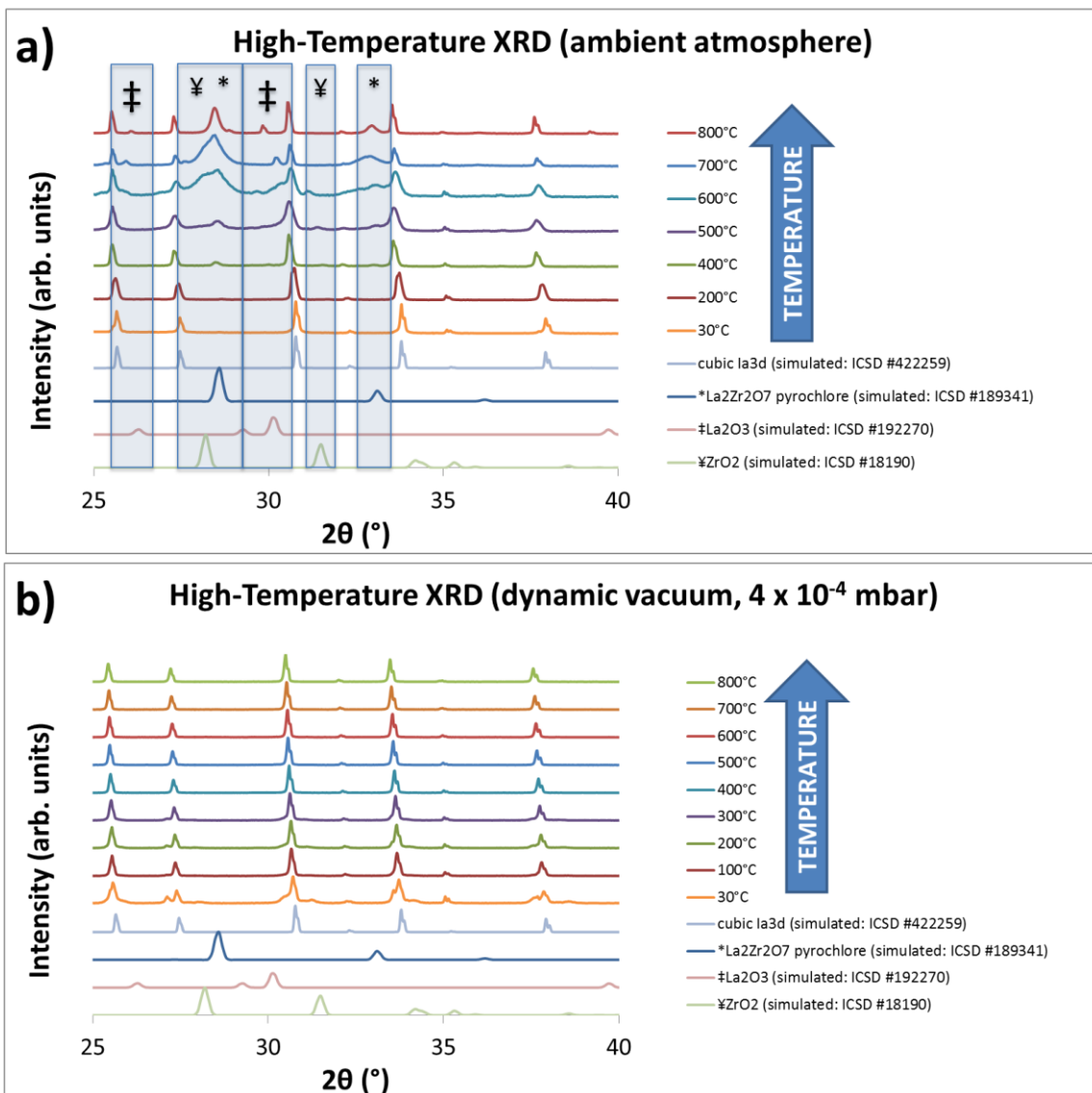


Figure 4.8: High temperature XRD of Li_{6.55}Ga_{0.15}La₃Zr₂O₁₂ in a) ambient air atmosphere and b) dynamic vacuum. No evidence of impurity phases are detected in the latter, except for a slight tetragonal-phase fraction at 30°C.

Ambient air catalyzed phase decomposition into La₂Zr₂O₇, La₂O₃ and ZrO₂ (highlighted peaks in Figure 4.8a). This began as early as 400°C, progressed to circa 700°C and then, unexpectedly, underwent garnet phase-reformation beginning at 800°C. A sequence of phase-decomposition followed by phase-reformation is unusual and hinted of an interacting agent which loses efficacy at high temperatures. The suspicion of nitrogen interaction was ruled out, because any Li₃N (ICSD#156894 and #156895) if present was beyond the detection limit for all temperatures. Of all the other components found in air, H₂O is the most active agent both for degrading lithium-based chemistries (e.g.

LiMn₂O₄, LiFePO₄) and oxide materials (e.g. silica). Hence, the effect of water-contamination will be examined deeper in Section 5.4.

On the other hand, under dynamic vacuum (Figure 4.8b) no such phase decomposition occurred. A progressive thermal expansion from 100°C to 800°C, as hinted by lower 2θ Bragg angles was observed. The XRD patterns allowed analytical Le Bail-type fits, which yielded the lattice parameters plotted in Figure 4.9. These results were then compared with similar work, but on Al-doped LLZO by Hubaud *et al.* [7].

At high temperatures (>700K or >400°C), the lattice constants for Li₇La₃Zr₂O₁₂ doped by either Ga or Al, were comparable. Extrapolating this trend to room temperature predicted a unit cell edge length of 12.98Å, in agreement with Awaka *et al.*'s neutron refinement data on a single-crystal cubic-phase Li₇La₃Zr₂O₁₂ (nominal, Al-doped in reality) [8]. However, an evident kink was noticeable between 384K (111°C) to 558.15K (285°C) in Hubaud *et al.*'s publication. This suggested the onset of an atmosphere-stabilized cubic phase with dynamics already described in literature (section 1.2.2.1.2) [9-12]. This meant effectively that an Al doping level of 0.092 p.f.u. in Hubaud *et al.*'s sample was insufficient to stabilize the cubic-phase at room-temperature.

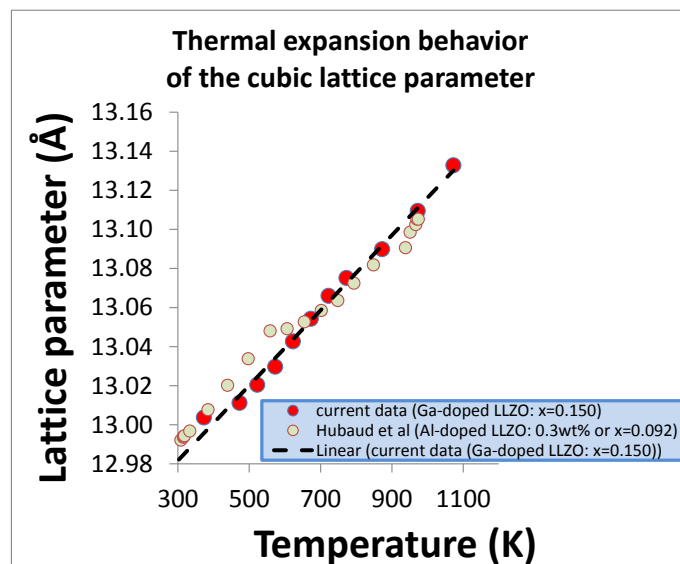


Figure 4.9: Thermal expansion of lattice parameter in cubic-phase Li_{7-3x}Ga_xLa₃Zr₂O₁₂ (x=0.150), compared vs literature values for Li_{7-3x}Al_xLa₃Zr₂O₁₂ (x=0.092) [7].

Nonetheless, Hubaud *et al.* derived a lattice thermal expansion coefficient between $1.3 \times 10^{-5} \text{ K}^{-1}$ to $1.6 \times 10^{-5} \text{ K}^{-1}$ and concluded that anode/cathode active materials like

Li₄Ti₅O₁₂, LiCoO₂ and LiFePO₄ which have coefficients of $1.2 \times 10^{-5} \text{ K}^{-1}$ to $1.5 \times 10^{-5} \text{ K}^{-1}$ would be most compatible for thin film battery assemblies. The derived value for this study was $1.56 \times 10^{-5} \text{ K}^{-1}$ and agreed well.

An important point was made from these results. Figure 4.8 clearly highlighted the sensitivity of the formation of the desired phase to the firing atmosphere. **Hence from this point onwards, all powders were exclusively calcined (800°C) under pure O₂ flow.** The ramp rate was always kept at 5°C/min. The dwell times were set 12h for calcination and 6h for sintering.

The reason for using a pure O₂ atmosphere, even though the cations (Li⁺, Ga³⁺, La³⁺, Zr⁴⁺) were expected to have stable oxidation states (see Appendix B), was to minimize oxygen defects in the anion sublattice if any. To empirically test the viability of using O₂, calcined powders (Li_{6.55}Ga_{0.15}La₃Zr₂O₁₂) were pressed into pellets and fired to **sintering temperatures** under controlled gas flows: **ambient air, Ar (99.99% pure) and O₂ (99.99% pure)**. The first and third were produced using the facilities within CIC Energigune. The second was produced with facilities at Imperial College London (c/o Dr. Ainara Aguadero).

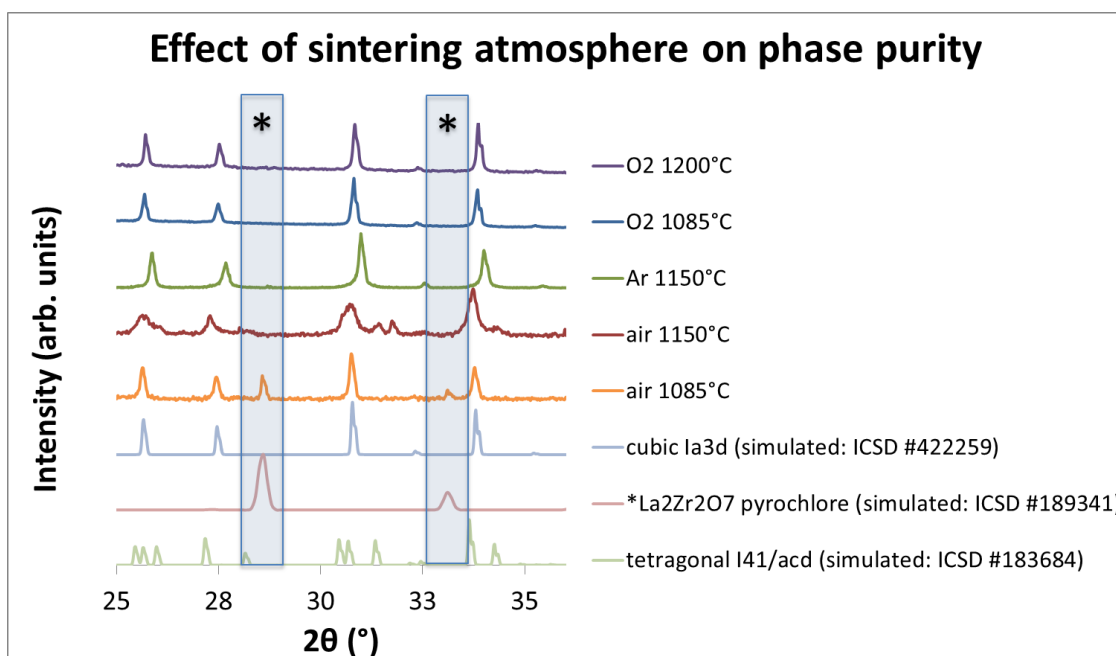


Figure 4.10: XRD patterns of pulverized pellets obtained from taking calcined powder ($x=0.150$, Li_{7-3x}Ga_xLa₃Zr₂O₁₂) to sintering temperatures in air, dry Ar (99.99% pure) and dry O₂ (99.99% pure). (*) denotes a pyrochlore impurity phase (La₂Zr₂O₇).

The effects of sintering atmosphere on phase purity are shown by XRD patterns in Figure 4.10. Heat treatments in ambient air (1085°C and 1150°C) produced degraded samples, as expected. On the other hand, either using Ar or O₂ appeared to yield similar phase-pure materials. For reference, Table 4.2 shows that the refined lattice constants agreed well with Awaka's value of 12.98 Å [8]. The relatively low crystallinity in the sample fired in ambient air at 1150°C was reflected in the uncertainty in the lattice parameter. Again, this may be a hint of H₂O-catalyzed lattice rearrangements [9].

Table 4.2: Influence of firing atmosphere on the resultant lattice parameters of room-temperature samples.

Firing atmosphere	firing temperature	room-temperature lattice parameter (Å)
Open air	1085°C	12.9918(6)
Open air	1150°C	13.02 (4)
Ar (99.99% pure)	1150°C	12.9807 (3)
O ₂ (99.99% pure)	1085°C	12.9695 (10)
O ₂ (99.99% pure)	1200°C	12.9757 (2)

4.3.3 Effects of Ga-substitution level

The findings related to atmospheric degradation effects were a crucial aspect of materials synthesis. This enabled a proper rigorous study on **ionic conductivities** with **sintered ceramics**.

Materials were produced following section 0 with calcination under an O₂ atmosphere. Five compositions were studied: $x = \{0.050, 0.100, 0.150, 0.200 \text{ and } 0.300\}$ Ga p.f.u. following the stoichiometry Li_{7-3x}Ga_xLa₃Zr₂O₁₂. The powders were ground inside the Ar-filled glovebox, and pelletized into 6.35mm (1/4"). Duplicate specimens for each composition were sintered at 1085°C for 6h under O₂ flow, following sections 2.1.3, 2.1.4, 2.1.5 and 2.1.6. The theoretical densities were calculated based on a fixed unit cell volume of $2.19 \times 10^{-21} \text{ cm}^3$, as Le Bail fits showed 12.98 (± 0.01) Å unit cell edge lengths for the said compositions.

Ionic-transport values were obtained using EIS according to section 2.2.3.1, with both Li-foil and Ag-paint electrode setups.

Typical EIS spectra (Figure 4.11a) indicated distinct semi-circles. By comparing the two EIS configurations, an identification of the ionic resistance contributions could be made. The important feature was the **Warburg diffusion tail** at the low frequency end for the trial with Ag-paint electrodes (green line). Its existence confirmed negligible alloying during data acquisition and, being an interfacial phenomenon, its counterpart for the trial with the Li-metal electrodes (low frequency end, blue curve), must have been a resistance linked to ionic transfer from the ceramic electrolyte to the Li-metal bulk ($R_{\text{interface}}$).

Therefore, the first semicircle must be assigned as the convolution of bulk (R_{bulk}) and grain-boundary (R_{GB}) resistances, similar to Section 3.2. To support this, fitted capacitances for this component yielded 10^{-11} to 10^{-10} F with Debye-type dispersion ($n=1.0$), similar to findings in Figure 3.6. SEM micrographs will be shown later in Section 5.1, also revealed large grain sizes leading to reduced grain-boundary surfaces. Effectively, $R(\text{bulk+GB})$ was therefore composed predominantly of $R(\text{bulk})$.

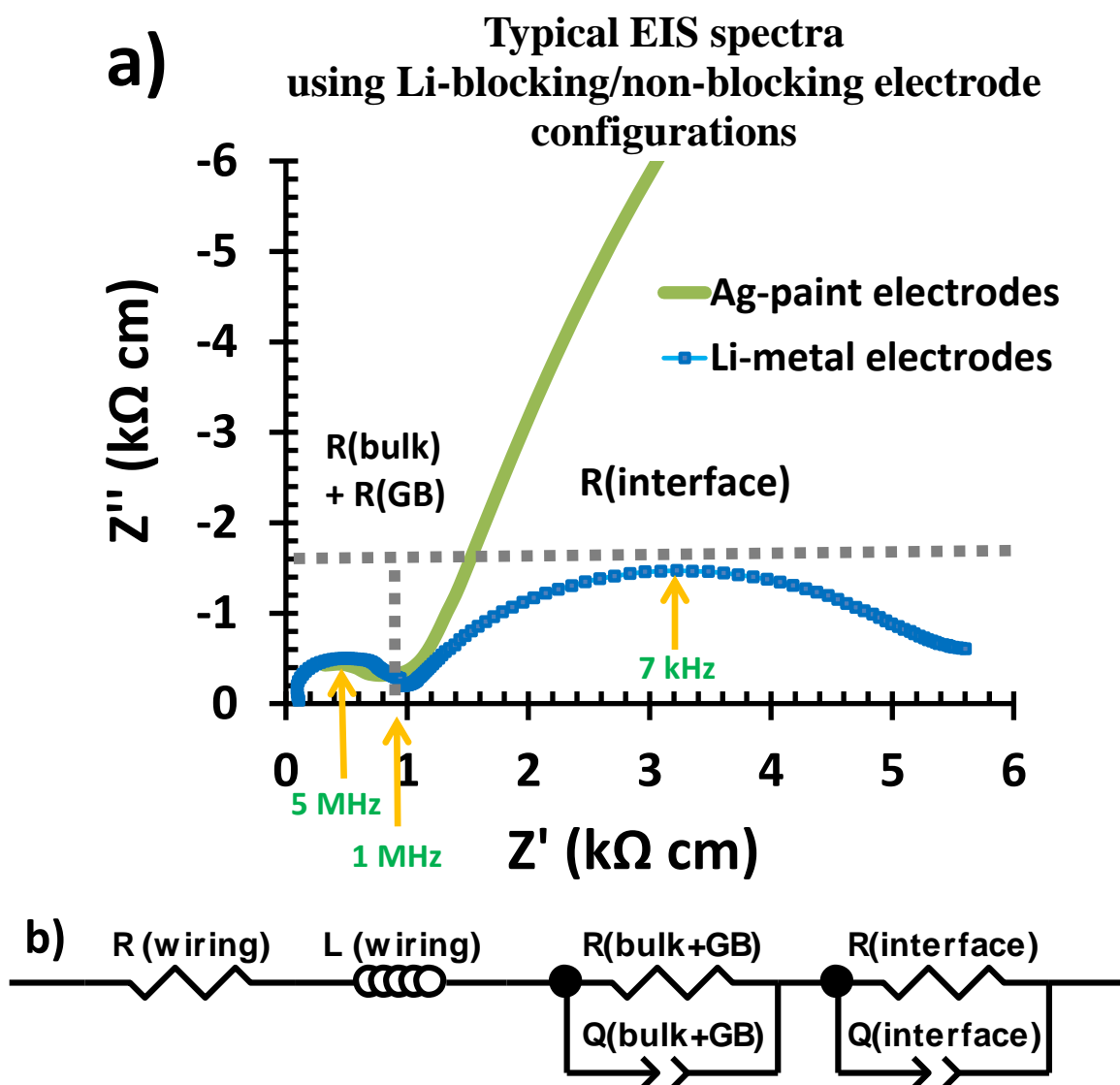


Figure 4.11: a) EIS spectra (Nyquist diagram) of a sintered pellet of $\text{Li}_{6.55}\text{Ga}_{0.15}\text{La}_3\text{Zr}_2\text{O}_{12}$ obtained using the two-probe configuration of the Solartron 1260 module. The yellow arrows indicate the frequencies at the maxima and minima of the semicircles. “ $R(\text{bulk}) + R(\text{GB})$ ” corresponds to the convolution of grain interior and grain-boundary resistance contributions, while “ $R(\text{interface})$ ” corresponds to charge-transfer resistance from the ceramic pellet to the Li-foil. b) Equivalent circuit model corresponding to (a).

The experiments have thus yielded “bulk” conductivities. These can be directly compared with simulated lattice diffusivities from R Jalem’s MD models [4]. The computed activation energies were in a narrow range of 0.24-0.30. Using this, predictions of room-temperature conductivities via extrapolation could be attained by applying the Nernst–Einstein equation:

$$\sigma_{Li} = [Li] F^2 \frac{D_{Li}}{kT}$$

wherein σ_{Li} is the bulk conductivity, [Li] is the Li carrier concentration per unit volume, F is Faraday's constant, D_{Li} is the self-diffusion constant (derived from simulated mean-square displacements), k is the Boltzmann constant, and T is the temperature in kelvins.

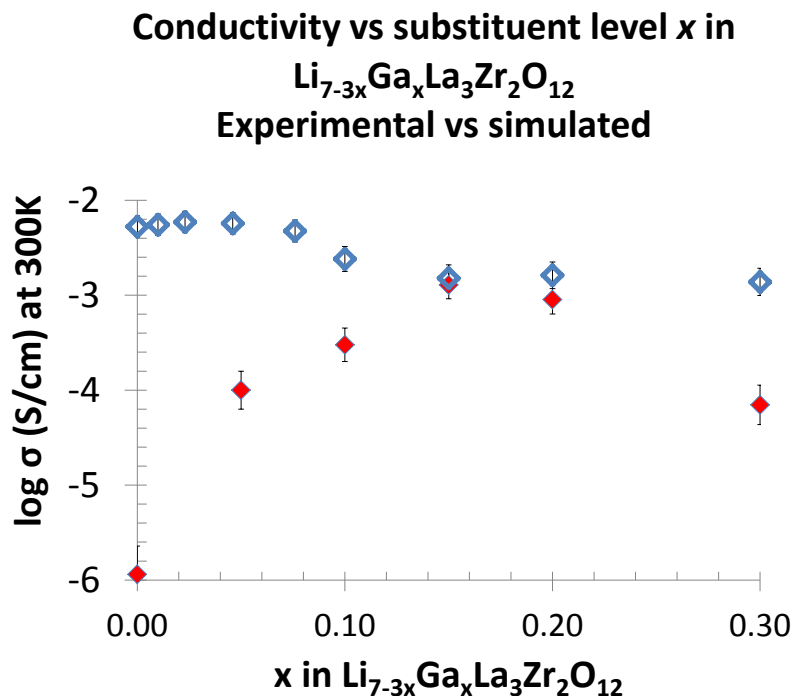


Figure 4.12: Comparison between experimental bulk conductivities (blue diamonds) and predicted lattice conductivities (black spheres) at room temperature [4]. Experimental error bars are within 5% of values, masked by markers.

The results are plotted in Figure 4.12. A caveat with these high-temperature simulations is the neglect of cubic-tetragonal phase transitions, which may be thermodynamically-driven at lower temperatures. One readily observes that the predicted conductivity value at $x=0$ (or stoichiometric Li₇La₃Zr₂O₁₂) is artificially high for a “forced” cubic structure (simulated ~5 mS/cm vs the experimental ~0.001 mS/cm). Another caveat is that an idealized system omits microstructural imperfections, which may explain the trends for doping levels $x>0.150$.

Nonetheless, the experimental series yielded 1.28 (± 0.01) mS/cm for a composition of $x=0.150$. This was highly encouraging as it gave good agreement with the predicted value. Further, the simulations predicted that if it were possible to stabilize a cubic-phase garnet at room-temperature with higher than 6.55 Li p.f.u. (corresponding to a doping level of less than 0.150 Ga p.f.u.), bulk conductivity might increase to as much as 6 mS/cm.

4.3.4 Effects of excess lithium in starting stoichiometry

The simplest approach to stabilize a cubic phase at $x < 0.150$ (in Li_{7-3x}Ga_xLa₃Zr₂O₁₂), was to try varying the Li overstoichiometry. The reader is reminded that the standard synthesis procedure (Section 0), called for adding 10% excess Li in the stoichiometry to compensate for lithium loss due to high-temperature evaporation [13].

Le Chatelier's principle argues that excessive overstoichiometry for one crystallographic site may produce competition, in this case between Li and Ga during phase formation. A precise control of lithium content is thus important. The two opposing behaviors observed can be seen in Figure 4.13 comparing syntheses using 5%, 10% and 15% excess Li levels.

Low dopant ($x < 0.150$ p.f.u.) and low Li excess (5%) produce both a tetragonal garnet phase and a pyrochlore impurity (peaks marked by *). This coexistence phenomenon is curious. A tetragonal phase suggests insufficient Li-site vacancies within the crystal structure to stabilize the cubic phase (i.e. **too much Li** content). A pyrochlore presence suggests insufficient lithium to compensate for charge balance requirements of a stable garnet structure (i.e. **too little Li**).

An explanation is that the vacancies produced by the low doping level (Li_{7-3x}Ga_xLa₃Zr₂O₁₂) were insufficient to stabilize the cubic phase. Meanwhile, adventitious loss of Li (e.g. volatilization) progressed until off-stoichiometry of the garnet composition, leading to the pyrochlore (*) phase.

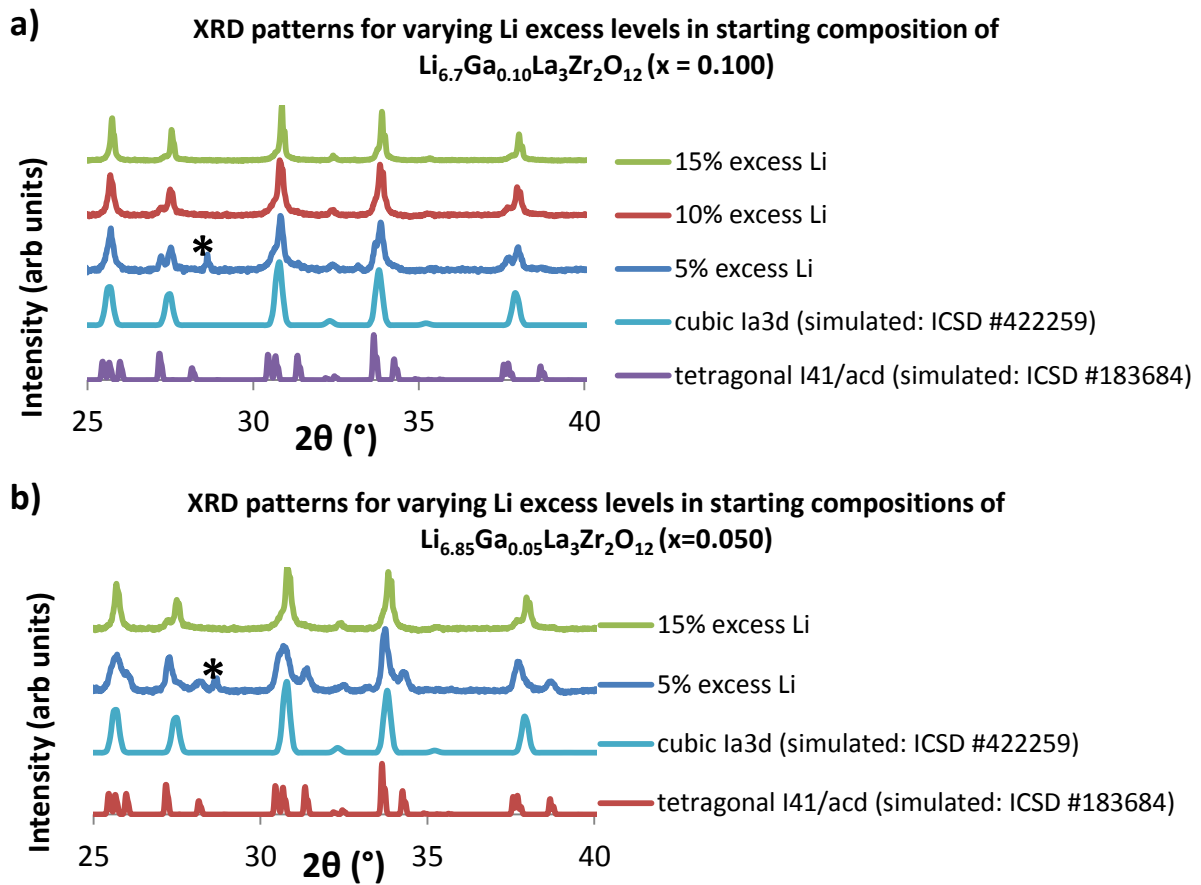


Figure 4.13: XRD patterns ($\lambda = \text{Cu}_{\alpha 1}$) after pulverizing pellets taken to a sintering temperature of 1085°C for 6h under dry O₂ atm, of compositions Li_{7-3x}Ga_xLa₃Zr₂O₁₂ where a) x=0.100 p.f.u. and b) x=0.050 p.f.u. Varied excess percentages of stoichiometric Li were added in the starting compositions. (*) denotes a La₂Zr₂O₇ pyrochlore impurity.

For higher excess levels of lithium (10% and 15%, Figure 4.13a), different mechanisms were at work. This was suggested by a direct correlation between the cubic character and the amount of lithium excess. Normally, a Li-Ga competition argument would have promoted the opposite trend, i.e. pushing Ga out of stoichiometry, decreasing vacancies and increasing tetragonal character. The only reconciliation is that more lattice vacancies were now present from another unknown contaminant/dopant.

Table 4.3. Relative densities of sintered pellets, following compositions Li_{7-3x}Ga_xLa₃Zr₂O₁₂.

	5% excess Li	10% excess Li	15% excess Li
x=0.050	77%	92%	94%
x=0.100	69%	92%	96%

As Table 4.3 indicates, relative densities also increased with higher excess of lithium. Similar phenomena had been reported in the case of Ta-doped LLZO compositions [14, 15]. Increased densification was attributed to liquid-phase sintering due to a Li₂O-Al₂O₃ melt. With Ga-doped samples, chemical analyses (ICP-OES) revealed an increase from 0.02 Al p.f.u. to 0.20 Al p.f.u. in moving from 10% excess Li in starting compositions to 15% excess Li.

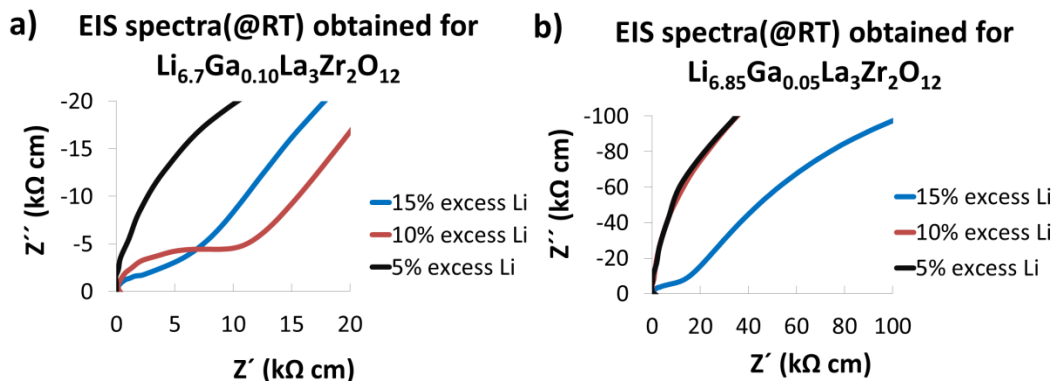


Figure 4.14: EIS spectra obtained for nominal $\text{Li}_{7-3x}\text{Ga}_x\text{La}_3\text{Zr}_2\text{O}_{12}$ materials wherein a) $x=0.100$ and b) $x=0.050$, for varied Li overstoichiometries in starting compositions. Impedance measurements were collected at room-temperature.

Higher ionic conductivities were obtained the higher the cubic-phase fraction was (Figure 4.13). Maximum conductivities were obtained for the inadvertently Ga-Al dual-doped samples using 15% excess Li. The normalized bulk conductivity values were $0.137 (\pm 0.002)$ mS/cm and $0.095 (\pm 0.002)$ mS/cm for compositions with $x=0.100$ and $x=0.050$, respectively as fitted from Figure 4.14. These values were an order of magnitude lower than for $x=0.150$ (~ 1.3 mS/cm, Section 4.3.3).

It was now clear that $x < 0.150$ Ga p.f.u. alone was insufficient to stabilize at room-temperature, the cubic phase of lithium lanthanum zirconate garnets. Further, a 5% Li excess (less than the 10% in the standard procedure) in the starting stoichiometry resulted in garnet phase decomposition and pyrochlore formation, whereas a 15% Li excess promoted excessive Al contamination. It was thus decided to maintain Li excess levels at 10% for the rest of the study.

4.4 Chapter summary

A concise description on Ga-doped LLZO synthesis has been presented beginning with a rigorous campaign of material optimization. Because superionic conductors are highly reactive, synthesis calls for systematically controlling variables. Ultimately, the chosen criteria for optimization were phase purity, lattice ionic conductivity and sintered ceramic density.

1) The Ga-doping of Li₇La₃Zr₂O₁₂ occurs experimentally with Ga entry unto tetrahedral sites (Li 24d), following this chemical formula: Li_{7-3x}Ga_xLa₃Zr₂O₁₂.

For mixed-phases, increasing Ga content increases cubic-phase character (Figure 4.13, $x < 0.150$), suggesting a partial relief of crystallographic stress (i.e. reduction of tetragonal-phase character from excessive populations of interstitial lithium). For already cubic-phases, increasing Ga content reduces Li carriers, and therefore lattice conductivity. (Figure 4.12, $x \geq 0.150$). The maximum Ga-doping level which maintained a cubic-phase garnet with no impurities was $x = 0.500$ p.f.u.

2) The optimum doping level for maximum lattice conductivity (with negligible grain boundary contribution) is $x = 0.150$ with the nominal formula Li_{7-3x}Ga_xLa₃Zr₂O₁₂ (section 4.3.3). This material exhibited total conductivities of more than **1 mS/cm at room-temperature. This corresponds to a lithium content of **6.55**. Experimental ICP values yielded **6.48 (±0.12) Li** p.f.u. in agreement.**

3) The optimum amount of stoichiometric Li excess per formula unit is about 10% for $x < 0.150$ in Li_{7-3x}Ga_xLa₃Zr₂O₁₂ (section 4.3.4) Too little lithium excess yielded pyrochlore. Too much excess Li produced substantial amounts of Al contamination.

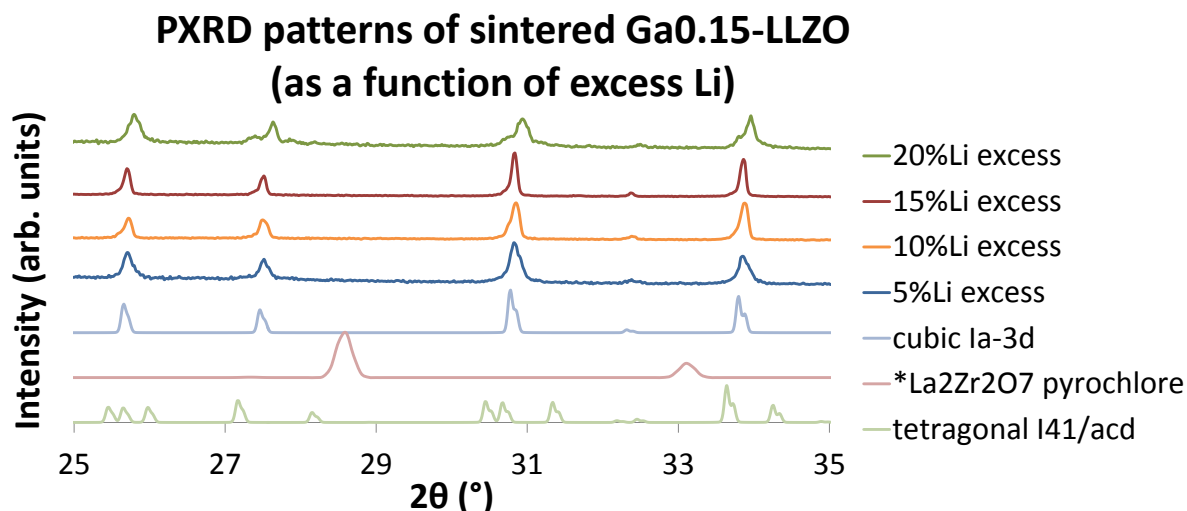


Figure 4.15: XRD patterns ($\lambda = \text{Cu}_{\alpha 1}$) for nominal $\text{Li}_{6.55}\text{Ga}_{0.15}\text{La}_3\text{Zr}_2\text{O}_{12}$ pellets prepared with varying levels of lithium, taken under Kapton[®] film seal and Ar atmosphere. Samples were sintered to 1200°C for 6h under dry O₂ atmosphere, prior to pulverization. The $Ia\bar{3}d$, $I41/acd$ and pyrochlore(*) phases were simulated from ICSD# 422259, 183684 and 189341, respectively.

A follow-up trial for $x=0.150$ was carried out, with XRD patterns shown in Figure 4.15. The 5% Li excess sample produced friable samples which could not be handled as an integral mass. Again a good compromise between cubic-phase character and suitability for handling was found with the material prepared with 10% Li excess. By 20% Li excess, the competition between Li and Ga/Al for tetrahedral sites was evident, producing tetragonal-phase garnets.

4.5 Perspectives

A cubic-phase is necessary for high ionic conductivities in garnet-type materials. There is no question about that (Chapter 3). Where people disagree on is what the main descriptor for ensuring maximum lithium conductivity is. There are three schools of thought: (a) lattice volume, (b) total lithium population and (c) active vacancy densities. The presently-obtained ionic conductivities are discussed under this context.

The argument of lattice volume (lattice parameter) is anchored more on coincidence rather than causality. As Zeier argues, it just so happens that cubic-phase garnets containing high lithium content produce proportionally larger unit cells [16]. Garnet unit cells can be artificially-compressed by substrate-induced strains in thin films, but

this risks distorting the cubic symmetry to induce tetragonality. DFT simulations also predicted constricted bottlenecks and lower simulated conductivity in isotropically-compressed structures [17, 18] But such materials would probably need ultrahigh isotropic pressures at phase formation temperatures. Regardless, a counterexample readily disproves the notion that a fixed lattice parameter directly predicts ionic conductivity, as shown by the conductivities spanning 3 orders of magnitude with approximately the same edge length (Figure 4.16).

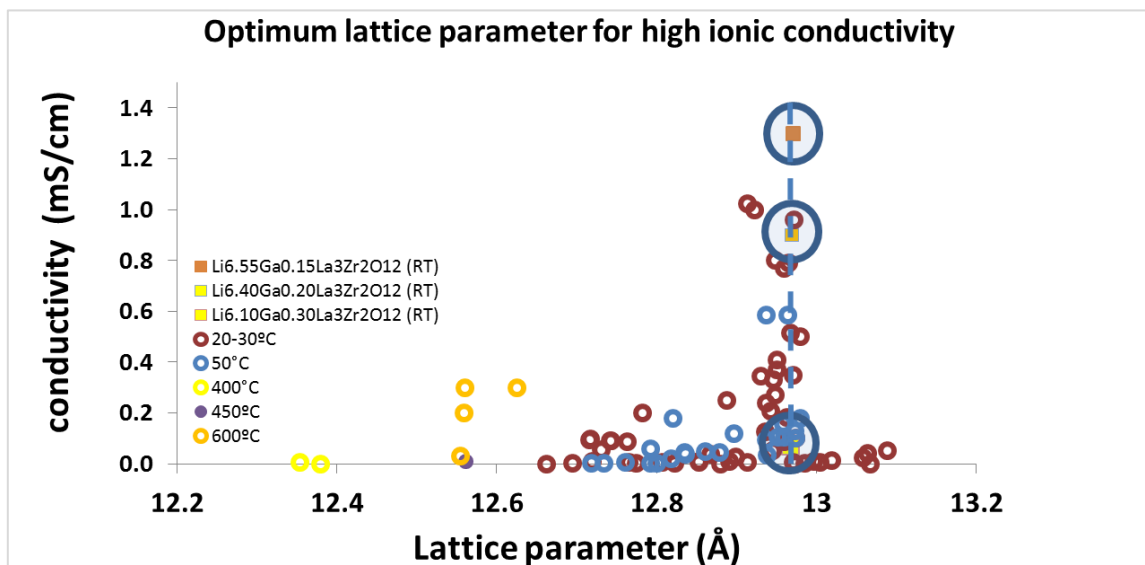


Figure 4.16: Tabulation of lattice ionic conductivities of garnets with different compositions, as adapted from Zeier [16]. The list includes the present Li_{7-3x}Ga_xLa₃Zr₂O₁₂ compositions with $x=0.150, 0.200, 0.300$, as encircled. The dashed vertical line highlights a lattice edge length of $12.969 (\pm 0.001) \text{ \AA}$.

What finds more rational credence is the interplay between lithium populations and vacancies. Essentially for supervalent dopants on Zr-sites, it has been directly observed that increased lithium content not only redistributes lithium across possible Td/Oh sites but decreases activation energies [19, 20]. This means ionic conductivity is not linearly related to the number of lithium carriers multiplied by the number of vacancies, i.e. $\sigma \neq k[\text{lithium}][\text{vacancies}]$, where k is a proportionality constant. But rather, pseudo-exponential increases are expected according to the Arrhenius equation ($\sigma T = Ae^{\frac{-E_A}{kT}}$, where both the jump attempt frequency factor A and activation energy E_A simultaneously vary with increasing lithium content at constant temperature). This trend in ionic conductivity is as expected from a concerted

migration mechanism of lithium ions, as Jalem *et al.* predicted by DFT-MD methods on cubic-phase LLZO [21].

However, for supervalent dopants on Li-sites, the story is different. Dopants that displace lithium by themselves occupying lithium sites are elements such as Al, Zn and Ga. These atoms produce considerable electrostatic repulsion on the immediate octahedral Li neighbors, forcing them to be vacant. This means these sites are permanently excluded from the lithium percolation network. Chen *et al.* probed deeper by neutron diffraction, and articulated that any dopant-induced vacancies are trapped beside the dopant. [22] In effect, this reduces the total number of effective vacancies participating in the actual ion migration. Essentially, an analogy would be a restaurant having 10 seats for customers to eat in, but say 6 seats are then permanently occupied by staff. Consequently, the turnover rate for customers would drastically be reduced.

Chen *et al.* went further, by identifying how lithium distributes between Td/Oh sites when the supervalent dopant atoms are occupying a certain number of tetrahedral sites. They found a factor of ~3.2 vacancies per dopant atom were always generated among the 24 tetrahedral sites. They did not explain why the correlation is so. But what can be drawn up to roughly represent this, has already been shown in Figure 4.6 in the present work. The reader is reminded that Al and Zn in Chen's work can also partially substitute on the Zr-octahedral sites, and that neutron diffraction refinement is a non-local technique that yields only a description of the average structure. Nonetheless, using this factor of ~3.2 vacancies per dopant atom, the "active vacancy density" participating in the actual ion migration can be estimated. Based from this, they further extrapolated on what dopants on LLZO would yield the highest ionic conductivities. The measured conductivities in this work agree with their predictions.

REFERENCES:

- [1] Shannon, R. D. *Acta Crystallographica Section A* **32**(SEP1), 751–767 (1976).
- [2] Awaka, J., Kijima, N., Hayakawa, H. and Akimoto, J. *Journal of Solid State Chemistry* **182**(8), 2046 – 2052 (2009).
- [3] Bernstein, N., Johannes, M. D. and Hoang, K. *Physical Review Letters*. **109**, 205702 (2012).
- [4] Jalem, R., Rushton, M. J. D., Manalastas, W., Nakayama, M., Kasuga, T., Kilner, J. A. and Grimes, R. W. *Chemistry of Materials* **27**(8), 2821–2831 (2015).
- [5] Rettenwander, D., Geiger, C. A., Tribus, M., Tropper, P. and Amthauer, G. *Inorganic Chemistry* **53**(12), 6264–6269 (2014).
- [6] El Shinawi, H. and Janek, J. *Journal of Power Sources* **225**, 13–19 (2013).
- [7] Hubaud, A. A., Schroeder, D. J., Ingram, B. J., Okasinski, J. S. and Vaughey, J. T. *Journal of Alloys and Compounds* **644**, 804–807 (2015).

- [8] Awaka, J., Takashima, A., Kataoka, K., Kijima, N., Idemoto, Y. and Akimoto, J. *Chemistry Letters* **40**(1), 60–62 (2011).
- [9] Larraz, G., Orera, A. and Sanjuan, M. L. *Journal of Materials Chemistry A* **1**, 11419–11428 (2013).
- [10] Galven, C., Fourquet, J.L., Crosnier-Lopez, M.P. and Le Berre, F. *Chemistry of Materials* **23**(7), 1892–1900 (2011).
- [11] Matsui, M., Sakamoto, K., Takahashi, K., Hirano, A., Takeda, Y., Yamamoto, O. and Imanishi, N. *Solid State Ionics* **262**, 155–159 (2013).
- [12] Wang, Y., Klenk, M., Page, K. and Lai, W. *Chemistry of Materials* **26**(19), 5613–5624 (2014).
- [13] Murugan, R., Thangadurai, V. and Weppner, W. *Angewandte Chemie-international Edition* **46**(41), 7778–7781 (2007).
- [14] Li, Y., Cao, Y. and Guo, X. *Solid State Ionics* **253**, 76–80 (2013).
- [15] Liu, K., Ma, J.T. and Wang, C.A. *Journal of Power Sources* **260**, 109–114 (2014).
- [16] Zeier, W. G. *Dalton Transactions* **43**(43), 16133–16138 (2014).
- [17] Bachman, J. C., Muy, S., Grimaud, A., Chang, H.H., Pour, N., Lux, S. F., Paschos, O., Maglia, F., Lupart, S., Lamp, P., Giordano, L. and Shao-Horn, Y. *Chemical Reviews* **116**(1), 140–162 (2016).
- [18] Miara, L. J., Ong, S. P., Mo, Y., Richards, W. D., Park, Y., Lee, J.-M., Lee, H. S. and Ceder, G. *Chemistry of Materials*. **25**(15), 3048–3055 (2013).
- [19] Wang, D. *Chemistry of Materials*. **27**, 6650–6659 (2015).
- [20] Adams, S. and Rao, R. P. *Journal of Materials Chemistry*. **22**(4), 1426–1434 (2012).
- [21] Jalem, R., Yamamoto, Y., Shiiba, H., Nakayama, M., Munakata, H., Kasuga, T. and Kanamura, K. *Chemistry of Materials* **25**(3), 425–430 (2013).
- [22] Chen, Y., Rangasamy, E., Lang, C. and An, K. *Chemistry of Materials* **27**(16), 5491–5494 (2015).

5 Li₇La₃Zr₂O₁₂ (Ga-doping):

On handling, storage and contamination

The study had determined that an optimum Ga-loading of $x=0.150$ p.f.u. produced the most ionically-conductive materials. From this point onwards, discussion is devoted in the context of applying these sintered ceramics for actual electrolyte applications.

Of prime concern are the handling and storage. Ceramic processing is a multi-step process. This creates extended periods of exposure to potential contaminants. Because highly-reactive materials are at greatest risk, it is unwise to scale-up such materials without a solid understanding of detecting and evaluating degradation effects.

There are two main contaminants for LLZO garnets: atmospheric moisture and adventitious elements from crucibles. This chapter begins with H₂O due to its pervasive nature.

5.1 Effects of moisture on ionic diffusion

H₂O effects on calcined powder had already been seen in section 4.3.2. Phase impurities detectable by XRD arose either with aging or refiring under ambient air conditions. Hence, dry-processed powders began to be exclusively used. These were powders calcined in 99.99% O₂ and stored in <0.1ppm H₂O conditions.

In this section, cold-pressed pellets were sintered at 1085°C (6h) either under dry O₂-flow or inside an air-exposed muffle furnace. Samples yielded 90% and 70% relative densities, respectively. A pyrochlore impurity arose for the latter as was shown in Figure 4.7. This meant cold-pressing alone could not sufficiently reduce percolation surface area and close pores. Hence during firing, moisture-induced decomposition dynamically progressed.

The resulting ionic conductivities varied by two orders of magnitude as shown in Figure 5.1. The higher activation energy (0.54eV) indicates that the lower conductivity of the air-processed sample was not simply due to less Li carriers.

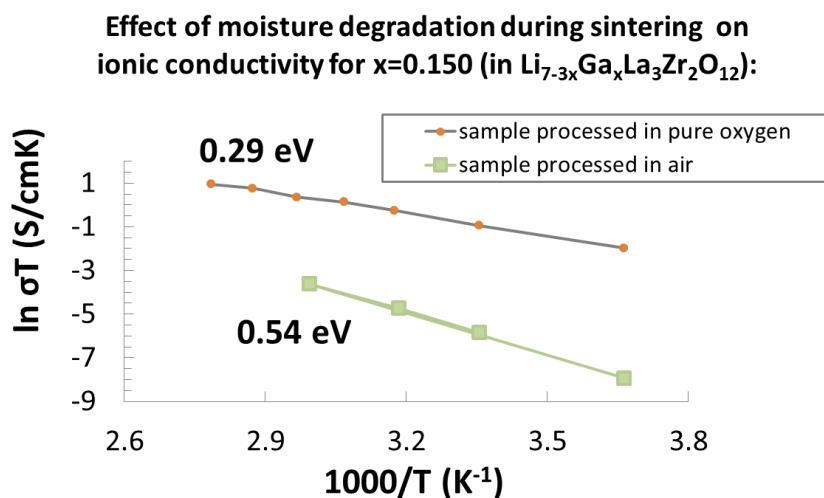


Figure 5.1: Arrhenius plots of bulk ionic conductivities taken between 0°C and 86°C for pellets, highlighting differences when sintering under either ambient air or controlled O₂-flow (99.99% pure) conditions. Pellets were sintered for 6h at 1085°C, and stored in an Ar-glovebox immediately after cooling. EIS was done with Li electrodes.

Carrying on with this work, how moisture affects an already densified ceramic was investigated.

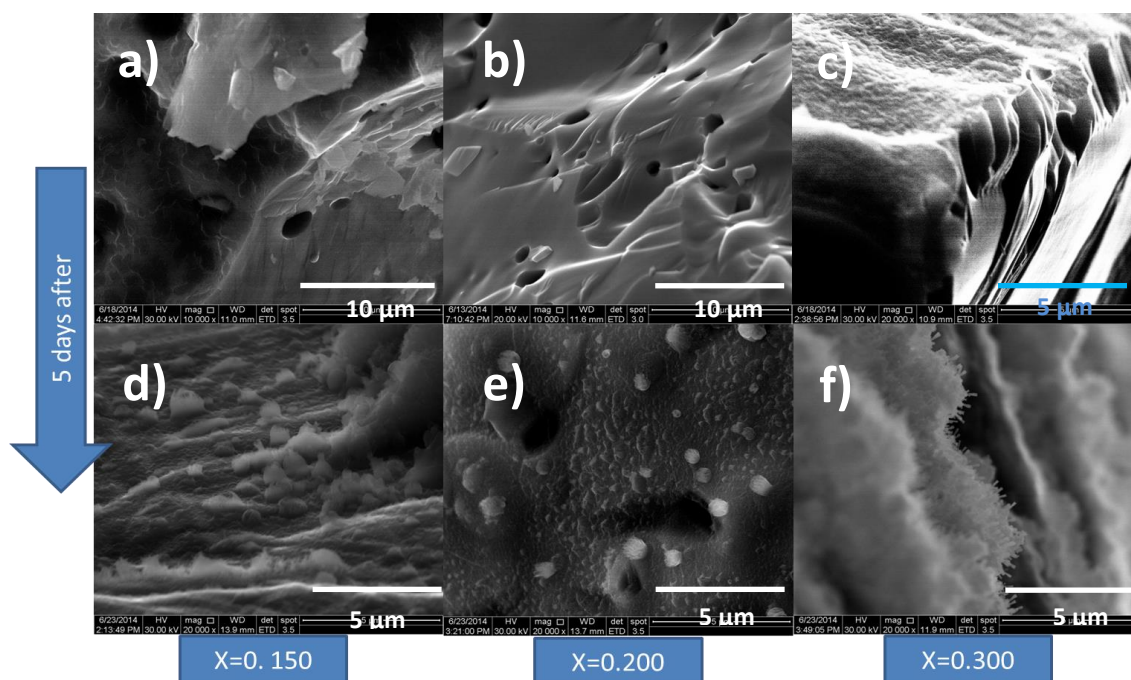


Figure 5.2: SE micrographs of fracture surfaces of $\text{Li}_{7-3x}\text{Ga}_x\text{La}_3\text{Zr}_2\text{O}_{12}$ sintered at 1085°C (6h) under dry O₂-processing, for a) $x=0.150$, b) $x=0.200$ and b) $x=0.300$ compositions, and after aging in open air for 5 days (d, e, f, respectively). Notice the needle growths on the surface for the aged samples.

Figure 5.2 compares the cross-sections of several pellets with different compositions of Li_{7-3x}Ga_xLa₃Zr₂O₁₂, freshly-broken and after aging in open air (5 days). Freshly-broken pellets showed surfaces (a-c) with smooth contours and scattered spherical pores, suggestive of trans-granular fracturing. After aging (d-f), needle-like growths with propagation normal to the pellet surface were evident. This was suggestive of a surface corrosion process, with a mechanism likely related to the PXRD-observed impurities in aged and heated powder (Figure 4.7-4.8).

At this point, the reader is reminded that Figure 5.1 showed how the ionic conductivity of a uniformly **phase-impure** sample behaves. This highlights the importance of **synthesis** atmosphere. On the other hand, Figure 5.2 used **phase-pure** materials and highlights the importance of **handling** atmosphere.

Corrosion effects were expected to alter the ionic conductivity of a **phase-pure** sample. These were explored using EIS (pellet level) and NMR (powder level) experiments.

5.1.1 Moisture-corrosion effects on Li-ion conductivity: pellet level

To probe macroscopic effects by EIS, a protocol for accelerated moisture aging was designed for a test pellet. This was in order to avoid spectral artefacts from ambient dust accumulation.

The O₂-sintered pellet in the previous section was recovered from its coin cell. It was lightly polished to remove the Li-metal contacts, then submerged in boiling liquid H₂O for 1h and subsequently underwent vacuum drying for 24h at 30°C within the antechamber of an Ar-filled glovebox. This was so that there would be no contact with ambient air once again after the sample was dry. Using this pellet, a new coin cell with Li-foil electrodes was assembled, and its EIS spectra were taken.

To test if the corrosion products could be reduced into some form of highly-conducting phase simply by contacting with metallic lithium, the coin cell assembly was heated to 175°C (64h) under external dynamic vacuum. Again, EIS spectra were taken.

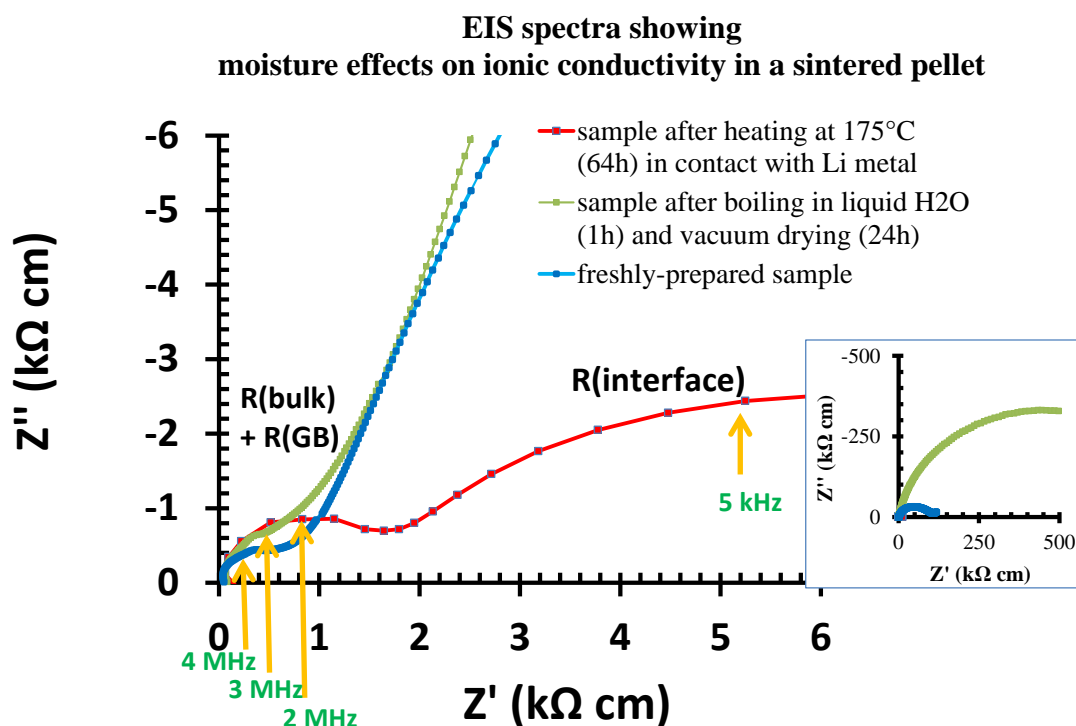


Figure 5.3: EIS spectra taken for a pellet of composition $x=0.150$ (in $\text{Li}_{7-3x}\text{Ga}_x\text{La}_3\text{Zr}_2\text{O}_{12}$) using Li-foil electrodes. The main figure shows a magnified view of the high-frequency region; inset shows the low-frequency region.

The three sets of EIS spectra are shown in Figure 5.3.

The freshly-prepared sample (blue curve) had a large semicircle at the low-frequency region yielding an area-specific resistance ($R_{\text{interface}}$) of about $4000\ \Omega\text{cm}^2$, which increased by a factor of at least 10 after the boiling H₂O treatment. This meant there was poor contact between the lithium foil and the freshly-prepared dry ceramic initially, and that this was aggravated by moisture attack.

What was interesting was that by taking the Li-metal/H₂O-treated ceramic/Li-metal assembly to 175°C, the interfacial resistance dropped back to $450\ \Omega\text{cm}^2$, similar to what Buschmann reported for freshly-prepared Al-doped LLZO samples [1]. This indicates that taking lithium metal close to its melting point (180°C) improves the ceramic-Li metal contact despite the moisture-exposure history.

On the other hand, the resistances associated with the high-frequency region ($R_{\text{bulk+GB}}$) for the three pellet states ranged within an order of magnitude, i.e. $718 \pm 6\ \Omega\text{cm}$, $892 \pm 9\ \Omega\text{cm}$ and $1490 \pm 30\ \Omega\text{cm}$ for the freshly-prepared sample, after H₂O-treatment, and after heating with Li-foil contact, respectively. The small resistance increase suggests that for a relatively-dense sample (93% in this case), moisture-induced degradation (at least for the bulk component) occurs on a much slower scale. It is notable that protons

inserted within the garnet lattice have been shown to be immobile at room-temperature, hence the bulk ion-transport contribution must have been from lithium [2].

The loss of lithium-carriers in LLZO garnets (from a transient moisture exposure) is further inferred to be not reversible with a simple prolonged contact against solid Li-metal. This is despite the latter being a rich lithium source, its reputed insertion/alloying tendencies in many materials, and its commonly quoted standard oxidation potential (3.04 V vs H₂/H⁺).

The reason follows. The reader is reminded that electrochemical cells involving liquid electrolytes, behave differently to dry solid systems, e.g. all-solid-state batteries. Standard reduction potentials used to describe the former are experimentally obtained using 1M aqueous solutions, wherein solvation effects dominate. The solvation energies adjust the Gibbs free energies for electron gain/loss for the light elements, and these translate via the Nernst equation to the oxidation/reduction potentials available in chemistry textbooks. It is therefore important to not only to identify which cationic or anionic species are possibly labile, but in which state. **In a vacuum or a dry system, lithium would not reduce H⁺ to H₂, and hydrogen would be the most electropositive element** [3].

5.1.1 Moisture-corrosion effects on Li-ion conductivity: powder level

To understand moisture effects on the atomic level, solid-state magic-angle-spinning NMR (ssMAS-NMR) was performed by Dr. Juan Miguel Lopez del Amo (inhouse at CIC Energigune). A discussion dedicated to technical details of ssMAS-NMR can be found in Section 2.2.2.4.

A polished O₂-sintered ceramic (x=0.150, heated 6h at 1085°C) was pulverized inside an ultradry Ar-glovebox (<0.1 ppm H₂O), and loaded unto an NMR rotor. A fine rotor diameter of 1.3mm was chosen in order to enable ultra-fast spinning at 50kHz and deconvolute artifacts known as spinning sidebands. To study gallium (⁷¹Ga), proton (¹H) and lithium (⁷Li) nuclei, a Bruker Avance III 500 spectrometer was calibrated and determined to have Larmor frequencies of $\nu_0 = 152.56$ MHz, $\nu_0 = 500.24$ MHz and $\nu_0 = 194.41$ MHz for the respective nuclei.

5.1.1.1 ssMAS-NMR: ⁷¹Ga

A representative ⁷¹Ga spectrum is illustrated in Figure 5.4, with its simulated fitting using the parameters in Table 5.1. The fitting is described below.

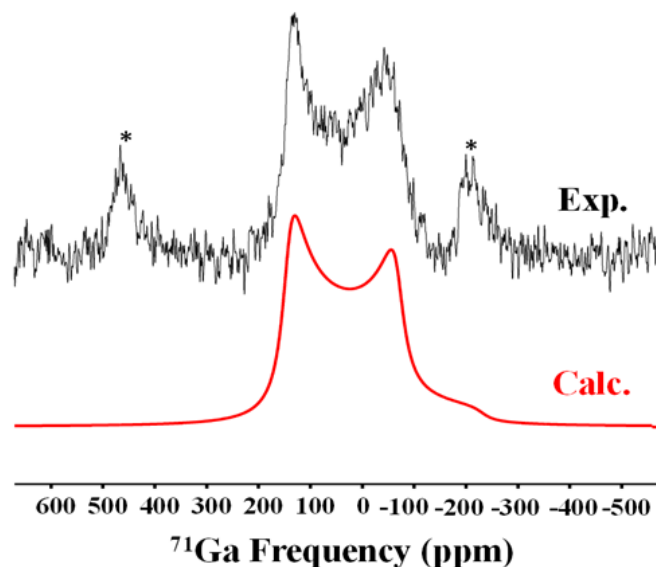


Figure 5.4: Experimental ⁷¹Ga spectrum recorded for a pulverized pellet of composition $x=0.150$ ($\text{Li}_{7-3x}\text{Ga}_x\text{La}_3\text{Zr}_2\text{O}_{12}$), compared to a simulated spectrum using parameters in Table 5.1. Asterisks (*) denote the location of spinning sidebands.

The main clues for understanding ⁷¹Ga crystal chemistry are the **chemical shift** (δ_{iso}) and the **quadrupolar coupling constant** (C_Q) for the ⁷¹Ga nuclei. The former is indicative how much environmental electron density (i.e. shielding/deshielding) there is, and the latter, its spatial distribution. Despite magic-angle spinning, the ⁷¹Ga spectrum is considerably broadened due to its quadrupolar nucleus ($I = 3/2$). The quadrupolar moments interact with the electric field gradients, introducing anisotropic broadening that can only be partially neutralized by magic-angle spinning. Hence, δ_{iso} and C_Q values are difficult to pinpoint by mere visual inspection.

Educated guesses can be made by comparing with a similar material (e.g. oxide vs oxide). The Y₃Ga₅O₁₂ (YGG) lattice contains Ga housed in both tetrahedral (Ga_{Td}) and octahedral sites (Ga_{Oh}) in a garnet-structure lattice. Literature exists on its solid-state NMR behavior as well. Hence, it was a good choice for a model material [4]. Interestingly, a single set of fitting parameters can be used to model the experimentally-recorded ⁷¹Ga spectrum (Figure 5.4). Table 5.1 provides good

consistency only with a **tetrahedral-coordination** (Ga_{Td}). That the asymmetry factor (η_Q) is close to zero supports the suggestion that the ceramic is a cubic garnet phase and further rejects notions of Ga clustering.

Table 5.1: ⁷¹Ga NMR parameters for octahedral (Ga_{Oh}) and tetrahedral (Ga_{Td}) positions measured for the Y₃Ga₅O₁₂ (YGG) garnet by Vosegaard *et al.* [4], and the parameters obtained for Li_{7-3x}Ga_xLa₃Zr₂O₁₂ (x=0.150) in the present work.

Compound/Site	δ_{iso} (ppm)	C_Q (MHz)	η_Q
YGG ²⁹ /Ga _{Oh}	5.6 ± 1.2	4.1 ± 0.06	0.03 ± 0.04
YGG ²⁹ /Ga _{Td}	219 ± 19	13.1 ± 0.2	0.05 ± 0.03
Li _{7-3x} Ga _x La ₃ Zr ₂ O ₁₂ /Ga _{Td}	207 ± 10	12.7 ± 0.3	0.05 ± 0.05

Another comparison can be made with MAS-NMR studies of Al-doped LLZO. For analogous compounds, ⁷¹Ga shifts bear a linear relationship to the ²⁷Al shifts. In principle, this allows the ⁷¹Ga shift of any unknown compound to be inferred from the ²⁷Al shift of the Al analogue via the relationship [5].

$$\delta^{71}Ga = 2.84(\delta^{27}Al) - 1$$

Using this equation and the tetrahedrally-coordinated ²⁷Al chemical shifts published by Geiger *et al.* [6] for a cubic Li_{7-3x}Al_xLa₃Zr₂O₁₂, the predicted tetrahedrally-coordinated ⁷¹Ga chemical shifts are 192 and 229 ppm for Li_{7-3x}Ga_xLa₃Zr₂O₁₂, which are also within current experimental values and error. Further, the existence of an Li₅GaO₄ impurity (analogous to Li₅AlO₄, which shows up at 92 ppm in ²⁷Al NMR) for gallium would have been predicted to appear at 260 ppm, and which was not seen in our spectra. LiGaO₂ (242 ppm) was also not detected [7].

The ⁷¹Ga spectra with or without moisture exposure (protocol explained below) were identical, hence a duplicate is not displayed.

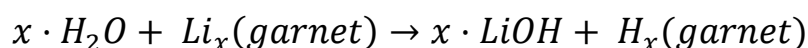
5.1.1.2 ssMAS-NMR: ¹H and ⁷Li

Moisture effects on other solid-state ionic conductors have been documented before [8-10]. Thus, the discussion on ¹H and ⁷Li nuclei are complementary. Relevant NMR line shape spectra, T1 relaxation profiles and a schematic mechanism are illustrated in Figure 5.5.

In this section MAS NMR results are reported for the same sample in two different states: when the material was freshly prepared (“dry”), and after 3 days closed-rotor aging in ambient air (“after atmospheric exposure”). The reader is reminded that the protocol for preparing the “dry” sample involved special precautions, such as handling in an ultra-dry Ar-glovebox (<0.1 ppm H₂O) and ceramic polishing to remove any surface contaminants prior to grinding. It is also pertinent to remember that the NMR rotors are not 100% hermetically sealed.

The ¹H line shape spectra are first examined (Figure 5.5a). The main ¹H resonances occurred at -1.5 ppm and 4.8 ppm, which had integrated intensities in an almost 1:1 ratio. The former shift is in good agreement with the presence of LiOH [11], and the latter coincides with the chemical shift value for ¹H nuclei (protons) in Li_{7-x}H_xLa₃Sn₂O₁₂, a protonated version of a LLZO analogue identified by neutron diffraction [12]. The peak intensities of proton signals increased drastically after atmospheric exposure compared to the nominally “dry” sample. The intensity evolution followed a time-dependent behavior reminiscent of progressive proton-related corrosion in perovskite-type lithium ion conductors (occurring at 3.5 to 8ppm for LLTO) [10, 13]. The minor ¹H signal at 1 ppm is time-independent, and attributed to a minor non-garnet impurity, likely organics adsorbed during handling.

This provisional assignment implies molecular incorporation of H₂O as a pair of dissociated species H⁺/OH⁻ (to maintain a 1:1 ratio), followed by a solid-state displacement reaction:



The reaction products are curious, in particular the LiOH. The LLZO garnet has a tightly-packed structure that can easily accommodate H⁺. However, it has hardly any space to sterically accommodate the insertion of an additional OH⁻ unit. This OH⁻ unit (ergo LiOH) must then exist on the surface of the ceramic particles, hence extracting lithium from the garnet lattice and forming a corroded surface, as illustrated in Figure 5.5b.

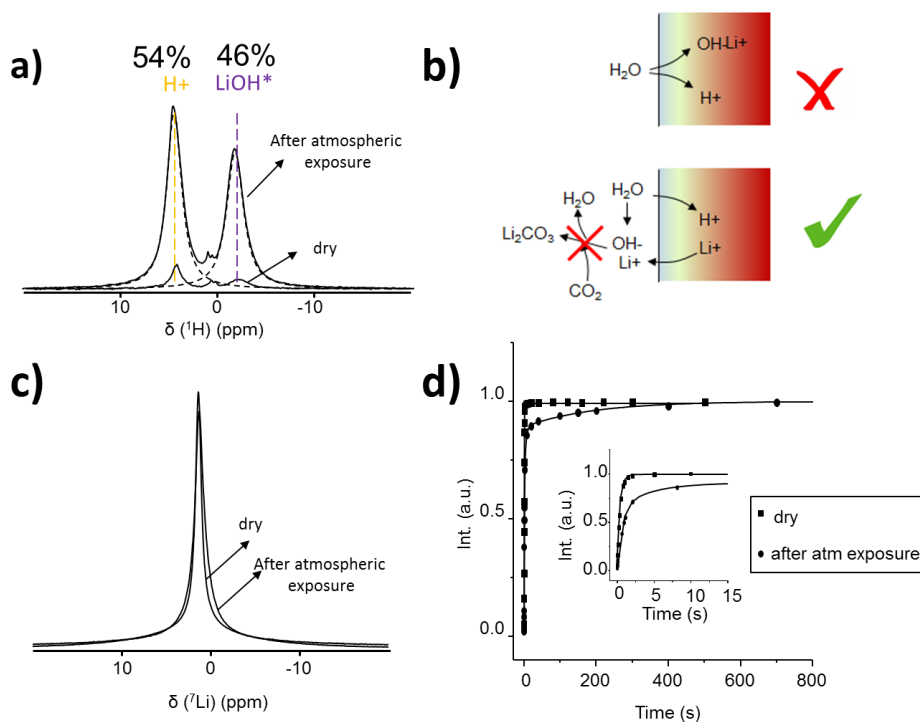


Figure 5.5: ssMAS-NMR monitoring of a high-conductivity Li_{7-3x}Ga_xLa₃Zr₂O₁₂ ceramic powder (previously calcined to 1085°C for 6h in O₂ atmosphere) during two stages: an atmosphere-isolated dry stage and an atmosphere-exposed stage (3 days controlled exposure to open air): a) ¹H NMR line shapes, b) proposed chemistry for observations in a, c) ⁷Li NMR line shapes, and d) ⁷Li T₁ relaxation profiles from a saturation recovery experiment.

Lithium extraction reduces the mobile ion concentration, and proton-insertion may disrupt Li-Li ion dynamics and hence reduce the Li mobility. Both these effects are assumed to have a detrimental effect on the ionic conductivity.

The ⁷Li line shape spectra should therefore show differences between the dry and the moisture exposed samples in Figure 5.5c. After atmospheric exposure, a peak broadening was indeed observed. It is an indication of the averaging out of the ⁷Li nuclei interactions with the environmental electron density, and therefore isotropic fast-ion motion, has been **reduced** in the NMR-time scale. However, the extent of this disruption cannot be elucidated directly due to strong peak overlapping.

A ⁷Li T₁ saturation recovery experiment enables better deconvolution of the components of the ⁷Li signal. The results of this experiment are shown in Figure 5.5d. The normalized intensity (in a.u.) is indicative of the nuclei population that has recovered their initial spin states after a T₁ magnetization pulse sequence. The time needed to reach 1.0 (the plateau) illustrates how fast this relaxation occurs, and indirectly, the ionic mobility.

Trends for each component usually follow an exponential decay pattern, e.g. $f(t) = \sum_y (1 - e^{-t/T_{1y}})$, herein $f(t)$ is normalized, t is elapsed time and T_{1y} is the component y 's characteristic T_1 time constant.

In the graphical plots (Figure 5.5d), the “dry” state exhibits magnetization recovery that is almost instantaneous compared to the “exposed” state. Analytical fittings (Table 5.2) provide a more precise description.

Table 5.2: Optimized fits of the T_1 -relaxation build-up curves in Figure 5.5c.

Sample	Amplitude	T_1 (s)
Dry	100 %	0.38
After atmospheric exposure	Component A	10%
	Component B	60%
	Component C	30%
		189
		0.65
		4.1

The relaxation behavior for the “dry” sample can be fitted using a single exponential function, along with a short T_1 value (0.38s). This is consistent with uniform lithium mobility within the NMR timescale.

The relaxation behavior for the “exposed” sample can only be fit using a tri-exponential function, consisting of a slow component {189s} and two relatively fast components {0.65s,4.1s}. This is consistent with reduced lithium mobility.

The slow component (relaxing at 189s) is rationalized as surface LiOH in an amorphous state due to these factors: a) It had a minor quantity (10%) as expected from a localized corrosion process; b) Its T_1 constant scaled with literature values for bulk LiOH [14]; c) LiOH crystalline XRD peaks were absent in air-exposed samples (e.g. Figure 4.7) or even with liquid H₂O contact; d) previous work on Al-substituted LLZO showing a minor population (15%) of low-mobility Li with a long T_1 relaxation of 500-1000s (vs 5-7s for the faster component) was also ascribed to a secondary phase precipitation [15-17].

The other components (relaxing at 0.65s and 4.1s) are rationalized as manifestations of lithium ion-transport bottlenecks within the garnet structure due to disruption by proton insertion. The assumption is that 24d Li populations are increasingly trapped in local sites, as previously demonstrated by Galven *et al.* for proton-exchanged Li₇La₃Sn₂O₁₂ [12]. For the present study, a categorical assignment of T_1 component

quantities (60% and 30%) to average 24d and 48g/96h occupancies, respectively, is tempting but must be scrutinized carefully.

The reader is reminded that the test powders were sourced from sintered ceramics. This was in order to ascertain high Li-ion conductivity independently by electrochemical impedance techniques, prior to atmospheric exposures. It is imperative for ultrafast magic-angle-spinning (MAS, 50kHz) to load the NMR rotor with a uniform center of gravity, i.e. the sample loaded must be in pulverized powder or liquid form, therefore large ceramic chunks cannot be used.

Mechanical milling cannot be applied as the process would actively create microcrystalline domains and alter defect populations in lithium-rich garnets, distorting lattice-sensitive NMR data. Notably, this impact of the degree of crystallinity of a phase to its mobility and hence in the longitudinal relaxation values had already been investigated previously [18].

On the other hand, sintering introduces grain-coarsening that is not averaged out simply by prolonged hand-milling, especially in ceramics with high elastic moduli. This inevitably produces a powder distribution with unequal grain sizes, a combination of fine and coarse powder. Fine powder exposes large surface areas compared to coarse powder, i.e. it would have a higher mass percentage of corrosion products on a per grain basis. This is illustrated in Figure 5.6 (a,b), which is an extension of Figure 5.5b.

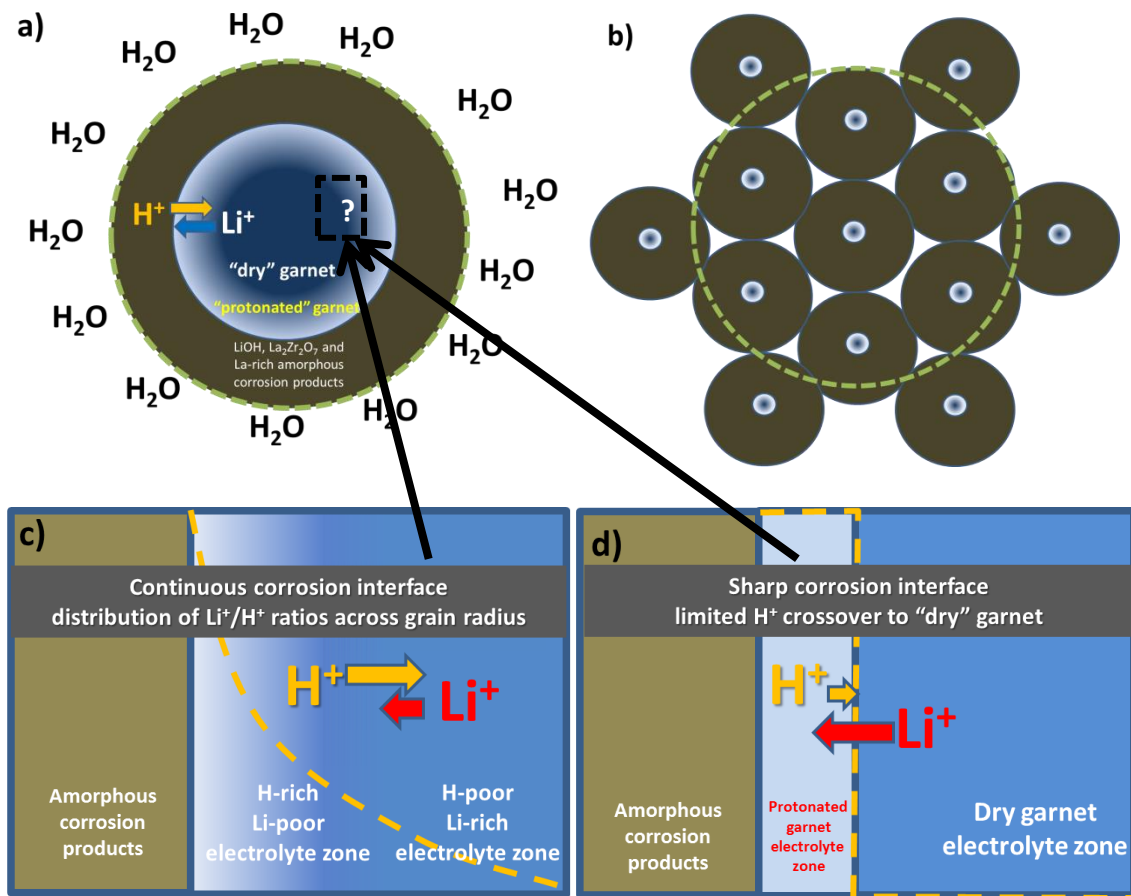


Figure 5.6: Schematic of atmospheric corrosion in a) one large grain and b) many small grains; roughly normalized to the same volume. Spalled decomposition products are found in the outermost layer (green), followed by a zone of proton-exchanged garnet, and the "dry" garnet core. The diffusion of H⁺/Li⁺ traced along the "protonated" garnet zone; c) Schematic of deep penetration of protons within the garnet grain; d) Schematic of shallow penetration of protons within the garnet grain.

This is important because for decomposition layers of say, 1 μm (see needle-growths in Figure 5.2f), the corrosion is dependent on the rate and extent of H⁺/Li⁺ exchange. The proportion of lithium mass extracted from a 5 μm electrolyte grain and that from a 50 μm electrolyte grain within the same corrosion timeframe would be very different. But in either case a commensurate amount of charge-compensating protons must be inserted.

The decomposition layer may be assumed to be porous and amorphous. Beneath this decomposition layer, proton diffusion is initiated by a garnet zone of high proton concentration contiguous to a garnet zone of zero proton concentration. It is expected that this chemical gradient provides the driving force for proton diffusion. It is further

expected that proton self-diffusion (proton-proton exchange) in an equilibrated Li_{7-3x+y}Ga_xH_yLa₃Zr₂O₁₂ grain (arising from thermal vibration) is negligible at room-temperature due to strong H-O interactions, i.e. once the chemical gradient is insufficient to drive further protonation, the inserted protons would stay put in their positions [2].

An important question is how deep into each electrolyte grain do protons reach. The more protons there are, the less lithium charge carriers there would be within each grain. This may or may not trigger an Td-Oh occupancy redistribution in the lattice level. Two general scenarios may occur. Rough schemas are provided in Figure 5.6c-d.

a) **H⁺ has a relatively high chemical diffusion gradient. The H⁺/Li⁺ exchange proceeds deep within the bulk ceramic, but is limited by the rate of Li expulsion and LiOH formation that maintain charge balance.** This scenario represents an eventual averaging of composition within the entire electrolyte grain.

Garnet grains can be tagged each with an amount of “fluid” or mobile lithium lost to corrosion. Because a particle size distribution exists, not all grains have the same proportion of corrosion volume to garnet volume. Illustrating this, there can be one large grain with an average lithium content of say, 6 p.f.u., and one small grain with an average lithium content of say 4 p.f.u. The grain lithium content forms the basis for lithium redistribution among the 24d and 48g/96h sites using an average formula: Li_{7-3x-y}Ga_xH_yLa₃Zr₂O₁₂. Extend this logic, and it is self-evident that there is not one 24d vs 48g/96h occupancy ratio, but a distribution of ratios in one batch of powder sample.

This scenario presents a paradox: The lower the stoichiometric Li in the formula above means lower Li conductivity, down as much as 5 orders of magnitude (1 mS/cm to 10⁻⁵ mS/cm). This results in a decrease in the lithium counter flux to the incoming protons [19]. Corollary, this means the deeper the protonation, the slower the rate of Li expulsion, until the advance of the protonated front is brought to a virtual standstill by a sluggish charge balance compensation.

b) **H⁺ has a relatively low chemical diffusion gradient. The H⁺/Li⁺ exchange proceeds very slowly at the zone barrier.** This implies a sharp interface between the “protonated” garnet and the “dry” grain core will form. The native 24d and 48g/96h lithium populations (and consequently Li-Li ion dynamics) are conserved in the dry core, and the contribution of the lithium atoms trapped in the “protonated” garnet are negligible and will not be seen in the ⁷Li T₁ relaxation experiments.

In either scenario, it is evident that the corrosion propagation is kinetically self-limited, either by a slow H⁺ diffusion or a slow Li⁺ diffusion. The ⁷Li T₁ relaxation experiments (Table 5.2) suggest that the reality is a combination of these two scenarios, considering two facts: The T₁ relaxation profile for the bulk garnet components consist of just two exponential functions, deviating from scenario (a), and the lower T₁ constants suggest lithium trapping in certain sites, deviating from scenario (b).

5.1.2 Proton-diffusion in bulk ceramics: FIB-SIMS experiments

The preceding section has demonstrated that **the corrosion layer must be finite**. This brings back the question: **how deep can protons penetrate into the bulk ceramic?**

To answer this, an experiment using the Isotopic Exchange Depth Profiling (IEDP) method was designed for bulk ceramic fragments [20]. The isotropic tracer utilized was deuterium (sourced from 99.8% enriched D₂O, Alfa Aesar) due to its low natural abundance (0.0115%) and expected ionic behavior similar to ¹H protons (both are stripped of electron clouds). **Selected samples were immersed in boiling D₂O (101.4°C) for 20 minutes, quickly decanted and quenched in dynamic vacuum back to room-temperature.**

High temperatures induce deuterium diffusion unto the ceramic, whereas quenching immediately stops any further deuterium movement. The resulting deuterium distribution was expected to be static at room-temperature, as an inference from proton behavior within the LLZO garnet structure [2]. This allows secondary ion mass spectrometry (SIMS) to reliably analyze the ceramic composition layer by layer. The result is a precise depth composition profile.

The diffusion coefficient can be analytically determined assuming semi-infinite diffusion regimes with Fick's laws and Crank's solution to the diffusion equations [21]. In this work, least-squares optimization module in the TraceX software package was applied for profile fitting with help from Prof. John Kilner and Dr. Samuel Cooper (Imperial College London) [22].

The ceramic samples were sputtered using a 30keV gallium focused ion beam (FIB) . This beam was incident at 30° relative to the ceramic surface with a 1.12 nA beam current. The crater size for the depth profiles was 20 μm x 20 μm. The secondary ion intensities were recorded , using two SIMS detectors operating in a 'simultaneous positive and negative' (SPN) detection mode. The positive ions were detected by a FEI

SIMS detector system; the negative ions were detected by a Hiden EQS SIMS detector system [23, 24].

Gallium secondary ions were monitored to check that it was valid to assume linearity between sputter-rate and sputter-depth. Prior to analysis residual gas analysis (RGA) and instrument calibration (checking conformity to natural isotopic ratios of measured elements) were undertaken to eliminate artifacts from beam misalignment, detector mistuning and atmospheric contamination. A differential vacuum of 10^{-5} mbar was maintained at all times during the measurements. All FIB-SIMS operations were performed by Dr. Richard Chater (Imperial College London).

For this section, four samples were tested. All ceramics were sintered at 1150°C for 6h under Ar flow (5 mbar flow under dynamic vacuum). These were polished to a lustrous finish according to Chapter 5.

- (a) as-prepared nominal Li₇La₃Zr₂O₁₂ (undoped LLZO, 30% Li excess)
- (b) D₂O-treated nominal Li₇La₃Zr₂O₁₂ (undoped LLZO, 30% Li excess)
- (c) as-prepared Li_{7-3x}Ga_xLa₃Zr₂O₁₂ (Ga-doped LLZO, x=0.150, 10% Li excess)
- (d) D₂O-treated Li_{7-3x}Ga_xLa₃Zr₂O₁₂ (Ga-doped LLZO, x=0.150, 10% Li excess)

A low magnification micrograph of a Ga-doped LLZO sample is shown to emphasize that the analyzed area was within a dense single-grain of ceramic material (Figure 5.7a). Sporadic pores of small sizes are sometimes observed within grains; large sizes along grain boundaries. Why such pores appear will be discussed in Chapter 9. At this point, it is simply to be noted that these sites have been avoided during sputtering.

Representative crater micrographs after Ga-ion sputtering are displayed in Figure 5.7 b-e. Because the 20µm x 20µm craters were within grains 100µm across, this confirms that the analyses from sputtered compositions are free from artefacts arising from possible secondary phases along grain boundaries.

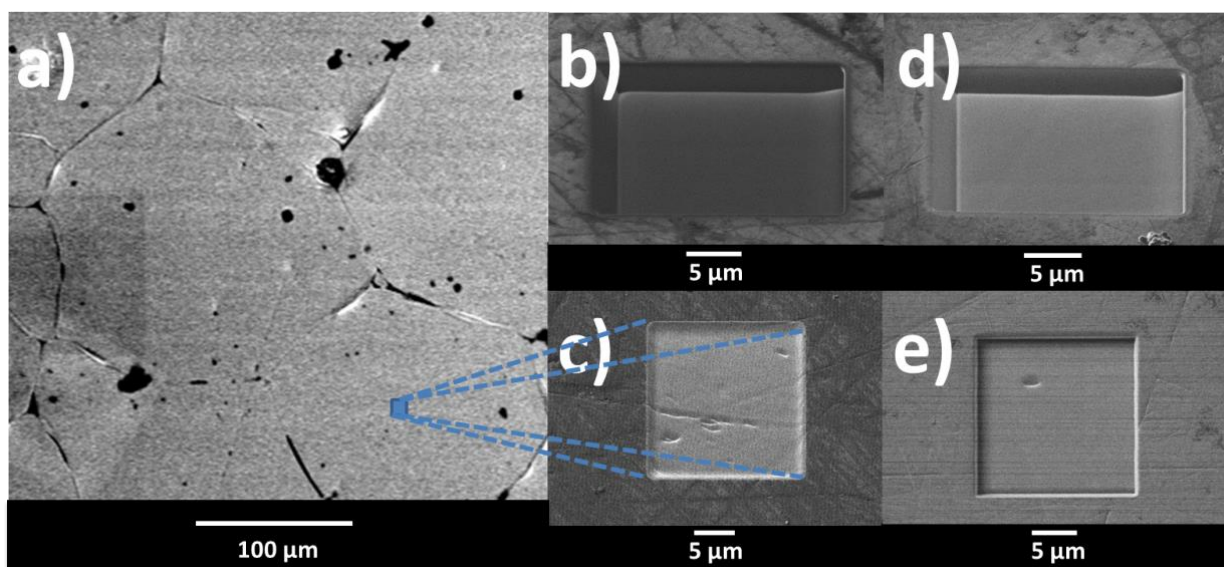


Figure 5.7: a) low magnification BE micrograph of as-prepared $\text{Li}_{7-3x}\text{Ga}_x\text{La}_3\text{Zr}_2\text{O}_{12}$ ($x=0.150$, sintered at 1150°C for 6h in Ar atmosphere); high magnification SE micrographs of post-sputter craters of b) as-prepared LLZO, c) as-prepared Ga-LLZO, d) after D_2O treatment of the sample in b, and e) after D_2O treatment of the sample in c. The figures for b and d appear elongated due to a 45° angle tilt, but all samples have sputter areas of $20\ \mu\text{m} \times 20\ \mu\text{m}$.

The sputtered craters for undoped LLZO (as-prepared and D_2O -treated) were pore-free, exposing a smooth crater base.¹ The counterparts for the Ga-doped LLZO exhibited minor sporadic pores. These were present in small quantities in an otherwise fully-dense grain.

Both samples did not show any evidence of pitting corrosion of the abraded surfaces with boiling D_2O treatment, suggesting that the LLZO garnet lattice (or at least the protonated garnet zones in Figure 5.6 are quite kinetically stable and do not simply dissolve in aqueous media [25].

According to the depth-dependent composition profiles, the thickness of the “protonated” garnet zones extend down mainly $1\text{-}2\ \mu\text{m}$ beneath the surface of the ceramic (Figure 5.8 a/c). The corresponding lithium profile is manifested by a concentration dip, which is limited to this region supporting H^+/Li^+ exchange (Figure 5.8 b/d). Interestingly, this exchange penetration has very little dependence on the

¹This is due to the Li excess promoting Al-aided sintering (see section 5.2). This was intentional; otherwise a disintegrated product resulted, which could not have been handled for the current experiment.

initial lithium ion conductivity of the garnet composition. To remind the reader, the nominally “undoped” sample is expected to have a lithium ionic conductivity between 0.001 mS/cm to 0.1 mS/cm, whereas the Ga-doped sample has a high value of 1 mS/cm. **This means that consistent with the mechanism in Figure 5.6d, the propagation front of corrosion is limited by the slow diffusion of protons.**

The deuterium distribution followed an exponential decay profile for both D₂O-exchanged compositions (undoped and Ga-doped, Figure 5.8 a/c), whereas a flat profile was observed for both the unexchanged compositions (undoped and Ga-doped, Figure 5.8 a/c). This verifies that deuterium diffusion is a real phenomenon, and that a precise diffusivity constant can be determined. Fitting to the appropriate solution to the diffusion equation for a semi-infinite medium yielded a ***D*** value (diffusion constant) of **1.88 x 10⁻¹² cm²/s at 101.4°C**. Note that this was a normalized profile where the intensity profile had been normalized to the maximum intensity of the deuterium. This is not exactly correct as the profile should have been normalized to a matrix signal and then further normalized to the maximum of this ratio. This may explain why the profile does not fit so well in the tail, however it would not have affected the value of *D*.

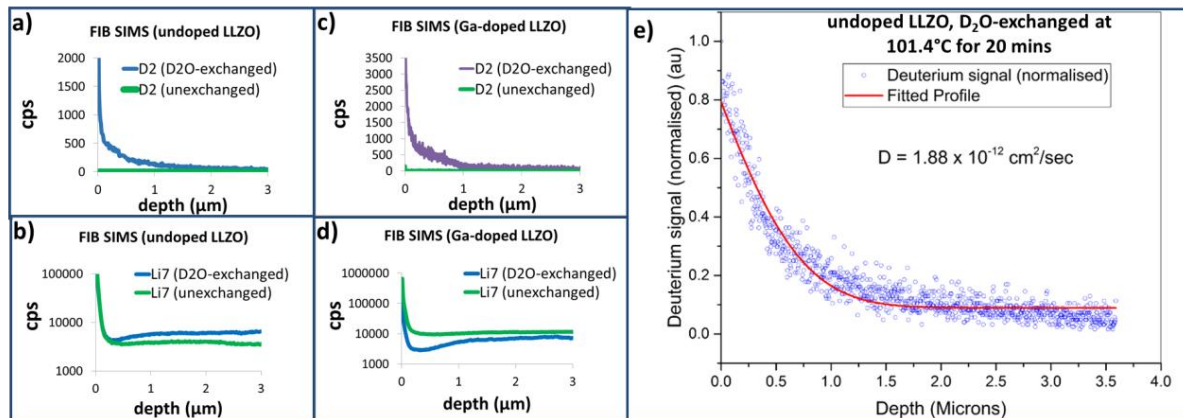


Figure 5.8: Depth profiles of selected isotopes obtained from focused-ion beam secondary ion mass spectrometry: a) deuterium profiles of the experimental vs control sample for nominally “undoped” LLZO (Li₇La₃Zr₂O₁₂) composition; b) corresponding Li7 profiles for the samples in a; c) deuterium profiles of the experimental vs control sample for Ga-doped LLZO (Li_{6.55}Ga_{0.15}La₃Zr₂O₁₂); d) corresponding Li7 profiles for the samples in c. A linear relationship between sputter-depth and sputter-time was assumed. e) fitting of the diffusion profile in a to an appropriate solution to the diffusion equation.

The finding that the proton penetration (or more precisely, deuterium) was limited to a couple of microns under relatively extreme conditions (boiling in liquid D₂O, compared to atmospheric contact at room-temperature) enables a return to reinterpret results in section 5.1.1, wherein EIS measurements were done on a pellet before and after boiling H₂O treatment.

Armed with a known thickness (~2 μm) of the “protonated” garnet zone, a direct determination of its lattice ion diffusivity (consisting only of lithium mobility) using EIS could be demonstrated for the very first time. The bulk resistance component in Figure 5.3 is the sum of the contributions of the “protonated” garnet zone and the “dry” garnet core. This meant that the resistance increase in this component, comparing before and after H₂O treatment, corresponds to the resistance contribution of the “protonated” garnet zone. This value was about 770 Ω before dimensional normalization. After normalization, this translated to about 10⁻⁷ Ωcm or 0.0001 mS/cm, about four orders of magnitude lower than the ionic conductivity of the garnet material. **This finding has profound implications for thin film battery applications, underscoring the importance of stringent dryness and atmosphere control during processing and assembly.**

Corollary, this explains why many reports in the literature show high bulk ionic conductivities despite atmospheric storage, because the “protonated” garnet resistance contribution (few microns) is drowned out during dimensional normalization of millimeter-scale test pellets [26]. On the other hand, because the interfacial resistance component is dependent only on the contact area of the “protonated” garnet zone, its significant effects are readily observable.

5.2 Effects of crucible choice/sintering protocol

The previous section dealt with one of the two main contaminants in LLZO garnets: atmospheric effects. This section focuses on the other: **adventitious aluminum**

To begin, the evolution of synthesized powders at each stage was monitored. The three important steps are combustion, calcination and sintering.

Combusted material (Figure 5.9) showed grain sizes of less than 5 μm, and good dispersion of constituent elements for the Ga-doped LLZO material according to EDAX mapping. Residual carbon was detected after a 600°C firing in ambient air, suggesting some organic material remained.

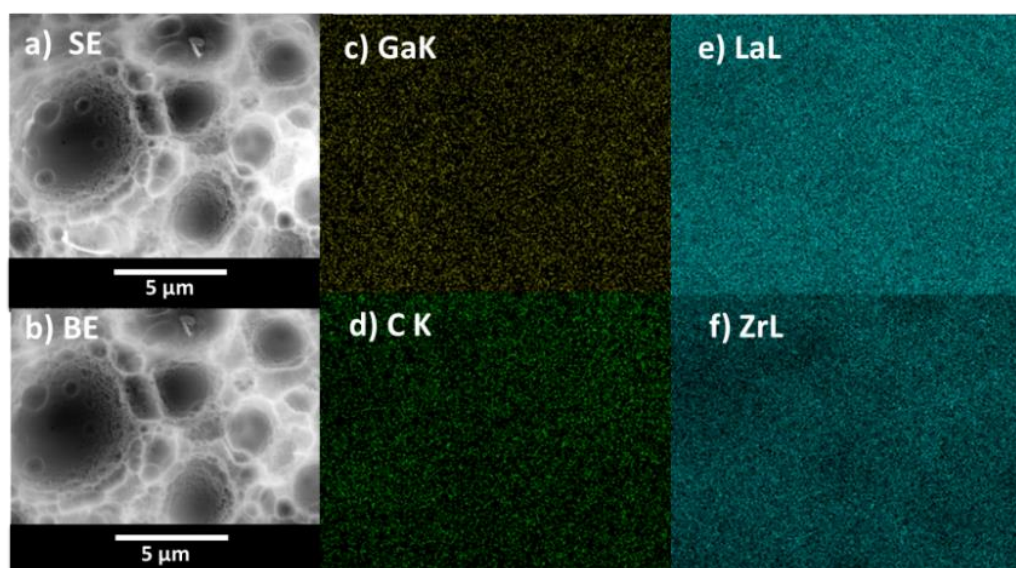


Figure 5.9: Citrate-route material after preliminary calcination at 600°C (12h) in a porcelain (mullite) evaporating dish and a box-type muffle furnace: a) secondary electron image, b) backscattered electron image, and EDAX maps of stated xray lines: c) Ga K, d) C K, e) La L and f) Zr L. An electron accelerating voltage of 12kV was used for all images. The images correspond to material with starting stoichiometry for $\text{Li}_{6.55}\text{Ga}_{0.15}\text{La}_3\text{Zr}_2\text{O}_{12}$.

The calcination step at 800°C (12h in dry O₂) is crucial to remove these remnant organics. Calcined powder retained ~5-μm grain sizes (Figure 5.10-c,d,g,h compared with Figure 5.10 -a,b). Combusted and calcined powders showed consistency between multiple synthesis runs.

The sintering step at 1085°C (6h in dry O₂) produced inconsistent results in moving from a large furnace (1m tube) to a smaller (~500 cm tube) furnace, probably due to inhomogeneity of the “hot zone” mentioned in Section 2.1.2. Sintering at 1200°C (6h in dry O₂) produced more repeatable results in both furnace tubes. Sintering cold-pressed pellets over Al₂O₃ crucibles showed abrupt grain growth to the scale of 50-500 μm (Figure 5.10 e,f).

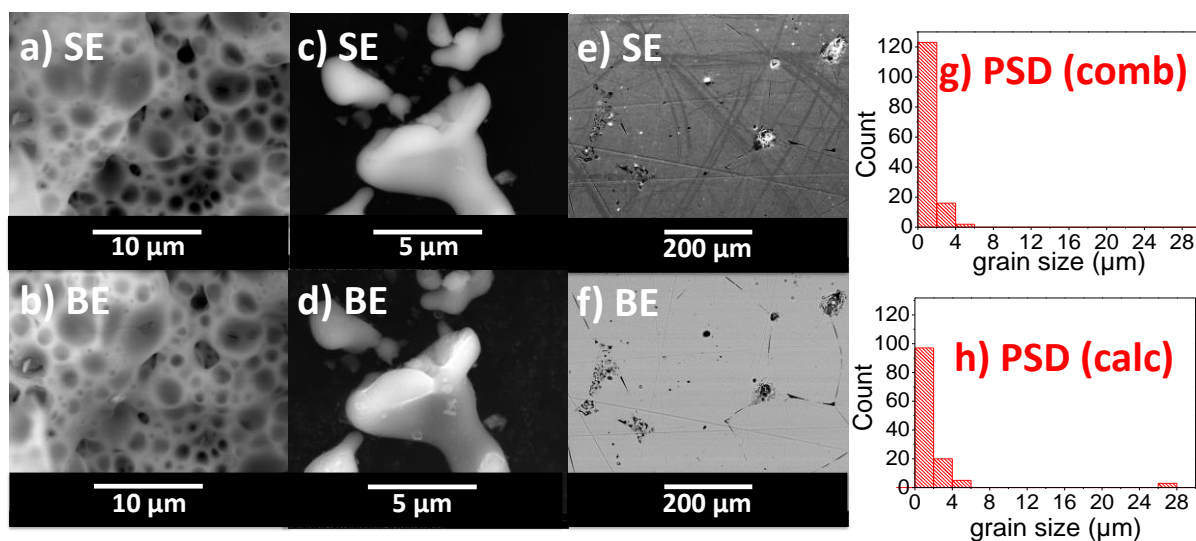


Figure 5.10: Evolution from combusted material (a,b), to calcined material (c,d), to sintered material (e,f). SE - secondary electrons; BE - backscattered electrons. Combusted material corresponds to the same material in Figure 5.9. An electron accelerating voltage of 30kV was used for all images. The images correspond to material with starting stoichiometry for $\text{Li}_{6.55}\text{Ga}_{0.15}\text{La}_3\text{Zr}_2\text{O}_{12}$. The histograms for particle size distribution are illustrated: g) combusted material and h) calcined material.

A visual inspection of crucible contents freshly pulled-out of the sintering furnace revealed unexpected changes.

Using alumina crucibles, a color change on the mother powder cushioning the test pellet against the crucible was observed. This seems to have extended from the bottom up, as the mother powder on top of the pellet remained white. (Figure 5.11 a,b). This is indicative of the $\text{Li}_2\text{O}-\text{Al}_2\text{O}_3$ melt interaction earlier mentioned in Figure 1.16. The pellets sintered using a ZrO_2 base did not exhibit this discoloration, and remained white (Figure 5.11 c,d).

With regards to crucibles after sintering, whereas the Al_2O_3 crucible remained intact, the ZrO_2 crucible showed visible cracks. To explain this crack, an argument based on crystallographic shear due simply to volume mismatch brought by lithium insertion is invalid, as both alumina and zirconia have lithium-containing species that produce 441% and 386% normalized volume expansion compared to the binary oxide forms (Li_5AlO_4 vs Al_2O_3 and Li_8ZrO_6 vs ZrO_2 , respectively). What is more likely, was that LLZO pulled out the critical sintering aids from the ZrO_2 crucible (e.g. Y^{3+} , present in ~1% quantity), destabilizing the sintered form of the crucible.

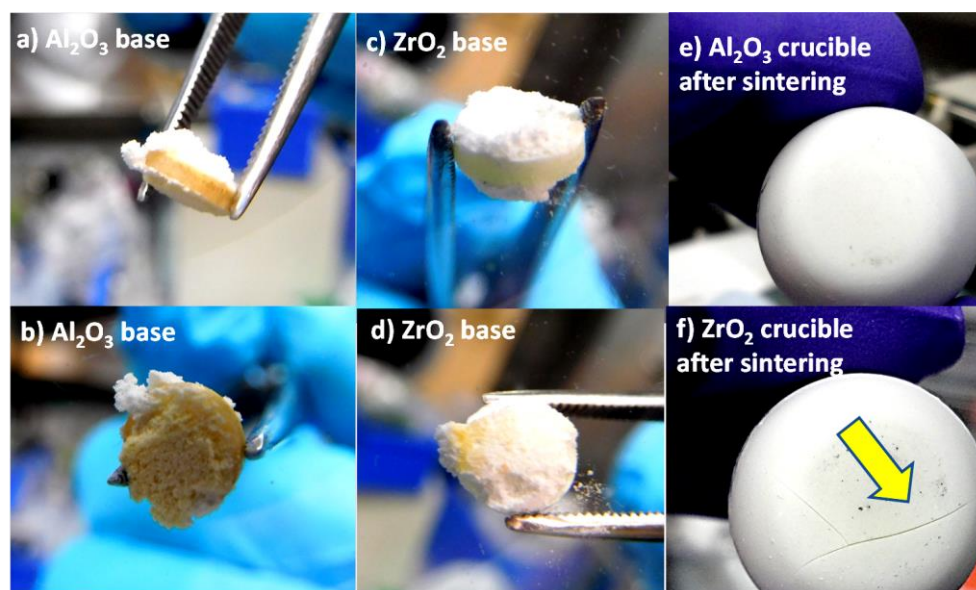


Figure 5.11: Pellets sintered using an Al₂O₃ crucible (a,b) and those using a ZrO₂ crucible (c,d) and the respective crucible supports (e,f) after firing pellets. The sintering protocol was 1200°C 6h under O₂ flow in both cases. A crack (yellow arrow) is seen in f, a consistently observed phenomenon for ZrO₂ crucibles.

A closer inspection by electron microscopy of the discolored mother powder in the Al₂O₃ crucible is demonstrated in Figure 5.12 a,b. A transformation front can be discerned as having propagated from the direction of the crucible surface to the test pellet. This front left behind its wake a clear distinction in the form of larger LLZO particles, with a light-element secondary phase connecting the aggregated grains (Figure 5.12c).

EDAX shows two notable points:

(a) Discounting the expected high mass percentages of lithium and oxygen elements, the secondary phase consisted mainly of gallium (15%) and aluminum (85%), as indicated by Figure 5.12d. This suggests Ga had been dissolved in a diffusing Al-rich melt, and to a high extent due to the exposed surface area of the fine LLZO powder.

(b) The La:Zr ratio in the affected LLZO grains (Figure 5.12e) was between 3.00:1.00 to 3.00:1.30, suggesting that Al-interaction also locally displaces Zr. The Al content from the melt was not readily absorbed into garnet grains (0.02 to 0.08 Al p.f.u.) and persisted along “grain boundaries”. This suggests that aluminates require longer treatments times (currently 6h at 1200°C) to completely diffuse within the LLZO structure.

Taken together, these micrographs constitute the first ever direct observation of the lithia-alumina melt acting as a sintering aid for LLZO garnets.

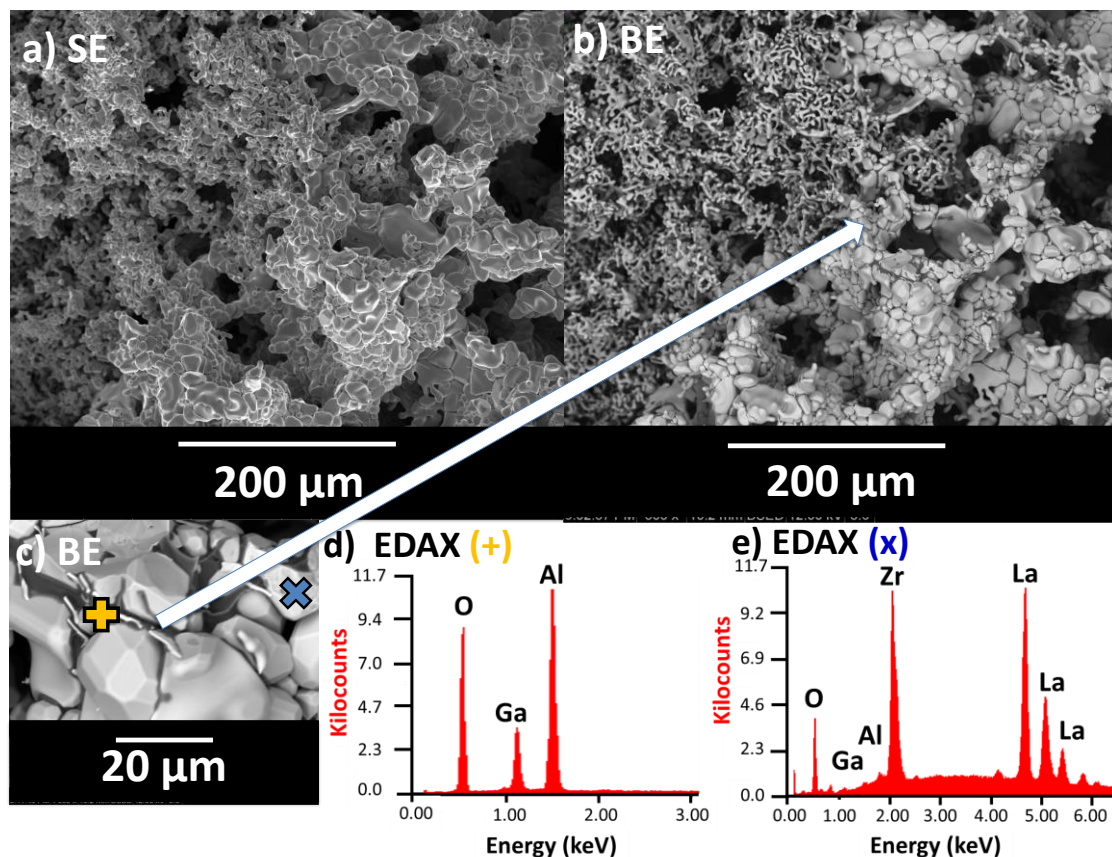


Figure 5.12: (a) low magnification SE image of the mother powder of a Li_{6.55}Ga_{0.15}La₃Zr₂O₁₂ pellet after sintering at 1200°C for 6h under O₂ flow, and using an alumina crucible; (b) BE image of *a*; (c) high magnification BE image of *b* showing region pointed by white arrow; (d) and (e) EDAX point scans (12kV) for the regions marked in a yellow cross (darker shade, lighter elements along grain boundaries in *c*) and blue cross (lighter shade, heavier elements in a single ceramic grain in *c*).

To better observe microstructural effects and the crystal chemistry changes brought with an advancing Al-rich melt, the following experiment was devised. A ceramic pellet was sintered using a ZrO₂ crucible, but thermally etched on top of an Al₂O₃ crucible while standing on its pellet edge. This made sure Al levels in the pellet were negligible prior to Al exposure. The exposure treatment was a 5°C/min heating to 1000°C with a 20 min dwell, followed by rapid quenching. A dry inert Ar atmosphere was maintained at all times. The resulting micrographs are illustrated in Figure 5.13.

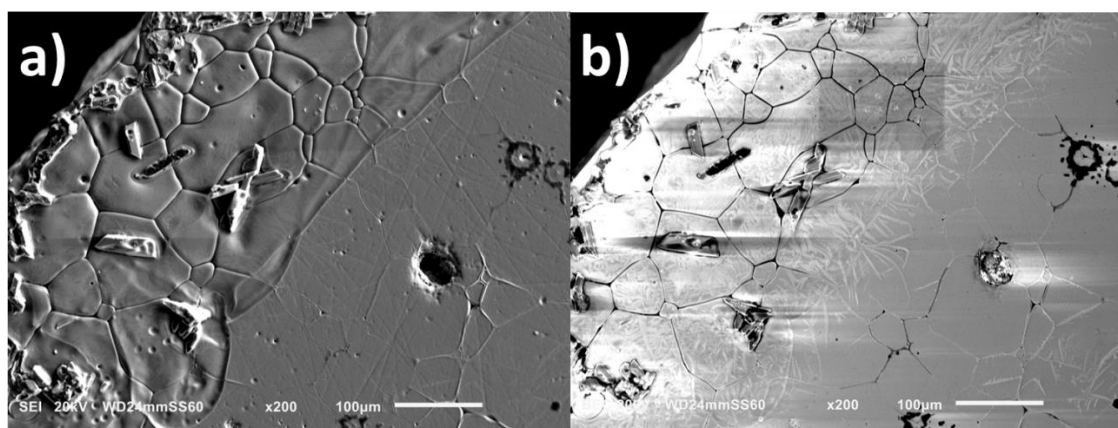


Figure 5.13: Electron microscopy images of thermally-etched samples of Li_{6.55}Ga_{0.15}La₃Zr₂O₁₂. Pellets were produced using zirconia crucibles, but etched using an alumina base support while the pellet was standing on its edge. A heating dwell at 1000°C for 20 mins was applied, using slow heating (5°C/min) and rapid cooling (quenching). (a) SE image (20kV) and (b) BE image (20kV).

A melt front emanating from the contact region between the sample and the Al₂O₃ crucible, is highlighted by a secondary electron image (Figure 5.13a). As the melt advanced (from the lefthand side), it etched grain boundaries and produced precipitates with apparently crystalline motifs. On the righthand side, an inner region adjacent to a pore had started to be etched as well, suggesting liquid capillary action of the liquid melt.

The backscattered electron image (Figure 5.13b) shows the precipitates consisted mostly of heavy elements, whereas the reacted grain boundaries had light elements. Precipitate formation occurred near grain boundaries. Dendritic patterns containing heavy elements also appeared, suggesting La- or Zr-enrichment of the melt as it progressed. It seems the melt underwent a rapid change in surface tension during quenching, forming dendritic patterns reminiscent of non-equilibrium cooling of metal alloys.

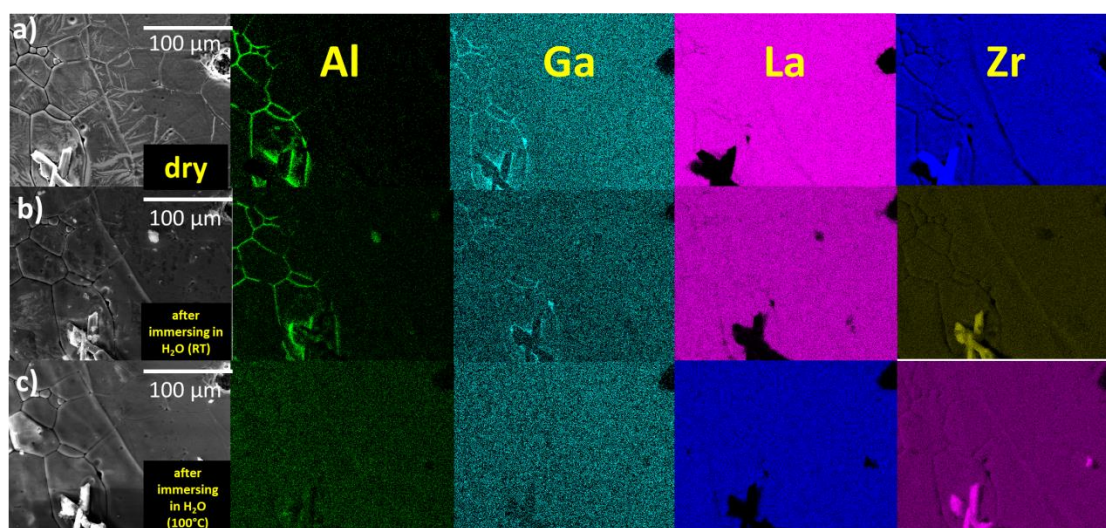


Figure 5.14: Backscattered electron images along with EDAX elemental maps (Al, Ga, La, Zr) of the sample shown in Figure 5.13. EDAX cannot detect lithium. Row (a) corresponds to the said as-quenched sample prior to further treatment. Row (b) is the sample after immersing in liquid H₂O (ambient temperature) for 4 hours followed by overnight vacuum drying. Row (c) is the sample after immersing in liquid H₂O (boiling) for 4 hours followed by overnight vacuum drying.

EDAX mapping and chemical treatments led to the identification of material compositions. Elemental mapping was monitored at 3 stages: (a) the as-quenched “dry” sample; (b) a mild treatment with liquid H₂O at room-temperature, i.e. a 4h immersion followed by overnight vacuum drying; (c) a harsh treatment with liquid H₂O at boiling temperature (100°C), i.e. again with the same immersion and drying protocol.

The “dry” sample (Figure 5.14a) indicated the presence of mostly Al and Ga along the grain boundaries, and Zr in the precipitate. The mild H₂O treatment suggests that the quench-induced melt dendrites were ternary oxides rich in Li, as they were readily water-soluble, e.g. lithium lanthalates or lithium zirconates. The harsh H₂O treatment confirms that the **precipitates were made of zirconia** and the etched grain edges were composed of **lithium aluminates and lithium gallates**.

The precipitation of zirconia as a consequence of aluminum rich melt contact with the garnet material indicated stoichiometric **Al-Zr exchange**. The way the dendrites formed from the melt with quenching, suggested that somehow the **resultant microstructure was sensitive to the cooling rate**. Paying attention to these factors, further scrutiny of the pellets sintered using the two different crucible materials (Al₂O₃ and ZrO₂) can now be presented.

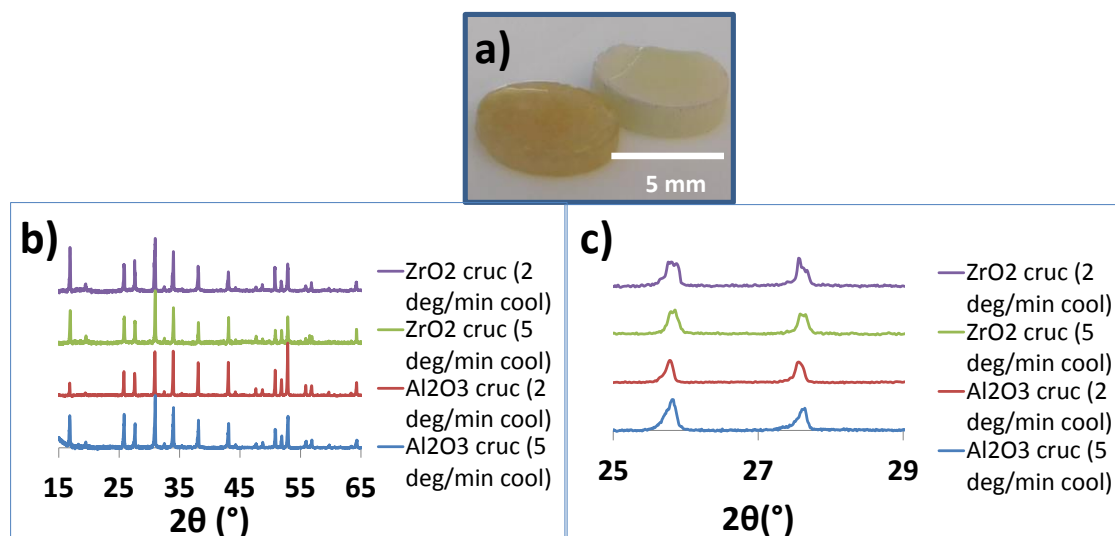


Figure 5.15: Photograph of juxtaposition of Li_{6.55}Ga_{0.15}La₃Zr₂O₁₂ pellets sintered in an Al₂O₃ crucible (left) and in a ZrO₂ crucible (right); XRD patterns ($\lambda = \text{Cu}\alpha_1$) for pulverized pellets sintered with varied crucibles (Al₂O₃ and ZrO₂) and varied cooling rates (5°C/min vs 2°C/min), showing 2 θ regions between b) 15°-65° and c) 25°-30°.

Light reflected from the polished surface of both pellets indicated relatively high densities (Figure 5.14a). Notably, this only occurred for Ga-doped LLZO. Stoichiometric Li₇La₃Zr₂O₁₂ sintered in a ZrO₂ crucible was friable, i.e. it disintegrated into powder readily. This is a positive indication of gallium-aided sintering action. Again as shown in Figure 5.11, strong discoloration was evident in the sample sintered with an Al₂O₃ crucible support. Its counterpart for the ZrO₂ crucible retained a white color. The densities were 95-96% for former and 87-88% for the latter, irrespective of cooling rate.

Sintered Li_{6.55}Ga_{0.15}La₃Zr₂O₁₂ material showed mainly XRD peaks (between 2 θ = 15° to 80°) conforming to a cubic garnet symmetry ($1a\bar{3}d$), regardless of crucible material or cooling rate (Figure 5.14b). Scrutiny revealed a slight tetragonal distortion as evidenced by peak splits in the PXRD patterns for materials sintered in ZrO₂ crucibles however (Figure 5.17c). For samples fired in Al₂O₃ crucibles, the edge lengths of unit cells varied within 1% comparing the two cooling rates.

Microstructural analysis confirmed a fundamental difference in samples when using different crucibles, again irrespective of cooling rates (Figure 5.16 a,b and Figure 5.16 e,f). In particular, pellets were composed of large grains (hundreds of μm across) when using an Al₂O₃ crucible as revealed by thermal etching (Figure 5.16 c,d), whereas uniform nanograins (<1 μm) made up pellets sintered with a ZrO₂ crucible (Figure 5.16

g,h). This size reduction is noteworthy given that the initial grain size (for combusted powder) was about 5 μ m, possibly hinting a recrystallization process. Unfortunately, all samples involved in Figure 5.16 produced short-circuits within a few minutes using a symmetrical Li electrode/Li electrode configuration with a linear step voltammetry to 500mV.

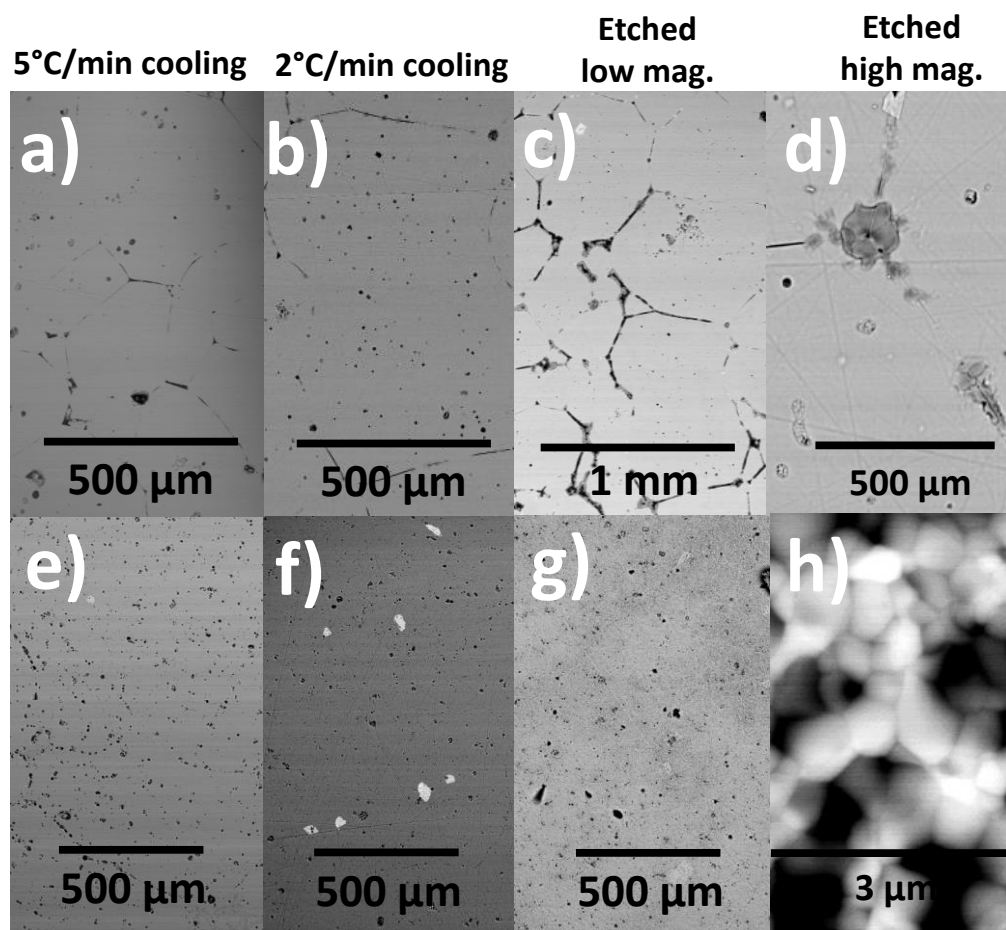


Figure 5.16: Microstructural analysis: BE imaging of Li_{6.55}Ga_{0.15}La₃Zr₂O₁₂ pellets sintered at 1200°C for 6h under O₂ flow with the following varied parameters: a) Al₂O₃ crucible, 5°C/min cooling; b) Al₂O₃ crucible, 2°C/min cooling; c) thermally-etched sample in *b* (low magnification); d) thermally-etched sample in *b* (high magnification); e-f) respective counterparts for a-d, but using ZrO₂ crucibles. The thermal etching program was a 5°C/min heating to 1000°C with a 20 min dwell, followed by rapid quenching; all under dry Ar atmosphere.

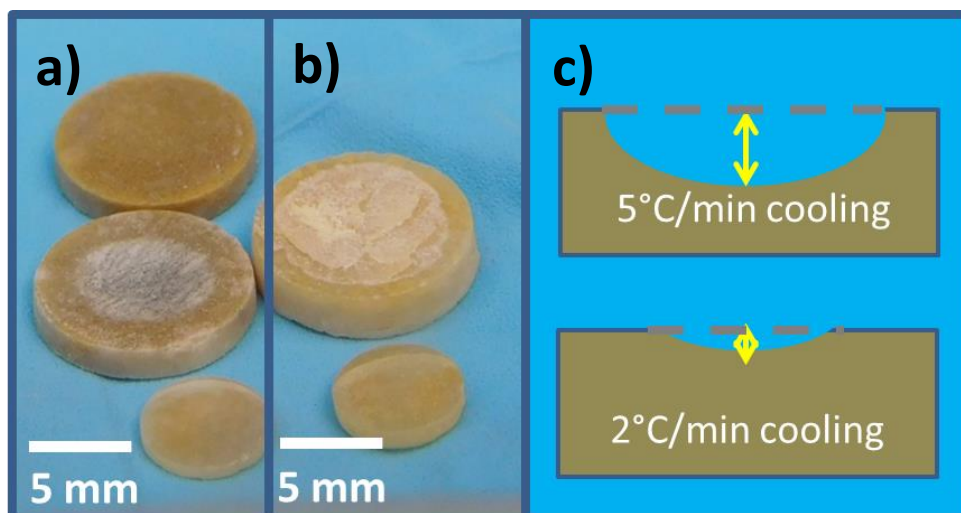


Figure 5.17: Macrostructural analysis: Photographs of Li_{6.55}Ga_{0.15}La₃Zr₂O₁₂ pellets sintered over an Al₂O₃ crucible at a cooling rate of a) 2°C/min and b) 5°C/min; c) cross-section schematic highlighting the effect on the shape of the resulting pellet after similar sintering dwells, but cooling at different rates.

Macrostructural effects are evident with a faster or slower cooling rate for large pellets (10mm-diameter); This was not seen for small pellets (5mm-diameter). This is shown in Figure 5.17 (a,b) wherein a “crater” consisting of poorly-sintered powder on top of a well-sintered pellet body remained after firing. The thin non-uniform layer is easily polished off for the slowly-cooled pellet (2°C/min, Figure 5.17a top), but not for the fast-cooled pellet (5°C/min, Figure 5.17b). This effect of cooling rate is schematized in Figure 5.17c, highlighting the height difference of the craters.

Lattice expansion/contraction in solid-state sintering is insufficient to explain this phenomenon. Going back to the lattice thermal expansion coefficient in Figure 4.9, extrapolation leads to a volume change of only 5% even under extreme quenching conditions. Considering that the crater begins close to the edges of the fast-cooled pellet (5°C/min), the height variation caused by the crater should be barely discernible to the naked eye, considering a ~2-mm thick pellet of 10mm diameter.

What is more likely is that liquid phase sintering induced by a Li₂O-Al₂O₃ liquid is playing a significant role. In particular, between 800°C and 1200°C, the slower cooling rate (2°C/min vs 5°C/min) adds an additional 2h time for the associated melts to rearrange particles, carry more Al or equilibrate compositions. This angle will be explored more in a while with a series of samples with varied sintering dwells.

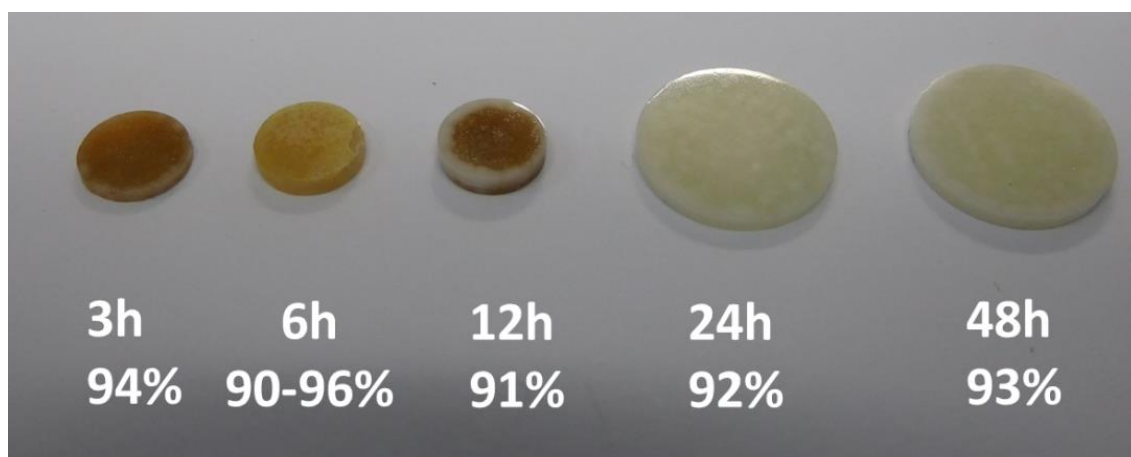


Figure 5.18: Photograph of Li_{6.55}Ga_{0.15}La₃Zr₂O₁₂ pellets sintered at 1200°C under O₂ flow, at 2°C/min cooling, with varied dwell times and relative densities as indicated within the figure.

The pellet series hinted that there are structural changes with increasing dwell times at the sintering temperature, as shown by the obvious contrast of pellet colors in Figure 5.18. In fact, the sample at 12h calls for special attention due to a mixture of brown and white colors. Judging by the color trend, one may presume that this sample is in an intermediary state for the composition across the pellet to reach equilibrium. This implies that shorter sintering times are only producing metastable phases, i.e. a thermodynamically unequilibrated cation distribution.

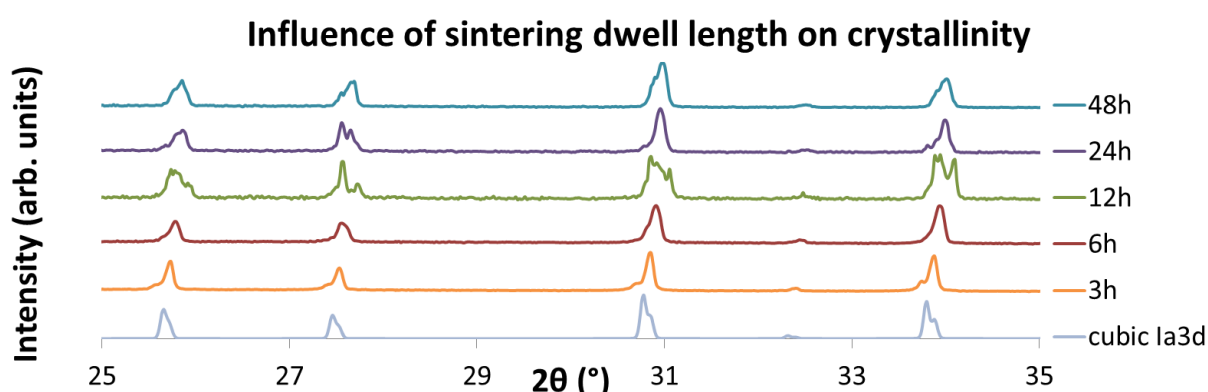


Figure 5.19: XRD patterns ($\lambda = \text{Cu}_{\alpha 1}$) for sintered Li_{6.55}Ga_{0.15}La₃Zr₂O₁₂ pellets at 1200°C under O₂ flow, at 2°C/min cooling, with varied dwell times (3h, 6h, 12h, 24h and 48h), along with a simulated XRD pattern ($\lambda_1 = \text{Cu}_{\alpha 1}$; $\lambda_2 = \text{Cu}_{\alpha 2}$) from Awaka's single crystal analysis (ICSD # 422259).

This makes sense in the light that there is progressive Al diffusion from the crucible. Scrutiny of the XRD patterns of pulverized pellets was consistent with this trend, as can be pointed out in Figure 5.19. The 3h-sample had a minor shoulder for each characteristic reflection. This grew in the 6h-sample, significantly manifested itself in the 12h sample, then receded in the 24h- and 48h-samples.

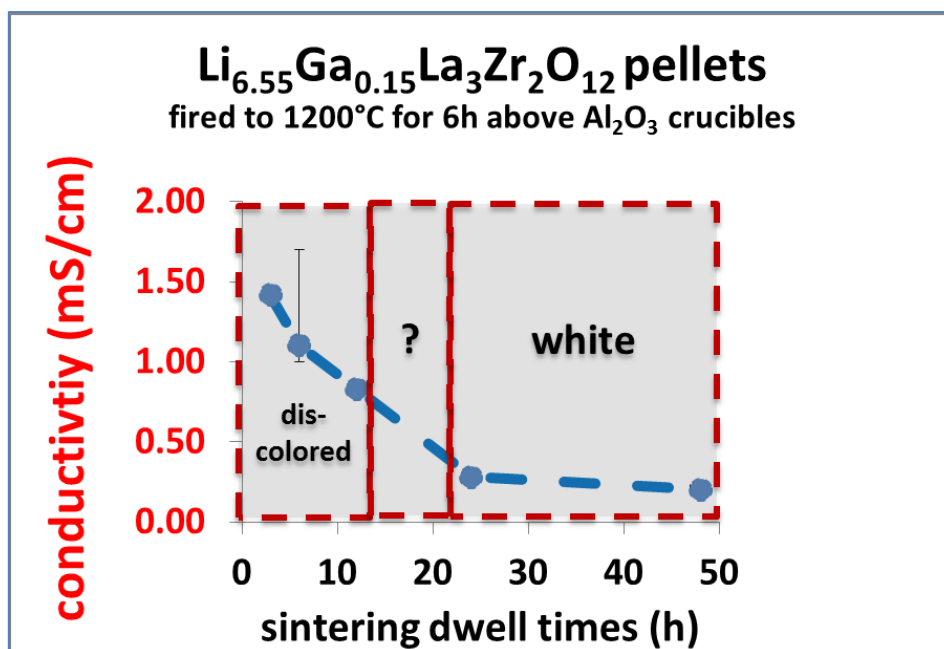


Figure 5.20: Lattice (or bulk) ionic conductivity trends for pellets described in Figure 5.18 and Figure 5.19. Error bars are masked by conductivity markers. A “?” is placed between 12h and 24h as samples between these dwell times were not investigated.

This should have effects on lattice ionic conductivities, and indeed it did. The respective bulk ionic conductivities are plotted in Figure 5.20. Lattice conductivities steadily decreased with longer sinter times, indicative of Al entry into the garnet lattice and replacement of lithium ion carriers. The conductivity drop was within an order of magnitude. Interestingly, the trend plateaus at 0.2 mS/cm for longer sinter durations, consistent with literature values for Al-doped LLZO [27]. This can mean either of three things: a) the garnet lattice had reached its solubility level for Al incorporation or b) Al was substituting both on Li and Zr sites, thus maintaining a stable amount of lithium carriers, or c) Al was accumulating along grain boundaries and needed more time to diffuse into the lattice, meanwhile becoming more significant in terms of mass fractions relative to the main phase, increasing overall bulk-transfer resistances.

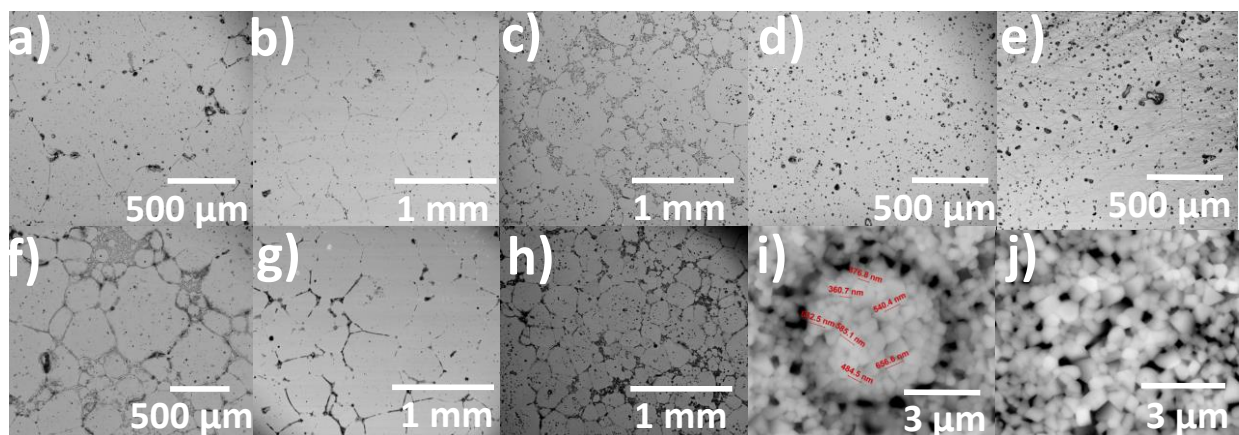


Figure 5.21: Backscattered electron images (30kV) of sintered Li_{6.55}Ga_{0.15}La₃Zr₂O₁₂ pellets sintered at 1200°C under a pure O₂ atmosphere, for varied sintering dwell times: a) 3h, b) 6h, c) 12h, d) 24h and e) 48h. The thermally-etched counterparts are shown in f-j, respectively.

The thermal etching program was a 5°C/min heating to 1000°C with a 20 min dwell, followed by rapid quenching; all under dry Ar atmosphere.

A microstructural examination provides some clues. Figure 5.21 shows the micrographs of as-polished samples (a-e) sintered for 3h, 6h, 12h, 24h and 48h and their thermally-etched counterparts (f-j). The reader's attention is pointed to the scale bars (μm to mm) to provide a quick grasp how grains grew and diminished in size again. For a statistical view, a grain-size distribution histogram is provided in Figure 5.22, for which manual-counting was employed as Voronoi-type and watershed automated processing implemented in the ImageJ analysis software treated the small grains as noise.

Interpreting Figure 5.21 : At 3h-sintering, several nucleation sites had sporadically initiated grain growth and progressed midway; At 6h-sintering, grain growth had achieved a maximum; at 12h-sintering, excess aluminum had begun triggering local crystallographic shear due to excessive dislocation densities brought about by the dopants, breaking grains; At 24h-sintering, this had progressed to recrystallization of the erstwhile metastable grains; At 48h-sintering, this had relatively stabilized due to depletion of excess lithium (presumably evaporated or transported away by the Al₂O₃ crucible).

The phenomenon of recrystallization is recurrent in liquid-phase sintering and is well-studied. For further details, see Palmour [28] and Burke [29].

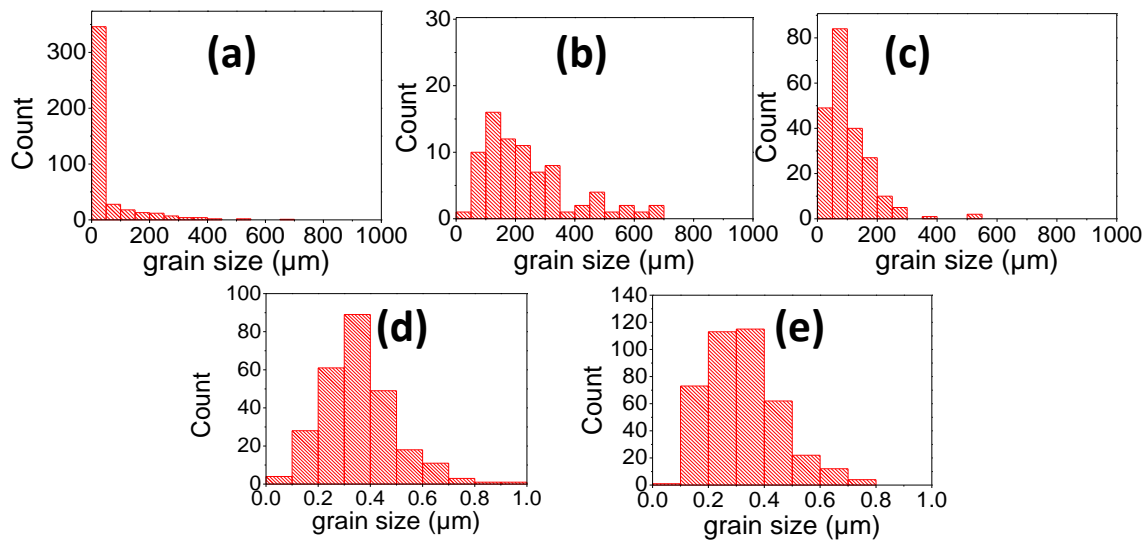


Figure 5.22: Grain size distribution histograms of manually-counted grains per etched sample in Figure 5.21: a) 3h-sintered, b) 6h-sintered, c) 12h-sintered, d) 24h-sintered and e) 48h-sintered. The ASTM grain sizes are not quoted due to the wide grain size distribution (ranging from a few microns to hundreds of microns).

To support this, the extent of Al-penetration as a function of sintering time can be probed by SEM-EDAX. The edges where grains meet form crevices where the melt diffusion can seep through while at the eutectic temperature. Abrading the top surface (opposite of crucible base) to a smooth polish, followed by thermal etching, forces the melt out and reveals clues about its cationic composition. This is shown in Figure 5.23, Figure 5.24 and Table 5.3.

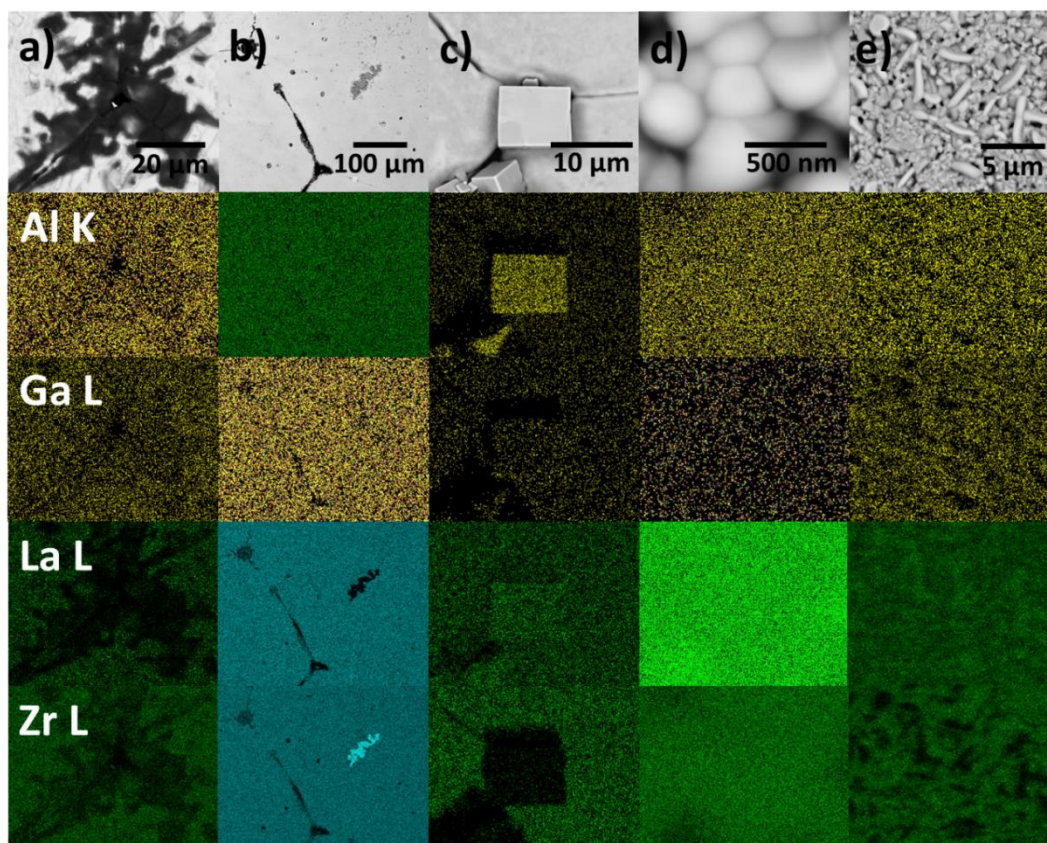


Figure 5.23: Backscattered electron images of thermally-etched samples, which were previously sintered at 1200°C under dry O₂ atmosphere using Al₂O₃ crucibles for a) 3h, b) 6h, c) 12h, d) 24h and e) 48h. Columns correspond to EDAX maps for each sample. Rows correspond to x-ray maps according to energies corresponding to Al K, Ga L, La L and Zr L lines. The images were taken at the pellet surface most distant from the Al₂O₃ crucible during sintering.

At 3h sintering, only a small amount of aluminum had penetrated from the bottom to the top of the pellet. At 6h sintering, this had progressed measurably (Table 5.3), with twice the Al concentration in the melt. The Al-Zr exchange (Figure 5.14) was observed with the appearance of a ZrO₂ secondary phase in Figure 5.23b. At 12h sintering, the melt had reached a maximum Al content, forming what appears to be LaAlO₃, indicated by the approximately 1:1 ratio of La vs Al. Adding to this, the cubic symmetry of LaAlO₃ seems to have manifested in the formed crystal habit (Figure 5.23c). This implies as the Al-rich melt was moving between the grains along the interconnected porosity, it selectively absorbed lanthanum triggering an elemental redistribution. This produced defects in the lanthanum site of LLZO, which progressed to crystallographic shear, and thus triggered a recrystallization phenomenon. That

zirconia was precipitating out was a consequence of this phenomenon. This explains why some groups have reported vacancy defects on the La-site in the garnets [30].

This elemental disproportionation is a transient phenomenon. At 24h and 48h, the aluminum contents within the melt had decreased, suggesting both starvation of supply from the crucible source (due to a depletion of the melt as Li evaporates) and Al absorption into garnet grains.

Table 5.3: Elemental analyses of melt composition transported from the crucible to the top surface of the pellet. Values correspond to the tripartite boundary of grains from thermally-etched ceramics as shown in Figure 5.23.

sintering dwell	EDAX count ratios normalized p.f.u. (using La as basis)				
	3h	6h	12h	24h	48h
La L	3.00	3.00	3.00	3.00	3.00
Zr L	2.2 (± 0.4)	2.8 (± 0.7)	0.03 (± 0.02)	2.37 (± 0.07)	2.2 (± 0.2)
Al K	0.11 (± 0.02)	0.22 (± 0.11)	2.5 (± 0.3)	0.09 (± 0.05)	0.04 (± 0.00)
Ga L	0.19 (± 0.05)	1 (± 1)	0.14 (± 0.04)	0.04 (± 0.01)	0.06 (± 0.01)

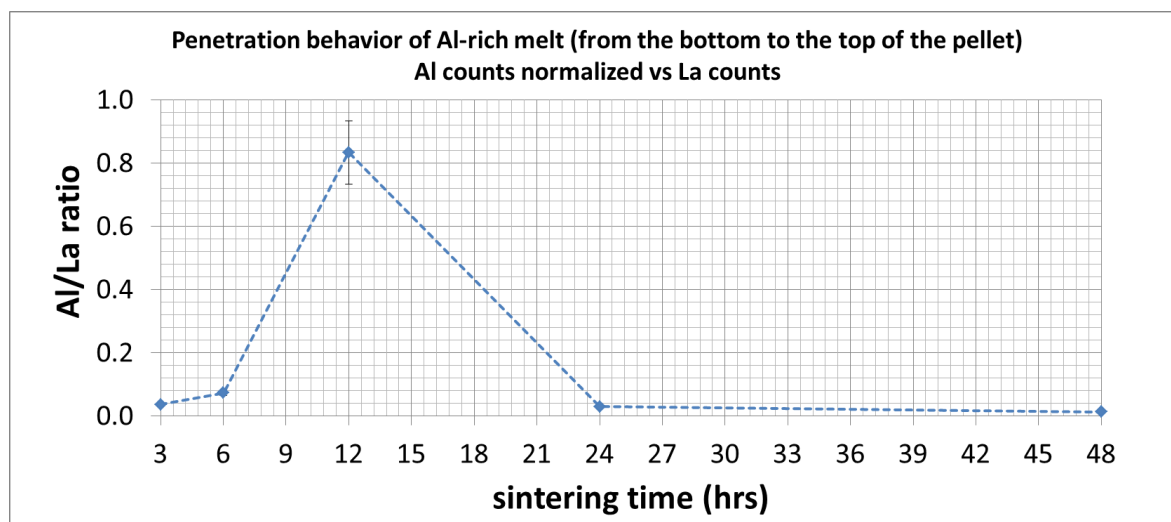


Figure 5.24: Point-EDAX scans (12kV) taken at the tripartite boundary of grains from thermally-etched ceramics as shown in Figure 5.23. Values correspond to Al K counts normalized to La L counts.

5.3 Chapter summary and perspectives

1) Ga-doped LLZO garnets are highly sensitive to atmospheric moisture degradation. This is true whether during firing or during storage (sections 4.3.2 and 5.1).

In particular, moisture is identified as a critical contaminant, which catalyzes a corrosion depth of less than 5 μm per grain as determined by FIBSIMS (section 0). The corrosion thickness has been measured precisely for the first time (cf. LIBS experiments by Cheng *et al.* [31]).

The corrosion product is mostly an amorphous LiOH film with a protonated garnet interface, followed by a dry garnet core. The corrosion surface is predicted to be kinetically self-passivating at room-temperature. This is demonstrated by similar penetration depths, at extreme conditions, of deuterium in a LLZO-garnet with much lower lithium conductivity and the Ga-doped LLZO sample exhibiting high lithium conductivity. Notwithstanding, powdered samples corrode extensively, rendering most of the mobile lithium atoms locked in an immobilized form (section 5.1.1.2)

This has profound consequences for the industrial scale-up of this material. One, thin garnet films (50nm to 10μm) risk complete degradation with atmospheric contact. Reversing this is problematic with thermal annealing due to atomic diffusion from the substrate, defect formation and crystal structure degradation [32]. A possible solution is localized laser-based annealing, which has shown success yielding garnet phases [33].

Two, thick garnet sheets (10μm – 1mm), once sintered, do not need to be constantly stored in ultradry conditions, which represent significant pumping costs (in terms of vacuum environments) or space costs (in terms of dry-room facilities) or intermediate packaging costs (in terms of hermetic sealing). The relatively shallow depth of corrosion implies laser ablation techniques can be incorporated in the assembly line to create a non-contaminated surface in-situ. As of the manuscript date, handheld laser optics are already available for instantly removing rust layers or paints on metal alloy surfaces. Pulsed laser techniques represent precise polishing of ceramic surfaces facilitating better contact with anodes/cathodes. Further, they effectively run the material through multiple quenching cycles which may be expected to improve retention of high-temperature cubic symmetries.

Of course however, laser-based experiments are beyond the scope of this thesis, and are reserved for another PhD project.

2) The diffusion of an Al-rich melt was observed in LLZO garnets both in powder form and pellet forms (section 5.2). With melt contact, grain growth and densification was observed for powders. Whereas for pellets, a Al-Zr substitution was observed, resulting in ZrO₂ crystal precipitation.

The Li₂O-Al₂O₃ melt catalyzed rapid grain growth by a mechanism of liquid phase sintering. The maximum grain sizes were achieved at 6h sintering, followed by recrystallization to submicron grains. Notably, this recrystallization to submicron grains at long sintering times is has not been observed for LLZO garnets with only Al-dopants [34, 35]. This suggests that gallium may facilitate in-situ recrystallization.

REFERENCES:

- [1] Buschmann, H., Doelle, J., Berendts, S., Kuhn, A., Bottke, P., Wilkening, M., Heitjans, P., Senyshyn, A., Ehrenberg, H., Lotnyk, A., Duppel, V., Kienle, L. and Janek, J. *Physical Chemistry Chemical Physics* **13**(43), 19378–19392 (2011).
- [2] Larraz, G., Orera, A., Sanz, J., Sobrados, I., Diez-Gomez, V. and Sanjuan, M. L. *Journal of Materials Chemistry A* **3**(10), 5683–5691 (2015).
- [3] Ong, S. P., Chevrier, V. L., Hautier, G., Jain, A., Moore, C., Kim, S., Ma, X. and Ceder, G. *Energy & Environmental Science* **4**(9), 3680–3688 SEP (2011).
- [4] Vosegaard, T., Massiot, D., Gautier, N. and Jakobsen, H. *Inorganic Chemistry* **36**(11), 2446–2450 (1997).
- [5] Massiot, D., Vosegaard, T., Magneron, N., Trumeau, D., Montouillout, V., Berthet, P., Loiseau, T. and Bujoli, B. *Solid State Nuclear Magnetic Resonance* **15**(3), 159–169 (1999).
- [6] Geiger, C. A., Alekseev, E., Lazic, B., Fisch, M., Armbruster, T., Langner, R., Fechtelkord, M., Kim, N., Pettke, T. and Weppner, W. *Inorganic Chemistry* **50**(3), 1089–1097 (2011).
- [7] Ash, J. T. and Grandinetti, P. J. *Magnetic Resonance in Chemistry* **44**(9), 823–831 (2006).
- [8] Dunbar, B. and Sarian, S. *Solid State Communications* **21**(8), 729–731 (1977).
- [9] Fuentes, R., Figueiredo, F., Marques, F. and Franco, J. *Solid State Ionics* **139**(3-4), 309–314 (2001).
- [10] Aguesse, F., Lopez del Amo, J. M., Roddatis, V., Aguadero, A. and Kilner, J. A. *Advanced Materials Interfaces* **1**(7), 1300143 (2014).
- [11] Hu, Y.Y., Liu, Z., Nam, K.W., Borkiewicz, O. J., Cheng, J., Hua, X., Dunstan, M. T., Yu, X., Wiaderek, K. M., Du, L.S., Chapman, K. W., Chupas, P. J., Yang, X.-Q. and Grey, C. P. *Nature Materials* **12**(12), 1130–1136 (2013).
- [12] Galven, C., Dittmer, J., Suard, E., Le Berre, F. and Crosnier-Lopez, M.P. *Chemistry of Materials* **24**(17), 3335–3345 (2012).
- [13] Boulant, A., Bardeau, J. F., Jouanneaux, A., Emery, J., Buzare, J.Y. and Bohnke, O. *Dalton Transactions* **39**(16), 3968–3975 (2010).
- [14] Follstaedt, D. and Biefeld, R. *Physical Review B* **18**(11), 5928–5937 (1978).

- [15] Kuhn, A., Narayanan, S., Spencer, L., Goward, G., Thangadurai, V. and Wilkening, M. *Physical Review B* **83**(9), 094302 (2011).
- [16] Kuhn, A., Epp, V., Schmidt, G., Narayanan, S., Thangadurai, V. and Wilkening, M. *Journal of Physics: Condensed Matter* **24**(3), 035901 (2012).
- [17] Kuhn, A., Choi, J.-Y., Robben, L., Tietz, F., Wilkening, M. and Heitjans, P. *Zeitschrift Fur Physikalische Chemie-international Journal of Research In Physical Chemistry & Chemical Physics* **226**(5-6), 525–537 (2012).
- [18] Lopez del Amo, J. M., Langer, U., Torres, V., Buntkowsky, G., Vieth, H.M., Perez-Torralba, M., Sanz, D., Claramunt, R. M., Elguero, J. and Limbach, H.H. *Journal of the American Chemical Society* **130**(27), 8620–8632 (2008).
- [19] Xu, M., Park, M. S., Lee, J. M., Kim, T. Y., Park, Y. S. and Ma, E. *Phys. Rev. B* **85**, 052301 (2012).
- [20] Chater, R., Carter, S., Kilner, J. and Steele, B. *Solid State Ionics* **53**(2), 859–867 (1992).
- [21] Crank, J. *The Mathematics of Diffusion*. Oxford Science Publications (1975).
- [22] Cooper, S., Niania M. and Kilner J.A. TraceX: Isotope Exchange Data Analysis, Back-Diffusion Simulation and Profile Fitting. Poster in *Solid State Ionics Conference, Keystone Colorado*, (2015).
- [23] Chater, R. J., Shollock, B. A., McPhail, D. S., Smith, A. J. and Cooke, G. *Surface and Interface Analysis* **46**(1, SI), 372–374 NOV (2014). 19th International Conference on Secondary Ion Mass Spectrometry (SIMS), Jeju, SOUTH KOREA, SEP 29-OCT 04, 2013.
- [24] Chater, R. J., Smith, A. J. and Cooke, G. *Journal of Vacuum Science and Technology B* **34**(3), 1234 (2016).
- [25] Ma, C., Rangasamy, E., Liang, C., Sakamoto, J., More, K. L. and Chi, M. *Angewandte Chemie-International Edition* **54**(1), 129–133 (2015).
- [26] Thangadurai, V., Narayanan, S. and Pinzaru, D. *Chemical Society Reviews*. **43**, 4714–4727 (2014).
- [27] Rangasamy, E., Wolfenstine, J. and Sakamoto, J. *Solid State Ionics* **206**(0), 28–32 January (2012).
- [28] Palmour III, H., Spriggs, R. M. and Uskokovic, D. *Science of sintering: new directions for materials processing and microstructural control*. Springer Science & Business Media, (2013).
- [29] Burke, J. *Recrystallization and Sintering in Ceramics*, 17–38. Springer Netherlands, Dordrecht (1990).
- [30] Robben, L., Merzlyakova, E., Heitjans, P. and Gesing, T. M. *Acta Crystallographica Section E-Crystallographic Communications* **72**(3), 287+ MAR (2016).
- [31] Cheng, L., Crumlin, E. J., Chen, W., Qiao, R., Hou, H., Lux, S. F., Zorba, V., Russo, R., Kostecki, R., Liu, Z., Persson, K., Yang, W., Cabana, J., Richardson, T., Chen, G. and Doeff, M. *Physical Chemistry Chemical Physics* **16**(34), 18294–18300 (2014).
- [32] Tan, J. and Tiwari, A. *ECS Solid State Letters* **1**(6), Q57–Q60 (2012).
- [33] Teng, S., Tan, J. and Tiwari, A. *Current Opinion in Solid State and Materials Science* **18** (1), 29-38 (2013).
- [34] Xia, W., Xu, B., Duan, H., Guo, Y., Kang, H., Li, H. and Liu, H. *ACS Applied Materials & Interfaces* **8**(8), 5335–5342 (2016).
- [35] Cheng, L., Park, J. S., Hou, H., Zorba, V., Chen, G., Richardson, T., Cabana, J., Russo, R. and Doeff, M. *Journal of Material Chemistry A* **2**(1), 172–181 (2014).

6 Ceramic electrolyte integration in a full-cell device

A ceramic electrolyte with superior ionic conductivity and high density was developed. The next challenge was how to engineer it into a lithium-metal battery system.

6.1 Rationale

A battery cell consists of a negative electrode, an electrolyte and a positive electrode. The two electrodes create a potential difference, powering electrons through an external load to perform useful work.

However, with electron release, cations are generated locally on one electrode. The charge-separation of electrons and cations can create an electrostatic buildup opposing the applied voltage bias. This manifests as an internal resistance consuming part of the energy supplied within the circuit, in other words, a partitioning of voltage drops (Figure 6.1). What this means in practical terms is that during battery discharge, the actual electromotive force available to power the external load is reduced. Conversely, charging of the battery can only be accomplished with an external power supply delivering current at a higher voltage than the nominal Nernst equilibria requirements. This is the “overpotential” effect.

Hence, it is imperative to dissipate this ionic charge buildup. Batteries achieve this via cation migration through an internal electrolyte and recombination with externally-carried electrons upon arriving at the opposite electrode, often containing transition-metal redox centers.

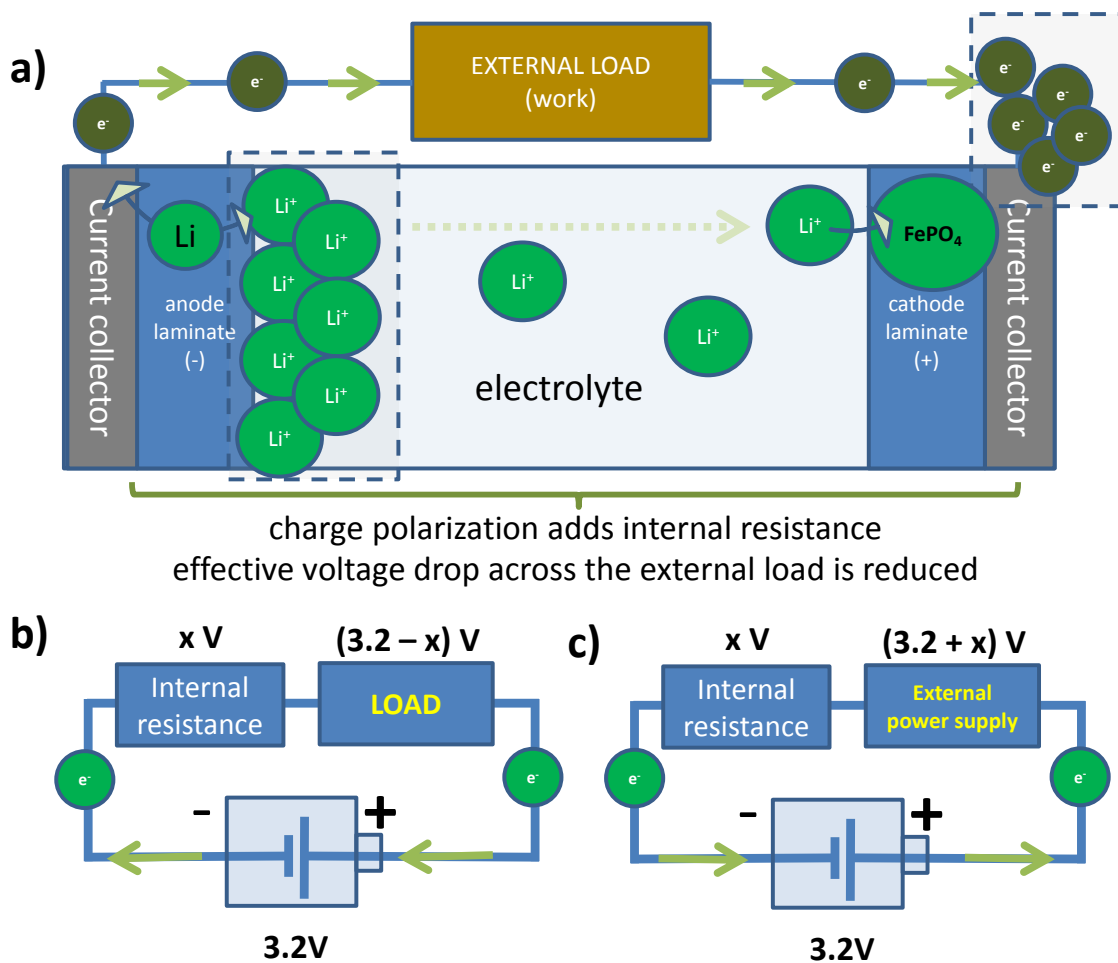


Figure 6.1: a) The flow of charge carriers during battery discharge, wherein electrochemical half reactions can be exemplified by $\text{Li}^0 \rightarrow \text{Li}^+ + \text{e}^-$ at the anode and $\text{Li}^+ + \text{e}^- + \text{FePO}_4 \rightarrow \text{LiFePO}_4$ at the cathode; illustration of internal resistance as an additional circuit component for a supplied electromotive force during (b) battery discharging and c) battery charging.

An ideal electrolyte layer is selectively permeable to cations.* Designing a battery system requires consideration of the electrolyte resistance (R) to ion migration, as dictated by a combination of the material conductivity (σ), its contact area (A) and its thickness (t), i.e. $RA=t/\sigma$. The thicker the electrolyte is, the larger the distance ions must migrate from one electrode to the opposite electrode. The higher its ionic conductivity, the faster is the cation delivery and the better the charge buildup dissipation. Effectively, ion mobility within the electrolyte thus contributes to power rate limits, i.e. how much time is necessary to fully charge a battery or how much energy can be released immediately when required.

*The reader is reminded that the electrolyte must be electronically insulating. It must separate the opposite electrodes to prevent an internal short-circuit of electrons. Otherwise the electron energy is not converted by the external load to perform useful work, but instead results in an abrupt and internal exothermic reaction.

This scenario assumes a perfect battery. In reality this is often not the case. An all-solid-state configuration aggravates problems associated with the contact of components: delamination can occur during operation owing to extreme volume changes with conversion-type reactions (e.g. a Li metal anode)[1]. Delamination reduces access to the active battery materials, leading to poor rate capabilities and short cycle-lives. Preserving an intimate stacking of the electrode-electrolyte-electrode trilayer is therefore crucial [2].

Furthermore, lithium metal anodes seem to be governed by complex electroplating dynamics which are not so well understood. The basic proof-of-concept test for lithium transport through a ceramic electrolyte is the lithium stripping/plating test: i.e. lithium electrodisolution from one electrolyte surface, ionic migration through the ceramic, and lithium electrodeposition on the opposite electrolyte surface. This had recently been demonstrated with Al-LLZO at low current densities of $<50\mu\text{A}/\text{cm}^2$ over hundreds of hours in a stable manner provided the absence of a thin surface layer of resistive Li_2CO_3 . However, cells systematically exhibited abrupt cell failure at higher current densities within as quickly as 1000s [3-5]. To put values in perspective, industrial electrode laminates balanced with areal capacities of $5\text{mAh}/\text{cm}^2$ would take 100 hours to fully recharge at $50\mu\text{A}/\text{cm}^2$, making them impractical.

Why such electroceramics are constrained to operate below certain current densities, has been loosely attributed to concentrated current pathways due to poor component contacts [4, 6, 7]. Optimized mechanical contact between metallic lithium and the ceramic surface had been achieved by taking metallic lithium near its melting point, and Sharafi *et al* pointed out that elevated operating temperatures widened ranges of applicable current densities for stable Li deposition [3]. The problem is that even at 100°C , Sharafi *et al*'s reported material (Al-doped LLZO, $\sigma_{\text{total}} = 0.2\text{mS}/\text{cm}$, $i_{\text{cr}} = 800\mu\text{A}/\text{cm}^2$), implied a recharge time of 6h minimum (against a $5\text{mAh}/\text{cm}^2$ loading). On the other hand, Long *et al*. have shown that higher lithium plating/stripping rates, i.e. $1.25\text{mA}/\text{cm}^2$, are possible with an Au-coated Ta-doped LLZO electrolyte ($\sigma_{\text{total}} = \sim 0.8\text{mS}/\text{cm}$) at 100°C , corresponding to a reduced recharge time of 4h [6]. *Ceteris paribus*, the intrinsic interfacial resistance of contact areas may be related with a material's bulk conductivity due to better matching of lithium activities against Li metal. This implies that a material with $\sigma_{\text{total}} > 1\text{mS}/\text{cm}$ (e.g. the current Ga-doped LLZO material) may allow a more practical 3h recharge time but still only at 100°C or higher. Such a strategy can only improve this battery class thus far.

A novel paradigm is necessary. Understanding how such electroceramics fail is the crucial first step to successfully engineering room-temperature batteries applying this technology.

Asl *et al.* suggested another approach to bypass the interface problem: use a two-compartment electrolyte combining ceramic and liquid organic electrolytes [8, 9]. Their setup consisted on liquid electrolyte being placed on both cathode and anode sides in order to ease Li^+ charge transfer at the electrode-ceramic interfaces and ameliorate interfacial resistance.

In this chapter, insights into the battery operation and the failure mechanism of a garnet-structured polycrystalline ceramic (Ga-substituted $\text{Li}_7\text{La}_3\text{Zr}_2\text{O}_{12}$) are presented.

6.2 Experiments

Galvanostatic cycling with intended anode and cathode materials

A modified experiment was devised applying concepts from both Sharafi *et al* [3] and Asl *et al* [9], using the currently-developed electrolyte material. Full electrochemical cells were assembled as illustrated in Figure 6.2. The electrodes were lithium metal (Rockwood Lithium, battery grade) and LiFePO_4 laminates (~80% LFP active material, ~10% binder, ~10% conductive additive). The ceramic electrolytes were sintered from a $\text{Li}_{6.55}\text{Ga}_{0.15}\text{La}_3\text{Zr}_2\text{O}_{12}$ (Ga0.15-LLZO) composition, at 1150°C for 6h under 99.99% O_2 atmosphere, from powder stock prepared following the citrate-nitrate route outlined in Sections 2.1.1 and 4.3. Pellet densities were evaluated to be ~90% by geometrical analysis compared to the theoretical density ($5.15 \text{ g}\cdot\text{cm}^{-3}$).

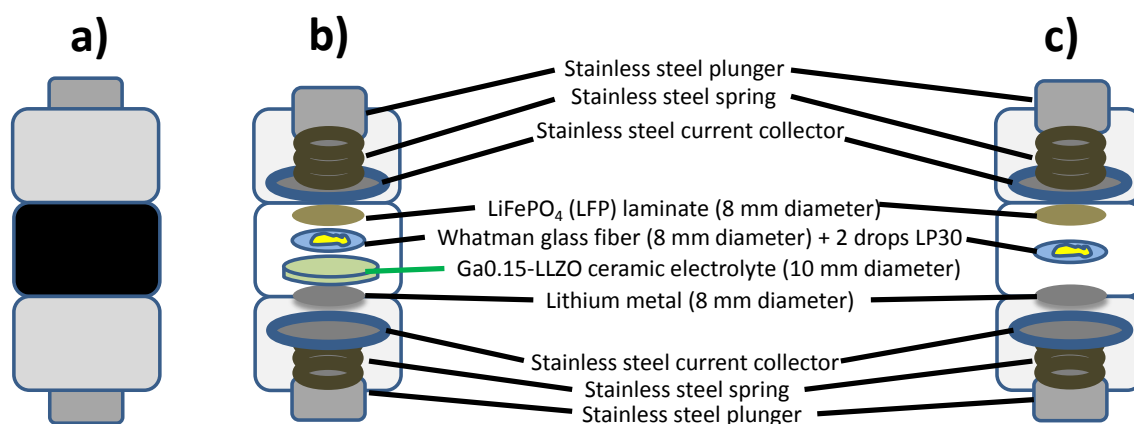


Figure 6.2: a) External view of a Swagelok cell when bolted; b) the experimental Swagelok stack containing ceramic electrolyte used for constant-current cycling tests; c) the control setup omitting the ceramic electrolyte.

On the anode side, fresh lithium foil is soft and readily adheres, and was thus applied directly unto a duly polished ceramic electrolyte. On the cathode side, a glass fiber separator (Whatman) with 2 drops of 1M LiPF₆ in EC:DMC (LP30) provided wetting between the ceramic and the LiFePO₄ cathode material. The stack was encased within a Swagelok unit, hermetically sealed and bolted with an internal steel spring to maintain contact pressure between components. Control samples without the ceramic electrolyte, i.e. employing only the glass fiber with LP30 liquid electrolyte, were also assembled and cycled as benchmarking references. All manipulations were carried out inside an Ar-filled glovebox.

These as-prepared Swagelok cells were allowed to rest for one night prior to EIS measurement and constant-current cycling. A potentiostat/galvanostat controller (Biologic VMP3- Claix, France) was used to monitor the dynamic voltage and the amount of charge passed. A current density of $170\mu\text{A}/\text{cm}^2$ was maintained against Li metal at room-temperature, corresponding to a charge-discharge rate of C/10 or 10hrs constant polarization prior to current direction reversal. An identical set was prepared and cycled to evaluate effects at a higher temperature of 55°C.

Static-probe solid-state ⁷Li NMR

The Swagelok cell was disassembled after cycling, and the ceramics were recovered. A ceramic piece was duly polished on both sides to remove any adherent lithium metal. This was done using multiple polishing papers, discarding each paper after single use, to ensure no cross-contamination. Abrasion depths of 100μm were deemed sufficient

for the purpose. Using the blunt edge of a pestle, the ceramic was shattered and only the discolored interior shards were collected. These were loaded onto an NMR rotor, for measurement in a 200 MHz Bruker Avance III NMR station.

Electronic conductivity measurements

A Swagelok cell containing a polished garnet ceramic (10 mm diameter, 3mm thick, of Ga_{0.15}:LLZO) sputtered with Au on both of the opposite sides, was subjected to chronoamperometry at fixed voltages. Bias was held at 0.5V, 1V, 2V, 3V, 4V and 5V for 15 minutes each.

Determination of voltage stability window

A Swagelok cell containing a polished garnet ceramic (5.6 mm diameter, 1 mm thick, composed of Ga_{0.15}-LLZO) was sputtered with Au only on one side. The other side was contacted with a pressed foil of Li-metal. In this configuration, the Au layer served as the working electrode and the Li foil served as both reference and counter-electrode. A copy was prepared. Two tests were performed: a relatively fast CV sweep (10 mV/s) ranging from -0.5 to 5V, and relatively slower CV sweeps (1 mV/s) ranging from -0.5 to 3.0V, respectively.

Lithium plating/stripping experiments: through-pellet geometry

Swagelok cells containing polished garnet ceramics (5.6 mm diameter, 1 mm thick, of Ga_{0.15}-LLZO) were prepared with lithium foil contacts on both of the opposite sides. A chronopotentiometry program was launched with constant-current polarization at 4 μ A/cm², 8 μ A/cm², 20 μ A/cm² and 40 μ A/cm², reversing current direction every 5 or 10 minutes.

Lithium plating/stripping experiments: lateral geometry

Polished garnet ceramics (5.6 mm diameter, 1 mm thick, of Ga_{0.15}-LLZO) were contacted with parallel lithium foils (Figure 6.3), followed by thin copper wires (0.1mm thickness) and crocodile leads connecting to the external potentiostat/galvanostat. This was achieved via hand-pressing and ocular inspection to achieve a final foil-to-foil lateral separation of about 100 to 650 μ m, within the Ar-glovebox. Samples were studied via FIBSIMS, electron, Raman and optical microscopy during 3 stages: at rest, after a 1V bias polarization and after a 5V bias polarization. Sample transfers to the analysis platforms were carried out using air-tight transfer modules.



Figure 6.3: Lateral configuration for lithium plating/stripping experiments using the currently-developed garnet ceramic (Ga_{0.15}:LLZO) and two parallel strips of lithium foil to serve as electrodes and lithium sinks.

6.3 Results and discussion

6.3.1 Charge/discharge cycling with LiFePO₄ in a battery cell

The electrochemical cell behaviors (with and without a ceramic electrolyte component) under galvanostatic cycling are presented in Figure 6.4. LiFePO₄ was chosen as the cathode material in this study as it presents a flat voltage profile at ~3.4V across oxidation states ranging from un lithiated (FePO₄) to completely lithiated (LiFePO₄) [10], which simplified determination of the overpotential levels necessary to sustain a unidirectional current flow.

The electrochemical tests at room-temperature provided three important observations:

- 1) The experimental setup exhibited a 30% reduction in overall cell impedance after 10 charge-discharge cycles at room-temperature (Figure 6.4a).

Cell impedances arise as a totality of effects arising from individual processes: events occurring within each material and events occurring between interfaces. By comparing similar charge-states (i.e. measurements at two points in time with similar x for Li _{x} FePO₄), intrinsic material contributions can be cancelled out. An evolution in the electrochemical frequency response may arise from degradation or interfacial effects. The former is usually accompanied by an impedance increase, whereas an impedance reduction suggests the latter: easier ionic transfer from one distinct material to another. In this setup, the major interfaces are: a) Li-metal vs ceramic electrolyte, b) ceramic electrolyte vs liquid electrolyte and c) liquid electrolyte vs cathode material.

This is interesting because in traditional Li-ion cells, the cell impedance increases with extended cycling due to decomposition of the liquid electrolyte to form an SEI film, through which lithium mobility is significantly lower [11]. Any chemical change associated with the liquid electrolytes should have led to an impedance increase over time. Therefore, considering the three interfaces mentioned above, the impedance decrease must be attributed to an in-situ contact improvement between the Li-metal and the ceramic electrolyte. Similar phenomena had been previously reported by Buschmann *et al* for symmetrical cells of Li-metal electrodes sandwiching a garnet electrolyte [12].

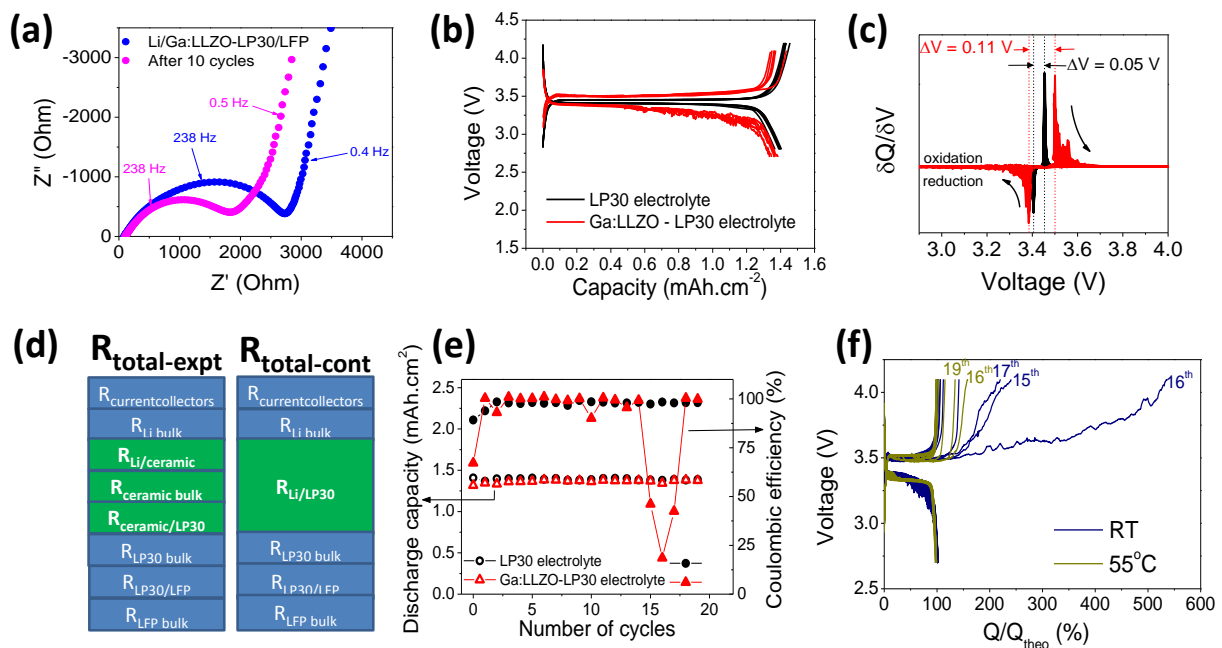


Figure 6.4: (a) Nyquist plots of EIS measurements on the assembled experimental cell before cycling and after 10 cycles at room-temperature. (b) Galvanostatic measurements (limited to cycles 2-7 for clarity) at room-temperature for the cell assemblies described in Figure 6.2. (c) Illustration of overpotential quantification using first derivative plots of *b*. (d) Resistance contributions in the full cells for the experimental setup with the ceramic electrolyte ($R_{\text{total-expt}}$) and the control setup without the ceramic ($R_{\text{total-cont}}$) (e) Discharge capacities and coulombic efficiencies as a function of cycle number. (f) Galvanostatic measurements (limited to cycles 15-19) demonstrating temperature effects (RT vs 55°C), wherein Q_{theo} is defined as the total charge passed on a discharge basis.

2) Galvanostatic cycling (Figure 6.4b) produced similar charge-discharge profiles comparing the experimental (with ceramic) and control (without ceramic) setups. Transforming these curves into their associated derivative plots ($\delta Q/\delta V$) allowed a precise analysis of the overpotential behavior (Figure 6.4c). For the cell prepared with LP30 as the only electrolyte (black lines), individual sharp peaks exhibited a 0.05 V

difference between oxidation and reduction processes. In contrast, the addition of the ceramic electrolyte component (thickness: ~ 0.6 mm) increased this to 0.11 V (red lines), corresponding to an extra 0.06 V resistance-induced overpotential. One notices that it is the LFP oxidation regime, when lithium deposition occurs on the anode side (charging step), that mainly contributes to this (~ 0.05 V).

Assuming ohmic behavior and an intrinsic ionic conductivity of the ceramic electrolyte (~ 1 mS/cm), the expected resistance increase due to the ceramic itself was 120 ohms, taking into account the electrode geometry (8 mm diameter). However, the overpotential increase corresponded to 280 ohms ($R_{\text{total-expt}} - R_{\text{total-cont}}$ in Figure 6.4d). A bit of arithmetic and dimensional analyses can estimate the interfacial ion-transfer resistance between Li-metal and the ceramic electrolyte after 10 cycles to be equal to or less than **80 ohm cm²** for this sample. This was assuming negligible charge transfer resistance between the ceramic electrolyte and the liquid electrolyte. This value is similar to or lower than the interfacial resistances reported for Al-doped LLZO (40-600 ohm cm²) [13].

3) Prolonged cycling with the current density (0.17 mA/cm²) at room-temperature eventually showed abrupt artifacts during charging steps as shown in Figure 6.4f, but not during discharge. It is important to bear in mind that the anode material (Li metal) was present in overwhelming overcapacity. This meant the discharge steps were limited by the cathode, and the total charge stored therein.[†] The retention of discharge capacities over cycling (Figure 6.4e) indicated full utilization of the cathodic active materials, with or without the ceramic electrolyte. This meant no dissolution or “poisoning” occurred due to the ceramic electrolyte elements interacting with the cathode material, or vice-versa, under the specified cycling conditions.

However, the total consumed coulombs during the charging steps were higher than what could be theoretically accommodated by the cathode material, i.e. one cannot further delithiate the cathode when the active material has already been completely converted to FePO₄. This is reflected in the low coulombic efficiencies (equal to $Q_{\text{discharge}}/Q_{\text{charge}} * 100\%$) during some cycles at room-temperature (Figure 6.4e). Interestingly, increasing the operating temperature to 55°C drastically reduced this anomaly as observed in Figure 6.4f.

[†] As represented by how much structurally-stable unlithiated FePO₄ there was and how much lithium could be intercalated during discharge, i.e. charged state = FePO₄, discharged state = LiFePO₄

One hypothesis was that somehow undesirable side-reactions may have occurred during the charging steps at room-temperature. The stability of cathode performance suggested the origin of the problem to be from the anode or the electrolyte. The absence of anomalies in the control cell (without the ceramic) further ruled out potential problems ascribable to instability of the liquid electrolyte. In turn, this meant that only the Li-metal anode and the ceramic electrolyte were left for scrutiny.

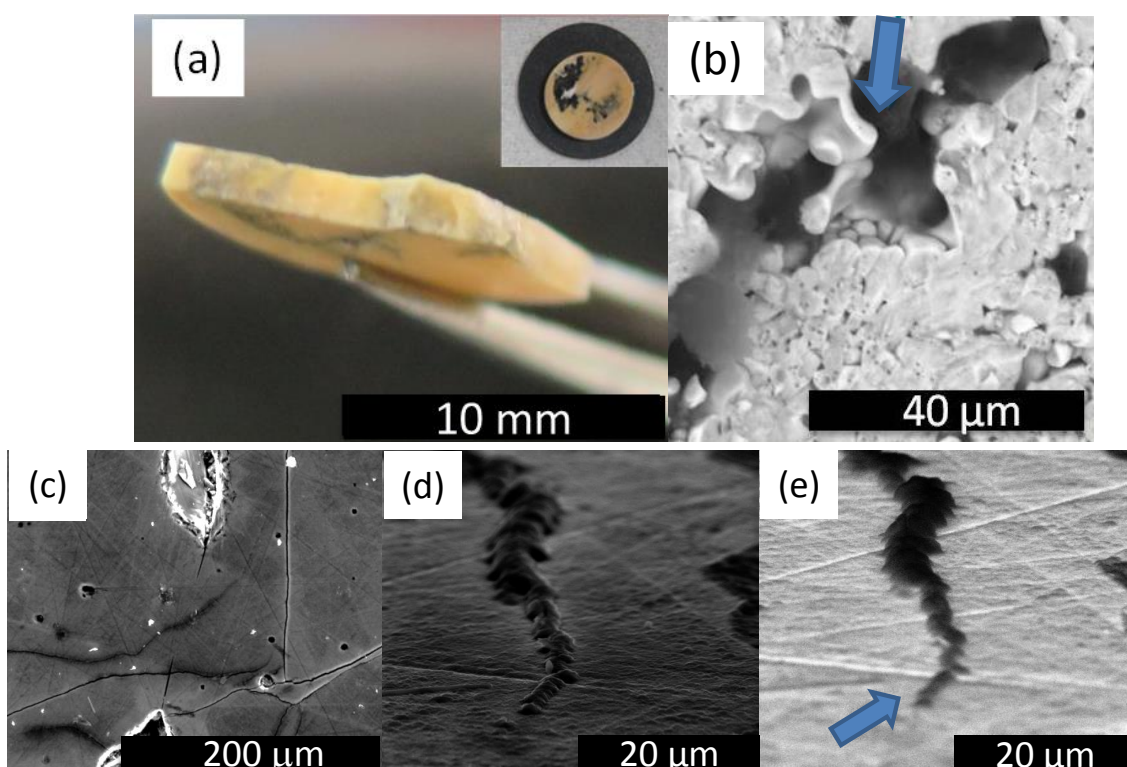


Figure 6.5: a) Photograph of the ceramic cross-section after 20 galvanostatic cycles (0.17 mA/cm^2) at room-temperature (inset: photograph of the ceramic electrolyte surface facing the liquid electrolyte and cathode laminate). b) BE image (30kV) of a fractured cross-section of *a*. c) SE image (30kV) of the ceramic electrolyte facing the liquid electrolyte and the cathode, taken normal to the surface plane. d) Same as *c*, but taken at a 45° angle to the normal plane. e) BE image (30kV) counterpart of *d*.

A post-mortem examination showed dark discolorations penetrating through the ceramic electrolyte after room-temperature cycling, as shown in Figure 6.5a. The discoloration was heavier on the Li-metal side rather than on the LiFePO_4 side, suggesting that the discoloration propagated from the anode. Backscattered electron imaging revealed areas of low atomic number material (darker color contrast) penetrating through the cross-section of the ceramic pellet (Figure 6.5b as pointed by the arrow). Furthermore, the pellet surface facing away from the Li-metal anode (i.e.

on the cathode side) also revealed meandering filaments which were similarly dark under the backscattered electron detector (Figure 6.5c), aside from obvious mechanical fracture. Inspection revealed one such filament with a slender propagation tip, roughly 1 micron wide (Figure 6.5d-e). It is likely that beneath the dark growths were cracks that provided the channels for material transport. Nonetheless, it is unknown whether this was an arrested sudden-crack tip or a progressive propagation.

The growths of low atomic number material were reminiscent of features detected in Ren *et al*'s study, wherein cell failure in a Li/Ta-doped LLZO/Li cell was attributed to a dendrite-induced short circuit [14]. Ren *et al* washed their ceramic using ethanol and found the dark growths disappeared, thus concluding the dark growths to be lithium-metal. This is problematic however, given that lithium ions can also insert into most inorganic lattices forming ternary oxides which may have reacted with ethanol, e.g. lithium aluminates, and that there was no evidence that discounted the possibility that the dark growths were simply mechanically washed away. **A more rigorous treatment of the lithium dendrite problem is provided in the current study.**

Extreme density variations (0.5 to 5.1 g/cc) make quantitative EDAX analyses erratic, due to poorly-contained electron cascade trajectories and ergo, sampling volumes [15]. Hence although many EDAX spectra were collected, the quantitative aspects of the results are not presented.

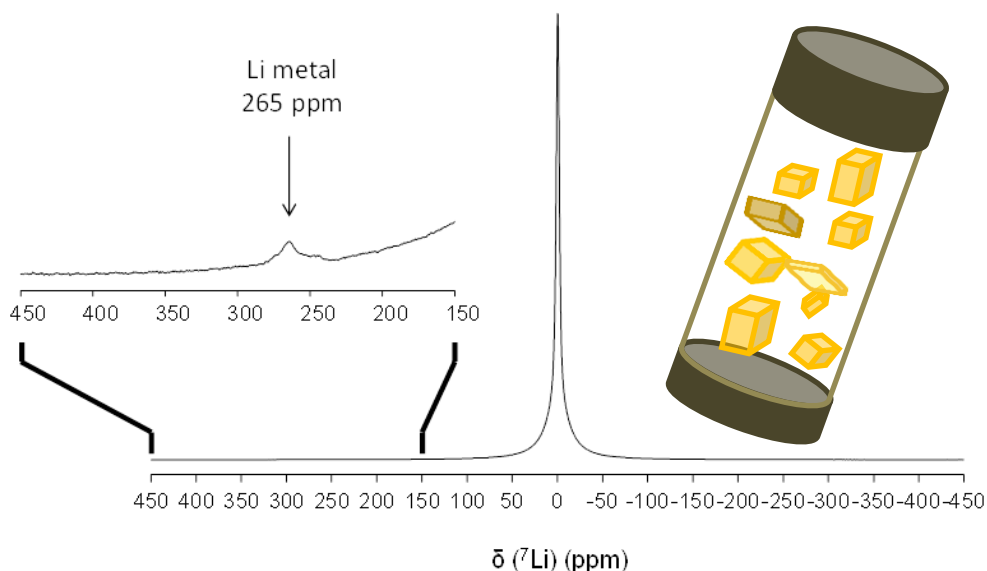


Figure 6.6: Solid-state NMR spectrum obtained under static mode from broken pieces of the ceramic electrolyte in Figure 6.5a. Inset left: a magnified view of the low field region between 450 to 150 ppm chemical shift of ${}^7\text{Li}$. Inset right: schema of the sample loaded within an NMR rotor.

The tool of choice was solid-state NMR, operated by Dr. Juan Miguel Lopez del Amo as before. A portion of the sample in Figure 6.5a had been previously reserved for this purpose.

Li metal is highly reactive, and may exhibit changes in NMR behavior with mechanical preparation. Hence to preserve as much native information as possible, the loaded sample was in the form of coarse chunks instead of fine powder. This however meant high-rpm spinning could easily destabilize the loaded rotor, causing a high impact collision within the NMR instrument. Thus, ^7Li nuclei were probed on static mode, yielding the spectra presented in Figure 6.6.

At a chemical shift of ~ 0 ppm, an intense band corresponding to Li-ion mobility within the Ga-doped LLZO ceramic could be identified. This band had been analyzed in previous studies and was resolved in more detail by magic-angle-spinning [16, 17]. At higher chemical shift (~ 265 ppm), not only were peaks detected indicative of Knight shift contributions for Li° metal [18], but also peak coupling suggesting Li^0 distribution in 3D space as small adjacent clusters.

The metallic form of lithium had thus indeed penetrated the ceramic electrolyte during cycling. The ratio of the two lithium populations (ionic and metallic) could be estimated through their respective peak areas. Fittings suggested 0.5% of the total lithium content was in metallic form within the sampled ceramic. Long *et al.* obtained similar NMR results confirming the presence of lithium metal after cycling in a symmetric Li-metal/Ta-doped LLZO ceramic/Li-metal setup [6].

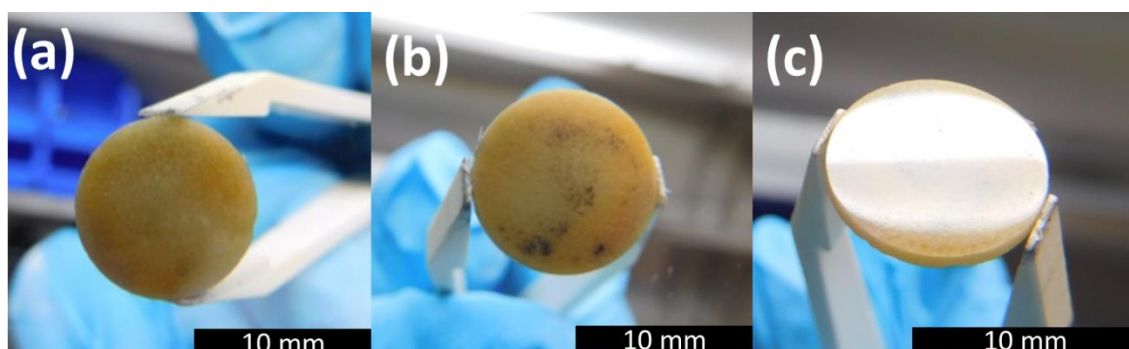


Figure 6.7: Photographs of the polished ceramic electrolyte after 20 galvanostatic cycles (0.17 mA/cm^2) at 55°C . (a) surface facing the LiFePO_4 cathode (b) surface facing the Li-metal anode (c) same as b but tilted to show mirror-like finish.

One may easily suspect, *a priori*, the presence of open porosity as the controlling factor for the development of a metal-dendrite junction from the anode to the cathode, and the associated short-circuit. However, the pathway of lithium deposits in Figure 6.5c suggested fracture-induced penetration rather than simply accretion along pores. A postmortem examination of the ceramic electrolyte cycled at 55°C, also revealed better structural integrity compared to the ceramic electrolyte cycled at room-temperature (Figure 6.7 vs Figure 6.5), explaining in part why the charge-discharge behavior was much better for higher-temperature cycling. The ceramic surface on the cathode-side (Figure 6.7a) showed no discoloration, as opposed to the anode-side. This confirmed that indeed the discolorations (Li-dendrites) originated from the Li-metal contact. Further, specular reflection (Figure 6.7c) from the polished material could highlight that the discolored features were embedded and not simply surface protrusions.

Thus, operating the ceramic electrolyte at a higher temperature (55°C) drastically reduced the Li-dendrite penetration rate, compared to cycling at room-temperature. The question is why. If the failure mechanism were simply a scavenging behavior of interconnected pores by lithium growths, a warmer temperature should have had no effect, or might even have been detrimental as the Li metal could have crept into the pore spaces more easily. Temperature-dependent suppression of dendrites, as demonstrated by the sample in Figure 6.7 hinted at some unidentified mechanism.

6.3.2 Voltage bias experiments in multiple configurations

6.3.2.1 Electronic conductivity

The first step to make sense of lithium dendrite propagation in the current material was in gaining an understanding of the electronic conductivity (σ_e) behavior of the ceramic electrolyte. This can be demonstrated by making use of Ohm's law ($V=IR$) as in Figure 6.8:

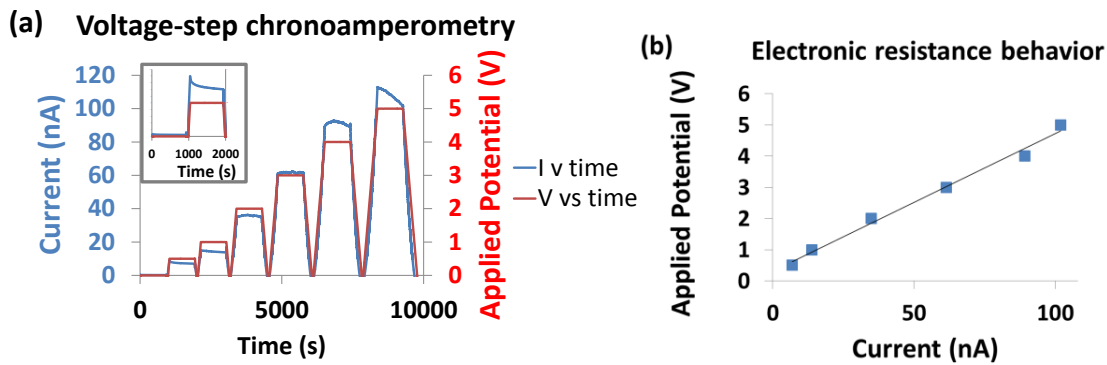


Figure 6.8: (a) Float-protocols at fixed voltages for a Au/Ga_{0.15}:LLZO/Au cell, where each Au layer serves as a Li-blocking electrode (inset: magnified view for current behavior at 0.5V bias) (b) Electronic resistance behavior as a simulated linear ohmic function.

An initial current spike arises at each voltage step as an ionic concentration gradient is established in response to the polarization bias. The total current decays progressively as ionic movement is impeded at the ion-blocking Au electrodes, leaving a residual electronic current (plateaus in Figure 6.8a, as magnified in the inset). A possible complication is the formation of a Li-Au alloy at the electrode. Nonetheless, Li-Au alloying fronts proceed sluggishly, even with thin films [19][‡]. The electronic component of the current, $I(t)$, can thus be estimated from the capacitive behaviour of the current decay, with a decay response of $I(t) = \frac{V_{\text{applied}}}{R} e^{-\frac{t}{\tau_0}}$ where τ_0 is the RC-time constant of a capacitor wherein the ceramic serves as the dielectric material. Fitting a linear regression (as illustrated in Figure 6.8b) between the applied potential V_{applied} and the semi-stabilized current $I(t=\infty)$ yields a normalized electronic conductivity value of at most $10^{-6} \text{ mS}\cdot\text{cm}^{-1}$. This represents a difference of 6 orders of magnitude between the ionic and electronic conductivities, i.e. $\sim 99.9999\%$ of the current within the internal circuit is carried by ions, meaning the ceramic bulk is a very good electronic insulator.

This is desirable since a ceramic electrolyte must have majority of charge passing through it in the form of ions, i.e. the transport number for ions must be very close to 1, while that for electrons close to zero. A very low electronic conductivity is required to mitigate current leakage and self-discharge in an assembled battery. However, this also means that the electronic resistance between two points on opposite electrodes

[‡] Nonetheless, the time regime under which a voltage bias is applied must be critically limited, otherwise the Li-Au alloying process may still induce non-equilibrium artefacts, hence the choice of 15 mins bias per step as a compromise. With ideal ion-blocking electrodes, the residual current after an infinite period of applied bias would be smaller. This means, the stated values only establish upper limits of the true electronic conductivity.

drops greatly for a minute extent of dendrite penetration, or even with small impurity concentrations. In contrast, for the same decrease in point-to-point distance, the change in ionic resistance would be relatively insignificant. The onset of dendrite formation in such a material creates drastic perturbations in electric field lines, and a higher rate of localized electrochemical reduction of alkali metal ions to maintain a balanced flux of ions vs electrons and preserve Kirchoff's circuit laws [20]. Effectively, the concentrated electron pathway produces an ion-focusing hotspot (Figure 6.10). The greater the disparity between the two types of currents (electronic vs ionic), the more focused the electric field is, and the more slender the dendritic filaments. This facilitates sharp metallic penetration, as in a needle. This explains why superionic conductors are much more prone to rapid dendritic short-circuits compared to poor lithium ionic conductors. Furthermore, the ceramic bulk possesses infinite conductivity compared to void space (0 S/cm until dielectric breakdown), hence dendrite propagation through pores is likely only a mechanical spillover effect rather than directly promoted by field-lines.

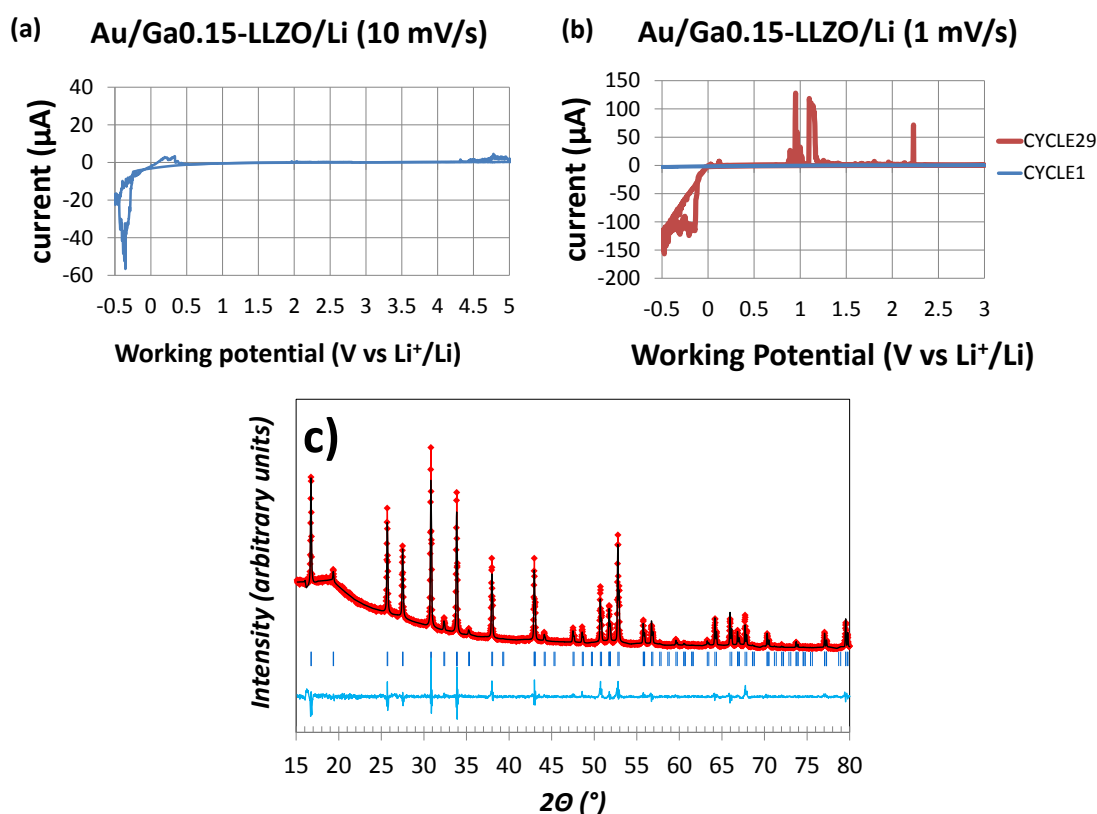


Figure 6.9: Cyclic voltammograms for Au/Ga_{0.15}-LLZO/Li using one fast sweep (a) vs multiple slow sweeps (b). Post-mortem PXR D pattern (Cu K_{α1}) showing reflections for the *la* $\bar{3}d$ symmetry for the sample in b.

6.3.2.2 Voltage stability window

The second step to make sense of lithium dendrite propagation in the current material was probing the voltage stability window. This is demonstrated in Figure 6.9a. With cyclic voltammetry (CV) tests, a high working potential induces oxidation on the working electrode (Au) and reduction on the counter electrode (Li). By using a noble-element working electrode (i.e. cannot be easily oxidized), any observed current can be ascribed to the response of the electrolyte. The equilibrium potential of Au^+/Au under standard conditions is at 4.5V vs Li^+/Li . Figure 6.9a thus confirms that the present Ga-doped LLZO ceramic is stable vs lithium metal at least within this voltage range. An applied potential below 0V vs Li^+/Li is simply a reversal in the polarization direction, and the negative current can be interpreted as partial electrodisolution of the Li electrode and lithium plating on the Au electrode. Repeating multiple CV cycles at a restricted maximum potential of 3V effectively creates a Li/Ga_{0.15}-LLZO/Li/Au configuration, and demonstrates perceived stability until cycle 28, prior to anomalies during cycle 29 (Figure 6.9b) and subsequent short-circuit failure. It is important to stress that failure thus occurred as a progressive process of dendritic penetration, and was not simply a manifestation of electrochemical instability of the electrolyte in contact with lithium metal; an inference supported by no evidence of crystallographic decomposition of the cubic-phase LLZO structure (Figure 6.9c).

6.3.2.3 Lithium stripping/plating experiments

The electrodeposition dynamics is further illustrated in a symmetric lithium electrode assembly, wherein the lithium stripping/plating behavior of the current material was studied (Figure 6.10a). The first bias step consisted of an in-situ interfacial amelioration on one electrolyte side by sourcing ions from partial contact dissolution on the other, eventually giving rise to a large contact resistance and therefore overpotential. This is because even though the nominal current density is $4\mu\text{A}/\text{cm}^2$, a much higher current density is found locally at point contacts due to imperfect adhesion between the Li metal and the ceramic electrolyte following manual pressing. With time, these contact areas are further “shaved” in order to supply the ionic current densities required, as schematized in Figure 6.10b. Increasing operating temperature increases lithium self-diffusion and feeds a more adequate supply of the ions from the bulk to the contact regions, mitigating this “shaving” behavior.

The lithium metal-ceramic electrolyte interface can be modeled as parallel circuits of Randles-type elements (with the capacitance components neglected here for

simplification). The aggregate impedance behavior would be the inverse sum of resistances, each normalized according to an arbitrary surface unit. Zones linking the anode bulk to the electrolyte would exhibit the intrinsic charge transfer resistance (R_{CT}), whereas zones of no contact would possess relatively infinite resistance ($R=\infty$). This results in: $1/R_{interface} = n(1/R_{CT}) + (1-n)(1/\infty)$, or essentially the interfacial resistance being inversely correlated with the ratio between the intimate contact area (n) and the normalized area (1). The potential evolution of interfacial decomposition products has been neglected in this model, but the relation holds regardless.

Going back to the first bias step in Figure 6.10a, the sudden increase in resistance after 300 seconds signals the depletion of lithium metal in direct contact with the ceramic interphase: current is increasingly carried by electrons and a higher system overpotential (from 0.02V to 0.12V) results. Recognition of this switch of carriers is crucial, as it implies that electronic current is not simply concentrated in a narrow pathway; the magnitude of total electronic current passing is amplified, driving localized electrodeposition further. The subsequent bias reversals redeposit lithium on the now poorly-contacted interface between lithium metal and the ceramic electrolyte, and exhibit similar behavior until eventual cell failure (at 22000s).

This reasoning implies that even with uniformly sputtered lithium metal films on the surface of a smooth ceramic electrolyte, contact loss between the two components grows during cycling in a pressureless environment and at relatively low temperature (e.g. room temperature). This would be especially significant during cold-starts of battery charging or discharging, i.e. dl/dt is very high. It follows that either the lithium metal or the ceramic electrolyte must mechanically yield in order to stabilize the contacts and, ergo, make possible the long term operation of the solid-state-battery. Obviously from Table 6.1, lithium metal can be elastically deformed much easier than garnet-oxide ceramics. As of manuscript date, the existence of high-strain rate superplastic ceramics has been shown possible by careful manipulation of grain size and grain-boundary sliding mechanisms, but unfortunately not demonstrated yet for materials exhibiting lithium-ion conductivity [21].

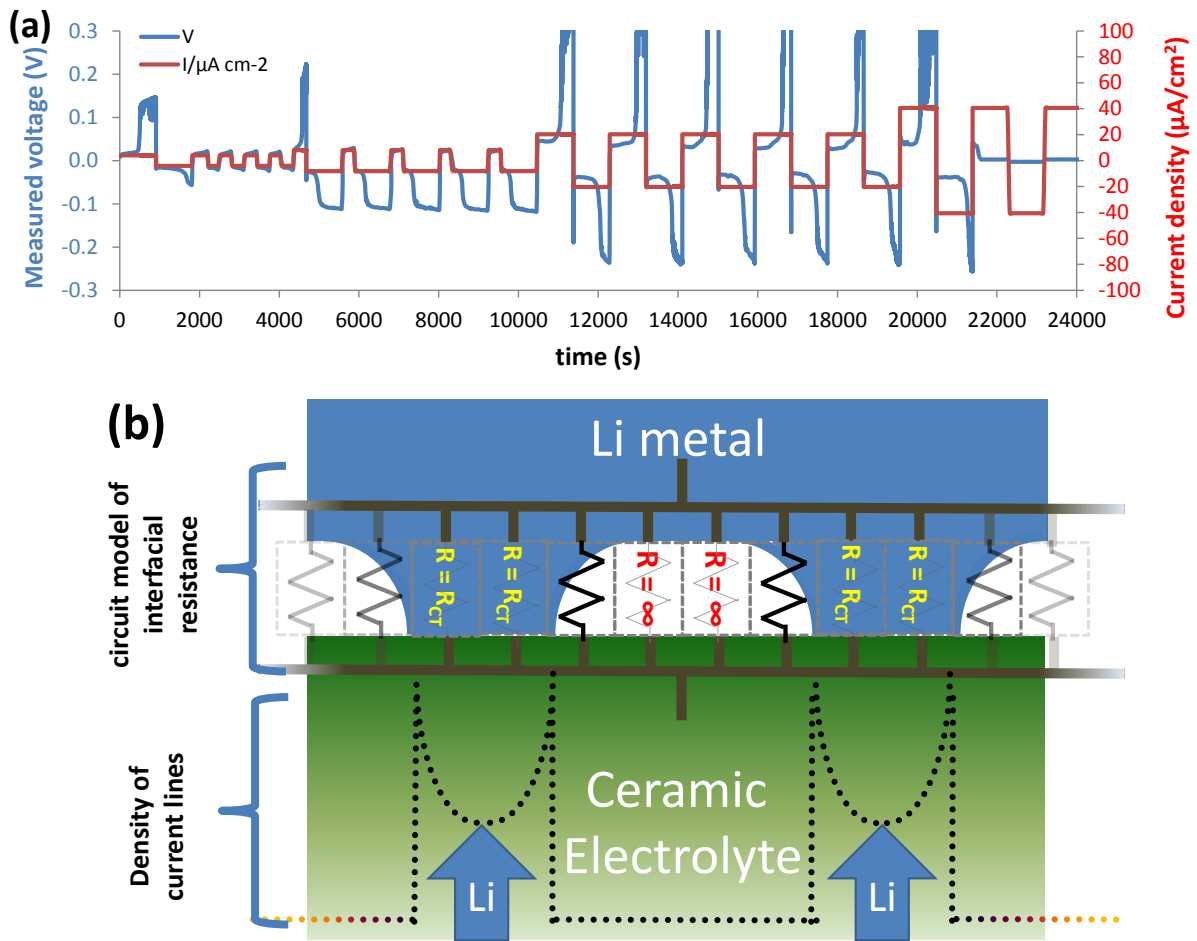


Figure 6.10: (a) Chronopotentiometric plating of lithium metal on a ceramic electrolyte at $4\mu\text{A}/\text{cm}^2$, $8\mu\text{A}/\text{cm}^2$, $20\mu\text{A}/\text{cm}^2$ and $40\mu\text{A}/\text{cm}^2$ current densities on alternating forward and reverse DC bias. (b) Schematic of the interface between the lithium metal bulk and the ceramic electrolyte surface, as resistor components connected in parallel; dashed green lines illustrate the reduction in contact areas with lithium dissolution when exceeding a certain current density threshold; black dotted lines indicate regions with concentrated current densities.

Table 6.1 Mechanical properties of bulk lithium metal vs a hotpressed Al-doped LLZO garnet oxide, as quoted from literature [22-28].

	Lithium metal	Al-doped LLZO
Bulk modulus (GPa)	11	~100
Young's modulus (GPa)	4.9	130-150
Shear modulus (GPa)	4.2	50-60

The action of flattening pressure can aid in dynamically maximizing the effective interfacial contact areas, and improve uniformity of current densities. Further, there exist suggestions that mechanical pressure alters the self-diffusion constant of lithium [29, 30]. Supplementary discussion on this subject can be found in Appendix C.

6.3.2.4 In-operando dendrite formation

To examine lithium dendrite penetration visually, a lateral Li-Li polarization setup was devised (Figure 6.3). Microstructural changes were examined by electron, Raman and optical microscopies after induced voltage biases.

Any form of mechanical abrasion creates surface defects. Abrasion marks were evident in the polished sample in Figure 6.11 (b,e). The ceramic also exhibited a bimodal size distribution characteristic of liquid phase sintering. The sintered material was mainly composed of large grains ($\geq 200\mu\text{m}$ across) with concentrated regions of small grains ($\leq 10\mu\text{m}$) and minor interspersed solitary pores.

After a low voltage polarization (1V), growths emerged along grain boundaries and pores (as indicated by blue circles in Figure 6.11 b,e). EDAX imaging could not be used to ascertain their identities due to the shallow thickness of the growths, rendering them transparent to EDAX due to the deep nature of X-ray penetration ($\geq 5\mu\text{m}$ depending on the electron density for the scanned area).

After a high voltage polarization (5V), catastrophic ceramic failure had occurred, showing multiple mechanical fracture lines and “bubbles” composed of elements of low atomic number. These bubbles seemed to occur along fracture pathways (Figure 6.11 c,f), and were consistently reproducible (Figure 6.12). Interestingly, these “bubble” outgrowths did not emerge out of pore voids, which would have intuitively been expected to present no mechanical resistance, but sprung up along the generated transgranular fracture lines. Another interesting point was that, crack initiation avoided the junction between three grains, where mechanical integrity would have been expected the weakest. This suggests some degree of inherent anisotropy of current lines associated with large-grain ceramics after passing a certain current threshold, a consequence of magnified current-focusing either due to non-uniform conductivity of the grain-boundaries surrounding a large grain or a gradient of doping concentrations within a grain wherein the radial center is the most ionically-conductive.

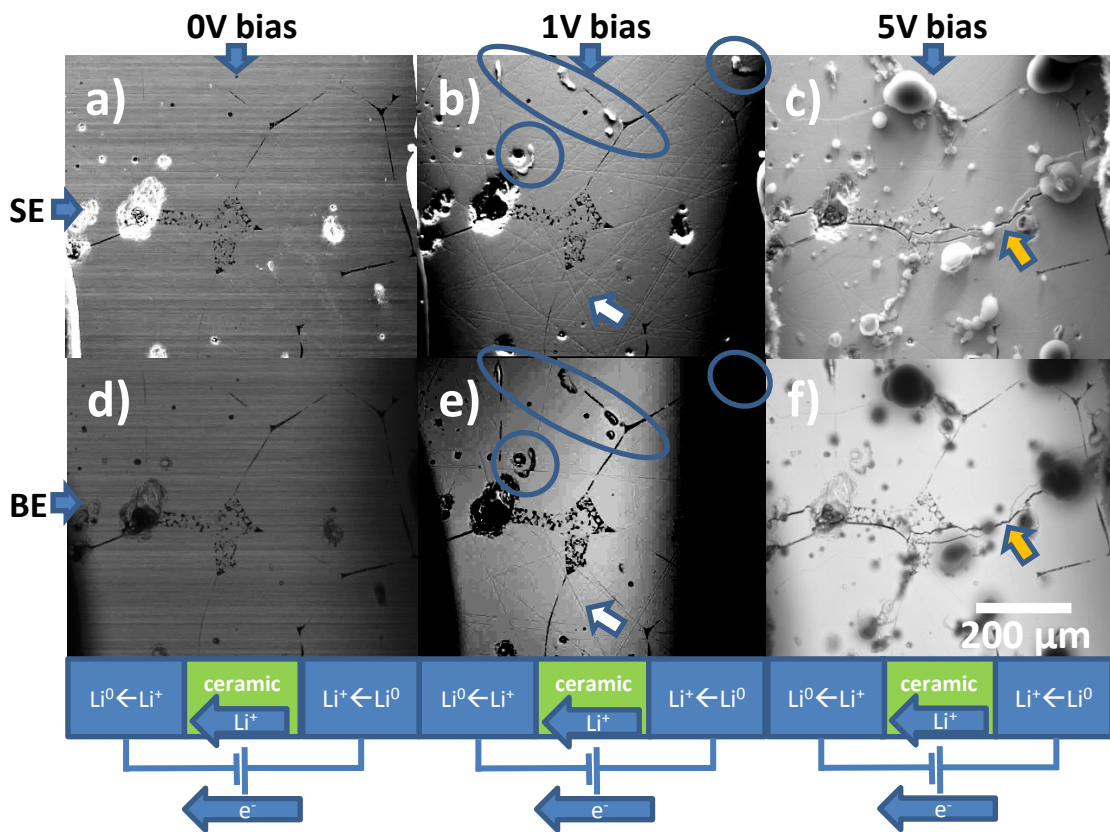


Figure 6.11: a) Secondary electron images of the ceramic surface prior to lateral polarization, b) after 1V bias for 30 mins, c) after 5V bias for 1 min; (d-f) respective backscattered electron images. The blue circles indicate bias-induced growths; white arrows indicate abrasion marks and the orange arrows indicate a fracture line.

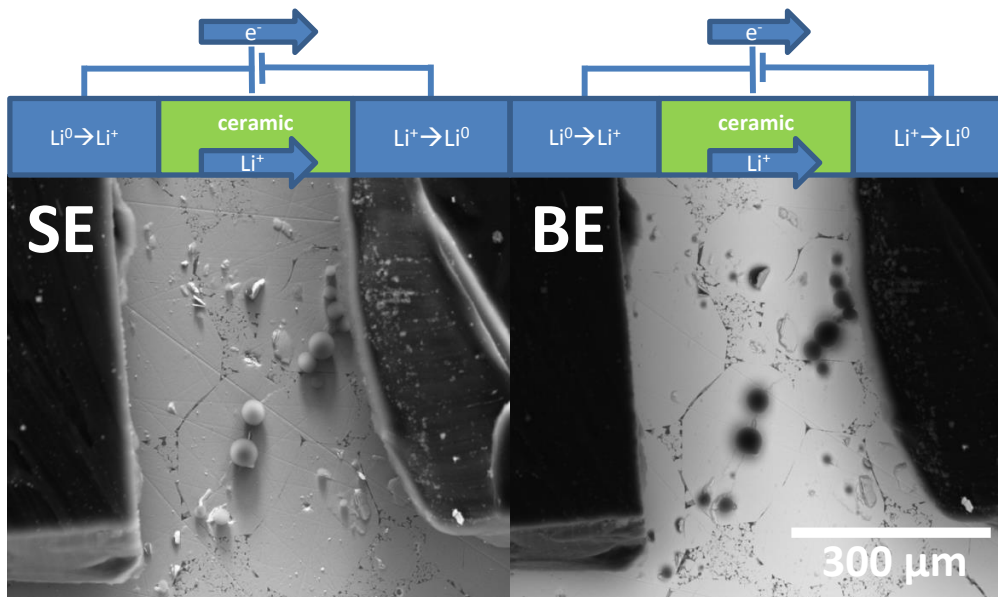


Figure 6.12: Electron microscopy images of another ceramic pellet surface after a 5V lateral polarization, displaying SE imaging on the left and BE imaging on the right.

At this point, any proposed failure mechanism would necessitate identification of the composition of the “bubbles,” whether they being decomposition products or lithium metal. The bubbles were further examined under the SEM microscope by orienting the beam 45° to the normal surface of the ceramic, as shown in Figure 6.13. Contact angles revealed poor wetting to the ceramic surface. Further, measurement of shape eccentricity confirmed that indeed the bubbles were mostly spherical. Elemental analyses by EDAX gave erratic ratios of elements expected in the ceramic material, and values were thus discarded due to lack of control over excited material volumes.

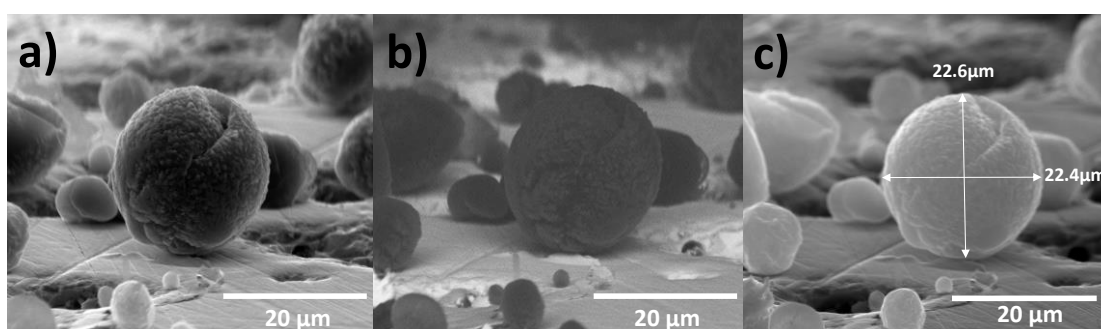


Figure 6.13: a) Secondary electron image at 12kV, b) backscattered electron image at 12kV and c) secondary electron image at 30kV with axial dimensions, of a “bubble” outgrowth.

Confocal optical-Raman microscopy provided complementary information. A bubble sitting along a ceramic fracture line exhibited optical luster (Figure 6.14a). Taking the Raman spectra of various selected points (Figure 6.14b) yielded Figure 6.14c. Of these, points 1-2-7 belonged to signals obtained from the lithium metal bulk; points 3-4-6 belonged to the “bubbles”; points 5-8 belonged to the ceramic surface. The ceramic surface exhibited a distinct Raman signature, whereas both the “bubbles” and the reference Li metal bulk revealed baseline Raman scattering, suggesting metallic nature of the “bubbles.” Metals do not exhibit Raman activity.

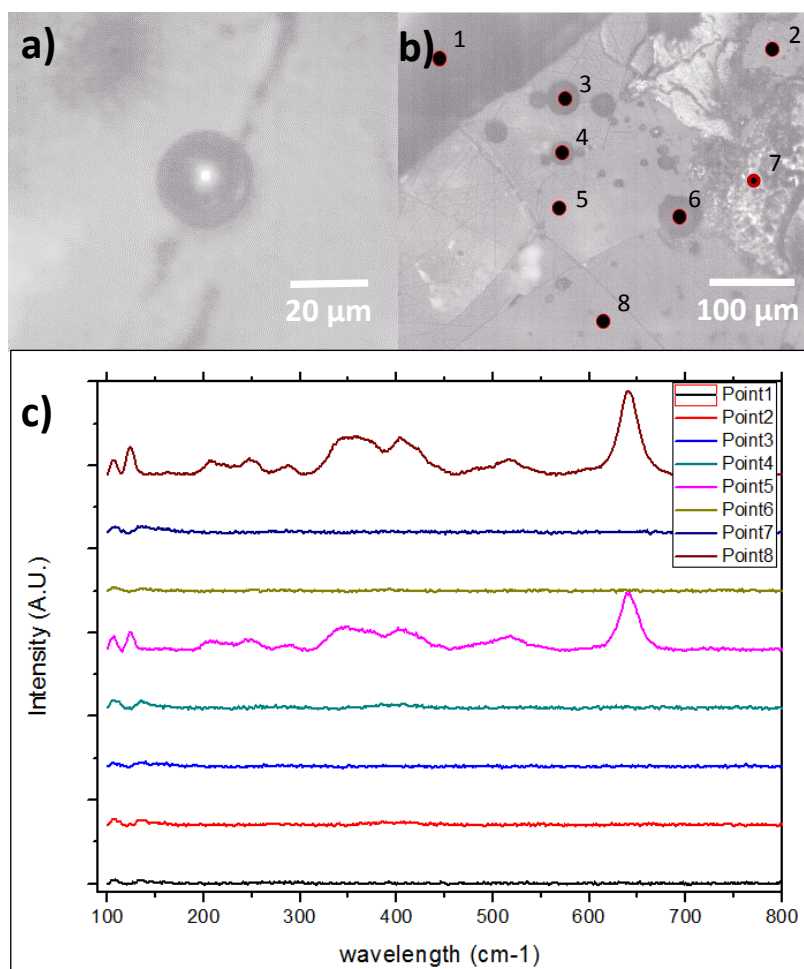


Figure 6.14: a) Optical microscopy image of a “bubble” outgrowth, b) Points of interest scanned by confocal Raman spectroscopy and c) their respective Raman spectra.

The ceramic electrolyte was composed of Li, Ga, La, Zr and O elements. Of these only the first four can precipitate out as solid metals or metal alloys. Further, the spherical shape suggested that the bubbles were for some time existent in the liquid state. The melting points of metallic Li, Ga, La and Zr are 180.5°C, 29.8°C, 920°C and 1855°C, respectively. This suggests the bubbles were composed predominantly of Li or Ga.

The “bubbles” were seen to be solid and pinpoint FIB-SIMS sputtering through the center of one of the spheres showed a high Li signal compared to the ceramic bulk (Figure 6.15). SIMS techniques are very good at the identification of light elements such as Li. It is mass-spectrometry based and elements such as Li have a high yield as secondary positive ions. This meant that if the growths were predominantly gallium, the Li7/Ga69 ratio should have dipped lower than the values obtained while sputtering through the ceramic proper.

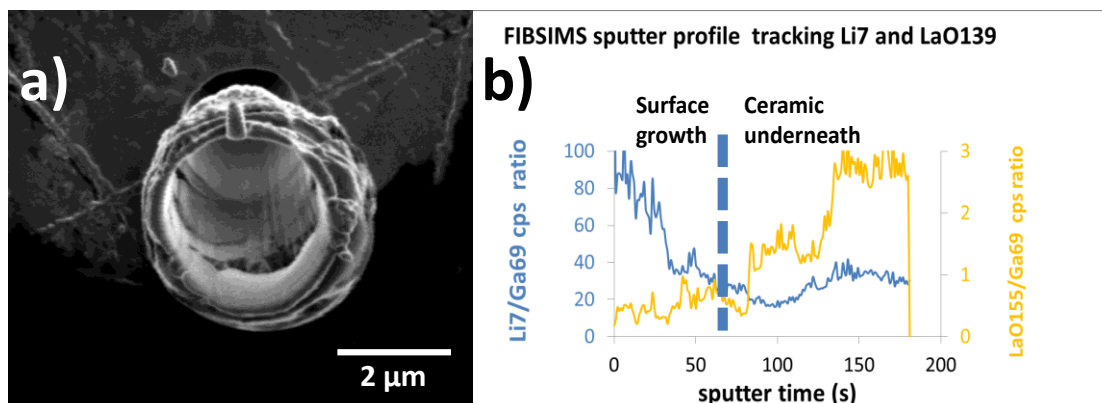


Figure 6.15: (a) Topview of a crater within a “bubble” outgrowth as sputtered with simultaneously analysis using the FIBSIMS module (positive-ion mode) (b) Time-dependent sputter profile generated from *a*, showing Li7 and LaO155 counts normalized to the Ga69 beam.

Supporting evidence for this is demonstrated in Figure 6.16, wherein the post-polarized ceramic was immersed in distilled H₂O. Discoloration marked the areas modified by the bias step experiment. These disappeared with water treatment, suggesting dissolution of lithium metal indeed. Gallium metal does not corrode in aqueous media due to the formation of a stable passivation layer of gallium oxide.

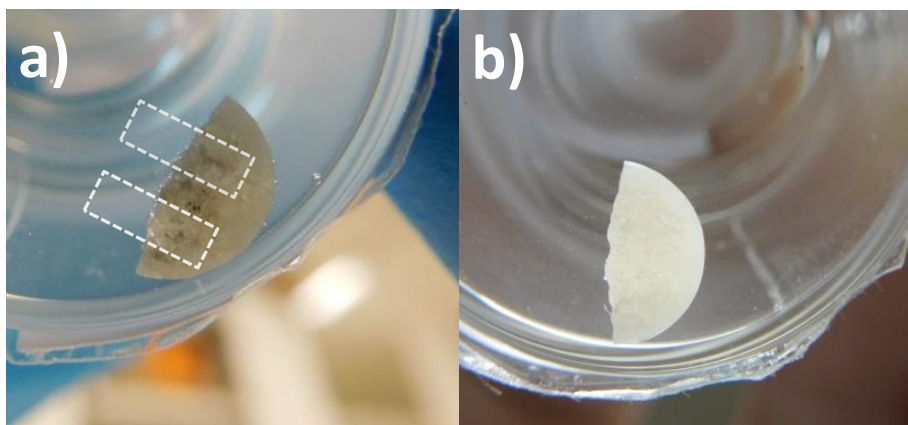


Figure 6.16: Camera photo of a ceramic piece after 5V-polarization between two lithium foil contacts; a) at the point of immersion in distilled H₂O at room-temperature and b) after immersing for 2h. The original positions of the lithium electrode strips are highlighted by the white boxes in (a).

The ceramic was recovered after this water treatment, and re-examined under the electron microscope (Figure 6.17). The original lithium metal contacts had disappeared exposing the ceramic features beneath. On the side of the counter electrode (Figure 6.17a, where lithium plating occurred), scattered small pits were generated, whereas only evidence for large spalled flakes were evident on the working electrode (Figure 6.17b, where lithium stripping occurred), in agreement with the concentrated electrodeposition preferences rationalized in Figure 6.10b.

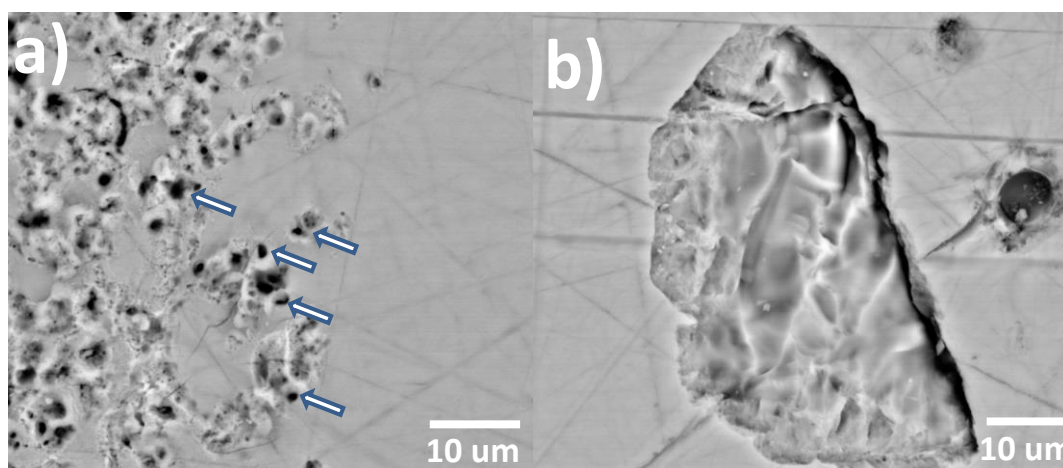


Figure 6.17: Backscattered electron images (30kV acceleration) of the ceramic surface where the lithium foils originally made contact for lateral polarization: (a) counter electrode area (lithium plating: $\text{Li}^+ \rightarrow \text{Li}^0$) and (b) working electrode area (lithium stripping: $\text{Li}^0 \rightarrow \text{Li}^+$).

It is evident from Figure 6.17a that pores had been “drilled” within large ceramic grains (white arrows). This was puzzling, given the relatively low yield strength of lithium metal (0.655 MPa) compared to ceramic oxides (approximately equal to its hardness, 6.3 GPa for Al-doped LLZO) [31]. As highlighted in Figure 6.12, mechanical fracture occurs with transgranular preference instead of simply along grain boundaries, further suggesting localized fluid pressure as a result of bias-driven accumulation of Li at points, until the ceramic yield strength was surpassed.

The phenomenon of low yield strength Li-metal penetrating a high yield strength garnet ceramic is akin to ultrapressurized water cutting through steel.

Bulk lithium metal does not flow. This impedes stress-strain relaxation. Under electrochemical bias in contact with an electrolyte, one may hypothesize that lithium ions pass through a fluid-like state in the immediate lithium metal-ceramic interface prior to consolidation to bulk lithium metal. The bulk modulus (β) of lithium metal is 11

GPa, translating by definition to an isothermal compressibility factor (κ) of 9.1×10^{-11} Pa, which is fairly constant for a liquid or a solid. It can be shown (Appendix D) using the definition of a work process that:

$$w = -P_0 V_0 [e^{-\kappa(P-P_0)} - 1] + \frac{V_0}{\kappa} \{1 - e^{-\kappa(P-P_0)} [1 + \kappa(P - P_0)]\}$$

Further, the maximum amount of energy converted to work is attainable only in a reversible process, resulting in the approximation:

$$w \approx \frac{V_0 \kappa}{2} [P^2 - P_0^2]$$

where V_0 is the volume occupied by lithium at room-temperature under no pressure

Consider a scenario with two uniform lithium plates, each of infinite area and thickness, placed parallel in opposite positions. The void in between is completely filled by an ideal electrolyte, with zero ionic charge transfer resistance for Li ions, and the concentration of lithium ions in the electrolyte is permanently constant. Since the concentration of lithium in lithium metal is unity, there are no transient contributions of enthalpies of mixing.

State functions are dependent only on the initial and final states.

If an atom or an atom cluster on the surface is moved from one electrode to the opposite, ΔU (internal energy) is zero for a miniscule change in lithium configuration. The same can be estimated for ΔS . This implies $\Delta G \approx \Delta H \approx w$. **In other words in this system, the difference in Gibbs energy arising from an applied potential bias can be correlated to a maximum compression work, via the Nernst equation.** The ΔG and w are extrinsic variables with dependence on n or how many atoms, atom clusters or atom moles are involved.

This gives, under assumption that ionization energy, sublimation enthalpy and energy of hydration all implicitly cancel out that:

$$\Delta G = -nFE_{\text{cell}} = w = n(\bar{w}) = n \frac{(0.01297 \text{ L/mol}) (9.1 \times 10^{-11} \text{ Pa}^{-1})}{2} [P^2 - P_0^2]$$

$$\frac{-2FE_{\text{cell}}}{(0.01297 \text{ L/mol}) (9.1 \times 10^{-11} \text{ Pa}^{-1})} + P_0^2 = P^2$$

What this equation is essentially saying is assuming all the bias-driven compressive work done by lithium metal is concentrated on a point contact on the ceramic, a corresponding pressure value can be derived.

Assuming zero P_0 , instantaneous $\text{Li}^0\text{-Li}^+$ and $\text{Li}^+\text{-Li}^0$ conversions, with no Li mass transfer limitations, this means that in such an ideal electrolyte, 0.1 to 10 GPa of Li point pressures are generated with applied bias at the instant of polarization. Plotting the expected maximum accumulable pressure vs the applied bias yields Figure 6.18, it is evident that a small maintained voltage bias of 0.25V provides enough lithium compression energy to surpass the ceramic yield stress, a value of 6.3 GPa or 9.8 on the log Pa scale.

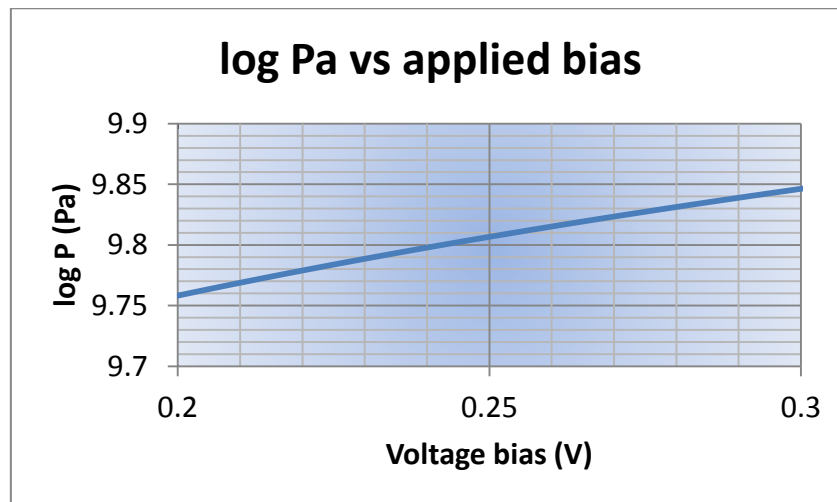


Figure 6.18: A correlation of maximum lithium pressure derivable from energy equivalence between isothermal compression work and the Nernst equation, under room-temperature conditions in an ideal system.

A further comment can be made based on the phase diagram of lithium under mechanical pressure as reproduced from Guillaume CL [32]. Under practical operating conditions, bulk lithium is always solid in phase, maintaining a *bcc* lattice, and never transforming into a liquid under cold melting, implying that the macroscopic lithium metal bubbles were a result of joule heating of lithium dendrites forming an electrode-to-electrode short-circuit.

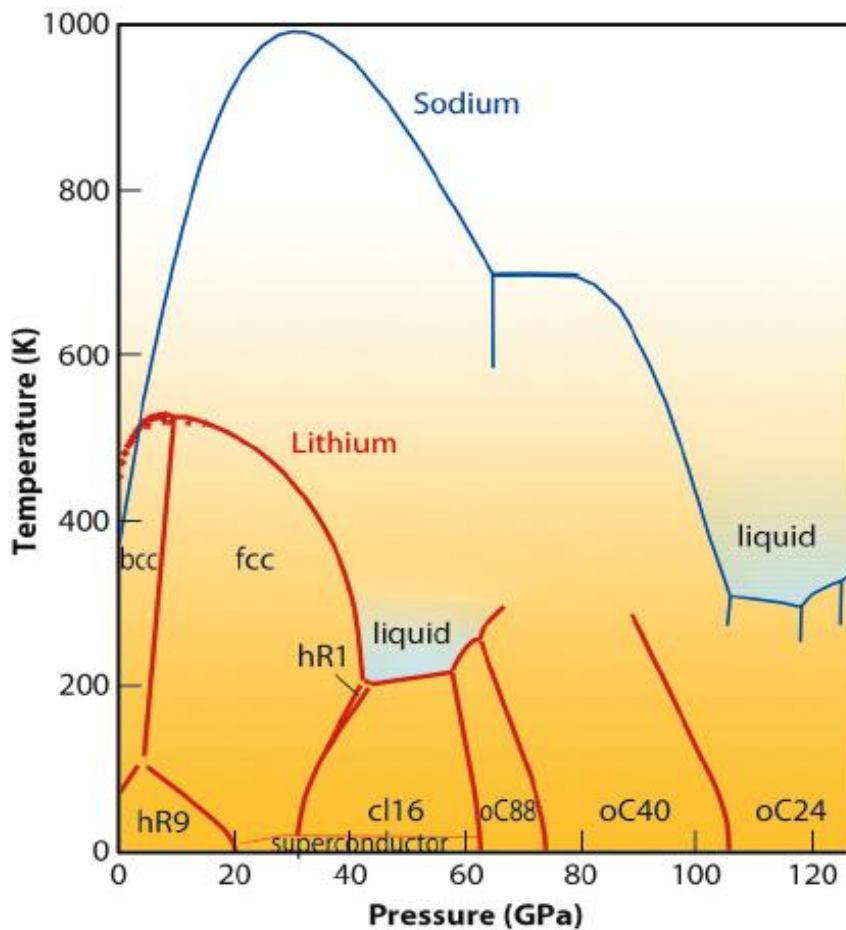


Figure 6.19: Phase diagram of lithium and sodium [32].

Lastly, a real-time observation was recorded for a 5V lateral polarization of the ceramic electrolyte with lithium metal contacts (Figure 6.20). It was observed that more than 600 seconds passed without the formation of a short-circuit junction. At 641s, a fracture line began to form, producing a physical pathway connecting the two lateral electrodes as evident at 648s. There was a tiny lag, but lithium dendrites subsequently filled this physical fracture in a prompt manner. A slender short-circuit junction of lithium metal was formed, followed by Joule heating, followed by lithium metal melting, and temporary disruption of the short-circuit, as seen at 674s. This was only temporary, as a thicker junction reformed with polarization maintaining the contact. The phenomenon explains why current spikes and then levels down and then spikes again sporadically as seen in cycle 29 of Figure 6.9b, prior to total cell failure. This sequence of events is in agreement with in-situ characterization of operational lithium battery cells employing a garnet-type ceramic electrolyte [33].

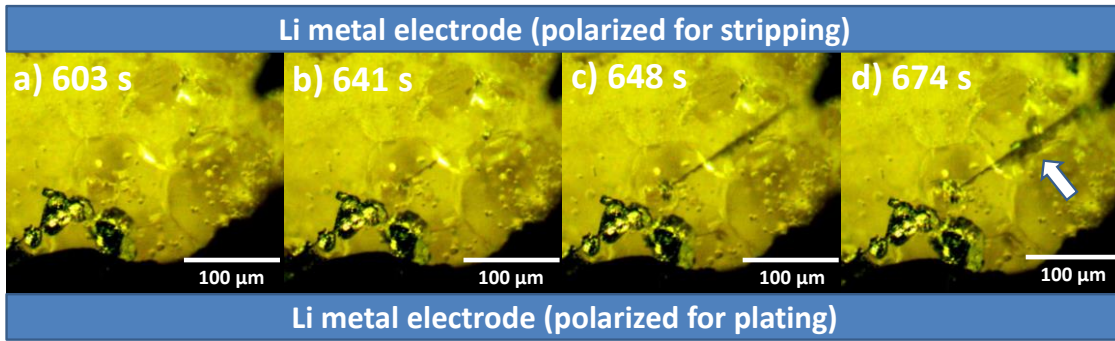


Figure 6.20: In-situ optical microscopy of a Ga_{0.15}-LLZO ceramic pellet with lithium foil contacts, for which snapshots of a 5V lateral polarization bias were taken at a) 603s, b) 641s, c) 648s and d) 674s. The crack begins at 641s and short-circuits the two lithium metal electrodes at 648s (white arrow).

6.3.2.5 Thermal conductivity

To substantiate this description of events, the thermal conductivity of the Ga_{0.15}-LLZO ceramic was measured as shown in Figure 6.21, and shown to be always 0.3 W/m·K or less. For comparison, the thermal conductivity of lithium metal is 85 W/m·K, that for polymer electrolytes is 0.1 W/m·K, whereas those for the industry standards of liquid electrolytes (e.g. 1M LiPF₆ in 1M EC:DMC) show about 20-30 W/m·K. It is therefore obvious that solid electrolytes for lithium batteries are poor thermal conductors, and that in the event of a short-circuit, temperature will rise rapidly locally. This has significant safety implications.

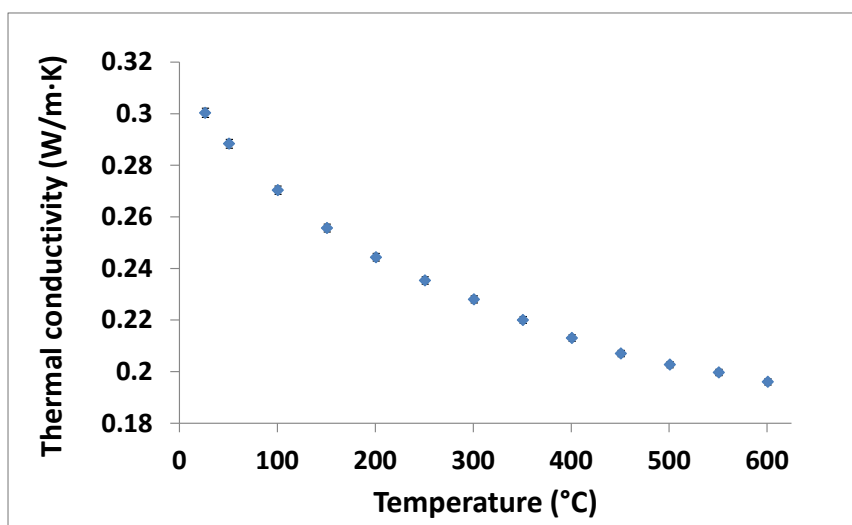


Figure 6.21: Thermal conductivity data for a Ga_{0.15}-LLZO ceramic pellet across temperatures from 25°C to 600°C.

In the event of a lithium-dendrite short, Joule heating occurs. Liquid electrolytes rapidly spread this heat across the system, thermally igniting the organics and sustaining a catastrophic thermal runaway. With solid electrolytes, the heat produced by Joule heating is maintained in the lithium filaments, thus immediately melting them due to the high current density carried locally by the dendrite filament, ergo high thermal power ($P = I^2V$). Within the timespan of contact, amperes of short-circuit current can pass in 1-3 seconds but is immediately cut-off thanks to this fuse-like safety mechanism. This avoids catastrophic thermal runaway, and preserves the integrity of salvageable components (e.g. casing, other individual electrochemical cells assuming a battery module), unlike in the case for liquid organic electrolytes.

6.3.3 Thermal melting of Li metal on the ceramic electrolyte

Dendrite-induced failure problems in the lithium lanthanum zirconate garnets bear heavy resemblance to those encountered with sodium β -alumina technology during the 1970's. A number of models have attempted to explain the mechanics behind sodium metal penetration within sodium beta-alumina ceramic. Armstrong [34] argued that the presence of microcracks generated from mechanical polishing act as stress concentrators for dendrite initiation and propagation, using a Poiseuille pressure model, and later extended by Shetty *et al* [35]. Both models argue solely on mechanical pressure and Griffith mechanics, require an assumption of a Newtonian fluid behavior, fixed viscosities, laminar fluid flow, and assume a known uniform dendrite radius with fixed crack lengths. However, Virkar pointed that the model was severely flawed, experimental values did not comply with values obtained from their proposed equations by 2 -3 orders of magnitude [36]. Richman and Tennenhouse [37] hypothesized that stress-corrosion mechanisms were at work, and indeed Virkar demonstrated this with a sodium melt on top of a sodium beta alumina ceramic that did corrode the ceramic surface [36]. Virkar had done extensive work on the subject, especially with the demonstration of stable sodium ion transport across a pinholed ceramic while maintaining operating temperatures above the melting point of sodium, but abrupt metallic dendrite penetration at the fusion temperature [38]. In relation to this, it had also been argued in literature that high dopant concentrations decreased β -alumina resistance to metallic penetration due to a higher sodium stoichiometry [39].

The objective of this section therefore was to examine the corrosion behavior of high-temperature molten lithium (300°C) against the developed garnet ceramic composition: $\text{Li}_{6.55}\text{Ga}_{0.15}\text{La}_3\text{Zr}_2\text{O}_{12}$ (nominal). High temperatures were expected to induce large ionic exchange currents at the interface of two distinct materials, and cause breakdown of passivation layers, if any.

Three samples sintered using different protocols were tested: (a) 1200°C for 6h under O_2 atmosphere (90% relative density), (b) 1200°C for 6h under Ar atmosphere (91% relative density) and c) 1200°C for 48h under O_2 atmosphere (93% relative density). The ceramic stability tests against molten lithium were carried out under dynamic vacuum (0.01 mbar). The visual results are displayed in Figure 6.22. Prior to contact with molten lithium metal, all three polished samples exhibited a smooth luster (Figure 6.22a-c). The samples sintered for only 6h under either O_2 or Ar exhibited a dark discoloration which diffused throughout the thickness of the ceramic, and caused pellet fractures, as shown by Figure 6.22d-e. On the other hand, the sample sintered for 48h under O_2 maintained excellent structural integrity, with no hint of degradation-related creep.

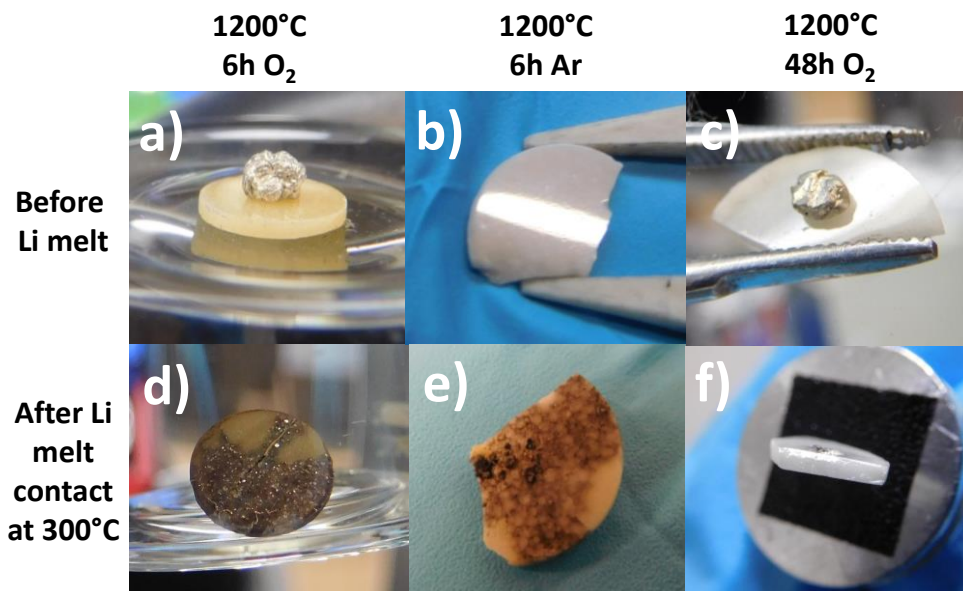


Figure 6.22: Polished ceramics obtained from sintering at 1200°C for a) 6h under 99.99% O_2 atmosphere b) 6h under 99.9% Ar atmosphere and c) 48h under 99.99% O_2 atmosphere; (d-f) the respective ceramics after contact to molten lithium at 300°C: d and e show the surfaces opposite the lithium metal contact, whereas f shows a fractured cross-section produced by breaking the pellet in the middle after the melt test.

Electron micrographs suggested that the ceramic degradation induced by hot lithium metal propagated along grain boundaries attacking oxides containing aluminum or gallium (Figure 6.23). Indeed, Eichinger had previously reported that of all lithium aluminates, only Li_5AlO_4 did not exhibit a severe reaction upon contact with molten lithium metal [40]. In Eichinger's study, the samples which did react suggested a LiAl decomposition product as deduced from XRD patterns, and displayed a visual black discoloration creeping along ceramic samples. In relation to the present material, there is a high likelihood that lithium gallate minority phases may have also displayed similar behavior.

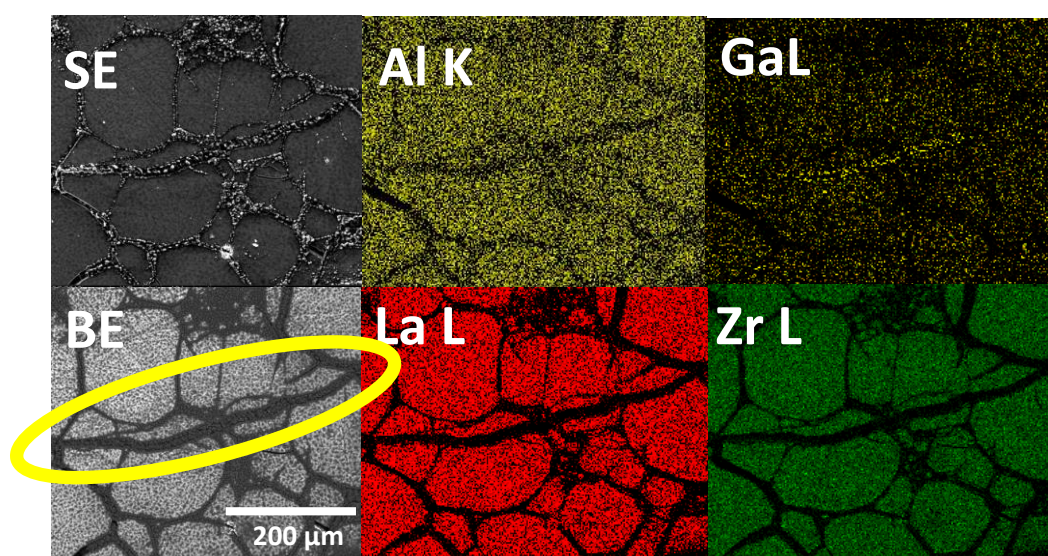


Figure 6.23: EDAX mapping of the ceramic sample sintered at 1200°C for 6h under O_2 atmosphere after exposure to a lithium metal melt at 300°C (Figure 6.22c) The yellow marker indicates a transgranular fracture line.

Detecting any hints of this aluminate or gallate decomposition behavior was made specially challenging due to the very low level of dopant concentrations (Al and Ga). Meticulous examination, nonetheless, eventually enabled acquisition of the backscattered electron images in Figure 6.24. Light-element outgrowths were detected sprouting from ceramic fracture lines (e.g. Figure 9.25a). Within the outgrowths, spheres composed of heavier elements (e.g. Figure 9.25b-c) were detected, the shape suggesting the material's existence in the liquid state at one point.

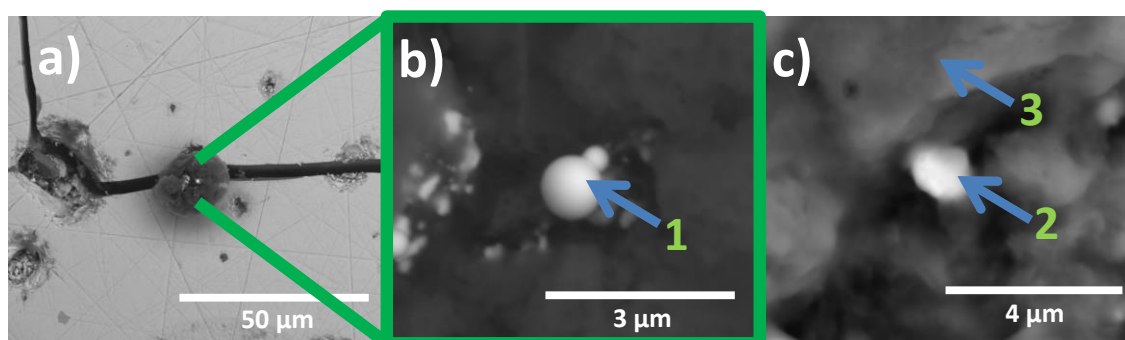


Figure 6.24: Backscattered electron images (12kV beam voltage) of Ga_{0.15}-LLZO ceramic samples after exposure to molten lithium metal. a/b) sintered for 6h under 99.9% Ar atm, and c) sintered for 6h under 99.99% O₂ atm. b is a magnified view of a. Arrows denote where point-EDAX spectra were taken (12kV beam voltage).

EDAX elemental profiling (Table 6.2) indicated the spheres to be overwhelmingly rich in gallium. It can be inferred that at 300°C, liquid lithium had extracted the gallium component from the grain boundaries of the ceramic, and promoted its reduction to a liquid metallic state which solidified upon cooling to room-temperature. This was evident from three facts: (a) lithium gallates are crystalline from room-temperature to 1100°C, hence would have always existed in the solid state under the present experimental conditions (300°C max temperature)[41-43]; (b) the known phase diagram for the Li-Ga system indicates no intermediate eutectic for the Ga-rich compositions (Figure 6.25); (c) the melting point of gallium metal is quite low (29°C).

Table 6.2: Elemental atomic percentages obtained by EDAX point analyses at a 12kV beam voltage for the regions marked in Figure 6.24b-c.

	Point 1	Point 2	Point 3
Element	At%	At%	At%
C (K line)	5.6	50.4	60.9
O (K line)	23.1	17.7	23.6
Ga (L line)	69.9	22.4	0.2
Al (K line)	0.3	8.6	0.3
La (L line)	0.6	0.7	8.6
Zr (L line)	0.4	0.2	6.3

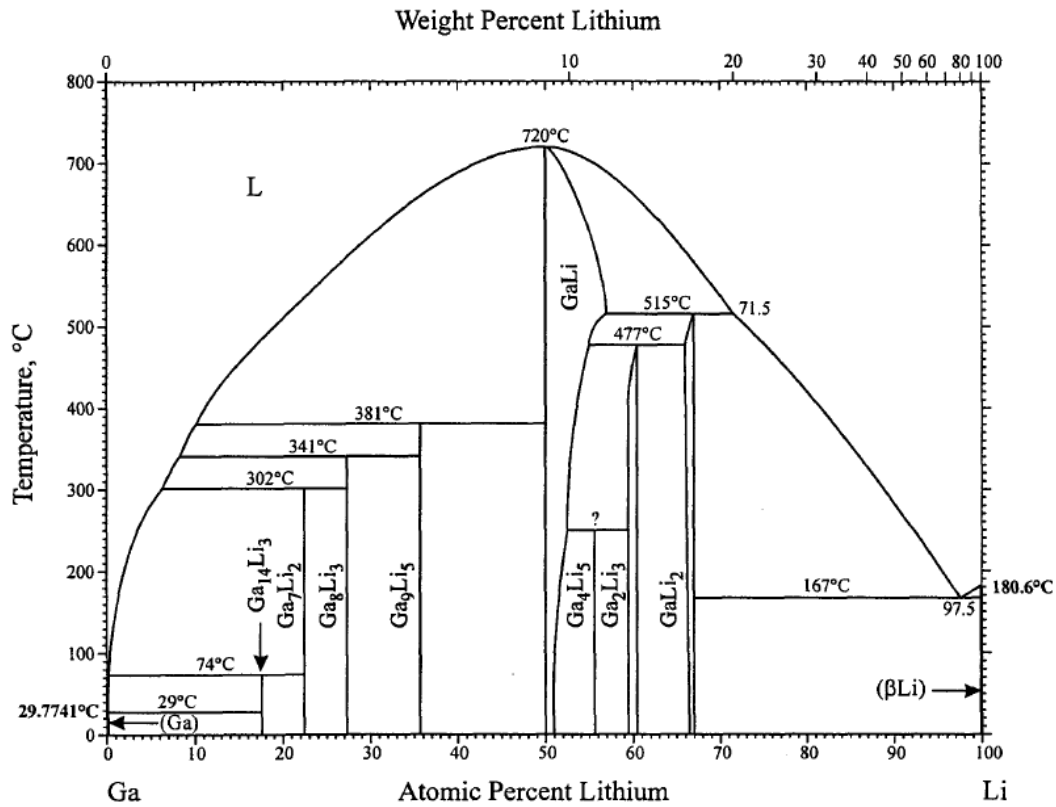


Figure 6.25 Phase diagram of the Ga-Li system [44].

EDAX linescans were further employed to investigate the effects of molten lithium contact on the ceramic. The dark areas in Figure 6.26a-c indicate areas with remnant lithium metal after surface scraping, with EDAX linescan directions as indicated by the inset arrows. Elemental ratios were taken against either the La L or the Zr L lines, and indicated higher concentrations of Al and Ga within or beneath the lithium metal. Furthermore, a decrease in the La/Zr ratio hinted the formation of the La₂Zr₂O₇ pyrochlore secondary phase, a major LLZO decomposition product as predicted by ab-initio thermodynamic simulations [45].

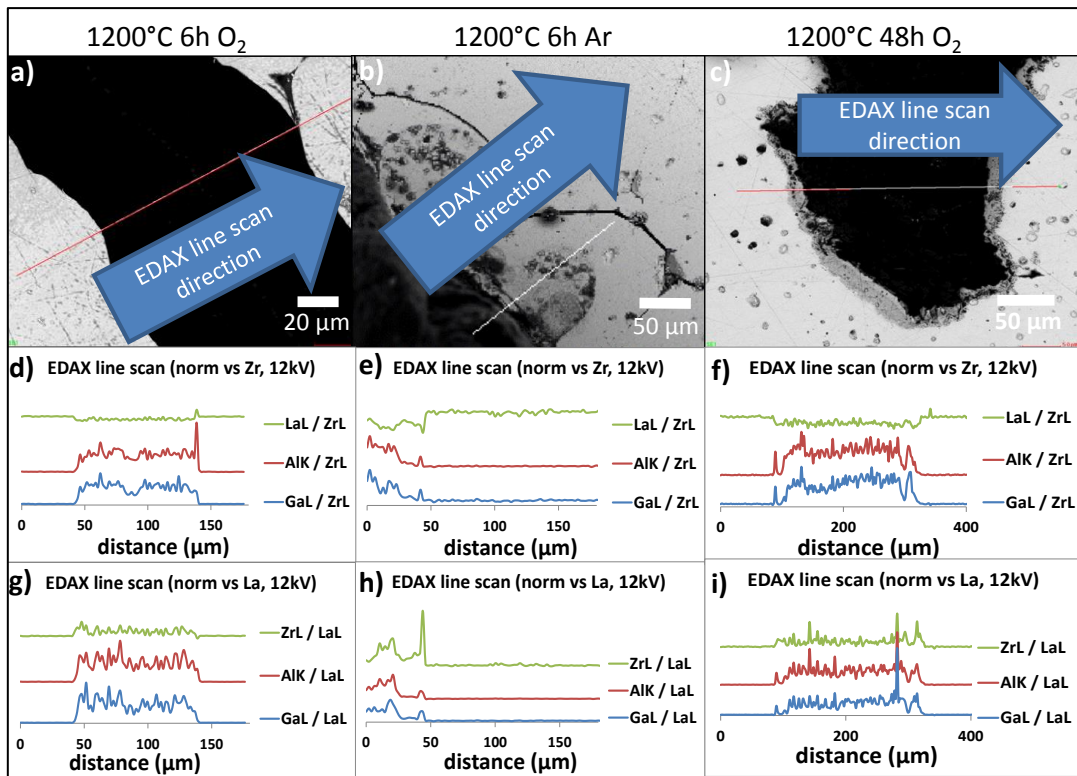


Figure 6.26 Backscattered electron images (a-c, 12kV beam voltage) and EDAX line scans (e-i, 12kV beam voltage) across ceramic surfaces previously subjected to molten lithium contact, showing increased Al and Ga content in the lithium-rich areas.

Finally, the lithium melt-exposed ceramics were immersed in distilled H_2O and monitored. The discolorations persisted for 3 months (Figure 6.27), indicating a permanent chemical degradation rather than simple mechanical penetration by metallic dendrites. This was in contrast to lithium-metal polarization experiments at room-temperature (Figure 6.16), wherein the impurities formed dissolved within 2 hours in distilled H_2O .

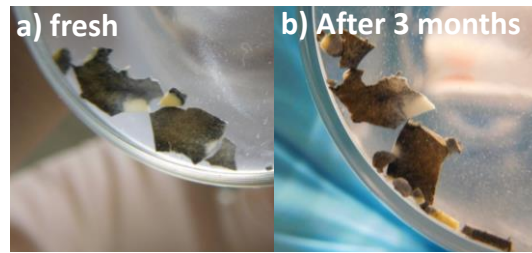


Figure 6.27 Photographs of the ceramic ($\text{Ga}_{0.15}\text{-LLZO}$ sintered at 1200°C for 6h under 99.99% dry oxygen) immersed in distilled H_2O after the molten lithium stability test, taken at two points in time: (a) right after placing in water (b) after 3 months.

This suggests that $\text{Ga}_{0.15}\text{-LLZO}$ ceramic failure occurs by two mechanisms, as had been deconvoluted in this study: (1) localized mechanical stress (Figure 6.28a) and (2) chemical corrosion (Figure 6.28b)

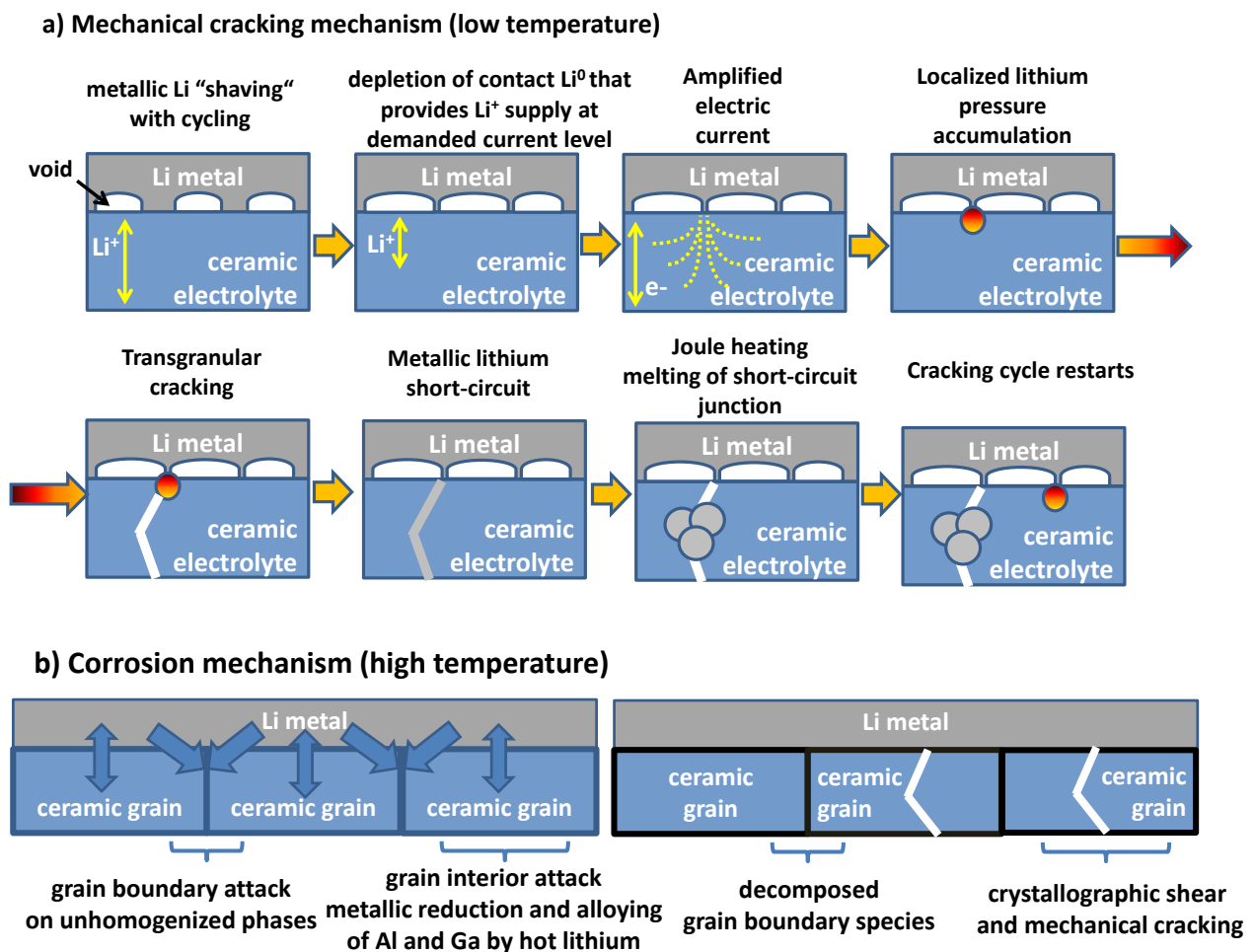


Figure 6.28: Proposed failure mechanism of ceramic electrolytes under electrochemical polarization in contact with Li metal (a) mechanical cracking and (b) corrosion mechanisms.

6.4 Chapter summary and perspectives

A Li-metal battery cell employing a highly-conductive garnet oxide electrolyte as solid anolyte and LP30 as liquid catholyte had been cycled. Galvanostatic charge/discharge curve profiles indicated remarkable system performance and minimal charge-transfer polarization for preliminary cycles but failure under prolonged fatigue. The latter had been simulated using repeated cycling voltammetry with cutoff voltages at -0.5V and 3V.

Electrochemical anomalies arose during the charging steps, but ~99% capacity retention and full discharge capacity were observed during the discharge steps, indicating full cell-level access to the cathode active material. Post-mortem analyses indicated solid electrolyte discoloration extending from the anode side to the cathode side, suggesting metallic dendrite penetration. Previous works on sodium beta-alumina and lithium-stuffed garnet oxides have recorded accounts of metallic alkali dendrite formation, but no direct elemental state identification. In this study, ^7Li -specific solid-state NMR directly confirmed the presence of Li metal and its sparing existence as contiguous clusters within the garnet ceramic. The findings support Long *et al*'s results and constitutes the first unequivocal direct observation of lithium metal dendrites within a garnet-based material during a full-cell battery operation [6].

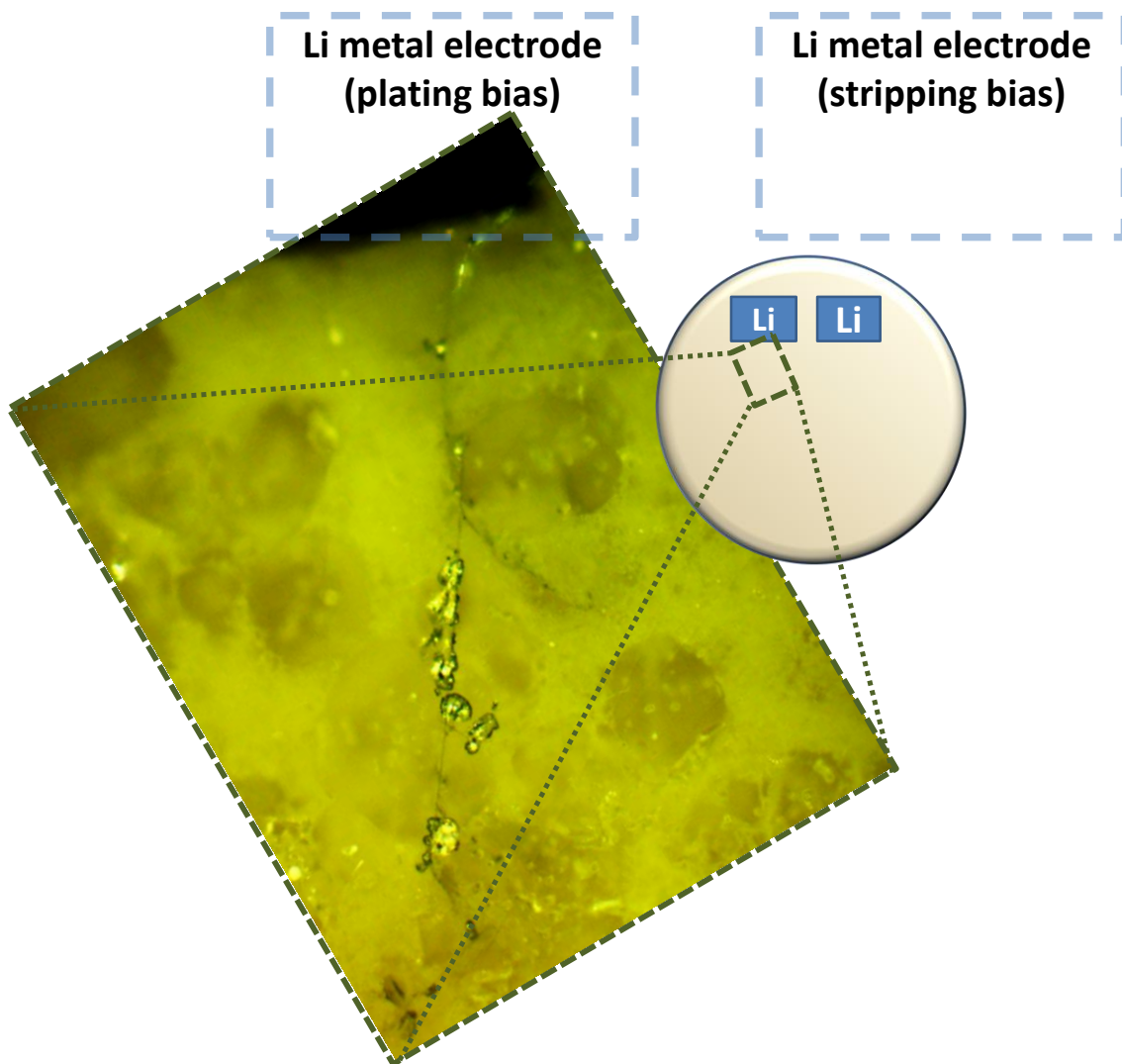


Figure 6.29: Eruption of lithium metal through a fracture line created by electrodeposition pressurization. Arrows indicate positions of lithium metal electrodes and the center of the tested ceramic pellet.

An extension in terms of Newtonian mechanics of the electrochemical rationalization of dendrite penetration within ceramic electrolytes has been proposed, which while rather simplistic in mathematical accuracy, does offer a plausible conceptual explanation of the initiation and propagation events accompanying ceramic failure. While exhibiting similarities to Virkar's explanation of sodium beta alumina failure, the present study has experimentally demonstrated that localized pressurization produces fracture lines through which pressurized lithium metal is guided into mechanically, and not necessarily electrochemically. Figure 6.29 provides an example wherein the pathway chosen by lithium metal growth from the anode, is away from and shows no relation to the expected current field lines.

This is the mechanism occurring at low temperatures, wherein areal current densities are insufficiently homogenized as a consequence of poor initial contacts between lithium metal and the ceramic electrolyte, and prolonged lithium stripping/plating. It is also argued that dendritic penetration is inevitable due to the enormous local pressures that can be generated with a modest voltage polarization ($\sim 0.25\text{V}$), unless some form of dynamic external aid applied, i.e. either an applied pressure to flatten point contacts during electrodeposition, apply a coating that inherently promotes uniform lithium wetting, or increase temperatures to level off disparities in ionic/electronic transport during lithium stripping and preserve as much of the immediate contact areas between the lithium metal and the ceramic electrolyte as possible.

It is also argued that the degree of current-line anisotropy within the garnet ceramic increases with grain size, as demonstrated with the preferential orientation of fracture lines (Figure 6.12). Hall-Petch strengthening provides all the more reason to produce sintered ceramics with smaller grain sizes, or standalone single crystals altogether. It is concluded that ceramic failure on a grain to grain basis is inevitable. What can be done is extend the ceramic lifetime as long as possible prior to failure.

Another curiosity with regards to failure during low-temperature operation is that any short-circuit induces immediate Joule heating and a fuse-like mechanism, which instantaneously disconnects the two electrodes from further damage. Finally, it was shown that at a high temperatures (300°C), irreversible corrosion effects dominate on the ceramic upon lithium metal contact, as evidenced by extraction, electrochemical reduction and alloying of certain elements with lithium metal.

REFERENCES:

- [1] Hovington, P., Lagaca, M., Guerfi, A., Bouchard, P., Mauger, A., Julien, C. M., Armand, M. and Zaghib, K. *Nano Letters* **15**(4), 2671–2678 (2015).
- [2] Sudo, R., Nakata, Y., Ishiguro, K., Matsui, M., Hirano, A., Takeda, Y., Yamamoto, O. and Imanishi, N. *Solid State Ionics* **262**, 151 – 154 (2014).
- [3] Sharafi, A., Meyer, H. M., Nanda, J., Wolfenstine, J. and Sakamoto, J. *Journal of Power Sources* **302**, 135–139 (2016).
- [4] Cheng, L. *Interface engineering of garnet solid electrolytes*. PhD thesis, UC Berkeley, (2015).
- [5] Ishiguro, K., Nakata, Y., Matsui, M., Uechi, I., Takeda, Y., Yamamoto, O. and Imanishi, N. *Journal of the Electrochemical Society* **160**(10), A1690–A1693 (2013).
- [6] Tsai, C.L., Roddatis, V., Chandran, C. V., Ma, Q., Uhlenbruck, S., Bram, M., Heitjans, P. and Guillon, O. *ACS Applied Materials & Interfaces* **8**(16), 10617–10626 (2016).
- [7] Yow, Z. F., Oh, Y. L., Gu, W., Rao, R. P. and Adams, S. *Solid State Ionics* **292**, 122 – 129 (2016).
- [8] Mahootcheian Asl, N., Kim, J.H., Pieczonka, N. P. W., Liu, Z. and Kim, Y. *Electrochemistry Communications* **32**, 1–4 (2013).
- [9] Asl, N. M., Keith, J., Lim, C., Zhu, L. and Kim, Y. *Electrochimica Acta* **79**, 8 – 16 (2012).
- [10] Yamada, A., Chung, S. C. and Hinokuma, K. *Journal of the Electrochemical Society* **148**(3), A224–A229 (2001).
- [11] Pan, J., Cheng, Y.T. and Qi, Y. *Physical Review B* **91**(13), 134116 (2015).
- [12] Buschmann, H., Doelle, J., Berendts, S., Kuhn, A., Bottke, P., Wilkening, M., Heitjans, P., Senyshyn, A., Ehrenberg, H., Lotnyk, A., Duppel, V., Kienle, L. and Janek, J. *Physical Chemistry Chemical Physics* **13**(43), 19378–19392 (2011).
- [13] Cheng, L., Crumlin, E. J., Chen, W., Qiao, R., Hou, H., Lux, S. F., Zorba, V., Russo, R., Kostecki, R., Liu, Z., Persson, K., Yang, W., Cabana, J., Richardson, T., Chen, G. and Doeff, M. *Physical Chemistry Chemical Physics* **16**(34), 18294–18300 SEP 14 (2014).
- [14] Ren, Y., Shen, Y., Lin, Y. and Nan, C.W. *Electrochemistry Communications* **57**, 27–30 August (2015).
- [15] Demers, H., Poirier-Demers, N., Couture, A. R., Joly, D., Guilmain, M., de Jonge, N. and Drouin, D. *Scanning* **33**(3), 135–146 (2011).
- [16] Bernuy-Lopez, C., William Manalastas, J., del Amo, J. M. L., Aguadero, A., Aguesse, F. and Kilner, J. A. *Chemistry of Materials* **26**(12), 3610–3617 (2014).
- [17] Kuhn, A., Narayanan, S., Spencer, L., Goward, G., Thangadurai, V. and Wilkening, M. *Physical Review B* **83**(9), 094302 (2011).
- [18] Bhattacharyya, R., Key, B., Chen, H., Best, A. S., Hollenkamp, A. F. and Grey, C. P. *Nature Materials* **9**(6), 504–510 (2010).
- [19] Bach, P., Stratmann, M., Valencia-Jaime, I., Romero, A. and Renner, F. *Electrochimica Acta* **164**, 81 – 89 (2015).
- [20] Virkar, A. V. *Failure of Ion-Conducting Materials by Internal Precipitation Under Electrolytic Conditions, in Engineered Ceramics: Current Status and Future Prospects*. John Wiley & Sons, Inc., Hoboken, NJ, USA, (2016).
- [21] Kim, B., Hiraga, K., Morita, K. and Sakka, Y. *Nature* **413**(6853), 288–291 SEP 20 (2001).
- [22] Ni, J. E., Case, E. D., Sakamoto, J. S., Rangasamy, E. and Wolfenstine, J. B. *Journal of Materials Science* **47**(23), 7978–7985 DEC (2012).
- [23] Deng, Z., Wang, Z., Chu, I.H., Luo, J., and Ong, S. P. *Journal of the Electrochemical Society* **163**(2), A67–A74 (2016).
- [24] Wolfenstine, J., Jo, H., Cho, Y.-H., David, I. N., Askeland, P., Case, E. D., Kim, H., Choe, H. and Sakamoto, J. *Materials Letters* **96**, 117–120 (2013).
- [25] Yu, S., Schmidt, R. D., Garcia-Mendez, R., Herbert, E., Dudney, N. J., Wolfenstine, J. B., Sakamoto, J. and Siegel, D. J. *Chemistry of Materials* **28**(1), 197–206 (2016).
- [26] Schultz, R. *Lithium: measurement of Young's modulus and yield strength*. Fermilab: Technical report TM-2191 (2002).

- [27] Williams, R.K., Coleman, G.L. and Yarbrough, D.W. *An evaluation of some thermodynamic and transport properties of solid and liquid lithium over the temperature range 200K to 1700K*. Oak Ridge National Laboratory: Technical report TM-10622 (1988).
- [28] Jeppson, D.W., Ballif, J.L., Yuan, W.W. and Chou, B.E. *Lithium literature review: Lithium properties and interactions*. Hanford Engineering Development Laboratory: Technical report HEDL-TME 78-15,UC-20 (1978).
- [29] Wang, Z. H. and Ni, M. J. *Heat and Mass Transfer* **48**(2), 253–257 (2012).
- [30] Hultsch, R. *The pressure dependence of self-diffusion in lithium and sodium*. PhD thesis, Iowa State University, (1961).
- [31] Tariq, S., Ammigan, K., Hurh, P., Schultz, R., Liu, P. and Shang, J. In *Proceedings of the 2003 Particle Accelerator Conference, Vols 1-5*, Chew, J and Lucas, P and Webber, S, editor, 1452–1454, (2003). 20th Biennial Particle Accelerator Conference, Portland, OR, MAY 12-16, 2003.
- [32] Guillaume, C. L., Gregoryanz, E., Degtyareva, O., McMahon, M. I., Hanfland, M., Evans, S., Guthrie, M., Sinogeikin, S. V. and Mao, H.K. *Nature Physics* **7**(3), 211–214 (2011).
- [33] Schmidt, R. D. and Sakamoto, J. *Journal of Power Sources* **324**, 126 – 133 (2016).
- [34] Armstrong, R., Dickinson, T. and Turner, J. *Electrochimica Acta* **19**(5), 187 – 192 (1974).
- [35] Shetty, D., Virkar, A., Bradt, R. G. R. and Hasselman, D. *Fracture mechanics of ceramics, Vol. 4*. Plenum Press: New York (1978). p. 65.
- [36] Viswanathan, L. and Virkar, A. *Journal of Materials Science* **17**(3), 753–759 (1982).
- [37] Richman, R. and Tennenhouse, G. *Journal of the American Ceramic Society* **58**, 63–67 (1975).
- [38] Virkar, A. and Viswanathan, L. *Journal of the American Ceramic Society* **62**(9-10), 528–529 (1979).
- [39] Sudworth, J. and Tiley, A. *Sodium Sulphur Battery*. Springer Science & Business Media, (1985).
- [40] Eichinger, G. *Solid State Ionics* **2**(4), 289–295 (1981).
- [41] Datta, R. *Journal of the American Ceramic Society* **54**(5), 119-272 (1971).
- [42] Chang, C. *Chemical reactions at high pressures and high temperatures*. PhD thesis, Rice University (1967).
- [43] Golubev, N. V., Ignat'eva, E. S., Sigae, V. N., Lauria, A., De Trizio, L., Azarbod, A., Paleari, A. and Lorenzi, R. *Physical Chemistry Chemical Physics* **17**(7), 5141–5150 (2015).
- [44] Okamoto, H. *Journal of Phase Equilibria* **20**(1), 92 (1999).
- [45] Zhu, Y., He, X. and Mo, Y. *ACS Applied Materials and Interfaces* **7**(42), 23685–23693 (2015).

7 General conclusions and perspectives

A survey of candidate solid electrolytes suggested that garnet-structured oxide ceramics possess the best combination of ionic conductivity, electronic insulation and electrochemical stability for use in lithium-metal batteries. Thus, efforts were concentrated on this material class, specifically pristine $\text{Li}_5\text{La}_3\text{Ta}_2\text{O}_{12}$ and $\text{Li}_{7-3x}\text{Ga}_x\text{La}_3\text{Zr}_2\text{O}_{12}$ ceramic preparations.

The solid-state-route and the citrate-route were compared in the syntheses of $\text{Li}_5\text{La}_3\text{Ta}_2\text{O}_{12}$. The citrate-route produced denser ceramics. The materials synthesized with this protocol exhibited grain boundary resistances negligible compared to bulk resistances due to ceramics being composed of interconnected large ($>100\mu\text{m}$) grains. The measured ionic conductivities displayed a positive trend with respect to ceramic densification, but no correlation with crystallographic lattice parameter. The same finding was reaffirmed with $\text{Li}_{7-3x}\text{Ga}_x\text{La}_3\text{Zr}_2\text{O}_{12}$ ceramics.

Via a pore-redistribution model, a fully-densified $\text{Li}_5\text{La}_3\text{Ta}_2\text{O}_{12}$ material was predicted to have a maximum attainable ionic conductivity of $\sim 80 \mu\text{S}/\text{cm}$ (25°C). Manipulation of the lithium stoichiometry by aliovalent doping was reasoned necessary to surpass this limit. Indeed, Sc-doping stood to improve the bulk conductivity to $160 \mu\text{S}/\text{cm}$ or higher. Substitution with Zn failed, which segregated to act apparently as a sintering aid during firing. Reactive sintering was rationalized to be an ineffective synthesis route, due to the almost 40% reduction in atomic packing volume with garnet-phase formation.

On the other hand, $\text{Li}_{6.55}\text{Ga}_{0.15}\text{La}_3\text{Zr}_2\text{O}_{12}$ exhibited more than $1 \text{ mS}/\text{cm}$ ionic conductivity at room-temperature. Its crystal structure: Ga-entry upon Li (24d) sites on substitution in $\text{Li}_7\text{La}_3\text{Zr}_2\text{O}_{12}$ was confirmed, which achieved two designed goals: lowering the stoichiometric lithium count and stabilizing the targeted cubic-phase. The action of atmospheric moisture was highlighted as detrimental during high-temperature synthesis of the composition. Surface corrosion (LiOH formation) as a consequence of $\text{Li}^+\text{-H}^+$ exchange was evident at ambient conditions, but this was shown via sputtered ion depth-profiling (FIBSIMS) to be self-limiting. This meant that ceramics, once fabricated, can be transported as normal cargo, and upon arriving at the assembly plant, only the superficialities ($\sim 5 \mu\text{m}$) need be sputtered away to reveal pristine ceramics within.

The sintering behavior of the garnet oxides was shown to be highly dependent on the eutectic melt behaviors. Liquid phase sintering in LLZO-based compositions is more facile due to mutually-interacting melt action from $\text{Li}_2\text{O}-\text{Al}_2\text{O}_3$ (1055°C) and $\text{Li}_2\text{O}-\text{ZrO}_2$ eutectics (1050°C). This contrasts with $\text{Li}_2\text{O}-\text{Al}_2\text{O}_3$ (1055°C) and $\text{Li}_2\text{O}-\text{Ta}_2\text{O}_5$ (1550°C) eutectic systems encountered in sintering $\text{Li}_5\text{La}_3\text{Ta}_2\text{O}_{12}$, explaining the marked difficulty to sinter $\text{Li}_5\text{La}_3\text{Ta}_2\text{O}_{12}$ green bodies for all the temperatures tested.

A full-cell battery incorporating a high-conductivity ceramic $\text{Li}_{6.55}\text{Ga}_{0.15}\text{La}_3\text{Zr}_2\text{O}_{12}$ was demonstrated to cycle. The discharge steps indicated full access to the cathode material thanks to a wetting catholyte, but the charge steps occurred with Li dendrite penetration through the ceramic. The metallic propagation was examined visually using SEM, Raman and optical microscopy. It was shown that garnet ceramics failed when polarized in contact with lithium metal via two modes: (a) localized build-up of lithium pressure (ambient temperature) and (b) corrosion by selective alloying at high temperatures (300°C).

The action of how external pressure, specifically on the lithium foil undergoing electrodeposition, improves metal/ceramic interfacial contact was rationalized using Bernoulli dynamics (Appendix C). On the other hand, a fluid compression model (Appendix D) as a function of applied voltage bias suggested that metallic lithium dendrites are inevitable. Failure due lack of mechanical compliance of both the ceramic and lithium metal, and current focusing, cannot be prevented, but can be delayed. This can be accomplished by introducing Griffith fracture disruptors such as pores which distribute stress forces to a larger area or improving the ceramic wettability to Li metal via the use of coatings. This study believes that producing homogeneously smaller grains (close to the amorphization limit) or a single crystal is a prerequisite for maximizing the lifetime of a ceramic electrolyte.

On the basis of more fundamental studies, such as determining intrinsic charge-transfer resistances and exchange currents between lithium metal and the ceramic, vapor deposition techniques on thin film substrates are recommended to establish favorable initial contacts. Afterwards Butler-Volmer or Tafel-type kinetic studies could be carried out.

A. On the model used for molecular dynamics simulations

For a basic unit cell of the garnet structure, the ensemble for computation consists of a minimum of 163 atoms. Whereas first-principle methods (e.g. DFT) provide accuracy by encompassing quantum orbital-dependent interactions, computing time increases exponentially with heavy atom count and symmetry reduction. This means a routine 1x1x1 simulation run (atom count in one unit cell) taking 2 weeks, translates to over a year for a 3x3x3 simulation (atom count in 27 unit cells) using the same platform. Further, adding a dopant atom (foreign element) increases the complexity by breaking symmetry constraints that normally expedite analytical convergence. These two effects mean that first-principle methods are forced by time considerations to run in constrained simulation sizes for doped materials, and therefore always run the risk of periodic boundary artefacts. This is a fundamental weakness, because events occurring in a single unit cell are not necessarily mirrored simultaneously in all the thousands of unit cells in a single crystal, thus invalidating any conclusions.

Conversely, entropy dictates that, not one, but a distribution of Li atom-dopant-vacancy configurations can exist that minimizes lattice energy. A fast, high-throughput, statistical approach using large supercells (e.g. 3 x 3 x 3 or higher) is therefore necessary both to minimize the mirroring problem and derive energetically favourable configurations.

B. On the thermal reduction of Li^+ , Ga^{3+} , La^{3+} and Zr^{4+} ions to their metallic states

An Ellingham diagram provides information (Figure B.1) on the thermodynamic spontaneity of elemental reduction to metals, This is on the basis of temperature and oxygen partial pressures ($p\text{O}_2$). Why the two factors influence can be explained as follows: A higher temperature provides more kinetic energy to break bonds in metal-oxide lattices. When these bonds are broken the metal and oxygen species can remain separated or recombine. By adding or removing oxygen molecules (i.e. varying $p\text{O}_2$), the metal oxide or the metal can be the thermodynamically dominant state. Quite simply, this is a nuancing of equilibrium being a dynamic phenomenon, and of Le Chatelier's principle.

In these regards, Hess' law can also be applied. Materials with exergonic reactions can provide both the energy source and the oxygen scavenger, in order to promote the reduction of a metal oxide. Examples are carbothermal reduction pathways utilizing C or CO.

Ellingham drafted the diagram in such a way that the equilibrium $p\text{O}_2$ at any given temperature can be determined graphically. This is done by drawing a straight line from the point defined by the intersection of zero energy on the ordinate and absolute zero (0 K) on the abscissa, towards and crossing through the temperature point along the Ellingham lines for the system in question. To illustrate in Figure B.1, to effect spontaneous reduction of Li_2O , Al_2O_3 and ZrO_2 to metallic states by heating and vacuum purging, a $p\text{O}_2$ of less than 10^{-26} bar is needed even at 1300°C . Even if a carbon source were provided (e.g. from reduced carbonates), the equilibrium $p\text{O}_2$ would still be at about 10^{-17} bar. Because Figure B.1 is given in atm units, the reader is reminded that 1 atm pressure is roughly equal to 1 bar pressure. (1 atm = 1.01325 bar)

Ellingham Diagrams

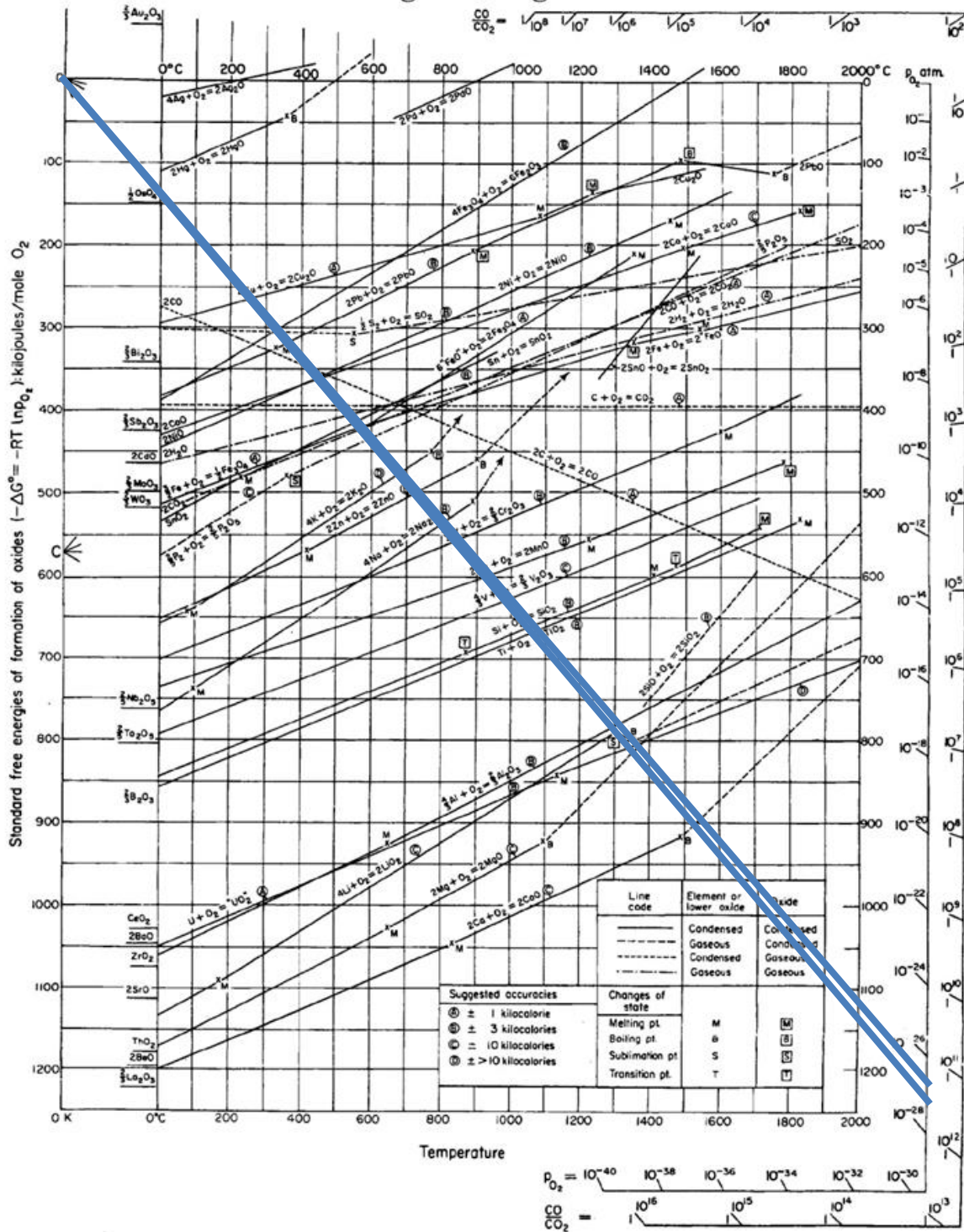


Figure B.1: Ellingham diagram representing thermodynamic net formation energies of elemental oxides from their respective metal equivalents under standardized O_2 partial pressure conditions, reproduced as drawn by HJT Ellingham. The blue lines indicate the O_2 partial pressures at which the metal vs metallic oxide are in steady-state equilibria at $2000^\circ C$ [1].

Some additional phase diagrams as a function of temperature and $p(\text{O}_2)$ are also given in Figure B.2. At a temperature of 1300°C , the $p\text{O}_2$ above which the elemental reduction of La_2O_3 (a), Ga_2O_3 (b) and Al_2O_3 (c) occurs spontaneously are 10^{-40} , 10^{-11} and 10^{-25} bar respectively.

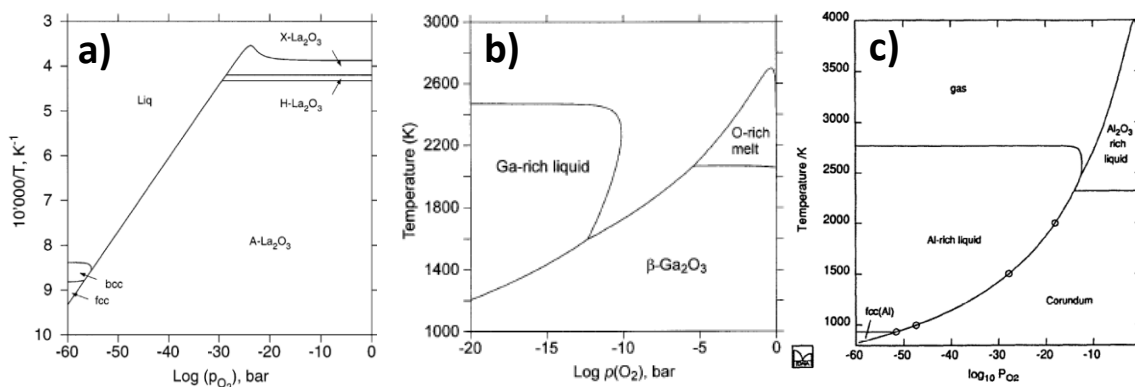


Figure B.2: Phase diagrams for the a) La-O system [2], b) Ga-O system [3] and c) Al-O system [4], where the abscissa are given as dependencies to $\log(p\text{O}_2)$ expressed in bars.

For reference, the best turbomolecular and diffusion pumps available commercially can achieve a reduced pressure of 10^{-13} bar value at lowest, and only under very stringent setups. On the other hand, a nominal 99.99% pure Ar-flow would only reduce $p\text{O}_2$ to between 10^{-6} and 10^{-2} bar, assuming complete gas displacement.

Therefore given that syntheses conditions always have higher $p\text{O}_2$ than the equilibrium values, industrial firing conditions under O_2 , Ar, vacuum or even N_2 would unlikely affect material chemistry from an elemental reduction standpoint, provided they are extremely dry.

This, of course, does not discount the possibility that small amounts (<7%) of oxygen vacancies may be introduced as demonstrated by Carniglia *et al* for ZrO_2 [5]. Insufficient data is available from literature to determine effects on ternary oxides and eutectic compositions, based from this analysis.

C. Modeling of lithium as a fluid reservoir

A hypothetical setup (Figure C.1) is examined based on Bernoulli's principles applied to two fluid reservoirs connected by a bottleneck, essentially a rephrasing of the law of energy conservation using a mechanical pressure energy term (P), a flux-related kinetic energy term ($\frac{1}{2}\rho v^2$) and a gravitational potential energy term (ρgh). Assuming conditions of lithium incompressibility (constant ρ_{Li}), negligible height difference ($h_1=h_2$) and that lithium flux (v) is constrained by ion migration through the ceramic electrolyte, it can be shown that:

$$\begin{aligned}
 P_1 + \frac{1}{2}\rho_{Li}v_1^2 + \rho gh_1 &= P_2 + \frac{1}{2}\rho_{Li}v_2^2 + \rho gh_2 \\
 P_1 - P_2 &= \frac{1}{2}\rho_{Li}(v_2^2 - v_1^2) \\
 P_1 - P_2 &= \frac{1}{2}\rho_{Li}\left[\left(\frac{kI}{A_2}\right)^2 - \left(\frac{kI}{A_1}\right)^2\right] \\
 P_1 - P_2 &= \frac{1}{2}\rho_{Li}\left[\left(\frac{kV}{R_2}\right)^2 - \left(\frac{kV}{R_1}\right)^2\right] \\
 P_1 - P_2 &= \frac{1}{2}\rho_{Li}k^2I^2\left[\left(\frac{1}{A_2}\right)^2 - \left(\frac{1}{A_1}\right)^2\right] = \frac{1}{2}\rho_{Li}k^2V^2\left[\left(\frac{1}{R_2}\right)^2 - \left(\frac{1}{R_1}\right)^2\right] \\
 \frac{P_1 - P_2}{I^2} &= \frac{1}{2}\rho_{Li}k^2\left[\left(\frac{1}{A_2}\right)^2 - \left(\frac{1}{A_1}\right)^2\right] \\
 \frac{P_1 - P_2}{V^2} &= \frac{1}{2}\rho_{Li}k^2\left[\left(\frac{1}{R_2}\right)^2 - \left(\frac{1}{R_1}\right)^2\right]
 \end{aligned}$$

where k correlates the measured current I to the volumetric flux, V is the applied voltage, R_1 is the interfacial resistance for the anode side, R_2 is the interfacial resistance for the cathode side, while A_1 and A_2 are the respective aggregate true contact areas. Here, the nominal contact areas are assumed identical.

Consider two scenarios with varied P_1 and P_2 . For the case when $P_1 \gg P_2$ and essentially no P_2 is applied, $A_1 > A_2$, i.e. lithium metal is uniformly being dissolved into solid solution but concentrates deposition onto a smaller area, initiating dendrites and setting off a cascade ultimately leading to catastrophic failure. For the case when $P_1 \ll P_2$ and essentially no P_1 is applied, $A_2 > A_1$, i.e. lithium metal is exhibiting the "shaving" behavior during dissolution as illustrated in Figure 6.10b, but is being electrodeposited more uniformly on the cathode for this bias step. What the expressions thus summarize essentially is that a larger pressure must always be applied on the side where lithium electrodeposition is occurring. The higher the current being passed (or voltage bias being held), the much greater the necessary applied pressure.

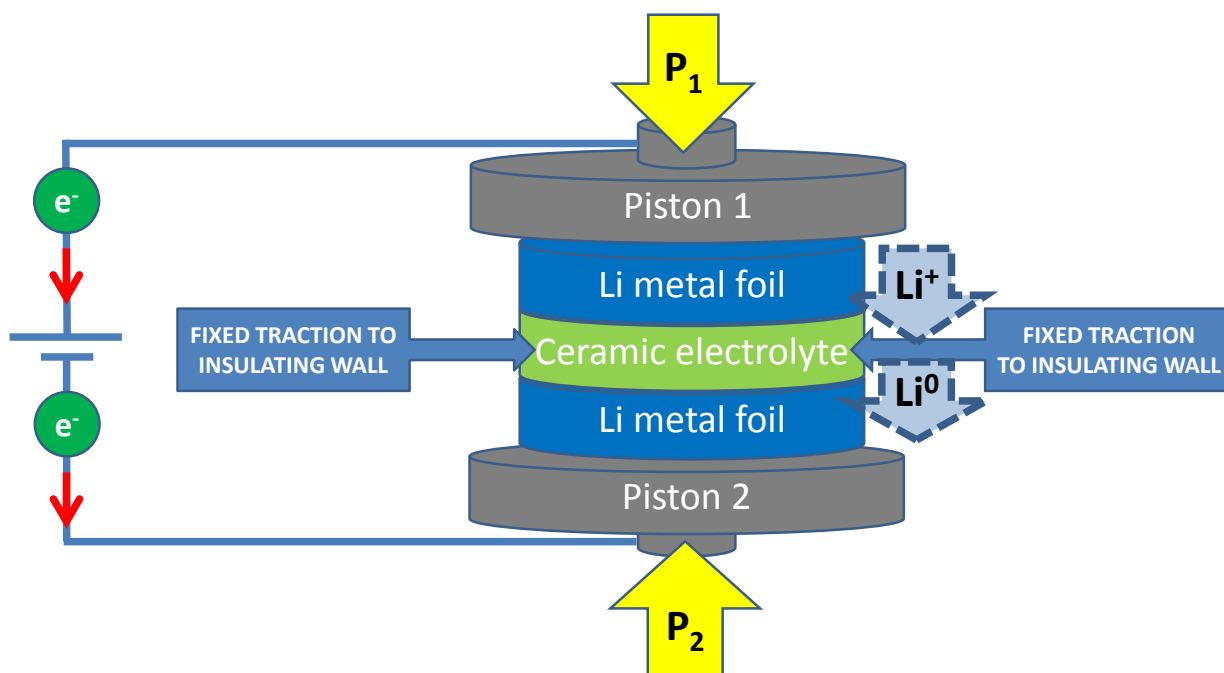


Figure C.1: Schema of possible mechanical macrovariables on a symmetric lithium cell utilizing a ceramic electrolyte. The ceramic electrolyte is held stationary in 3D space by fixed tractions, whereas mechanical pressing can be applied to either the lithium metal on the anode side (P_1 pressure by Piston 1) or on lithium metal on the cathode side (P_2 pressure by Piston 2) or both. Energy for electrochemical dissolution, transport through the electrolyte and redeposition on the opposite side is supplied by an external source.

When no external pressure is applied to the lithium foils, the expression predicts equal surface areas for electrodisolution/electrodeposition. That is, without mechanical flattening action, lithium plating occurs as dictated by the field lines established by initial contact areas. This would lead to the “shaving” effect alternately on each electrode as described in Figure 6.10b. Furthermore, the disparity in A_1 and A_2 , would be equalized by dendrite tips orthogonal to the nominal contact surface, since such formations provide the most efficient geometries in touching the most ceramic surface area. This would lead to progressive loss of planar contact surfaces with cycling, and dendrite formation at an exponential rate until eventual cell failure.

To counter the dendritic morphology of lithium electrodeposition, a ceramic surface with very high lithiophilicity is required.

D. Maximum compression work done at a point on the lithium metal/ceramic electrolyte interface with electrodeposition

The definition of bulk modulus (β) and isothermal compressibility(κ) are given by:

$$\frac{1}{\beta} = \kappa = -\frac{1}{V} \left(\frac{\partial V}{\partial P} \right)_T$$

κ is fairly constant for a liquid or a solid, and $\kappa \propto \frac{1}{P}$ for a gas.

With definite integration at constant temperature, the following relation holds when κ is constant:

$$\int_{P_0}^P \kappa dP = \int_{V_0}^V \left(-\frac{dV}{V} \right)$$

$$\kappa(P - P_0) = -\ln \frac{V}{V_0} \quad \rightarrow \quad P = \frac{1}{\kappa} \left(-\ln \frac{V}{V_0} \right) + P_0$$

$$e^{-\kappa(P-P_0)} = \frac{V}{V_0}$$

The definition of work (w) is given by:

$$\begin{aligned} w &= -\int_{V_0}^V P dV \\ &= -\int_{V_0}^V \left[\frac{1}{\kappa} \left(-\ln \frac{V}{V_0} \right) + P_0 \right] dV \\ &= \int_{V_0}^V \left[\frac{1}{\kappa} \left(\ln \frac{V}{V_0} \right) dV \right] - P_0 [V - V_0] \quad \text{: temporarily substitute dummy} \end{aligned}$$

variable $t = \frac{V}{V_0}$

$$\begin{aligned} &= -P_0 [V - V_0] + \int_1^t \left[\frac{V_0}{\kappa} (\ln t) dt \right] \\ &= -P_0 [V - V_0] + \frac{V_0}{\kappa} \left\{ [t \ln t]_1^t - \int_1^t t \left(\frac{1}{t} \right) dt \right\} \\ &= -P_0 [V - V_0] + \frac{V_0}{\kappa} [t \ln t - t + 1] \\ &= -P_0 V_0 [t - 1] + \frac{V_0}{\kappa} [1 - t(1 - \ln t)] \quad \text{: revert variables } t = \frac{V}{V_0} = e^{-\kappa(P-P_0)} \\ &= -P_0 V_0 [e^{-\kappa(P-P_0)} - 1] + \frac{V_0}{\kappa} \{1 - e^{-\kappa(P-P_0)} [1 + \kappa(P - P_0)]\} \end{aligned}$$

For a reversible process, $x = \kappa (P-P_0) \ll 1$

Hence, the exponential can be expanded in a Taylor series about $P=P_0$.

$$w = -P_0 V_0 [e^{-x} - 1] + \frac{V_0}{\kappa} \{1 - e^{-x} [1 + x]\} \quad \text{: But } e^x =$$

$$\sum_{n=0}^{\infty} \frac{x^n}{n!}$$

$$= -P_0V_0 [1 - x + O(x^2) - 1] + \frac{V_0}{\kappa} \{1 - [1 - x + \frac{x^2}{2} + O(x^3)][1 + x]\}$$

(where $O(x^2)$ and $O(x^3)$ are short-hand notations for the other Taylor series terms, with exponential diminution in magnitude for the 2nd, 3rd, 4th terms and so on so forth)

$$w = xP_0V_0 - P_0V_0O(x^2) + \frac{V_0}{\kappa} \{[1 - (1 - x + x - x^2 + \frac{x^2}{2})] + O(x^3)[1 + x]\}$$

$w = xP_0V_0 + \frac{V_0x^2}{2\kappa} + z$: where $z = -P_0V_0O(x^2) + \frac{V_0}{\kappa} \{O(x^3)[1 + x]\}$, which approaches 0

$$w = [\kappa(P - P_0)]P_0V_0 + \frac{V_0[\kappa(P - P_0)]^2}{2\kappa} + z$$

$$w = [\kappa(P - P_0)]P_0V_0 + \frac{V_0\kappa(P - P_0)^2}{2} + z$$

$$w = \frac{V_0\kappa}{2} [2PP_0 - 2P_0^2 + P_0^2 - 2PP_0 + P^2] + z$$

$$w = \frac{V_0\kappa}{2} [P^2 - P_0^2] + z \approx \frac{V_0\kappa}{2} [P^2 - P_0^2]$$

The bulk modulus(β) of Li is 11 GPa, which gives a compressibility factor (κ) of $9.1 \times 10^{-11} \text{ Pa}^{-1}$.

The molar volume of lithium at room-temperature is 0.01297 L/mol. Hence the compression work (\bar{w} , i.e. work per mole or $w = n\bar{w}$) done during lithium deposition is given:

$$\bar{w} \approx \frac{(0.01297 \text{ L/mol}) (9.1 \times 10^{-11} \text{ Pa}^{-1})}{2} [P^2 - P_0^2]$$

Consider a scenario with two uniform lithium plates, each of infinite area and thickness, placed parallel in opposite positions. The void in between is completely filled by an ideal electrolyte, with zero ionic charge transfer resistance for Li ions, and the concentration of lithium ions in the electrolyte is permanently constant. Since the concentration of lithium in lithium metal is unity, there are no transient contributions of enthalpies of mixing.

State functions are dependent only on the initial and final states.

If an atom or an atom cluster on the surface is moved from one electrode to the opposite, ΔU (internal energy) is zero for a miniscule change in lithium configuration (i.e. events in identical miller indices). The same can be estimated for ΔS . This implies $\Delta G \approx \Delta H \approx w$. **In other words in this system, the difference in Gibbs energy arising from an applied potential bias can be correlated to a maximum compression work, via the Nernst equation.** The ΔG and w are extrinsic variables with dependence on n or how many atoms, atom clusters or atom moles are involved.

This gives:

$$\Delta G = -nFE_{\text{cell}} = w = n(\bar{w}) = n \frac{(0.01297 \text{ L/mol}) (9.1 \times 10^{-11} \text{ Pa}^{-1})}{2} [P^2 - P_0^2]$$

$$\frac{-2FE_{\text{cell}}}{(0.01297 \text{ L/mol}) (9.1 \times 10^{-11} \text{ Pa}^{-1})} + P_0^2 = P^2$$

Assumption: ionization energy, sublimation enthalpy, energy of hydration cancel out instantaneous Li-Li⁺, Li⁺-Li, no mass transfer limitation. This means that in such an ideal electrolyte, 0.1 to 10 GPa of Li point pressures are generated with applied bias at the instant of polarization.

Li transport at interfacial zones are improved only to a certain limit dictated by the bulk diffusivity, thus temperature helps smoothen out the interfacial resistance. The interfacial resistance can be modeled as a population of many parallel RC circuits, which behave as parallel R circuits under DC load.

Poor ionic conductors would not pose this problem because the diffusion levels out quickly.

REFERENCES:

- [1] Ellingham, H. J. T. *Journal of the Society of Chemical Industry (London)* **63**, 5 (1944).
- [2] Grundy, A., Hallstedt, B. and Gauckler, L. *Journal of Phase Equilibria* **22**(2), 105–113 (2001).
- [3] Zinkevich, M. and Aldinger, F. *Journal of the American Ceramic Society* **87**(4), 683–691 APR (2004).
31st CALPHAD Meeting, Stockholm, SWEDEN, MAY 05-10, 2002.
- [4] Taylor, J., Dinsdale, A., Hillert, M. and Selleby, M. *CALPHAD-Computer Coupling of Phase Diagrams and Thermochemistry* **16**(2), 173–179 (1992).
- [5] Carniglia, S. C., Brown, S. D. and Schroeder, T. F. *Journal of the American Ceramic Society* **54**(1), 13–17 (1971).

LIST OF CONTRIBUTIONS

Publications

William Jr Manalastas, Richard Chater, Rowena Brugge, Frederic Aguesse, Lucienne Buannic, Anna Llordes, Randy Jalem, Juan Miguel Lopez del Amo, Masanobu Nakayama, Ainara Aguadero and John Kilner (2017) Tracking the lithium-proton exchange gradient in $\text{Li}_7\text{La}_3\text{Zr}_2\text{O}_{12}$ ceramics. *In preparation*.

William Jr Manalastas, Randy Jalem, Rowena Brugge, Frederic Aguesse, Lucienne Buannic, Anna Llordes, Masanobu Nakayama, Ainara Aguadero and John Kilner (2017) Mechanics of liquid-phase sintering in $\text{Li}_7\text{La}_3\text{Zr}_2\text{O}_{12}$ garnets. *In preparation*

William Jr Manalastas, Richard Chater, Jokin Rikarte, Frederic Aguesse, Lucienne Buannic, Rowena Brugge, Ainara Aguadero, Anna Llordés and John Kilner (2017). Metallic lithium propagation during cycling in polycrystalline garnet electrolyte. *In preparation*.

Frederic Aguesse, William Manalastas, Lucienne Buannic, Juan Miguel Lopez del Amo, Gurpreet Singh, Anna Llordés and John Kilner (2017) Metallic lithium formation during cycling in polycrystalline garnet electrolyte. *Submitted to ACS Applied Materials and Interfaces*.

Randy Jalem, Masanobu Nakayama, William Jr Manalastas Wang, John Anthony Kilner, Robin Grimes, Toshihiro Kasuga and Kiyoshi Kanamura (2015) Lithium Ion Conduction in the Garnet-Type Cubic $\text{Li}_5\text{La}_3\text{Ta}_2\text{O}_{12}$ Solid Electrolyte. *Journal of Physical Chemistry C*. 119(36), pp. 20783 – 20791.

Randy Jalem, Michael Rushton, William Jr Manalastas, Masanobu Nakayama, Toshihiro Kasuga, John Kilner and Robin Grimes (2015) Effects of Gallium Doping in Garnet-Type $\text{Li}_7\text{La}_3\text{Zr}_2\text{O}_{12}$ Solid Electrolytes. *Chemistry of Materials*. 27, pp. 2821 - 2831.

Carlos Bernuy Lopez, William Jr Manalastas, Juan Miguel Lopez del Amo, Ainara Aguadero, Frederic Aguesse and John Kilner (2014) *Atmosphere Controlled Processing of Ga-Substituted Garnets for High Li-Ion Conductivity Ceramics*. *Chemistry of Materials*. 26(12), pp. 3610 - 3617

LIST OF CONTRIBUTIONS

Conferences

- Oral** **William Manalastas Jr**, Randy Jalem, Carlos Bernuy-Lopez, Frederic Aguesse, Lucienne Buannic, Juan Miguel Lopez del Amo, Gurpreet Singh, Ainara Aguadero, Anna Llordés, Masanobu Nakayama and John A Kilner (2015)
A Full Study of a Garnet Ceramic Electrolyte: From Atomistic Simulation to Actual Application in Rechargeable Lithium-Metal Batteries. 20th International Conference on Solid State Ionics (USA)
- Oral** Frederic Aguesse, **William Manalastas Jr**, Lucienne Buannic, Man H Han, Juan Miguel Lopez del Amo and John A Kilner* (2015)
Ceramic processing of dense fast lithium ion conducting electrolytes in moisture-free environment
4th International Conference of the European Ceramic Society (Invited, Spain)
- Oral** **William Manalastas Jr**, Ainara Aguadero, Randy Jalem, Carlos Bernuy-Lopez, Juan Miguel Lopez del Amo, Frederic Aguesse and John A Kilner (2015)
From disorder to order: The case of the highly Li-ion-conducting $\text{Li}_{7-3x}\text{Ga}_x\text{La}_3\text{Zr}_2\text{O}_{12}$ garnet and its protonated analogue. 22^{èmes} Journées de la Diffusion Neutronique (France)
- Poster** **William Manalastas Jr**, Carlos Bernuy-Lopez, Ainara Aguadero, Juan Miguel Lopez del Amo, Frederic Aguesse and John A Kilner (2014).
Ga-substituted $\text{Li}_7\text{La}_3\text{Zr}_2\text{O}_{12}$ garnets revisited: Substitution for optimized Li-ion conductivity and aging effects. 65th Annual Meeting of the International Society of Electrochemistry (Switzerland)
- Poster** **William Manalastas Jr**, Carlos Bernuy-Lopez, Ainara Aguadero, Juan Miguel Lopez del Amo, Frederic Aguesse and John A Kilner (2014).
Effect of controlled atmosphere processing for the achievement of high conductivity Li-ion ceramics. 65th Annual Meeting of the International Society of Electrochemistry (Switzerland)
- Poster** Juan Miguel Lopez del Amo*, **William Manalastas Jr**, Nerea Lago, Frederic Aguesse, Devaraj Shanmukaraj, Oihane García-Calvo, Carlos Bernuy López, Ainara Aguadero, Anna Llordés, Michel Armand, John A Kilner and Teofilo Rojo (2014)
Performance optimization of Li+-based solid electrolytes monitored by solid state NMR. 8th International Conference on Advanced Lithium Batteries for Automobile Applications (Spain)



MANALASTAS, William Jr. W.

**Current Address:**

Avenida Gasteiz n°89-4C,
Vitoria-Gasteiz 01009 Alava, SPAIN
(+34) 644 368 732
william.manalastas.jr@gmail.com

Permanent Address:

Unit 112 Jade Garden Townhomes,
Don Pedro Village,
Valenzuela City 1440, PHILIPPINES

EDUCATION

- 2013 – 2016 **Doctoral Researcher, CIC Energigune (Spain)**
PhD Fellowship Grant.
Research-scale: Development of advanced ceramic electrolytes for safe solid-state batteries
- 2015 **Academic Visitor, Royal School of Mines - Imperial College London (UK)**
Diffusion studies with isotopic tracers, focused-ion beam etching with SIMS analyses, with short broadband impedance spectroscopy experiments at Vilnius University.
- 2010 – 2012 **Erasmus Mundus Masters Scholar, MESC track (France, Poland, Spain)**
European Union grant towards MSc in Materials Science and Electrochemistry.
Pilot-scale: Optimization of carbon powders for use in long-life lithium-ion batteries

WORK EXPERIENCE

- 2013 – 2016 **Doctoral Researcher, Solid-State Electrolytes – CIC Energigune (Spain)**
Ceramics: Pechini/solid-state production, doping chemistries, atmospheric control, crystallographic/microstructural/electrochemical analyses, prototyping
- Feb–Sep, 2012 **Research Intern, Powders and Grains Division – Saint-Gobain (France)**
Carbons: graphitization, powder processing (particle size, grain morphology, elemental purity, porosity control), compositing and battery implementation
- Jan–Feb, 2012 **Research Trainee, Surface Treatments Team – CIRIMAT (France)**
Fabrication of anodized/electrocolored AAO/Al substrates for Airbus, Toulouse
- May–Jul, 2010 **Metrobank Foundation Fellow, World Expo 2010 Shanghai (China)**
Cultural liaison/English-Chinese-Japanese translator for government VIPs
- 2009 **Assistant Lecturer, Chemistry Department, De La Salle University (Philippines)**
Taught inorganic and organic chemistry courses (laboratory component) for biology, chemistry and engineering majors.
- 2007 - 2008 **Research Assistant, Kasai Laboratory, Osaka University (Japan)**
Computational chemistry research on phthalocyanines and Pt-based compounds for anticancer applications; refereed scientific papers; submitted conference report on the Computational Materials Design Workshop 2008

WORKSHOPS ATTENDED

- Feb 16-18, 2015 **Internal FULLPROF School on Rietveld Refinement**
Institut Laue-Langevin, Grenoble (France)
- Sep 21-26, 2014 **22nd Meeting/School on Neutron Scattering**
French Neutron Society, Ile d'Oleron (France)
- Mar 4-8, 2008 **12th Computational Materials Design Workshop**
Japan Society for the Promotion of Science Core-to-Core Program "Computatio
Nanomaterial Design" (Japan)
- May 10, 2007 **3rd International Workshop on Oxidation reactions**
Spring-8, Japan Atomic Energy Agency and Osaka University (Japan)

UNDERGRADUATE BACKGROUND

- 2004 – 2008 **BSc in Chemistry, October 2008.**
Summa cum laude. De La Salle University – Manila (Philippines)
Consistent First Honors Dean's Lister (entire stay). Inducted into Jose Rizal Honors Society.
Ongking Foundation Scholarship Recipient (100% tuition & fees waived).
JASSO Short-term Student Exchange Scholarship (Osaka University, Japan – 1 year)
LICENSED CHEMIST (2nd highest out of 544 board exam takers nationwide)
Company orientor: 2006 on-campus Job Expo (affiliation: Office of Career Services)

PERSONAL DETAILS

- Birth:** Filipino-Chinese. Born on May 25, 1987 in Manila, Philippines.
- Languages:** English, Chinese, Spanish, Filipino (fluent), Japanese (JLPT2)¹
- Software:** DiffracEVA, FULLPROF, ImageJ, CASINO, SRIM,
Zview/Zplot (Scribner Associates), EC-Lab, Gaussian03
- Techniques:** XRD, SEM-EDX, EIS, ball-milling, powder sieving, spray-drying
Experience with neutron time at ISIS (UK) and ILL (France)
- Character :** Versatile, pragmatic and diligent

REFERENCES

- | | | |
|---|---|---|
| Prof. John A. Kilner
BCH Steele Professor of Energy
Materials, Royal School of Mine
Imperial College, London
UNITED KINGDOM
+44 (0) 207 594 6745
j.kilner@imperial.ac.uk | Frederic Aguesse, PhD
Postdoctoral Researcher
Solid Electrolytes Group
CIC Energigune, Miñano
SPAIN
+34 945 297 108
faguesse@cicenergigune.coi | Nancy Lazaro-Llanos, PhD
Professor
Chemistry Department
De La Salle University - Manila
PHILIPPINES
+63 2 524-4611
llanosn@dlsu.edu.ph |
|---|---|---|

¹ JLPT stands for Japanese Language Proficiency Test. Five certification levels are attainable. Level 1 is the highest. JLPT level 1 is the level of a "native Japanese speaker."







Development of ceramic lithium ion electrolytes for high performance batteries

A key enabler for all-solid-state batteries is an electrolyte with superior ion conductivity, closed porosity and mechanical resilience.

In this work, a superionic lithium-conducting ceramic ($>10^{-3}$ mS/cm) belonging to the garnet-structured oxide class was discovered via systematic syntheses. Its crystallography, sintering, aging, and behaviour with battery cycling were investigated.

The analyses carry practical insights important for the industrial scale-up of this material. For instance, a mechanism describing how metallic lithium dendrites form and propagate across a rigid ceramic electrolyte is proposed, along with possible strategies on how to mitigate it.

